UNIVERSITY OF BIRMINGHAM

OPTIMIZATION of SMALL-SCALE AXIAL TURBINE FOR DISTRIBUTED COMPRESSED AIR ENERGY STORAGE SYSTEM

By

Ali Bahr Ennil

Thesis Submitted in Partial Fulfilment of Requirements for the Degree of

Doctor of Philosophy

School of Mechanical Engineering
College of Engineering and Physical Sciences
The University of Birmingham
Edgbaston, Birmingham, UK
December - 2016

ABSTRACT

Small scale distributed compressed air energy storage (D-CAES) has been recognized as a promising technology which can play a major role in enhancing the use of renewable energy sources with affordable cost, environment friendly and flexible operation. Small D-CAES is a technology that is still under development and further research is required for improving the system overall efficiency. Due to the transient behaviour of the compressed air during the discharging phase, there are significant variations in air pressure, temperature and mass flow rate resulting in low turbine efficiency (18-52%). This research aims to improve the expansion process of the small scale D-CAES system through optimization of a small scale axial turbine that can operate efficiently over a wide range of operating conditions leading to higher efficiency.

Based on the dynamic modelling of the proposed small D-CAES using Matlab/Simulink, a small scale axial air turbine (1kW) has been developed using 1D Meanline approach and CFD modelling using ANSYS CFX 16.2. The turbine's performance was investigated for different blade profiles and the total losses were predicted using traditional loss schemes and CFD simulation. For improving the turbine efficiency, different optimization approaches like single and multi-operating point optimization were performed based on 3D CFD turbine modelling.

The turbine blade profiles for both stator and rotor have been optimized for minimum losses and maximum power output based on 3D CFD modelling and Multi Objective Genetic Algorithm (MOGA) optimization technique for single and multi-operating points. The single operating point optimization could increase turbine total to static efficiency at the design point by 7.56% through blade profile optimization for both

maximum efficiency and maximum output power. To achieve higher efficiency levels during off design operating conditions, multi-operating point optimization was performed for a range of mass flow rate. Using multi-operating point optimization, the maximum turbine total to static efficiency of 82.767 % was achieved at the design point and this approach improved the overall efficiency of D-CAES system by 8.07% for a range of inlet mass flow rate indicating the potential of this optimization approach in turbine design development. For more reliable turbine design, multidisciplinary optimization was conducted using CFD and finite element analysis (FEA) to ensure that the optimized aerodynamic blade profile can withstand the mechanical stresses. The multidisciplinary optimization approach could reduce the total equivalent stresses from 49.715 MPa to 41.729 MPa while maintaining the turbine total to static efficiency at 80.95%.

The developed design methodology was validated as a powerful design tool by manufacturing and testing the developed small axial turbine. By comparing the CFD simulation results with the experimental data, there were observed deviations with 16.5% and 12% in efficiency and power output respectively which can be reduced by considering the surface roughness in turbine CFD simulation. This method has improved the D-CAES overall efficiency by 8.07% thus reducing the effect of transient behaviour of the compressed air and improves the discharging phase through turbine design optimization.

ACKNOWLEDGEMENTS

I would like to express the deepest gratitude to my supervisor Dr. Raya Al-Dadah, for her continuous support of my PhD research, her patience, her motivation and her immense knowledge. Her guidance helped me in the entire time of my research, writing research papers, and writing of my thesis. Dr. Raya has supported me by providing not only research guidance, but also academically and emotionally during the difficult times to finish this research by giving support and the freedom I needed to develop.

I would like to thank Dr. Saad Mahmoud for his insightful comments, invaluable suggestions and encouragement through the period of my PhD research. His scientific guidance, his immense knowledge and his support in all of the research work are invaluable for the completion of my thesis.

Besides my supervisors, I have to thank Mr Simon Rowan for helping me to construct my test rig and for his continuous assessment and commissioning of the test facilities.

My sincere thanks also go to my Mother for her prayers, my Wife for her patience and my friends for their moral support during my PhD study.

Ali Bahr Ennil

2016

CONTENTS

LIST OF FIGURES

LIST OF TABLES

NOMENCLATURE

Symbols	Description	Unit
A	Area	[m^2]
b	Turbine blade span	[m]
c	Turbine blade chord	[m]
C	Flow absolute velocity	[m/s]
C_D	Drag Coefficient	[-]
C_θ	Tangential velocity	[m/s]
C_L	Lift Coefficient	[-]
Cp	Specific heat	[J/kg.K]
d	Diameter	[m]
D	Drag Force	[N]
F	Force	[N]
h	Static enthalpy	[J/kg]
ho	Total enthalpy	[J/kg]
i	Incidence angle	[degree]
K_P	Mach number Factor	[-]
L	Lift Force	[N]
m	Mass	[kg]
$\dot{m}$	Mass flow rate	[kg/s]
Ma	Mach number	[-]
N	Number of blades	[-]
P	Static pressure	[Pa]
Po	Total pressure	[Pa]

p_i	Initial tank pressure	[Pa]
p_f	Final tank pressure	[Pa]
Q	Heat transfer	[W]
r	Radius	[m]
R	Degree of reaction	[-]
Re	Reynolds number	[-]
s	Turbine blade pitch	[m]
S	Entropy	[J/kg.K]
T	Static temperature	[K]
To	Total temperature	[K]
U	Blade speed	[m/s]
V	Volume	[m^3]
V_i	Initial air volume	[m^3]
V_f	Final air volume	[m^3]
W	Work	[W]
w	Flow relative velocity	[m/s]
ΔW	Specific work	[W/kg]
x_i	Incidence factor	[-]
X_{Te}	Trailing Edge Correction factor	[-]
Y	Losses coefficient	[-]
Y_k	Tip Clearance Loss	[-]
Y_N	Nozzle Pressure Loss Coefficient	[-]
Y_R	Rotor Pressure Loss Coefficient	[-]
Y_s	Secondary Loss Coefficient	[-]

Y_{shock}	Loss due to shocks	[-]
Z	Zweifel's coefficient	[-]

Greek symbols	**Description**	**Unit**
α	Absolute flow angle	[Degree]
β	Relative flow angle	[Degree]
η	Turbine efficiency	[-]
μ	Flow viscosity	[Pa.s]
ρ	Flow density	[kg/s]
ω	Rotational speed	[RPM]
$\emptyset$	Flow coefficient	[-]
ψ	Loading coefficient	[-]
τ	Tip clearance	[mm]
ζ^*	Nominal loss factor	[-]
γ	Specific heat ratio	[-]
π	Pressure ratio	[-]
δ	Deviation angle	[Degree]
ε, ε	Deflection angle, Dissipation rate	[Degree], [m^2/s^3]
θ	Camber angle	[Degree]
σ	Stress	[Pa]
ζ_N	Nozzle Loss Coefficient	[-]
ζ_R	Rotor Loss Coefficient	[-]
$\Delta\eta$	Efficiency change	[-]
η_o	Efficiency at zero clearance	[-]

Subscripts	**Description**
hub	Blade hub
m	Blade mean
tip	Blade tip
tt	Total to total

ts	Total to static
th	Thermal
$stage$	Turbine stage
i	Incidence
θ	Tangential component
r	Radial component
in	Turbine rotor inlet
out	Turbine rotor outlet
t	turbine
c	compressor
i	Initial state
f	Final state

Acronyms	**Description**
A-CAES	Adiabatic compressed air energy storage
ANN	Artificial Neural Network
CAES	Compressed air energy storage
CFD	Computational Fluid Dynamics
CHP	Combined heat and power
CPG	Centralized power generation
D-CAES	Distributed compressed air energy storage
DOE	Design of experiments
DPG	Distributed power generation
FEA	Finite element analysis
GA	Genetic algorithm

HTF	Hot thermal fluid
ICE	Internal combustion engine
MOGA	Multi objective genetic algorithm
OF	Objective Function
ORC	Organic Rankine Cycle
PCM	Phase Change Material
PHS	Pumped hydroelectric storage
PV	photovoltaic
RANS	Reynolds averaged Navier-Stokes
RTD	Resistance temperature detector
SMES	Superconducting magnetic energy storage
SST	Shear stress transport
TES	Thermal Energy Storage
TIT	Turbine inlet temperature

LIST OF PUBLICATIONS

[1] Bahr Ennil, A., Mahmoud, S. Al-Dadah, R. "Minimization of loss in small scale axial air turbine using CFD modelling and evolutionary algorithm optimization. " Applied Thermal Engineering, 2016. 102: p. 841-848.

[2] Bahr Ennil, A., Mahmoud, S. Al-Dadah, R. Al-Jubori, A. "Optimization of Small Scale Axial Air Turbine Using ANSYS CFX." International Journal of Mechanical and Production Engineering, 2015. (3):59-62.

[3] Bahr Ennil, A., Mahmoud, S. Al-Dadah, R. and Rahbar, K. (2015). "Prediction of Losses in Small Scale Axial Air Turbine Based on CFD Modelling." Elsevier, *Energy Procedia* **75:**3271-3276.

[4] Rahbar, K., Mahmoud, S., Al-Dadah, R. and Bahr Ennil, A. (2015). "Preliminary mean-line design and optimization of a radial turbo-expander for waste heat recovery using organic Rankine cycle." Elsevier, *Energy Procedia* **75:**860-866.

[5] Bahr Ennil, A., Mahmoud, S., Al-Dadah, R. "Improvements in Distributed Compressed Air Energy Storage Efficiency through Turbine Multi-operating Point Optimization." Proceedings of Engineering & Technology (PET), 2016.

[6] Al-Jubori, A., Al-Dadah, R., Mahmoud, S., Bahr Ennil, A. "Development of Efficient Small Scale Axial Turbine for Solar Driven Organic Rankine Cycle." Turbomachinery Technical Conference and Exposition, 2016, Seoul, South Korai.

CHAPTER 1

INTRODUCTION

1.1 General Background:

In recent years, electricity consumption has increased due to significant growth of world population. This increase in electricity demand results in excessive consumption of conventional fossil fuels leading to significant increase in CO_2 emissions. According to the International Energy Agency (IEA), the expected trend of energy consumption shows an increase in energy demand of 70% by 2050 with 60% increase in global emissions (Agency 2014). The future scenario of energy production proposed by IEA aims to reduce the average temperature rise from 6^oC to 2^oC by 2050 through reducing CO_2 emissions. The general frame work proposed by IEA aims to create sustainable environmental friendly power generation systems based on distributed power generation (DPG) technology instead of the traditional centralized power generation (CPG). The power generation based on traditional CPG plants leads to 12% losses in delivered energy through transmission lines with an increase of 30 % in fuel consumption (Council 2013) and similar increase in CO_2 emissions. In this regard, great efforts have been carried out by EU to save 20% of the energy by 2020 using CPG systems based on renewable energy sources particularly in residential sector which consume around 27% of the total energy in EU (Micro 2010).

DPG system is a small on-site power generation plant which can generate electricity locally. This small generation unit is simple compared to conventional steam CPG systems. It can be operated at low temperature and pressure which can be achieved using low grade heat sources or renewable energy sources.

Chapter1: Introduction

Distributed power generation systems are classified according to cycle capacity into: micro DPG (1 W to 5 kW); small DPG (5 kW to 5 MW); medium DPG (5 MW to 50 MW); and large DPG (50 MW to 300MW). The importance of using distributed power generation systems is that their ability to reduce thermal losses and transmission losses through the grid which reach 30% in centralized power generation (Ackermann, et al. 2001).

The integration of DPG systems with renewable energy sources like photovoltaic and wind turbines is gaining the interest of many power production projects for more financial and energy savings with lower emissions. Although the technology of power generation using renewable energy sources has matured, it cannot meet consumer's electricity demand due to significant changes in weather conditions which make solar and wind uncontrollable and unpredictable energy sources. To enable further increase in using renewable resources in DPG there is a great need to implement energy storage technology to maintain electricity supply and provide controllable operation.

There are different storage technologies which are able to store energy in different forms (mechanical, electrical, and thermal) according to application, cost, safety, and life time. Batteries are the classical common storage technology for short life applications, however, they cannot fulfil long life cycle and recycling requirements (Lemofouet and Rufer 2005). Alternative energy storage solutions for long term and high storage capacity include compressed air energy storage (CAES) system.

Large scale CAES technology is a proven technology and its history goes back to the first power plant in 1978 Huntorf, in Germany with large underground cavern and could generate 290 MW for four hours. The second compressed air plant was McIntosh Alabama in USA which generated 110 MW for 26 hours (Safaei and Keith 2014). The power generation process in conventional CAES includes using the stored air for the combustion of fuel to

produce gases at up to 550^{o}C which increase the fuel consumption and CO2 emissions (Loose 2011). Also, there is a significant loss in heat during the compression stage which affects the cycle efficiency. Furthermore, the development of conventional CAES based on renewable energy has limitations due to the complex geological characteristics of large underground caverns (Fort 1983, et al. 2014).

Small D-CAES is an alternative option for distributed power generation based on compressed air energy storage with high pressure man-made vessels. This option is a promising technology for stand-alone power generation at consumption point based on wind and solar energy applications. In D-CAES the air is compressed and then stored in pressurized cylinders up to 300 bars for distributed power cycle with an overall efficiency reaching 50% (Ibrahim, et al. 2008).

The small D-CAES offers many advantages which include: long cycle time, safe technology, environmental friendly, high storage capacity compared with batteries, can be integrated with renewable energy sources for cost effective electricity supply, less installation restrictions, appropriate for small and micro power generation, non-toxic and simple manufacturing.

In the literature review, limited studies have been conducted on the developments of small D-CAES system. According to the literature review conducted by Venkataramani et al. (2016), Miroslav et al. (2013), Li et al. (2012), Villela et al. (2010), KIM et al. (2010), Paloheimo et al. (2009), Grazzini et al. (2008) and the future developments of small D-CAES systems depends on the integration of the system with renewable sources like solar and wind energy and adapting the system with high efficiency small compression and expansion devices. Also the small D-CAES technology is still under development and further in-depth research is required to achieve efficient and reliable systems. The main challenges associated with developments of small D-CAES include improving both compression and expansion phases (Luo 2013, Petrov, Arghandeh et al. 2013, Luo 2014).

In D-CAES systems, the small turbine is the main component which is used for power recovery by converting the energy stored in the compressed air to mechanical power. The overall performance of D-CAES system is strongly affected by turbine efficiency, operating conditions, and heat source (Bao and Zhao 2013, Saadatfar, et al. 2013). The design of high efficiency small turbine is the main important part in developing the D-CAES cycles. High efficiency small scale turbine (1-10kW) that can be operated using low temperature heat source with economic operation cost and low emission is still a great challenge in the field of power generation systems and many researchers are working to develop novel turbines with high efficiency and minimum cost(Qiu 2011). The existing gap in developing the expansion process of small D-CAES system is the design optimization of small scale axial turbine to achieve high efficiency in both on and off design operating conditions.

1.2 Research Objectives:

As discussed in the previous section, the small D-CAES system is a new technology and there is a great need to improve the system's overall performance through enhancing the compression and expansion processes. For the expansion process, the small turbine is the key component that affects the cycle overall performance. In D-CAES system the small turbine works in off design mode for long time due to the transient characteristics of compressed air leading to low efficiency levels. This research aims to improve the expansion process of the small D-CAES by developing an efficient small scale axial air turbine based on CFD modelling and design optimization. This can be achieved through the following objectives:

- Detailed dynamic modelling using Matlab/Simulink for the thermodynamic cycle of a small D-CAES system based on solar energy. The cycle dynamic modelling aims to define the stored capacity of the system, charging /discharging energy, charging/discharging time, and turbine design specification like output power, mass flow rate, and inlet pressure.

- Developing a new small scale axial air turbine using one dimensional meanline modelling for preliminary turbine design based on the D-CAES thermodynamic analysis. This initial design is followed by CFD modelling for better aerodynamic performance.
- Predicting the total aerodynamic loss for both stator and rotor using CFD simulation for more accurate performance and to investigate the impact of blade profile geometry on development of losses at different operating conditions.
- Improving the turbine efficiency by performing different optimization techniques including single and multi-operating point optimization. The multi-operating point optimization aims to improve the turbine performance for a range of operating conditions. Also performing multidisciplinary optimization in order to optimize the blade profile for maximum efficiency and minimum stresses at the same time to ensure that the optimum aerodynamic design does not conflict with mechanical design requirements.
- Manufacturing a prototype of the developed small axial turbine and constructing a test rig facility based on compressed air in order to validate the design methodology by comparing experimental results with turbine CFD simulation.

1.3 Thesis Outlines:

This thesis is divided into eight chapters. Chapter one provides a general introduction about the research background and thesis objectives. Chapter two reviews the distributed power generation systems, energy storage technologies, small scale expander's availability, design, and developments. Chapter three introduces a detailed thermodynamic analysis of small D-CAES cycle based on solar energy. Chapter four describes the design methodology of the axial turbine based on 1D meanline modelling, CFD simulation and mechanical design.

Chapter five describes different optimization techniques and explains the turbine optimization process based on 3D CFD modelling. Chapter six provides a detailed description of the test rig facility, measuring instruments, and uncertainty analysis. Chapter seven discusses the results of design methodology and experimental validation of the developed turbine. Chapter eight summarises the main findings and conclusions of this research.

CHAPTER 2

LITERATURE REVIEW ON DISTRIBUTED POWER GENERATION SYSTEMS

2.1 Introduction:

Distributed power generation (DPG) has become an attractive technology for reliable, clean, and cost-effective electricity generation. The trend has been set towards more developments in the DPG systems due to the rapid increase in energy demand, excessive consumption of fossil fuels, global warming concerns and significant energy loss in transmission lines for centralized power plants. This chapter provides a comprehensive literature review of DPG systems, working principles, applications and the expanders used as a key component in such DPG systems.

2.2 Distributed Power Generation Definition:

Although the technology of DPG is widespread over the world, there is still no consistent universal definition of the DPG. In the literature, the DPG is generally defined based on two aspects which are the location and power rating (Bhadoria, et al. 2006). According to the location, the DPG system is defined as a power generation unit which is installed on-site at the consumption point or connected directly to the distribution grid (Fraser 2002).

According to the power capacity of DPG system, there are many definitions in the literature as shown in Figure 2.1 which classifies the DPG systems based on the power rating into micro, small, medium, and large (Ackermann, et al. 2001).

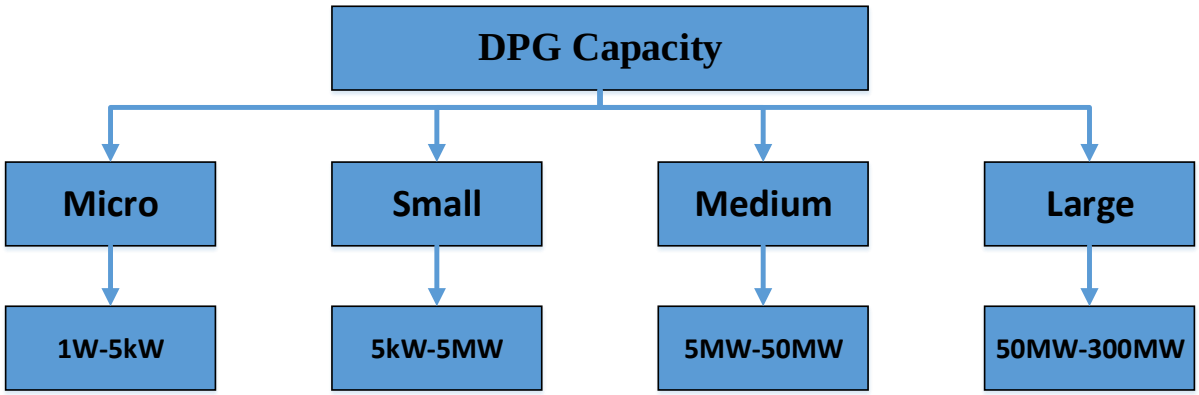

Figure 2.1 Distributed power generation power rating (Ackermann, et al. 2001).

The classification of DPG based on power rating varies over countries and international organizations as follows:

- The DPG is defined by the USA Department of Energy as a power generation system with a capacity of 1 kW up to 10 MW (Bhadoria, et al. 2006).
- The California Energy Commission defines the DPG as a small generation unit with power rating of 3 kW to 10 MW (Association 2016).
- The American Gas Association defines the DPG as systems with power rating of 5 kW up to 25 MW (Bhadoria, et al. 2006).
- The IEEE refers to the DPG as a small power unit which is connected directly to the consumption point with power rating less than 10 MW(L'Abbate, et al. 2007).
- According to the International Council on Large Electricity Systems, the power rating of DPG systems is 50 kW to 100 MW (Fraser 2002).
- The Electric Power Institute defines DPG as a small generation system with power capacity less than 20 MW (Gonzalez-Longatt and Fortoul 2002).

- The DPG systems are treated as the generation units with power rating up to 1,500 kW in Sweden, up to 300 MW in Germany, and up to 100 MW in England (Ackermann, et al. 2000, El-Khattam and Salama 2004).

Based on the previous discussion, there are many definitions of DPG systems with a wide range of power rating. For the purpose of this research and to avoid any confusion, the DPG has been defined as a small on-site power generation unit with power capacity of 1 kW up to 10 MW.

2.3 Distributed Power Generation Drivers:

The use of DPG systems for electricity generation is driven by many factors which increased the interest in small DPG developments. These drivers can be classified into environmental concerns, electricity market and national policy (Lopes 2007).

2.3.1 Environmental Drivers:

Due to the high consumption of fossil fuels by centralized power plants and other power generation systems, two thirds of gaseous emissions originate from the electricity generation sector (EPA 2011). In order to limit the air pollution and greenhouse effect, there is a need to integrate the DPG systems with renewable energy sources and CHP cycles. The other environmental aspects include avoiding the noise associated with large power units and large transmission networks. In this regard, small and medium DPG units based on renewable energy sources and waste heat from industrial processes can be a promising solution to reduce environmental concerns with cost effective solutions (Pepermans 2005, Lopes 2007).

2.3.2 Market Drivers:

The electricity generation market plays a major role in the development of DPG systems. The market players are looking for reliable DPG systems with lowest financial risks. For this reason, the DPG units with lower capital installation cost and lower maintenance demand are favoured by the electricity market. Furthermore, independent electricity generation in isolated areas and near to the load centre can improve the operation reliability and the power quality (Lopes 2007).

2.3.4 National Regulation Drivers:

To decrease the concerns about the energy security, the main focus of energy policy is how to keep the electricity generation secure and sustainable. The failure of centralized power plants has serious economic, social, and political impacts on the community. The small and medium DPG systems with quick installation and low starting time can be effective in emergency situations and can overcome the power capacity shortfalls at lower prices (Pepermans 2005, Martin 2009).

2.4 Overview of DPG Technologies:

For the purpose of distributed power generation, there are numerous technologies which are selected based on installation cost, level of CO_2 emissions, energy source, power rating and sustainability (L'Abbate, et al. 2007). The DPG technologies can be classified into non-renewable technologies (traditional generation) and renewable technologies or non-traditional technologies as shown in Figure 2.2 (El-Khattam and Salama 2004). The following sections introduce the various DPG technologies and their applications and a detailed comparison between these technologies are presented in Table 2.1.

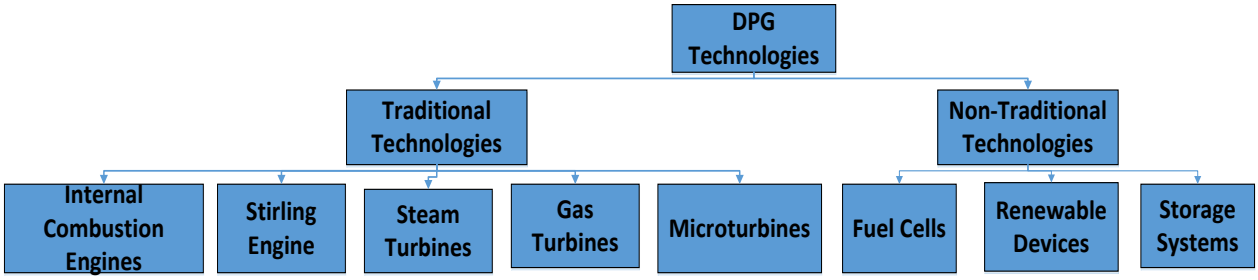

Figure 2.2 Classification of DPG technologies (El-Khattam and Salama 2004).

Table 2-1 Distributed power generation technologies

Technology	**Power rating**	**Application**	**Efficiency**	**Fuel type**	**Starting time**	**Emission [kg/MWh]**	**Capital Cost [€/kW]**	**Operation cost [€/MWh]**	Availability
Internal Combustion Engine	5kW-10MW	Stand by emergency generation	25-48% Up to 85% in CHP	Diesel Natural gas	10s-1min	Co_2:430-760 Co:0.2-27 NO_x:0.2-24	300-1400	5-20	Mature
Gas Turbines	1-250MW	Emergency power supply and CHP	20-45% Up to 80% in CHP	Gaseous-hydrocarbons-kerosene	2min-10min	Co_2:480-1030 Co:0.5-0.55 NO_x:0.2-4.3	200-1900	3-10	Established
Microturbine	30kW-1MW	DPG and CHP	14-30% up to 70%in CHP	Natural gases biogas	30s-2min	Co2:580-870 Co:0.2-0.8 NOx:0.9-0.6	600-2600	5-20	Established/ under development
Stirling Engine	2-10kW	DPG and CHP	12-30% up to 80%in CHP	hydrocarbon biogas – solar energy	Not obtained	Co2:670 Co:0.5 NOx:0.4	Not obtained	Not obtained	under development
Fuel cells	50kW-1MW	Transport and DPG		Methanol	Not obtained	Not obtained	Not obtained	5-40	Established/ under development
Solar PV	20W-100kW	DPG	5-25	Solar radiation	0-1min (optimal)	zero	3000-7000	1-4	Mature
Solar Thermal	1-10MW	DPG and CHP		Solar radiation	0-1min (optimal)	zero	Not obtained	Not obtained	Established/ under development
Wind Turbine	200W-3MW	Power generation	20-50	Wind energy	0-1min (optimal)	zero	800-3000	10-20	Mature

2.4.1 Non-renewable (Traditional) Technologies:

The DPG using these technologies is based on traditional power generation systems with small sizes and power rating. These traditional technologies include:

2.4.1.1 Internal Combustion Engines:

Reciprocating engine is an internal combustion (IC) engine which burns fossil fuels using compressed air and the energy released is used to move the pistons to drive electrical generator. The IC engines are widely used for DPG based on Diesel and Otto cycles coupled with electrical generator as shown in Figure 2.3. The power rating range of IC engines is 1kW up to 50MW with an average efficiency of 30-48% and 1500-3000RPM (L'Abbate, et al. 2007). The DPG using ICES increases the environmental pollution with combustion products like CO, CO_2, and NO_x gases. Furthermore, the high noise levels during engine operation, high operation cost, and maintenance demands are issues that limit their use (L'Abbate, et al. 2007, Martin 2009).

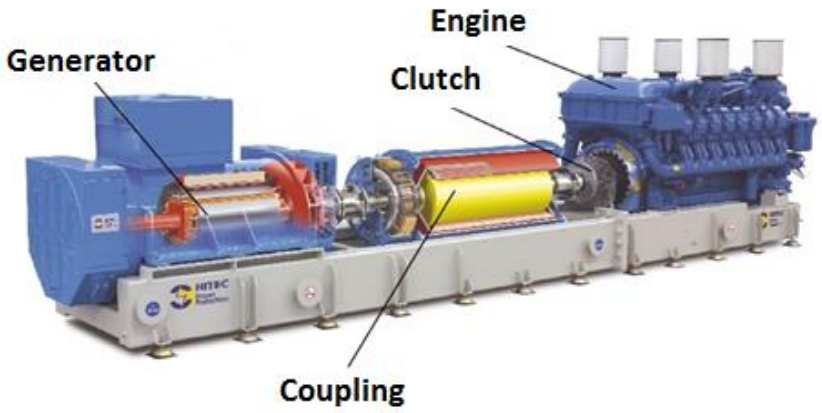

Figure 2.3 ICE coupled with electrical generator (L'Abbate, et al. 2007).

2.4.1.2 Stirling Engine:

This engine is an external combustion engine which converts the temperature difference between engine ends into useful mechanical power. The heat energy is generated by burning the fuel and air externally with limited CO_2 emissions compared to ICE. Figure 2.4 shows a typical Stirling engine with power rating of 55kW. The average efficiency range of the Stirling engine is 25-30% and the amount of dissipated heat in this engine is higher than the output power. The Stirling engine faces many technical issues which include starting up time, output power control, and overheat during high loads (L'Abbate, et al. 2007).

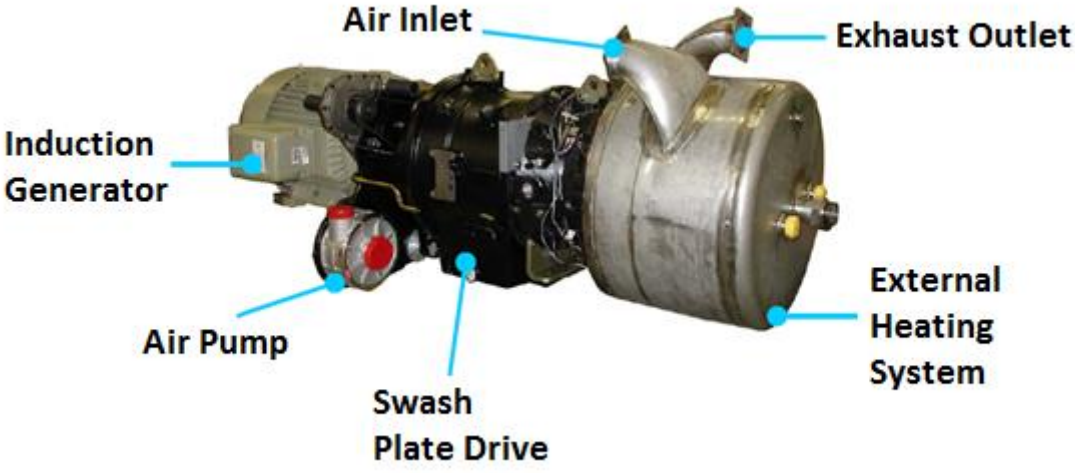

Figure 2.4 Typical Stirling engine with capacity of 55kW (L'Abbate, et al. 2007).

2.4.1.3 Steam Turbine System:

A steam turbine cycle can be used for small and large DPG applications with power rating from 50kW to 100MW. Figure 2.5 shows a steam turbine cycle in which the water is pumped and heated in the boiler by burning different fuels to generate high pressure steam. The high pressure steam then expands through a turbine to produce mechanical energy for the electrical generator

operation. After the expansion process, the steam is condensed to be circulated again in the cycle. The steam turbine cycle is used for combined heat and power (CHP) applications at higher cycle efficiency (L'Abbate, Fulli et al. 2007). The steam turbine cycle can burn different fuels like coal, wood, oil, and natural gases. The emission level of this system depends on the used fuel and emission control is required to reduce NO_x.CO, and CO_2 gases (Goldstein 2003).

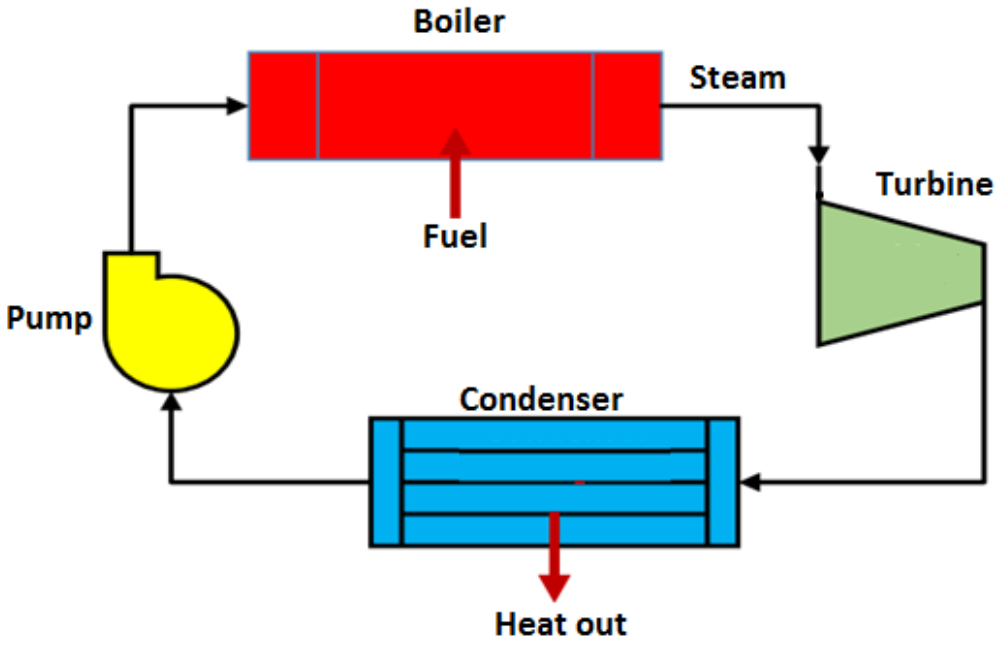

Figure 2.5 Steam turbine cycle components.

2.4.1.4 Gas Turbine System:

Gas turbine technology is available for DPG with power range of 500kW to 25 MW. It is commonly used as standby power units for peak shaving, and grid support (Goldstein, et al. 2003). The gas turbine system works based on a Brayton cycle as shown in Figure 2.6. In this cycle, the compressor is used to compress the atmospheric air to high pressure and this air is heated by burning fuel in the combustion chamber. The hot combustion products expand in the turbine which drives an electricity generator. Compared to steam turbine system, the gas

turbine has higher efficiency and higher power rating as a result of higher turbine inlet temperature and inlet pressure. Due to the high power of the gas turbine system, it is suitable for on-site electricity generation in industrial applications. For more cost effective operation, gas turbine units are operated in combined cycles of gas and steam turbine cycle configuration where the steam turbine cycle extract the high thermal energy in the gas turbine exhaust as shown in Figure 2.7. The gas turbine has high installation cost, high emissions, and regular maintenance demands (L'Abbate, et al. 2007).

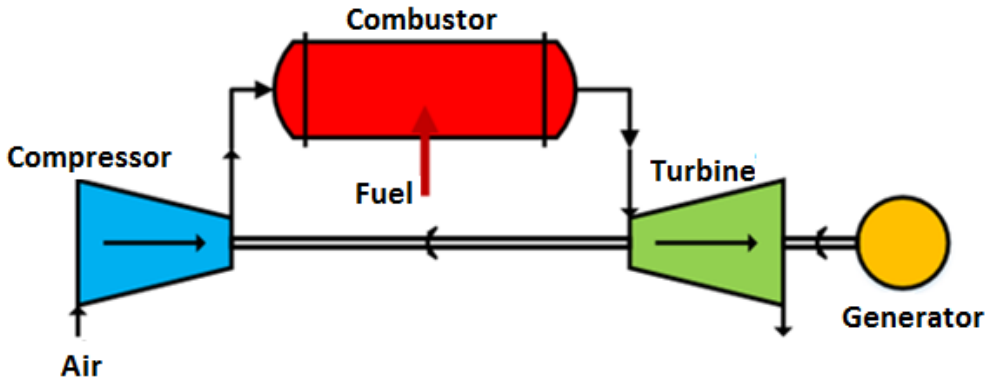

Figure 2.6 Gas turbine cycle components.

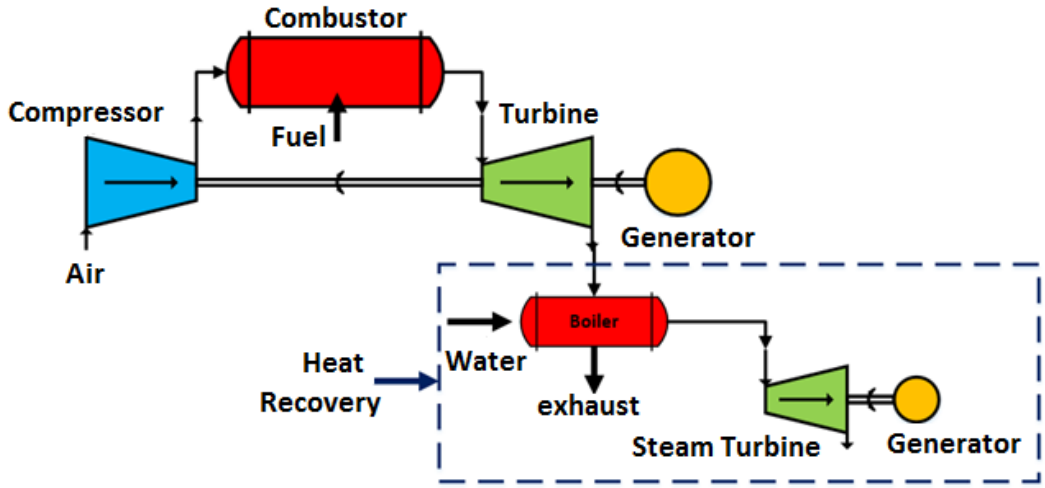

Figure 2.7 Gas turbine cycle with heat recovery system (Rahbar 2016).

For on-site DPG and CHP application, there is also microturbine which is very small gas turbine with power rating from 30kW up to 400kW as shown in Figure 2.8 (Goldstein, et al. 2003). Similar to large gas turbine units, the microturbine has high exhaust temperature (around 400^{o}C) which makes this technology attractive for waste heat recovery application like integration with small Organic Rankine Cycle (ORC) as shown in Figure 2.9. Compared to the ICEs, microturbine is simple DPG technology with higher efficiency and power rating and lower maintenance demands. However, there are some concerns of using microturbine in DPG which include high capital cost and high emission levels. Furthermore, the overall cycle performance require enhancement by improving the compressor and turbine design which experience high pressure loss due to small size (Goldstein, et al. 2003, L'Abbate, et al. 2007).

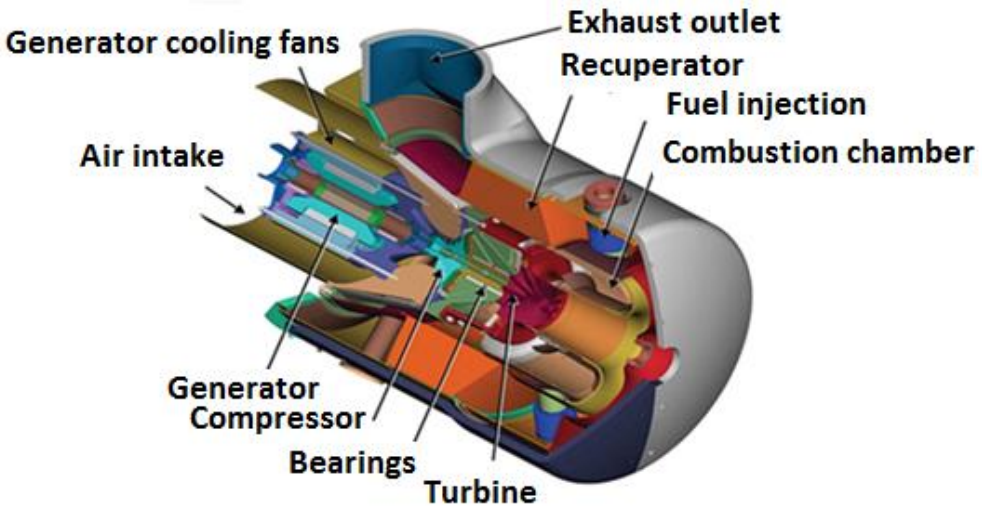

Figure 2.8 Microturbine system components (Goldstein, et al. 2003).

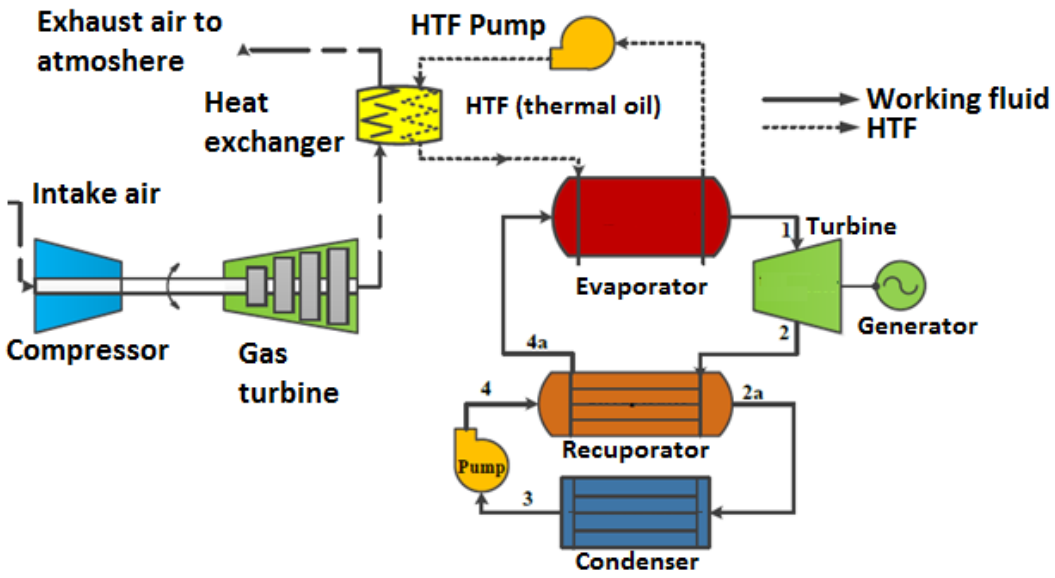

Figure 2.9 Microturbine integrated with ORC (Rahbar 2016).

2.4.2 Renewable DPG Technologies:

Distributed generation systems based on renewable energy sources play a major role in reducing the excessive consumption of fossil fuels with lower installation requirements and cost-effective energy operation. The DPG renewable technologies include:

2.4.2.1 Fuel Cells:

The fuel cell is a clean electricity generation technology based on electrochemical process for converting the chemical energy to electricity with an efficiency of around 60% and power rating from several kW to 6 MW (El-Khattam and Salama 2004). Fuel cells use different hydrogen rich fuels like propane, natural gases, biofuels and gasoline which react with oxygen producing DC current in each fuel cell. The DC current is converted to AC using a power

subsystem and the total output depends on the fuel type, number of cells and operating temperature which varies from ambient temperature to 200^{o}C (Hughes 2001, Rahman 2001).

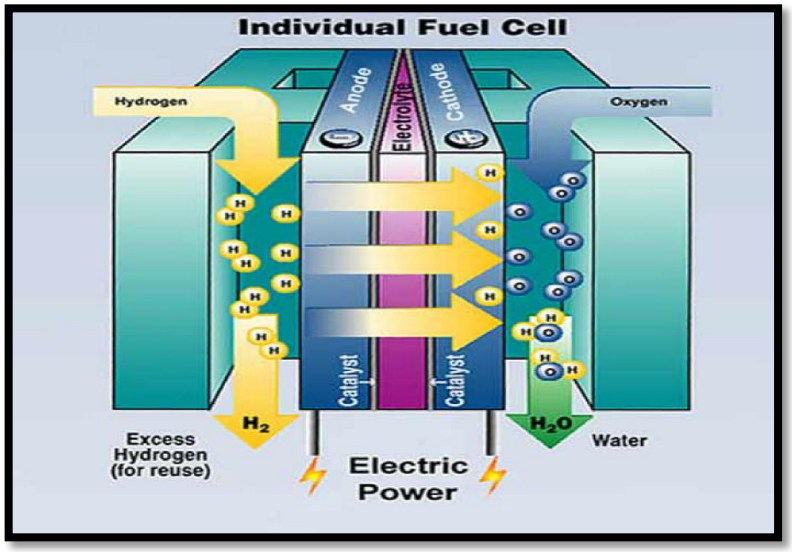

Figure 2.10 Fuel cell components (Hughes 2001).

Figure 2.10 shows a typical fuel cell device which contains two electrodes. The first electrode is known as anode and the second is named cathode. The fuel is passed through the anode and the air is fed through the cathode. Compared to traditional DPG technologies, the fuel cells provide cost effective power with low emission level. However, the hydrogen reforming process occurs at high temperature with a significant amount of wasted energy through the reformation device (Ellis, et al. 2001, Farooque and Maru 2001).

2.4.2.2 Solar Energy:

Solar photovoltaic panels convert the solar radiation into electrical energy. The PV cells generate DC current which is converted to AC using electrical converters a shown in Figure 2.11(L'Abbate, al. 2007). The PV cells can also bypass the solar radiation to DPG cycles to operate mechanical generators (Zobaa and Cecati 2006).

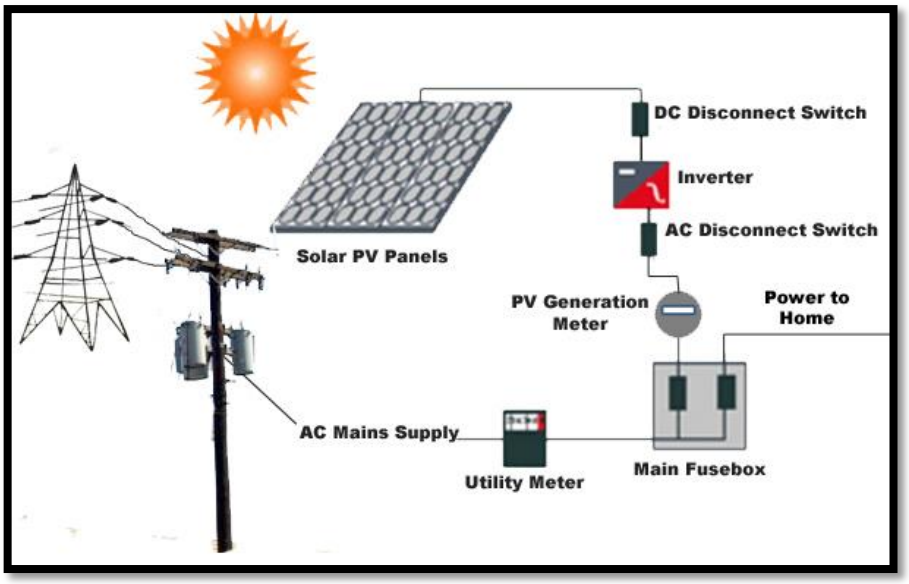

Figure 2.11 Electricity generation using solar PV (map watt 2015)

The PV cells are attractive technology for small DPG application with cost zero emissions. However, the PV cells have some limitations which include large space requirements for system installation, high installation cost, low power rating and implementation of high energy storage capacity technology is required for controlled and predictable operation (El-Khattam and Salama 2004, Zobaa and Cecati 2006).

The solar thermal energy can be used for DPG based on concentrated power units in which the solar collectors are used as a heat source in small thermodynamic cycles for energy conversion applications as shown in Figure 2.12 (L'Abbate, et al. 2007).

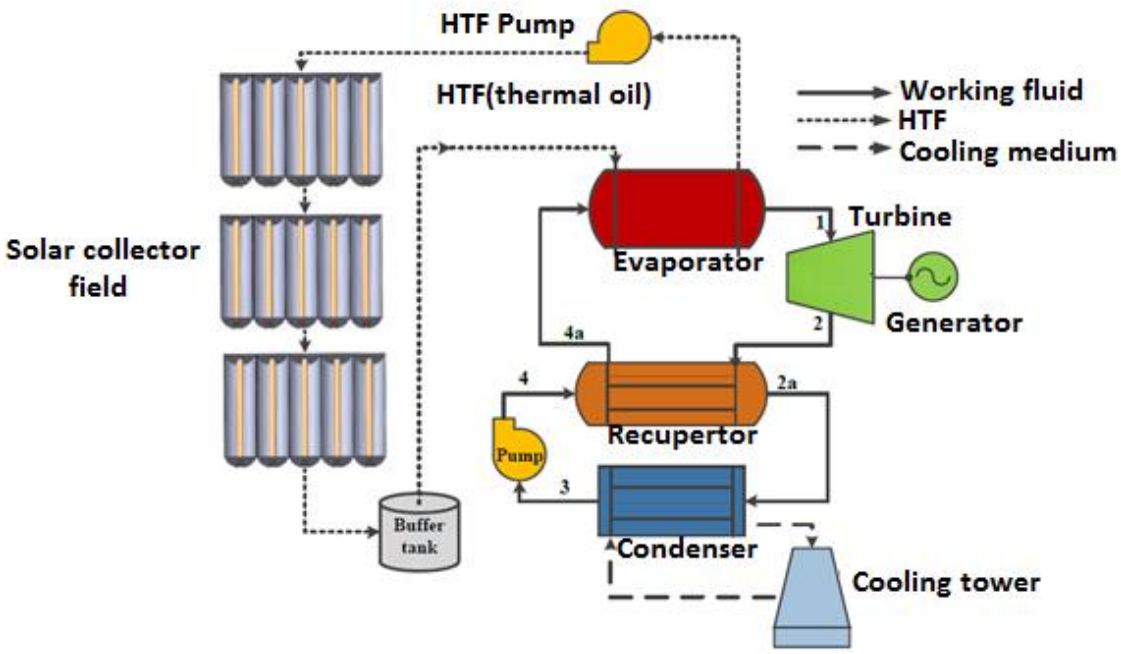

Figure 2.12 ORC power unit integrated with solar collectors (Rahbar 2016).

2.4.2.3 Wind Turbine:

Wind turbine is a set of rotor blades which use the wind energy to rotate a shaft. This shaft is coupled with electrical generator through gear box as shown in Figure 2.13. The wind turbines are available worldwide in small residential units and large wind farms with power rating up to 6 MW (L'Abbate, Fulli et al. 2007). This technology has high generation potential compared to other technologies due to large pressure difference between turbine blade surfaces leading to higher power output levels at moderate wind speed. However, wind turbines are limited by the wind speed and for sustainable predictable generation, applying high energy storage capacity is needed.

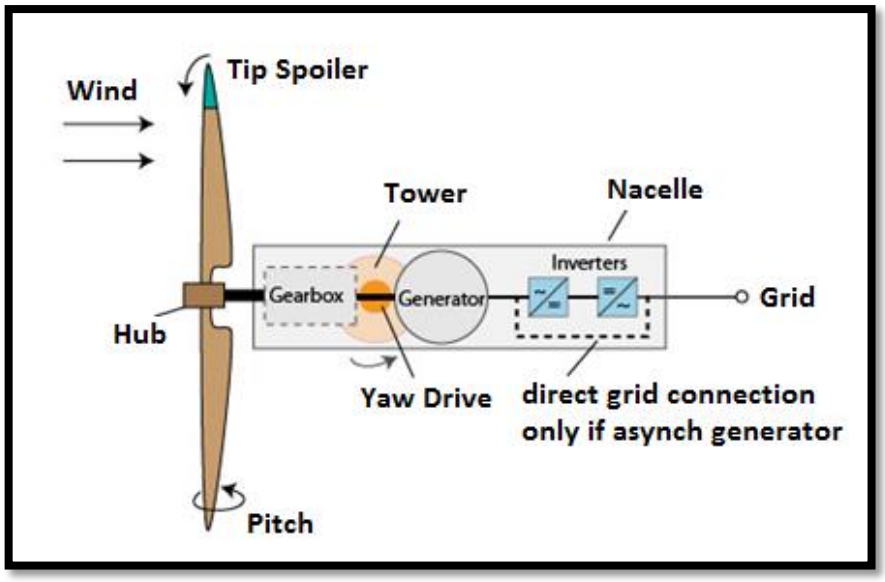

Figure 2.13 Wind turbine system (Energy 2013).

2.4.2.4 Energy Storage Systems:

To enable power generation using renewable energy, there is a great need for energy storage technologies in order to manage energy fluctuations and provide continuous supply (Ibrahim, Ilinca et al. 2008). The small DPG unit at point of use can be setup as a single hybrid system based on solar PV and/or small wind turbines with the implementation of energy storage to support energy demand and offer the opportunity of supporting the grid during peak hours (Ruiz-Romero 2013).

There are many energy storage technologies in which the energy can be stored in mechanical, thermal and chemical energy forms. Based on the application, the storage systems are classified into (Ibrahim, et al. 2008):

- Small power generation systems in isolated locations and for emergency units.
- Medium DPG systems for independent electricity generation in towns.

For small DPG applications, the energy can be stored using fuel cells, flywheels, batteries, and compressed air storage. These storage technologies are selected based on storage system characteristics which include storage time, storage capacity, charging /discharging duration, response time, safety and technology cost (Ibrahim, et al. 2008).

Table 2-2 provides detailed comparison of the characteristics of different storage technologies. As illustrated the pumped hydroelectric storage (PHS), CAES, and fuel cells have long storage duration with small discharge time compared with other storage techniques like batteries which are suitable for short storage period applications. Also, the CAES, PHS, and thermal energy storage (TES) are good choices in terms of low capital cost with relatively high storage density.

Table 2-2 Technical characteristics comparison for storage technologies (Succar and Williams 2008, Chen 2009, Howlett 2014, Rogers 2014)

Storage Technology	Power Rating (MW)	Discharge time	System Efficiency (%)	Energy density (kWh/m^3)	Storage duration	Capital Cost ($/kW)	Technical Maturity
Pumped hydroelectric storage PHS	100-5000	1-24hr	70-85	0.5-1.5	Hours-months	600-2000	Mature
Large CAES	5-300	1-24hr	42-54	3-8	Hours-months	600-800	Mature
Small CAES	0.003-3	Up to 1hr	≈ 42	0.5-2	Hours-months	200-250	Under development
Lead Acid Battery	0-20	Seconds-hrs.	75-85	16-33	Minutes-days	600-1800	Pilot Scale
Nickel-cadmium (Nicd) Battery	0-40	Seconds-hrs.	60-83	60-150	Minutes-days	500-1500	In use
Sodium Sulphur (NaS) Battery	50kW-8	Seconds-hrs.	89-92	150-250	Seconds-hours	1400-3200	Pilot Scale
Fuel cells	0-50	Seconds-24hr	20-50	500-3000	Hours-months	3000-10000	Evolving
Fly wheel	0-250	Seconds-minutes	89-95	20-80	Seconds-minutes	1600-3000	In use
Low temperature TES	0-50	1-8hr	20-50	37-92	Minutes-days	150-300	In use
High temperature TES	0-60	1-24hr	20-60	42-98	Minutes-months	150-300	In use

Figure 2.14 shows a comparison between energy storage technologies based on storage capacity and output power. This comparison shows the matching between storage technology and the application field. For small power generation systems, supercapacitors, batteries, and small compressed air energy storage (CAES) are the best choice. However, large CAES and pumped hydro suit high power demand applications (Schoenung 2001).

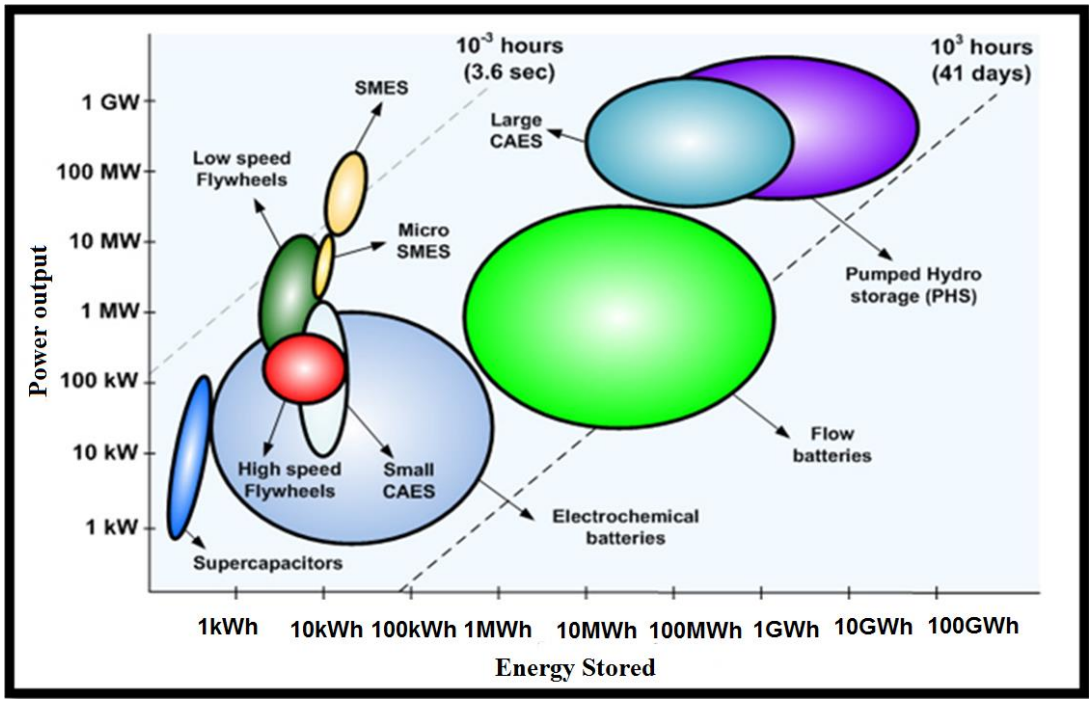

Figure 2.14 Storage technologies applications based on power output (Ibrahim, et al. 2008).

Figure 2.15 shows a comparison between energy storage technologies in terms of capital cost. It can be observed that fuel cells are a good choice in the case of short discharging time and lead-acid batteries for longer discharging time. The CAES can be competitive in both short and large discharging time (Schoenung 2001).

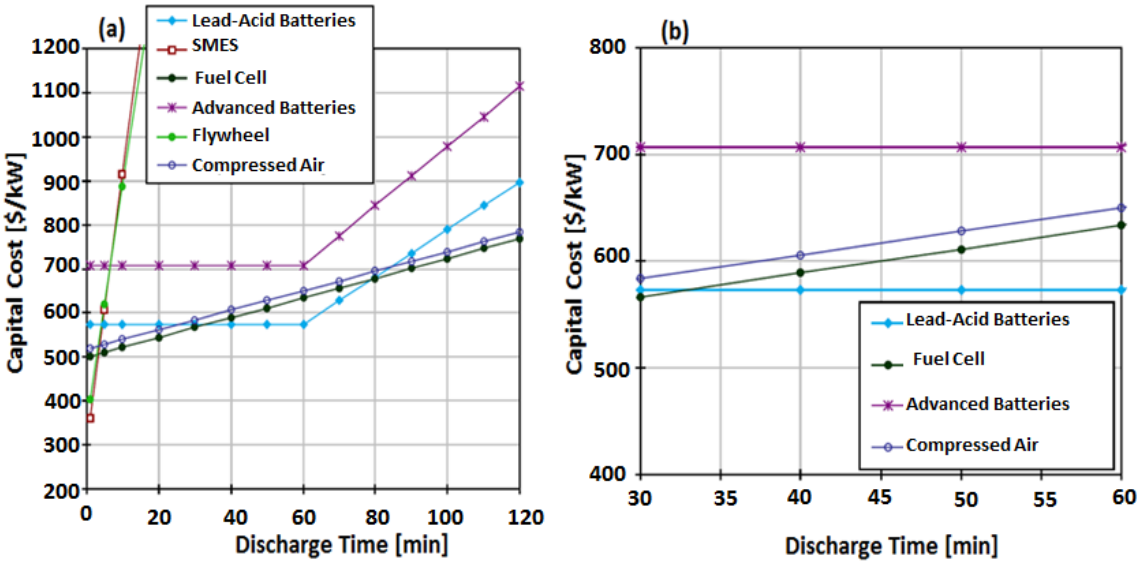

Figure 2.15 Storage technologies: (a) discharging time [10min-2hrs] (b) discharging time [30-60min] (Schoenung 2001).

The comparison between energy storage technologies based on storage duration and capital cost is shown in Figure 2.16 which shows that the cost increases with storage time and CAES and pumped hydro are less expensive compared to other storage technologies.

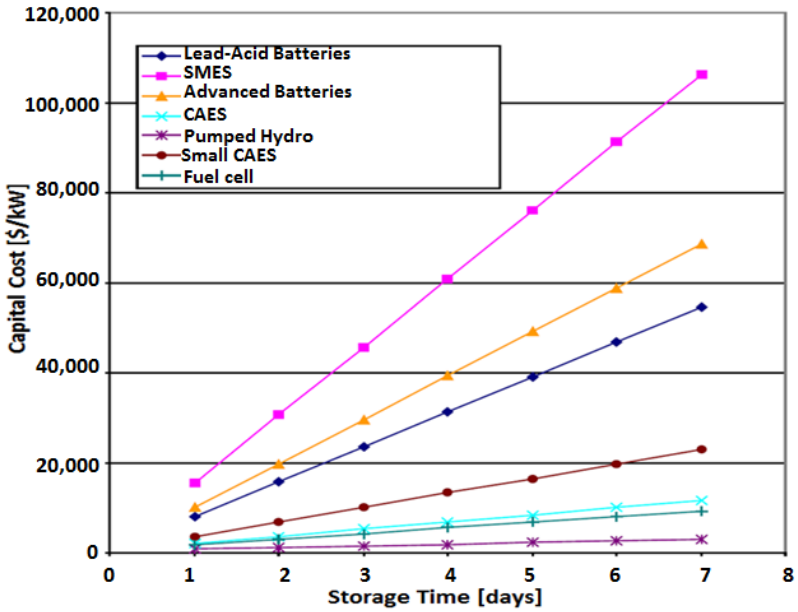

Figure 2.16 Storage technologies for different storage duration (Schoenung 2001).

2.5 Overview of Compressed Air Energy Storage (CAES):

CAES is a promising energy storage technology which has the ability to store renewable energy with high storage capacity reaching over 100 MW (Chen 2009). In conventional CAES power plant, the compressor is used to compress the air into underground large salt or rock cavern using off peak power as shown in Figure 2.17.

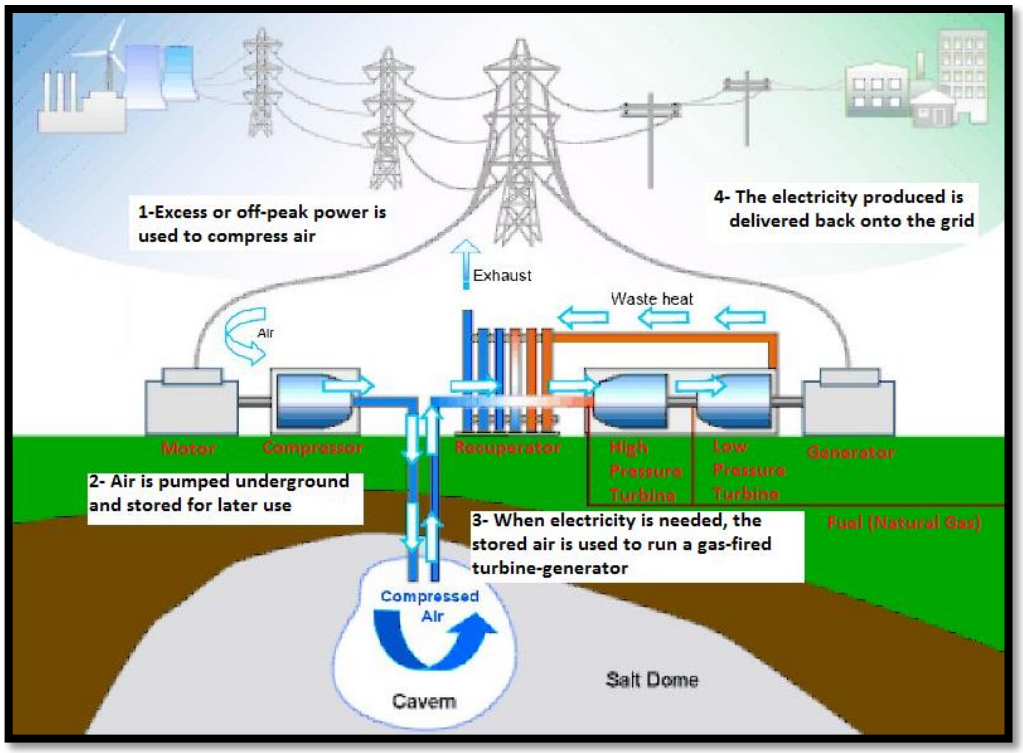

Figure 2.17 Compressed air energy storage cycle layout (Tan 2013)

In general the CAES cycles are classified into conventional CAES and alternative CAES systems. The main focus in developing CAES is to improve the cycle overall efficiency through new alternative CAES designs which include several CAES configurations which have been proposed as innovative cycles for higher performance (Fort 1983).

2.5.1 Conventional CAES:

The conventional or large CAES is a proven technology and its history extends back to the first power plant in 1978 Huntorf, in Germany with large underground cavern capable to generate 290 MW for four hours. The second compressed air plant was in McIntosh Alabama, USA which generated 110 MW for 26 hours (Safaei and Keith 2014).

The conventional CAES system relies on the implementation of CAES with a Brayton cycle where the compressed air is stored in underground caverns. The working principles of conventional CAES cycle are similar to a gas turbine plant. However, in CAES cycle the compressor and turbine are decoupled into separate operation phases which are the charging phase (compression) and discharging phase (expansion) (Ibrahim, et al. 2015). As shown in Figure 2.18, the schematic diagram of large conventional CAES includes:

- A motor – generator system which provides the clutching for compressor or turbine.
- Multi- stage compressor which is used for air compression process.
- Turbine train with both high and low pressure turbines for combustion gases expansion.
- Large CAES cavern or reservoir with some auxiliaries control units.

The power generation process in conventional CAES includes burning the fuel with the stored compressed air which increases the fuel consumption and CO_2 emissions (Loose 2011). Also, there are significant heat losses during the compression stage which affects the cycle efficiency. Furthermore, the development of conventional CAES based on renewable energy has limitations due to complex geological characteristics of large underground caverns (Fort 1983, Li and Dai 2014).

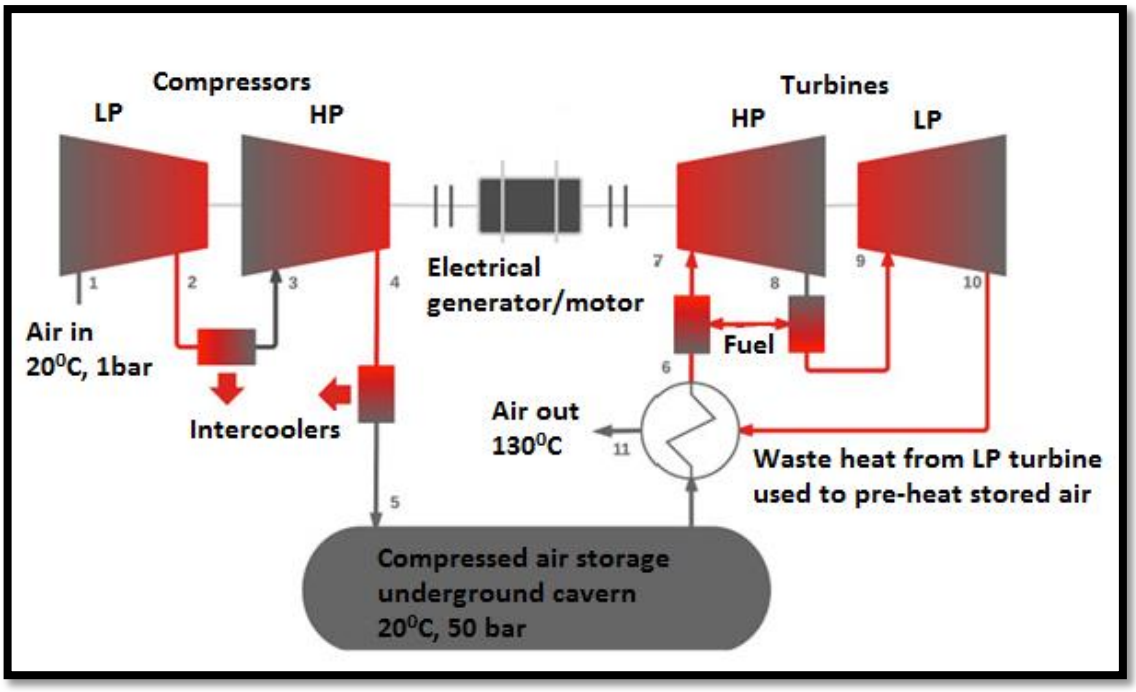

Figure 2.18 Schematic diagram of McIntosh CAES power plant (Ibrahim, et al. 2015).

2.5.2 Advanced Adiabatic CAES (A-A-CAES):

The Advanced Adiabatic CAES (A-A-CAES) is a new concept developed by European Project to enhance the conventional CAES performance (Bullough 2004). This configuration of CAES aims to decrease or eliminate the fuel consumption completely by the implementation of thermal energy storage (TES) technology as shown in Figure 2.19. The main function of TES is to store the heat dissipated during the compression process and then recover this heat during the expansion process to reheat the air entering to the turbine without fuel burning (Lemofouet-Gatsi 2006). The analysis of the A-A-CAES proves its ability to improve the overall performance of the conventional CAES and an improvement by 30% in system overall efficiency can be achieved as a result of applying TES technology (Grazzini and Milazzo 2008, Wolf 2011, Rogers 2014).

The A-A-CAES is still facing some technical issues which include: design of high capacity TES with minimum heat losses (Rogers 2014), low turbine efficiency due to deep off design

operating conditions, and the development of the compressor design for high compression ratio with ability to manage high temperatures (Wolf 2011).

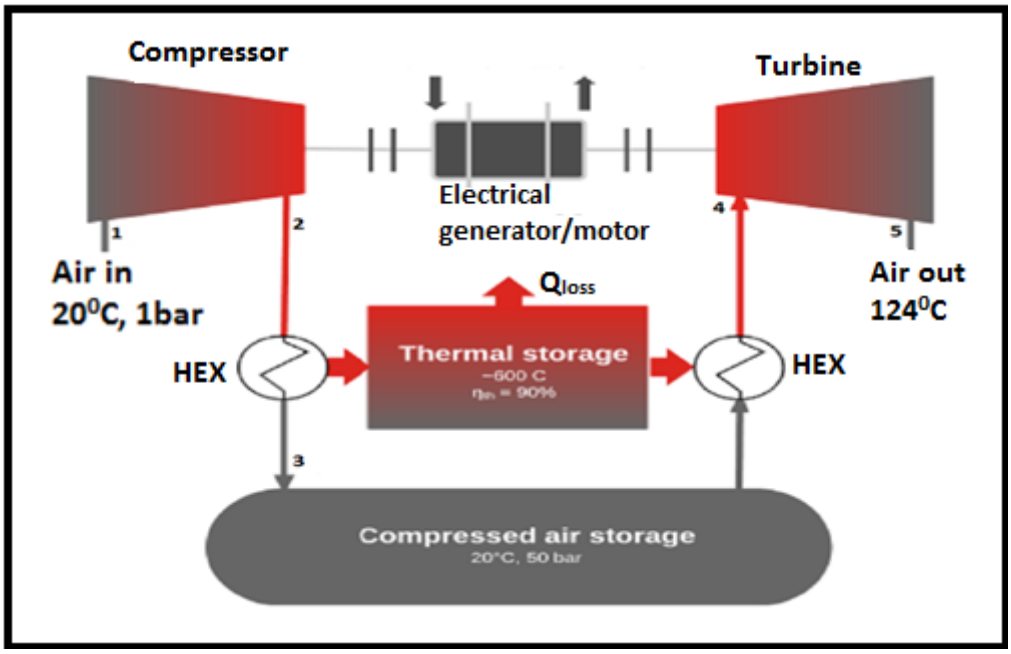

Figure 2.19 Schematic diagram of advanced adiabatic CAES plant (Lemofouet-Gatsi 2006)

Insulated vessel for storing both thermal and potential energy can be implemented to produce A-A-CAES as shown in Figure 2.20 (Lemofouet-Gatsi 2006). This option was investigated at University of Clausthal in Germany and the results showed that the insulated air receiver can be implemented only for short periods and it is not applicable for long storage time due to significant heat losses as a result of poor insulation (Kentschke 2004).

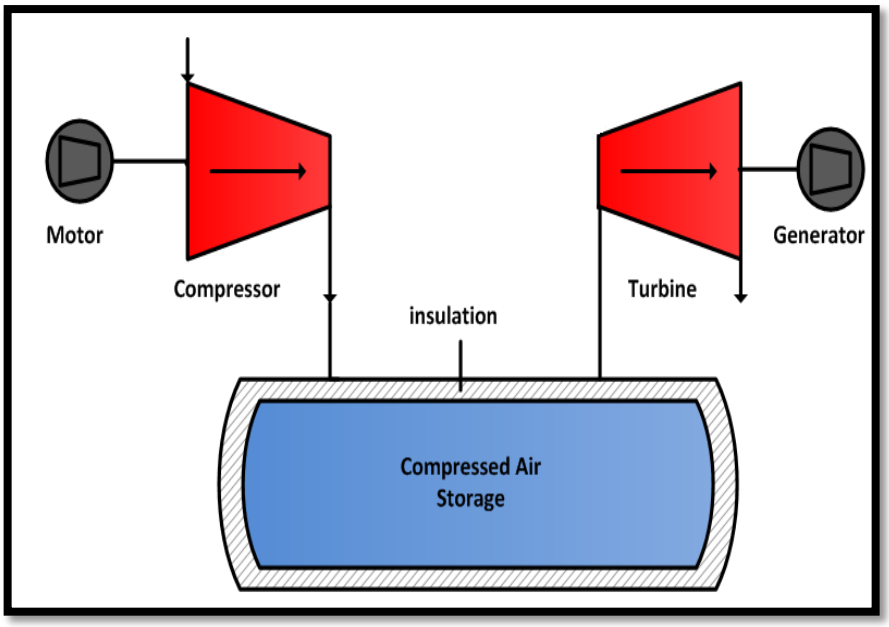

Figure 2.20 CAES plant with isolated tank (Lemofouet-Gatsi 2006)

2.5.3 Isothermal Compressed Energy Storage (I-CAES):

The isothermal CAES (I-CAES) configuration aims to avoid any heat exchange between the system and surrounding to achieve closely isothermal compression and expansion processes. (Rogers 2014). As shown in Figure 2.21 this system relies on the injection of water or oil during the compression process in a reciprocating piston cylinder and these hot liquids are re-injected during expansion phase to reheat the air entering the turbine (Crane, et al. 2012). The I-CAES is still under development and further improvements of heat transfer liquid and air with efficient liquid/air separation device (Luo and Wang 2013) are needed. There are some funded pilot scales I-CAES systems in operation including: General Compression (500MW), the project of Lightsail Enegy (8MW), and SustainX (2MW) (Bollinger 2010, Crane, et al. 2012, Ingersoll, et al. 2012).

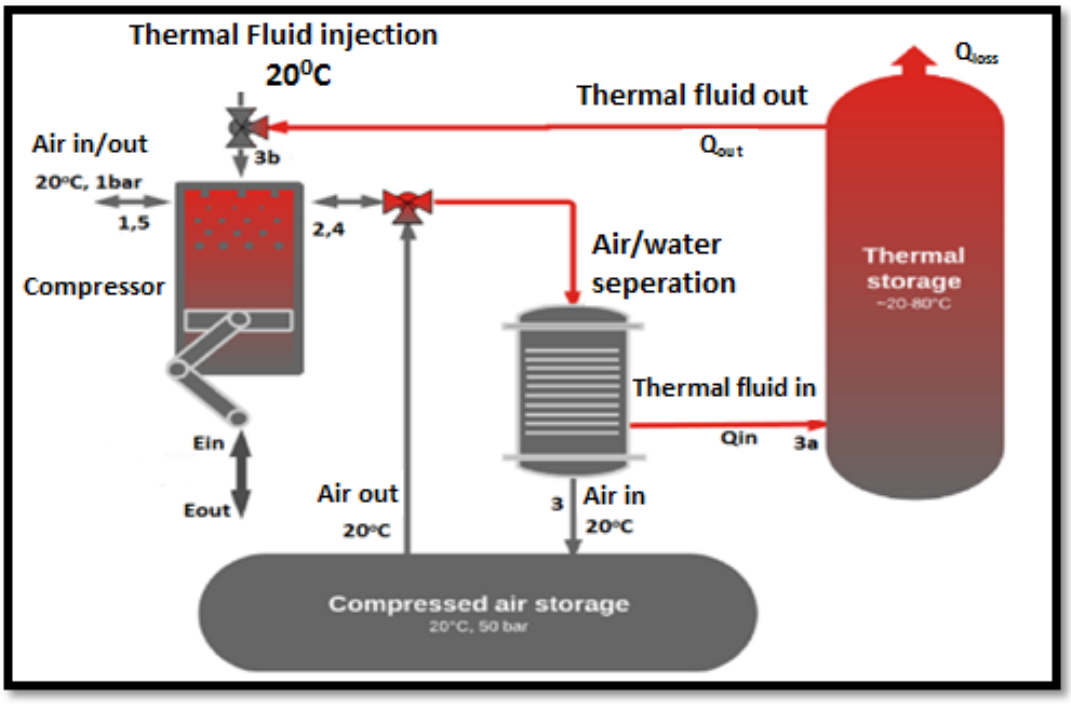

Figure 2.21 Schematic diagram of isothermal CAES plant (Ibrahim, et al. 2015)

2.5.4 Distributed Compressed Air Energy Storage (D-CAES):

Small scale CAES is an alternative option for distributed power generation based on compressed air energy storage with high pressure vessels as shown in Figure 2.22. This option is one of the promising technologies for small and medium stand-alone power generation at consumption point based on wind and solar energy applications. In D-CAES the air is compressed in pressurized cylinders up to 300 bars for distributed power cycle with an overall efficiency of 50% (Ibrahim, et al. 2008).

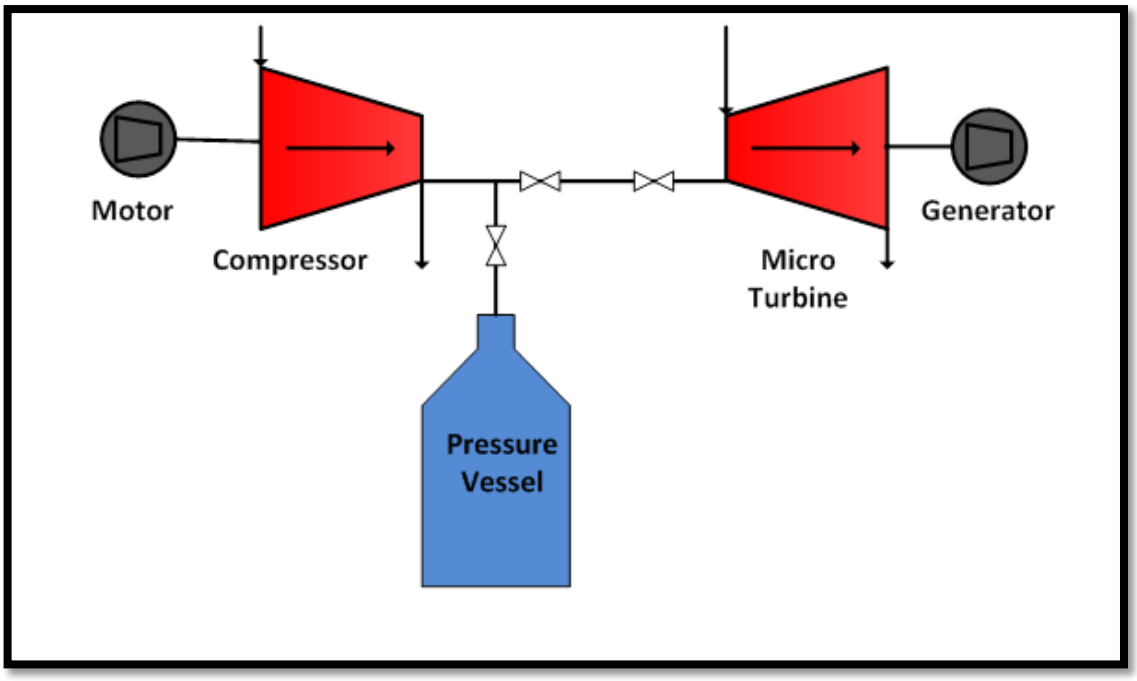

Figure 2.22 Schematic diagram of distributed CAES plant (Ibrahim, et al. 2008).

The small CAES system offers many advantages including: long cycle time, safe technology, environmental friendly, high storage capacity compared with batteries, can be generated with renewable energy sources for cost effective electricity supply, less installation restrictions, appropriate for micro power generation, non-toxic and simple manufacturing. The main disadvantage of small CAES is that the technology is not proven yet and further research is required to improve both compression and expansion processes to enhance the overall cycle performance.

2.6 Research and Development of Small D-CAES:

2.6.1 Theoretical Research:

Compared to conventional large CAES systems, there is limited reliable data available in the public domain regarding the research that has been conducted to examine the performance of

small D-CAES systems. This section discusses the limited published studies covering the use and analysis of small D-CAES.

The development efforts of D-CAES technology require improvements in all system relevant components which include compressor, turbine, thermal energy storage, and electrical systems. The research in D-CAES aims to improve the overall system efficiency with minimum capital and operation costs (Luo and Wang 2013). According to the review on the developments of small scale D-CAES systems conducted by (Venkataramani 2016), the future developments of small D-CAES systems depends on the integration of the system with renewable energy sources like solar and wind energy and adapting the system with high efficiency small expansion device.

The feasibility of the practical implementation of small D-CAES based on renewable energy sources was investigated by (Petrov, et al. 2013). This study concluded that a small D-CAES with 6.85m^3 air receiver could store 25kWh with expected profit of $500 annually leading to payback period of 15 years. Also the feasibility study of practical implementation of small CAES for portable electrical and electronic devices application based on small turbines was conducted by (Paloheimo and Omidiora 2009). This study concluded that the performance of small CAES unit is relatively low due to low efficiency levels of the small turbine which is still in the prototype phase and further research is required in developing high efficiency small turbines with low RPM for this application in order to improve the cycle overall performance.

A small scale compressed air storage system prototype for electricity generation based on solar PV for residential use was proposed by (Villela 2010). This work found that the system overall performance is correlated with both compressor and expansion machine RPM and efficiency. This design was considered as a first step and further research in developing small air storage system is required for both compression and expansion devices.

A variable configuration CAES system with input power of 500kW based on renewable energy sources was theoretically investigated by (Grazzini and Milazzo 2008) in order to estimate the overall efficiency of the system. The amount of stored energy was 14,400 MJ at pressure of 200 bars for charging duration of 8 hours. This study concluded that the system overall efficiency was overestimated (72%) as a result of simplified simulation assumption i.e. constant air properties, constant compressor and turbine efficiency, ignoring the pressure and heat losses. The proposed configurations can be used for off-the shelf applications and for DPG further improvements in compression and expansion processes are needed.

An innovative tri-generation system integrated with small CAES and TES was proposed by (Li 2012) for electricity generation and space heating/cooling applications. In this system, the compressed air expansion through the turbine was used as cooling power instead of absorption system. The thermodynamic analysis of this system concluded that the overall system efficiency was higher than the conventional absorption chilling systems and the overall performance of the system depends on the efficiency of individual components e.g. compressor, turbine, and TES.

A detailed energy and exergy analysis of small CAES for heating and cooling applications was performed and some innovative concepts were proposed by (Kim and Favrat 2010) for improving system overall performance. The analysis was conducted under different compression and expansion processes for a constant pressure vessel. The results showed that the potential of the CAES in terms of energy density and high efficiency levels (60%) can be achieved using quasi isothermal processes in both compression and expansion devices.

A detailed sizing of small D-CAES was carried out by (Minutillo, et al. 2015) in order to provide a general assessment of the optimal design and operating conditions for the D-CAES integrated with a solar PV as energy source for stand-alone power generation applications. In this study and to achieve an adiabatic system, an oil tank was used as a TES to recover the

compression dissipated heat. The sensitivity analysis of cycle overall performance found that for fixed compressor and turbine efficiency, the charging pressure is the key parameter which has a significant impact on the amount of stored energy and the size of solar PV cells.

The implementation of the technology of thermal energy storage (TES) in D-CAES is one of the key research areas in developing CAES for more efficient power production. A novel adiabatic small scale D-CAES with TES unit based on renewable energy source for energy supply to a radio mobile station was proposed by (Jannelli 2014). The sizing of all system components has been conducted in order to predict the cycle overall performance. The results highlighted the potential storage capacity of the system with good storage efficiency level (57%) and the cycle overall efficiency has increased by 17% as a result of applying TES. However, in this proposed cycle configuration the PV unit was oversized to meet the daily energy consumption.

2.6.2 Experimental Research

Although the small D-CAES technology is still in its early stages, there are some developed hybrid small CAES systems with power range of 2kW up to 1 MW (Luo 2014). The available small CAES systems in the market have been established by many companies including Energetix Group (UK), UK National Grid, Eskom (South Africa), and ATKA (USA). All the developed small D-CAES systems are based on scroll expanders which have low efficiency levels compared with other expansion devices like radial and axial turbines (Brandon , Wang 2011, Luo 2014).

A new hybrid CAES system integrated with wind turbine was developed by University of Warwick research team. The proposed D-CAES system aims to generate electricity using low wind speeds. The detailed dynamic modelling and thermodynamic analysis of this system was reported in (Sun 2011) based on scroll expander. The test rig facility for the system is still

under construction for theoretical analysis validation and more system investigations (Luo 2014).

A detailed analysis of mini CAES cycle was carried out by (Khamis 2011) for a system with pressure vessel of 270L at 11 bars for DPG using small turbine operating with 800RPM. The system could only obtain output voltage of 8V and the design goal was 12V. This gap is due to the drop in pressure and temperature of the air entering to the micro turbine. The main conclusion from this study is that the system experiences high energy losses and further improvement of the expansion device is required.

The power tracking for small D-CAES system was analysed and investigated experimentally by (Kokaew, et al. 2013) using air motor coupled with a DC generator. The air motor in this system was integrated with power controller in order to track the maximum power at different operating conditions. The theoretical analysis using Matlab/Simulink showed good agreement with the experimental results for different operating conditions. The maximum power of 50W was achieved at tank pressure of 6bar and motor speed of 18,000 RPM.

A new hybrid wind diesel system combined with CAES was investigated experimentally by Ibrahim et al (Ibrahim 2010). The main aim of this work was improving the efficiency of conventional diesel engine with minimum operation cost and less diesel consumption. The integration of the diesel engine with wind energy source and CAES system was proposed to solve the technical issues facing the development of DPG based on wind energy. The results showed that the diesel consumption in this new system with 10 bars air pressure was reduced by 27% compared to conventional system. Furthermore, the proposed configuration could be a competitive DPG technology in terms of life cycle and maintenance demands.

The coupling of wind turbine with small CAES was studied experimentally by (Shaw, et al. 2012). The main focus of this work was to improve the conversion efficiency of the wind energy into compressed air by developing a controller that adapts the gearbox to wind speed.

The results showed that the amount of stored energy depends on the maximum tank pressure which is controlled by the operating wind speed using a controller which was redesigned for wide range of wind speed.

It is clear from the review on the small D-CAES that this technology is still under development and further research is required to achieve efficient and reliable system. The main challenges associated with the developments of small D-CAES include improving both compression and expansion devices (Luo 2013, Petrov, et al. 2013, Luo 2014).

2.7 Expansion Devices:

In distributed power generation systems, the expander is used for power recovery by extracting the energy of a passing working fluid and converting it to mechanical work. This small expander is a vital element in the D-CAES system and affects the efficiency, performance, and cost of the power generation cycle (Bao and Zhao 2013, Saadatfar, et al. 2013). The design of efficient small expansion device is the main important part in developing the DPG cycles. The expanders are selected based on cycle operating conditions, system size, and working fluid properties (Qiu, et al. 2011).

In general, there are two main categories of expansion devices which include the velocity or dynamic type expansion devices (axial or radial turbines) and the volume or displacement type expansion devices (screw or scroll expander) (Qiu, et al. 2011). More detailed description of expander types are provided below.

2.7.1 Velocity Type Expanders:

The velocity type expansion machines are known as turbines or turbochargers which convert the kinetic energy of a passing fluid into mechanical energy by rotating shaft using set of rotor blades. The small turbines are similar to conventional steam turbines with small size and work using different fluids. However, the use of other working fluids instead of steam leads to

change in turbine features and design requirements. The use of high density fluids leads to too small turbine size with low efficiency levels as a result of losses (Bao and Zhao 2013). The turbines used in power generation systems are classified into axial and radial turbines.

2.7.1.1 Axial Turbine:

In axial turbines the fluid passes through the turbine in axial direction as shown in Figure 2.23. For this reason the axial turbine is common in high flow rate applications with low pressure ratio. Due to axial flow through turbine blades, the axial turbine has lower aerodynamic losses and higher efficiency (Yahya 2010).

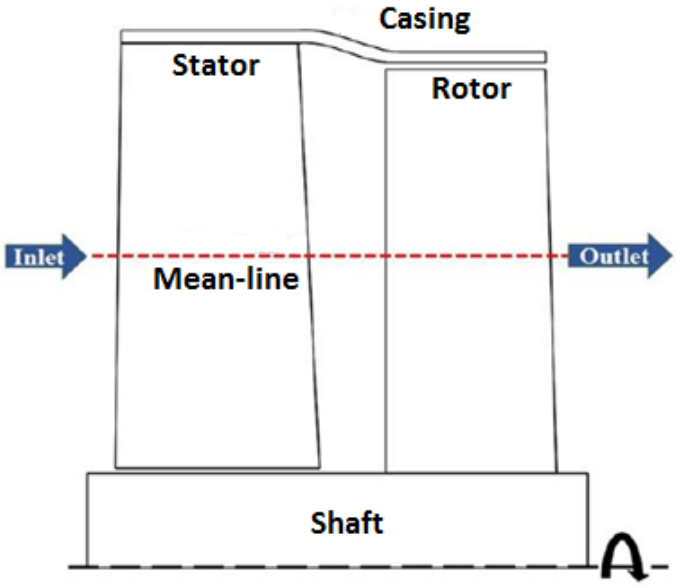

Figure 2.23 Flow through axial turbine stage

According to the type of the rotor blade, axial turbine is divided into: reaction and impulse turbine. In reaction turbine, the expansion is divided between stator and rotor. However, in impulse turbine the expansion process occurs only in the stationary stator vanes (Peng 2008).

2.7.1.2 Radial Turbine:

Radial turbine is a turbomachine that generates centrifugal force by passing fluid in radial direction as shown in Figure 2.24. In radial flow turbine the change in flow area is significant due to the variations of mean radius between entry and exit area (Yahya 2010). The radial turbines are the best choice for high pressure ratio with low mass flow rate and as a result of low flow rate the turbine blade geometry is small and expensive to manufacture (Krahenbuhl, et al. 2008, Dixon and Hall 2013).

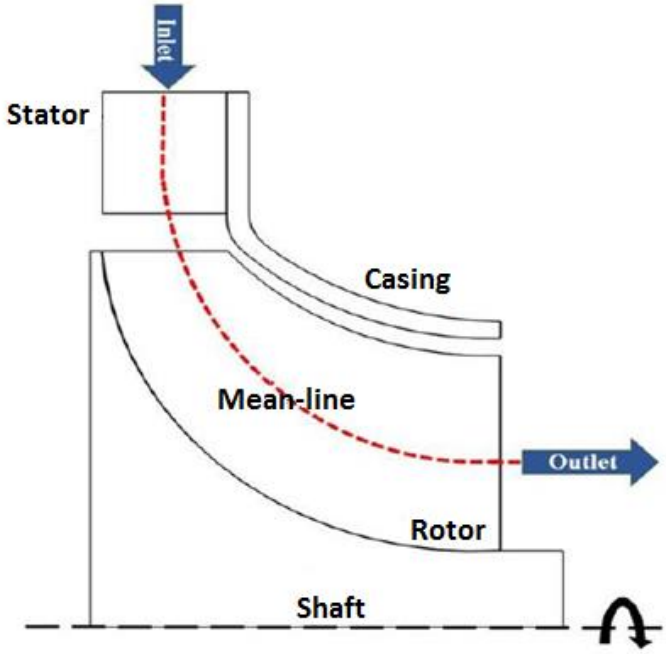

Figure 2.24 Flow through radial turbine stage.

2.7.2 Volume Type Expansion:

This type of expanders is common in micro-combined heat and power (CHP) systems. Volume expanders are considered in the cases of low mass flow rate, low RPM, and high inlet pressure (Lemort 2009).

2.7.2.1 Scroll Expander:

Scroll expander is an expansion machine that can be achieved by modifying the normal compressor to expander. Compared with turbine expander, it has low performance levels due to friction and pressure losses (Lemort 2009). The maximum reported isentropic efficiency was around 65% at the best operating conditions (Clemente 2013). Using spiral warps, the scroll expander can work either as a compressor or expander based on the movement direction as shown in Figure 2.25. Although the scroll expander has low efficiency levels, it is still attracting the attention of many researchers because of its simplicity and low capital cost (Qiu, et al. 2011).

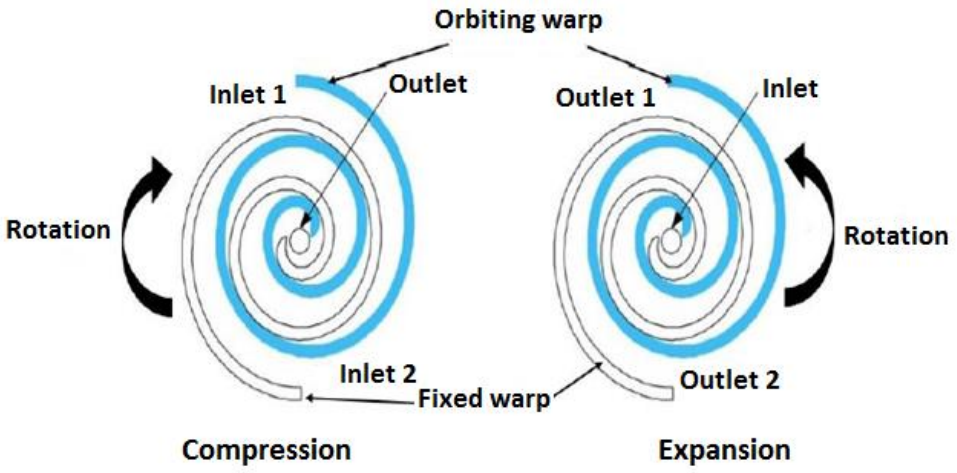

Figure 2.25 Scroll expander working principles (Qiu, et al. 2011)

2.7.2.2 Screw Expander:

Screw expander is simply a pair of male and female screw rotors in one case and the energy is transferring as a result of volume change between the rotors. The working mechanism of screw expander consists of three phases as shown in Figure 2.26: intake, expansion and exhaust. The high pressure fluid enters the intake leading to increase in the volume. In the expansion phase the high energy of the fluid is extracted and converted into power through

rotors rotation. The exhaust is the last stage in which the fluid leaves the expansion and the space volume deceases to zero (Qiu, et al. 2011, Bao and Zhao 2013). The screw expander is available in the market for waste heat recovery applications with power range of 20 to 50 kW with capital cost up to 2000 £/kW (Leibowitz, et al. 2006). However, screw expanders with small power rating (<10kW) is still under development and cannot be found in the market (Qiu, et al. 2011).

Figure 2.26 Screw expander working phases (Zhang 2014)

2.7.2.3 Reciprocating Piston Expander:

This type is a piston expander which is appropriate for internal combustion engine recovery applications. Piston expander is more complex compared to other expanders because of the complicated valves system for the intake and exhaust. Also, the overall cycle performance is affected by losses generated due to friction between piston and cylinder (Bao and Zhao 2013) and the maximum reported efficiency is around 60% (Glavatskaya 2012). The working principle of reciprocating expander is shown in Figure 2.27.

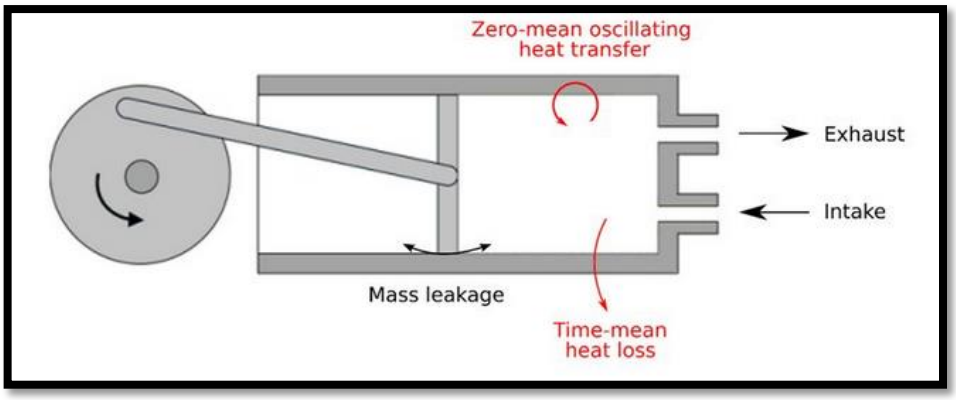

Figure 2.27 Working principles of reciprocating expansion/compression (Bloch and Godse 2006)

2.7.2.4 Rotary Vane Expander:

Rotary vane expander is also known as air motor expander that uses vanes driven by compressed air as shown in Figure 2.28. This expander is easy to manufacture and its production cost is low compared to other expanders (Qiu, et al. 2011). Rotary vane expander has low rotational speed (around 3000 RPM) that leads to low noise operation without gearbox (Bao and Zhao 2013). Figure 2.28 shows the working mechanism of vane expander in which the working fluid expands in the space between the chamber and rotor vane. This expander is available with power output of 1.5 kW with reported maximum efficiency of 55.45% (Qiu, et al. 2011).

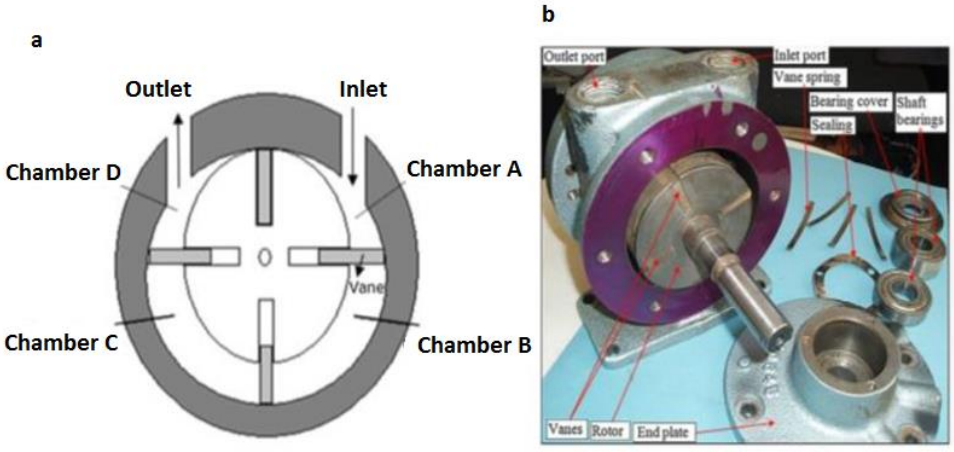

Figure 2.28 (a) Vane expander working mechanism (b) Vane expander components (Qiu 2012)

2.8 Evaluation of Small Expanders for DPG Cycles:

The current small DPG systems with different power capacity can achieve an overall efficiency of 24-30% which is relatively low. For this reason, significant interest have been generated by several researchers to enhance cycle overall efficiency and reduce operation cost with low emission. Developing efficient expansion machines (expanders or turbines), and selecting appropriate working fluid are the main factors in improving the overall conversion efficiency in certain energy cycles using renewable energy sources (Liss 1999). Improving the expansion process in DPG cycles can improve the system overall efficiency by 20% and reduce the CO_2 emissions by 10% (Pilavachi 2002).

Nowadays, the demand for small distributed generation has increased and the future of the commercial market points to implement these systems in residential buildings. There are many companies over the world which developed some small DPG systems based on small turbines to meet market need. These companies introduced commercial DPG systems in England, U.S.A, and Sweden. These companies include: Free Power, Turbec, Ingersoll-Rand Energy Systems & Power Works™, ORMAT Tech., Green Energy, Infinity Turbine LLC, AliiedSignal, and Elliott Energy Systems (Qiu, et al. 2011, do Nascimento, et al. 2013). Table2-3 summaries the available small DPG systems based on small turbines as expansion devices.

Table 2-3 The available small distributed power generation systems

Model	Company	Power Range(kW)	Expander Type	Heat Source Temperature	Working Fluid
IT10	Infinity	10	Radial turbine	-	R245fa
IT50	Infinity	200	Radial turbine	-	R245fa
IT100	Infinity	400	Radial turbine	-	R245fa
IT250	Infinity	1000	Radial turbine	-	R245fa
IC60	GMK	50	Axial turbine		Biogas

CHP2,3	Turboden	200-300	Axial Turbine	-	Steam
FP85	FreePowerUk	85	Axial Turbine	-	-
FP100	FreePowerUk	6-100	Axial Turbine	180^0C	-
FP120	FreePowerUk	200	Axial Turbine	-	-
SG10	Green Energy	10	Radial turbine	-	-
ORMAT	ORMAT,US	200	Radial Turbine	150^0C	n-Pentane
C30	Capstone	30	-	-	Natural gas
C65	Capstone	65	-	-	Natural gas
4200	Electratherm	35	Axial Turbine	93^0C	-
4400	Electratherm	65		170^0C	-
4500	Electratherm	110	Axial Turbine	240^0C	-
WB-1	Triogen	130	-	130^0C	-
TA45	Elliott Energy	45	-	-	-
TA80	Elliott Energy	80	Axial Turbine	-	-
TA100	Elliott Energy	100	Axial Turbine	-	-
TA200	Elliott Energy	200	-	-	-

The performance of small scale power generation system is strongly affected by turbine efficiency, operating conditions, and heat source (Saadatfar, et al. 2013). High efficiency small scale turbine that can be operated using low heat source (waste heat recovery application) with economic operation cost and low emission is still a great challenge in the field of power generation systems [12].

Qiu, et al. (2011) provided a review on available small scale expanders in the market that are used for micro-combined heat and power (CHP) systems. This review showed that small expanders (<10kW) that can be applicable for small DPG systems are still not available. The authors examined many types of expanders and the findings can be summarized as (Qiu, et al. 2011):

- Screw expanders require considerable modifications to be used in Micro-CHP to overcome sealing problems.
- Scroll expanders and multi vane expanders can be suitable for small CHP with output range of 1-10kW but with low efficiency values.

- Scaling down to achieve miniature turbines and expanders leads to unacceptable efficiency levels.
- Small scale turbines (1-10kW) are still under development and many researchers are looking for a novel turbine with high efficiency level and minimum cost.

A scroll expander was investigated experimentally by (Aoun and Clodic 2008) under different operating conditions (pressure ratio and rotational speed) using air and steam as working fluids in small power generation cycle. The results showed low efficiency values of the scroll expander due to significant flow leakage and mechanical losses. Furthermore, there were considerable heat losses through the expander body. The maximum efficiency was 60% at pressure ratio of 4 and 2850 RPM and for higher efficiency values the scroll expander needs significant modification to reduce flow leakage (Aoun and Clodic 2008).

The theoretical modelling and experimental testing of scroll expander in small Organic Rankine Cycle (ORC) were conducted by (Lemort 2009). Both the theoretical modelling and experimental validation were carried out using HCFC-123 as working fluid at different operating conditions (pressure ratio, mass flow rate, and RPM). The maximum efficiency was 58% indicating the high pressure and mechanical losses impacting on the expander efficiency (Lemort 2009).

The performance of a scroll expander was investigated experimentally in small ORC system by (Lemort, et al. 2012). The expander was designed to be used originally as a compressor and in this study was used as expander to deliver 2.5kW. The scroll expander was tested at different mass flow rates and pressure ratios using HFC-245fa as working fluid. The maximum achieved efficiency was 61.03% and this efficiency can be improved by modifying the compressor design to reduce the mechanical losses.

Clemente (2013) conducted a detailed thermodynamic analysis of small ORC model using different expanders (axial turbine, radial, scroll and reciprocating expander) with power output of 100kW. The main findings of this study are:

- The efficiency levels of dynamic expansion machines (axial and radial) are higher than scroll and reciprocating expanders.
- The turbine type (axial or radial) is selected based on operating conditions, manufacturing cost, the possibility of integration with other turbomachines.
- Compared to turbines, scroll expander is simple, cheaper, and has low RPM (3,000) but with low efficiency values (< 65%).

The thermodynamic analysis of micro gas turbine system with power rating ranging from 25 up to 500kW was conducted by (Galanti and Massardo 2011) based on small axial turbine. This study found that the system performance was strongly affected by turbine efficiency and the electricity cost decreased with increasing the turbine efficiency.

A microturbine system for electricity generation was developed by Holmes et al. (2004) at Imperial College London based on small axial turbine. The axial turbine was selected for this system because it can extract power from the flow at low pressure ratio with high efficiency compared to radial turbine. The developed axial turbine was modelled using CFD for a range of operating conditions and the optimum turbine efficiency of 52% was achieved at 1.1 pressure ratio and 14,000RPM with power rating of 10W. The experimental verification of the turbine CFD modelling showed very good agreement between CFD and experimental results (Holmes 2004).

A small axial air turbine for compressed air electricity generation cycle with power output of 28W was developed by (Peirs, et al. 2004) based on similarity design approach (scaling down large turbine). The developed small axial air turbine (10mm rotor) was coupled with DC electrical generator and whole system was tested using different compressed air pressure. The

turbine efficiency was very low (18%) due to high profile loss which represents 10 times higher than the original large turbine indicating the scaling down effect on turbine performance. For higher small turbine efficiency, improving design methodology and performing blade profile optimization to reduce the losses were recommended.

Krahenbuhl, et al. (2008) proposed a small compressed air electricity generation system based on small single stage axial air turbine with output power of 60W. Two different miniature axial turbines (impulse and reaction) were tested at different inlet pressures and mass flow rates. The maximum turbine efficiency of 28% was achieved using the reaction turbine. This low efficiency of the turbine was referred to the miniaturization impact on losses and for better system performance the small turbine needs a careful optimization methodology during the development.

Based on the previous review of small expansion devices, the majority of research aimed to increase the expander efficiency which is the key factor in increasing cycle overall performance. Turbines (axial and radial) have higher efficiency levels compared to volume type expanders. The radial turbine can reach an isentropic efficiency of 85% with high rotational speed greater than 65,000 RPM and at high pressure ratio of 5 (Bao and Zhao 2013). However, for low pressure ratio applications the axial turbine can achieve higher isentropic efficiency compared to radial turbines (Holmes 2004).

2.9 Axial Turbine Design:

There are no guidelines or methods specific for the design of small axial turbines and in most cases they are designed based on similar approaches as those used in conventional large scale turbines. In order to meet market need, preliminary studies are required to identify turbine design specifications which include output power, turbine pressure ratio, rotational speed, and turbine mass flow rate (Moustapha 2003).

In general, there are four published methods for turbine blade aerodynamic design. These methods include: similarity analysis, mean line modelling, 2D and 3D blade design (Wakeley 1997). Similarity or dimensional method involves scaling turbine by using dimensionless groups based on fundamental theory which states that the turbines are dynamically similar if they have similar geometry. This method is acceptable in the case of incompressible flow where the changes in density can be neglected. However, in the case of compressible flow this method is influenced by the changes in Reynolds number and Mach number (Moustapha 2003). Furthermore, the miniaturization of the turbines leads to unsuccessful prediction of turbine performance due to high losses and large difference in power density compared with large scale turbine (Peirs, et al. 2004).

One-dimensional mean line method is well-known simplified method which assumes that the flow properties through the turbine passage can be calculated at the mean diameter neglecting any variations in radial direction. Using mean line approach the turbine blade geometry is generated (blade flow angles-leading and trailing edge geometry- hub and tip dimensions) then turbine efficiency can be estimated using published efficiency correlations. Mean line design is usually established for preliminary design step and detailed analysis is carried out using throughflow analysis method to predict the variations in the flow properties in span wise direction and blade twist is calculated based on vortex development (Wakeley 1997, Moustapha 2003). Detailed description of the meanline design approach is provided by many text-books (e.g. (Cohen 1987), (Moustapha 2003), (Aungier 2006), and (Dixon and Hall 2013) and some assumptions and parameters selections are left to the designer for optimum blade configuration.

Meanline design calculations are followed by 2D or throughflow analysis which is performed to consider the variations in flow properties in both axial and radial directions. In other words, the throughflow design calculations are achieved by constructing meanline velocity triangles

at different span wise locations. Due to the rapid increase in computing power, the 3D design phase can be performed using 3D fluid flow solvers (Wakeley 1997, Moustapha 2003).

For the turbine design and preliminary performance estimation, there are well known published approaches for axial turbine based on mean line method for turbine sizing. These approaches provide charts and correlations derived from large scale axial turbine test data and there are no specific correlations in public domain for miniature turbine design (Benner, Sjolander et al. 1997).

In general, the precise turbine performance is determined by testing the new design and for preliminary performance estimation of the turbine, there are two common methods for axial turbine performance estimation. The first method is achieved using overall performance parameters (e.g. flow parameter, and stage loading). The second method is based on total loss estimation which is more appropriate for detailed design (Sieverding 1985).

In large scale axial turbines (gas or steam), Smith Chart and Soderberg correlations are examples of the methods used for preliminary axial turbine sizing. The Smith chart provides the results of axial turbine tests which were carried out by Rolls Royce in 1965. These results are presented in a figure that shows the axial turbine efficiency for different stage loading and flow parameters with Reynold number range (100,000-300,000) and reaction range (0.2-0.6). The impact of other parameters (e.g. incidence angle, flow angles, aspect ratio, tip clearance, Mach number, and trailing edge thickness) on turbine efficiency was neglected in Smith Charts (Dixon and Hall 2013). As a result the expected efficiency especially for miniature axial turbines will be less than the efficiency obtained from the chart.

The second method for performance estimation is based on loss prediction using common published correlations including Ainely and Mathieson (1951), Trauple (1958), Soderberg (1966), Balje and Binsley (1968), a Craig and Cox (1970), and Kacker and Okapuu (1982). These correlations are based on many simplified assumptions and some tests of blade loss

prediction for typical gas turbine engines. The use of traditional performance estimation methods in small steam turbine designs leads to unsuccessful results and significant improvements in the turbine design are required (Craig and Cox 1970, Dunham and Came 1970).

A review of existing correlations for losses prediction was provided by (Moustapha, et al. 1990). This review concluded that Ainely and Mathieson correlations cannot meet the recent turbine designs. The authors developed a new loss prediction scheme for loss prediction in axial turbine at off design conditions. A new loss prediction scheme was developed by (Benner, et al. 1997) for secondary losses prediction based on empirical data of (Benner, et al. 2006). This new losses prediction method was more consistent than other conventional techniques. Table 2-4 summarizes the common conventional performance methods for large axial turbines and there has been no work conducted to develop an approach for performance prediction in small scale axial turbines based on loss prediction (Perdichizzi 1981, Macchi and Lozza 1985, Angelino, et al. 2012).

In the past, detailed aerodynamic design of turbine blades was based on actual experimental tests for the developed models to identify the sources of the losses. Performing experimental tests for turbine performance prediction is too expensive and due to the development in numerical approaches and the increase in computing power, CFD has become an effective modelling tool which can improve the meanline design due to CFD capability in turbulence modelling, boundary layer development, and nozzle –rotor unsteady interactions.

Table 2-4 Performance prediction methods for axial turbines (Ainley and Mathieson 1951, Craig and Cox 1970, Dunham and Came 1970, Horlock 1973, Kacker and Okapuu 1982, Benner, et al. 2006)

Author (s)	Loss component	accuracy	notes
Soderberg(1949)	Profile and secondary loss	±3%	
Ainely& Mathieson (1951)	Profile ,secondary loss, and tip clearance loss	±2%	
Dunham & Came (1970)	Profile ,secondary loss, and tip clearance loss		Influence of Reynolds number included
Craig&Cox (1971)	Profile ,secondary loss, tip clearance loss, trailing edge loss	±1.25%	Reynolds number, Mach number, and aspect ratio are included
Kacker and Okapuu (1982)	Profile ,secondary loss, tip clearance loss, trailing edge loss	±1.5%	Influence of compressibility included
Moustapha (1990)	Profile ,secondary loss at off-design conditions		

At present, the use of modern CFD packages in turbine design allows the designer to change and modifying turbine geometry for a set of operating conditions to improve the aerodynamic performance of the turbine blades and an effective blade profile can be reached using iterative CFD simulation (Elder, et al. 2003).

A detailed review of CFD methods for turbomachinary design was provided by (Denton and Dawes 1998). The CFD methods were proven as a mature design tool which allowed the designers studying a range of design parameters for different operating conditions. The agreement between axial turbine CFD simulations and experimental results was reported by (Moroz, et al. 2005) showing very good agreement and proving the capability of CFD as successful tool for single axial air turbine. For multistage axial air turbine, the comparison between experimental and CFD results was provided by (Abdelfattah and Schobeiri 2012). The CFD modelling of multi stage axial turbine was performed based on steady and transient ANSYS-CFX Solver using different turbulence models. The comparison between CFD and

experimental data showed an over prediction in total to static efficiency by 12%. This difference was explained by the turbulence modelling accuracy, surface roughness, and transient interactions.

Today the turbine designers can perform simulation and full analysis for single stage/multistage based on steady/transient turbine simulation using modern CFD packages. However, CFD cannot treat all design issues and the designer should deal with CFD results carefully and model validation is required to reach the confidence in using CFD predictions (Moustapha 2003).

2.10 Turbine Design Optimization:

Although the approaches for designing axial turbines have been developed by many researchers, the design process of turbine blades is still considered a great challenge for the engineers to reach highest efficiency with low production cost. The consequence of simplified assumptions in performance prediction methods and flow complications can lead sometimes to unsuccessful design results and detailed improvements are required (Craig and Cox 1970). Also the turbine is designed to match specific operating conditions. However, in actual operation the turbine works in off design operating mode leading to low performance levels. In large gas turbines, adjustable nozzle guide vanes have been introduced by (Jacobi, Xu et al. 2013) to reduce the nozzle area at low mass flow rate. This solution is complex in small scale and micro turbines and design optimization for a range of operating conditions is required.

There is no optimum turbine profile shape and the judgment of the best blade profile or optimum design is left to the designer's experience. Thus, all recent work has attempted to improve the turbine by applying different optimization techniques on turbine meanline design (Wakeley 1997). The aerodynamic turbine blade optimization was moved from inverse shape design approach to multiobjective and multidisciplinary optimization where multi target

objectives are reliable and the blade profile can be reformed to achieve the most efficient design (Dulikravich and Dennis 2000).

A numerical technique for axial turbine design optimization was applied by (Balje and Binsley 1968) based on simplified loss prediction correlations integrated with meanline approach. This approach aimed to maximize turbine efficiency by varying blade profile geometry parameters and an increase of 5% in turbine efficiency was achieved. This work was developed by (Rao and Gupta 1980) through applying multiobjective optimization (maximizing efficiency and minimizing turbine mass). Using multiobjective optimization technique could decrease the turbine mass by 18% while improving the turbine efficiency by 2.48%. The use of multiobjective optimization approach integrated with meanline design code was developed by (Massardo and Satta 1990) and this approach could improve the efficiency by 1.7% through blade geometry variation.

For 2D and 3D blade profile optimization, the multiobjective optimization approach was developed by (Dennis 2001) using flow analysis code. The optimization aimed to minimize losses and number of blades and 18 design variables were parameterized. This study recommended using multi objective genetic algorithm as an effective flexible optimization tool for 2D and 3D blade design optimization.

Recently, computational fluid dynamic (CFD) has become the most powerful tool for turbine optimization based on viscous 2D and 3D simulation. Modern CFD packages are integrated with shape aerodynamic optimization tools which are able to perform turbine optimization for minimum losses (Sasaki, et al. 2001).

2.11 Review Summary:

According to the previous review the following points can be concluded:

- Small Distributed Power Generation (DPG) systems can play an important role in achieving clean, cost effective electricity generation at consumption point. The DPG can be achieved using different traditional and renewable power generation technologies. DPG based on renewable energy sources are attractive research areas in the development of DPG to achieve environment friendly energy supply (Ibrahim, Ilinca et al. 2008).
- The future developments of using renewable energy sources for DPG require the implementation of energy storage for sustainable energy supply. Compressed air energy storage (CAES) system can be an attractive, cheap storage technology with high storage capacity for both medium and small power applications (Schoenung 2001).
- Small distributed compressed air energy storage (D-CAES) technology is still not proven and further research is required for improving the overall energy conversion efficiency. The main research area in small D-CAES is the integration of the CAES system with renewable sources like solar and wind energy and adapting the system with high efficiency small expansion device (Venkataramani 2016).
- The development efforts of D-CAES technology require improvements in both charging and discharging phases. The research in D-CAES aims to improve the overall system efficiency with minimum capital and operating costs (Luo and Wang 2013).
- There is an urgent need for improving the expansion phase efficiency due to variations in tank discharging pressure and mass flow rate as a result of the turbine working extremely in off design conditions leading to significant loss in turbine efficiency.
- The majority of developments aim to increase the expander efficiency which is the key factor in determining cycle overall performance evaluation. Turbines (axial and radial) have higher efficiency levels compared to volume type expanders. The radial turbine

is selected for applications with high pressure ratio of 5 (Bao and Zhao 2013). However, for low pressure ratio applications the axial turbine can achieve higher isentropic efficiency compared to radial turbines (Holmes 2004).

- Small scale turbines (1-10kW) are still under development and many researchers are working to develop a novel turbine with high efficiency level and minimum cost. For the design methodology, there are no specific correlations for small turbines design and the design process uses the same conventional large turbine design approaches.

- All published performance prediction losses methods are developed for large conventional turbines and there is a need for developing performance predictions in small turbines due to the fact that small turbines experience significant losses development and accurate losses prediction in this field is needed (Bullock 1964, Benner, et al. 1997). For efficient small turbine design, comprehensive CFD simulation and performing an effective optimization technique are required.

CHAPTER 3

DISTRIBUTED COMPRESSED AIR ENERGY STORAGE

3.1 Introduction:

The future of sustainable power generation based on renewable energy sources depends on the implementation of energy storage technologies. To understand the concept of energy storage this chapter highlights the potential role of the energy storage technologies and provides a detailed description of the principles and applications of compressed air energy storage (CAES) as one of the most promising storage technologies for distributed power generation. In this chapter, full thermodynamic analysis of CAES and dynamic modelling for both charging and discharging processes has been conducted to identify turbine operating conditions and design specifications.

3.2 Thermodynamic of CAES System:

This section introduces the thermodynamic principles of standard adiabatic compressed air energy storage (A-CAES) system as shown in Figure 3.1. The thermodynamic analysis of the system is carried out to identify the stored energy in CAES and the work done to compress the air. The CAES is characterized by the thermodynamic properties of the air like pressure, temperature and volume.

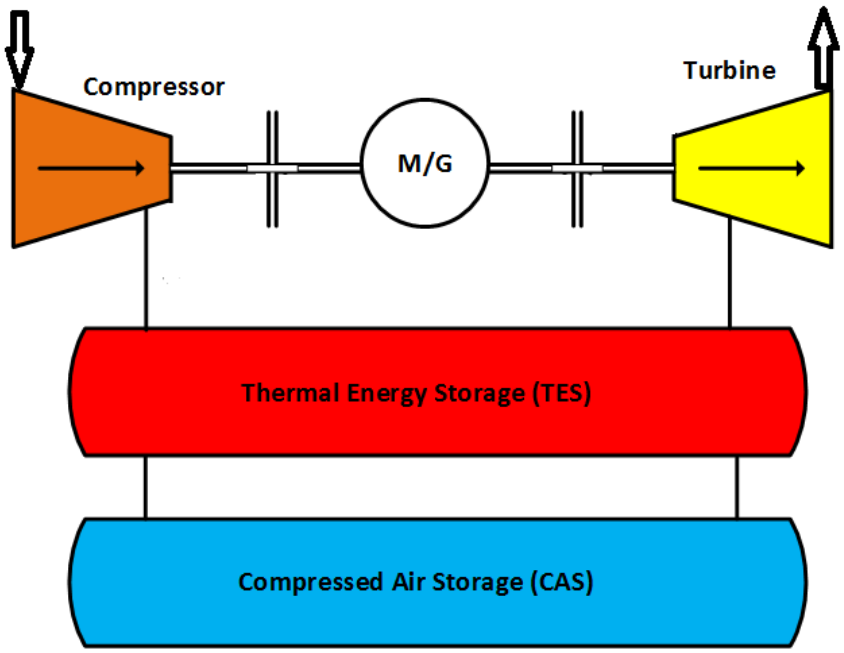

Figure 3.1 Adiabatic CAES cycle configuration

The thermodynamic characteristics of CAES can be analysed based on the first law of thermodynamics as (Proczka, et al. 2013, Safaei and Aziz 2014):

$$dU = dQ + dW \tag{3.1}$$

Where dU is the change in internal energy, dW is the work required to compress the air, and dQ is the heat added to the system.

As the air is assumed to be an ideal gas, the absolute air pressure can be determined using:

$$PV = mRT \tag{3.2}$$

Where P is the air pressure (Pa), V is air volume (m^3), m is air mass (kg), T is air temperature (K), and R is air gas constant ($J/kg.K$).

The compression can be assumed as isothermal or adiabatic compression processes. In isothermal compression, the change in system temperature is negligible and air temperature is assumed to be constant as a result the change in air internal energy $dU = 0$. In this process the work done is given by:

$$W_{i-f} = mRTLn\frac{V_f}{V_i} \tag{3.3}$$

For adiabatic compression process, the system is assumed to be insulated and no heat transfer to the surrounding and the work done by the system can be calculated by:

$$W_{i-f} = \frac{P_f V_f - P_i V_i}{\gamma - 1} \tag{3.4}$$

Where:

P_i , P_f : initial and final air pressure.

V_i , V_f : initial and final air volume.

γ: Air specific heat ratio.

3.3 Thermal Energy Storage (TES):

Thermal energy storage is the technology that can store thermal energy at certain temperature by changing material internal energy. This can be achieved through sensible heat storage (SHS), latent heat storage (LHS), and bond heat storage (BHS) (Ataer 2006, SOCACIU 2011). In adiabatic D-CAES systems, thermal energy storage is used to store the energy dissipated during the compression process (tank charging phase) and this stored energy is recovered during expansion process (tank discharging phase) to reheat the air entering the expansion device.

3.3.1 Sensible Heat Storage (SHS):

This storage option relies on raising material temperature to store the available thermal energy. The amount of stored thermal energy depends on the material type (solid or liquid) and specific heat capacity of the storage material. The common SHS includes: water, some oils, and other liquid materials. The stored thermal energy using SHS can be expressed in terms of storage media mass, specific heat capacity and temperature change as:

$$Q = \int_{T_i}^{T_f} m\, C_P dT = m\, C_P\left(T_f - T_i\right) \tag{3.5}$$

For solar power plant heat storage, solid media sensible heat storage is an attractive thermal energy storage technology due to simplicity, cost and storage capacity. The TES design considerations include high storage capacity and uniform heat exchange rate with minimum temperature loss. Concrete as a sensible heat storage was developed by German Aerospace Centre for solar power application and was shown to store thermal energy up to temperature of 400^{o}C (Laing, et al. 2008).

3.3.2 Latent Heat Storage (LHS):

In this technology, the thermal energy is stored using phase change material (PCM) in which the heat is absorbed during material state change from solid to liquid and liquid to gases. LHS technology is considered as the most effective thermal storage option due to its high storage capacity with small temperature difference compared to SHS (Farid, et al. 2004). Figure 3.2 shows the ideal enthalpy and temperature change for PCMs and the amount of storage capacity can be calculated as:

$$Q = \int_{T_i}^{T_{m1}} m\, C_{Ps} dT + \int_{T_{m1}}^{T_{m2}} m\, C_{Pm} dT + \int_{T_{m2}}^{T_f} m\, C_{Pl} dT \tag{3.6}$$

In equation (3.6), the first part represents the sensible heat needed to increase the temperature of the solid phase to the melting point; the second part is the amount of latent heat of fusion needed to melt the material, and the third term is the sensible heat used to increase the liquid temperature. According to enthalpy-temperature change of the PCM the specific heat is defined over temperature intervals as:

$$C_{P,PCM}(T) = \begin{cases} C_{PS} & T < T_{m1} \\ C_{Pm} & T_{m1} \le T \le T_{m2} \\ C_{Pl} & T > T_{m2} \end{cases} \tag{3.7}$$

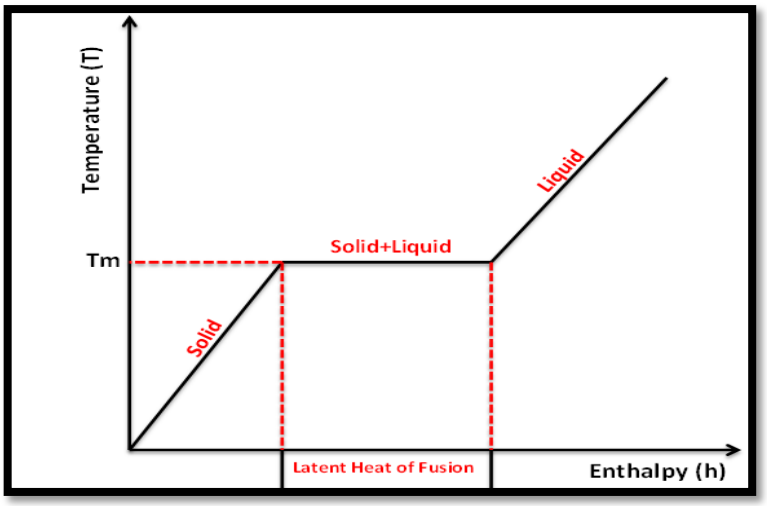

Figure 3.2 Ideal enthalpy change with PCM temperature

The PCMs are selected according to the energy storage application and based on the thermal properties of the material like melting/freezing temperature, high latent heat, good thermal conductivity, high density, and chemical stability. Figure 3.3 shows variety of PCMs which can be used for different heat storage applications and these materials are selected according to melting temperature and heat of fusion values (Farid, et al. 2004, Sharma, et al. 2009).

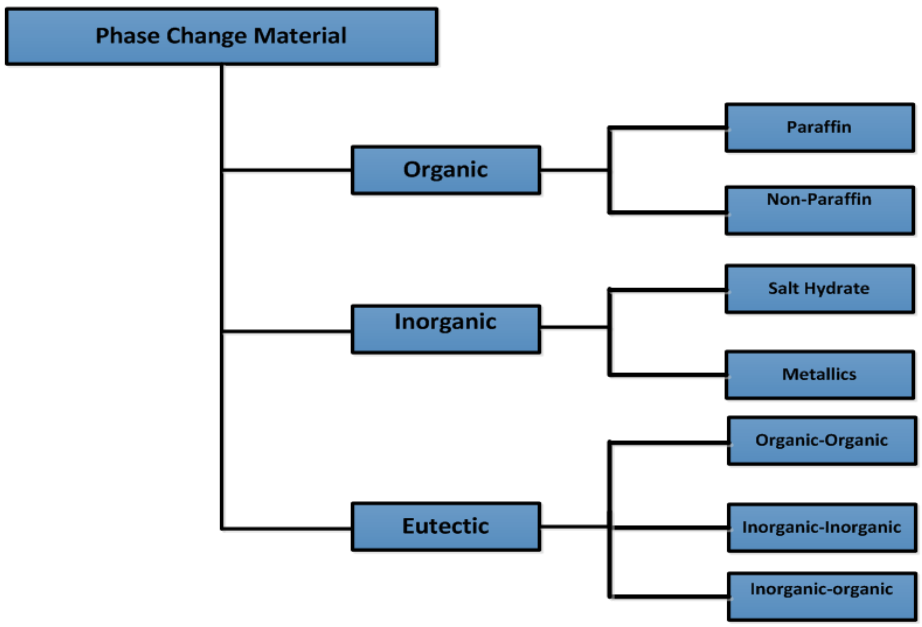

Figure 3.3 Phase change materials classifications (Sharma, et al. 2009)

3.3.3 Bond Heat Storage (BHS):

In this storage option, the heat is used to power chemical reactions and the heat is stored in the form of new products and this heat can be released by reversing the chemical reaction. The clear examples of heat storage based on BHS are the absorbtion the adsorbtion processes. Compared to SHS and LHS, the use of BHS is still limited and further developments are required for future use of BHS in wide range of applications (Ataer 2006).

3.4 CAES System Dynamic Modelling:

The CAES system can be described as an unsteady open system due to the significant variations in air temperature, pressure and mass during both charging and discharging processes (Grazzini and Milazzo 2012). In this study, small D-CAES based on solar PV as the energy source is proposed. The D-CAES cycle is implemented with TES for storing thermal energy generated during the compression phase and produce adiabatic D-CAES cycle. Figure 3.4 shows the proposed cycle configuration which consists of:

- Solar PV to generate the electricity needed to drive the air compressor.
- Air compressor for air compression to charge small vessel.
- Small high pressure cylinder to store the energy in the form of compressed air.
- Micro turbine in which the energy can be extracted via air expansion to produce power.

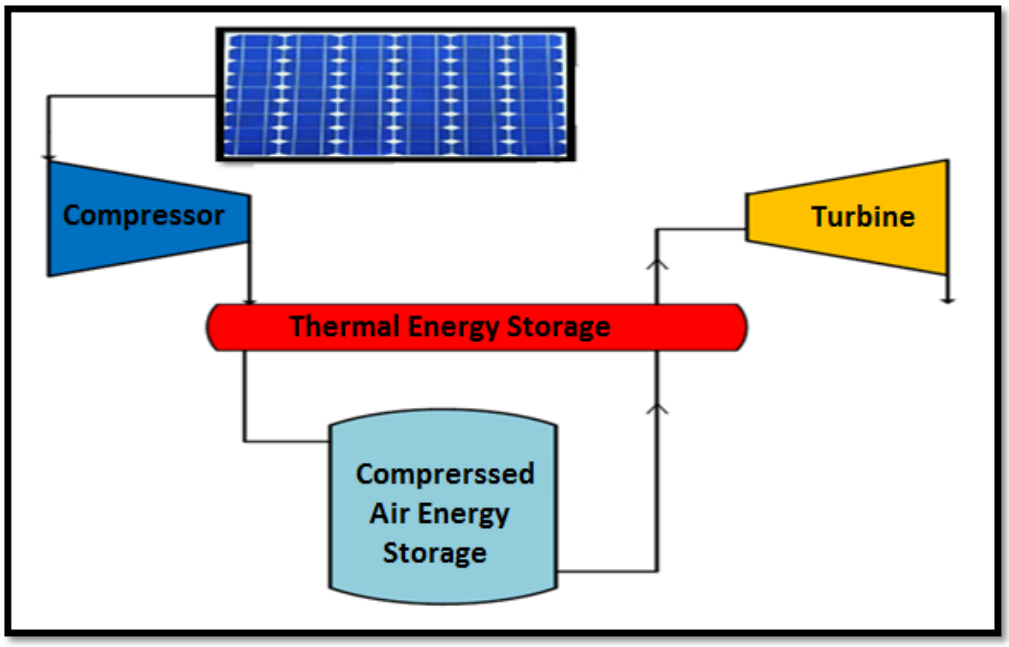

Figure 3.4 Proposed advanced D-CAES based on solar PV.

In the proposed cycle, the solar PV can be used to run the compressor to store the energy in the form of compressed air and the stored energy can be recovered to generate electricity by air expansion through micro turbine. The air entering the turbine can be heated up using TES.

3.4.1 Compression phase:

In the compression phase, the atmospheric air is compressed to the desired pressure. The outlet pressure and temperature of the air leaving the compressor can be calculated using:

$$p_{c,out} = p_{amb} * \pi_c \tag{3.8}$$

$$T_{c,out} = T_{amb} * (\pi_c)^{\frac{n_c-1}{n_c}} \tag{3.9}$$

Where:

$p_{c,out}$, $T_{c,out}$ are the outlet pressure and temperature.

p_{amb}, T_{amb} are the atmospheric pressure and temperature.

π_c is the compressor pressure ratio.

n_c is the polytropic index for the compressor.

The compressor power input can be calculated as:

$$W_c = \frac{1}{\eta_c} \dot{m}_{c,a} C_P T_{amb} \left[\pi_c^{\frac{n_c - 1}{n_c}} - 1 \right] \tag{3.10}$$

For high output pressure, a multi stage of compression processes are used.

3.4.2 Thermal Energy Storage:

To recover the thermal energy generated during compression processes to be used for reheating the air entering the turbine, TES was investigated using both sensible heat and phase change materials (PCM) in order to select the most effective thermal storage option for D-CAES cycle. For the sensible heat storage technology implementation in the proposed distributed CAES configuration, a concrete storage media was used to store the heat produced during the compression process. A cylindrical thermal insulated concrete with heat exchanger coils as shown in Figure 3.5 is studied.

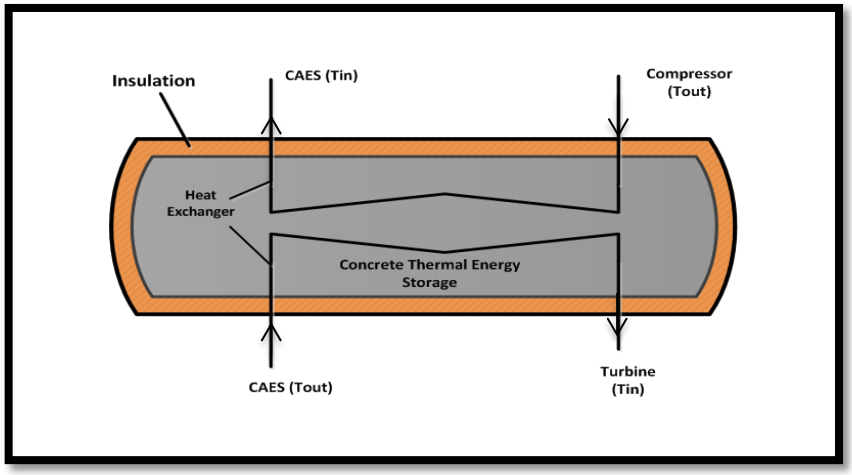

Figure 3.5 concret TES system with heat exchanger

The heat balance in the concrete TES includes two heat exchange processes. In the first process the concrete absorbs the heat produced during compression and in the second process the concrete heats the air before entering the micro turbine during discharging/expansion stage. The heat balance can be expressed as following:

$$m_{TES} C_{P(TES)} \frac{dT_{TES}}{dt} = \dot{q}_{compression} - \dot{q}_{expansion} - \dot{q}_{loss} \quad (3.11)$$

$$\rho_{TES}\, V_{TES} C_{P(TES)} \frac{dT_{TES}}{dt} = \dot{q}_{compression} - \dot{q}_{expansion} - \dot{q}_{loss} \quad (3.12)$$

Where the ρ_{TES} is the density of concrete TES (2750 kg/m^3), $C_{P(TES)}$ is the specific heat of concrete TES (916 J/kg.K), $\dot{q}_{compression}$ is the heat generated during compression, $\dot{q}_{expansion}$ is the heat required to reheat the air entering the turbine during expansion stage, and $\dot{q}_{loss}$ is the heat lost to the surrounding.

The change in TES temperature can be calculated by applying heat exchange theory (Sukhatme and Sukhatme 1996) as following:

$$\dot{q}_{compression} = \dot{m}_{com} C_P (T_{C-out} - T_{CAES-in}) \quad (3.13)$$

The temperature of the air entering the CAES can be calculated as:

$$\frac{T_{C-out} - T_{CAES-in}}{T_{C-out} - T_{TES}} = 1 - e^{\left[\frac{-(UA)_{TES}}{\dot{m}_{com} C_P}\right]} \quad (3.14)$$

Where U is the overall heat transfer coefficient of TES, A is the heat exchange area, T_{C-out} is the temperature of the air at compressor exit, $T_{CAES-in}$is the temperature of the air entering the CAES, $T_{CAES-in}$ is the temperature of the air at CAES inlet, and T_{TES} is TES temperature.

$$\dot{q}_{compression} = \dot{m}_{com} C_P (T_{C-out} - T_{TES})\left(1 - e^{\left[\frac{-(UA)_{TES}}{\dot{m}_{com} C_P}\right]}\right) \quad (3.15)$$

$$\dot{q}_{expansion} = \dot{m}_t \mathrm{C_P}(\mathrm{T_{TES}} - \mathrm{T_{TIT}})(1 - \mathrm{e}^{\left[\frac{-(\mathrm{UA})_{\mathrm{TES}}}{\dot{m}_t \mathrm{C_P}}\right]}) \tag{3.16}$$

$$\dot{q}_{loss} = (\mathrm{UA})_{\mathrm{TES}}(\mathrm{T_{TES}} - \mathrm{T_{\infty}}) \tag{3.17}$$

3.4.3 Air Storage Tank:

For the storage tank and assuming the tank is adiabatic with constant volume, both the charging and discharging processes can be described using ideal gas laws as:

$$\frac{dp}{dt} = \frac{d}{dt}\left(\frac{mRT}{V}\right) = \frac{R}{V}\frac{d}{dt}(mT) \tag{3.18}$$

For the ideal gas:

$$\frac{T^{\frac{\gamma-1}{\gamma}}}{p} = constant \tag{3.19}$$

Equation (19) can be written in a derivational form with respect to the time as:

$$\frac{dT}{dt} = \frac{T}{p}\left[1 - \frac{1}{\gamma}\right]\left[\frac{dp}{dt}\right] \tag{3.20}$$

Using equations (18) and (20) the rate of temperature change can be determined as:

$$\left[\frac{dT}{dt}\right]_{tank} = \frac{1}{m_{a_{tank}}}\left(1 - \frac{1}{\gamma}\right)\left[\dot{m}_{air}^{in} T_{air}^{in} - \dot{m}_{air}^{out} T_{air}^{out}\right] \tag{3.21}$$

Where $m_{a_{tank}}$ is the instantaneous air mas in the tank which can be expressed as:

$$m_{a_{tank}} = \int_0^t \left[\dot{m}_{air}^{in} - \dot{m}_{air}^{out}\right] dt \tag{3.22}$$

3.4.4 Expansion Phase:

In this phase, the compressed air is expanded through a turbine to extract the stored energy. The air entering the turbine is taken from the storage tank at nearly ambient temperature and

passed through the TES to recover stored thermal energy and to increase its temperature before entering the turbine. The output power of the turbine can be determined as:

$$W_t = \eta_t \dot{m}_t C_{P_a} T_{t,air}^{in} \left[1 - (\pi_t)^{\frac{n_t - 1}{n_t}}\right] \tag{3.23}$$

Where $\dot{m}_t$ is discharge mass flow rate and $T_{t,air}^{in}$ is the temperature of the air leaving TES and entering the turbine.

3.5 Simulink Model Descriptions:

Based on the previous thermodynamic equations 3.1 to 3.23, the D-CAES system dynamic modelling was conducted using Matlab/Simulink in order to identify the operating conditions map for the small turbine. Figure 3.6 describes the D-CAES cycle components in Matlab/Simulink. These blocks represent the physical components which are modelled based on dynamic relations of system variables and linked together to account for all interactions of cycle components. Each block consists of input and output functions which describe the operation mode for each physical component.

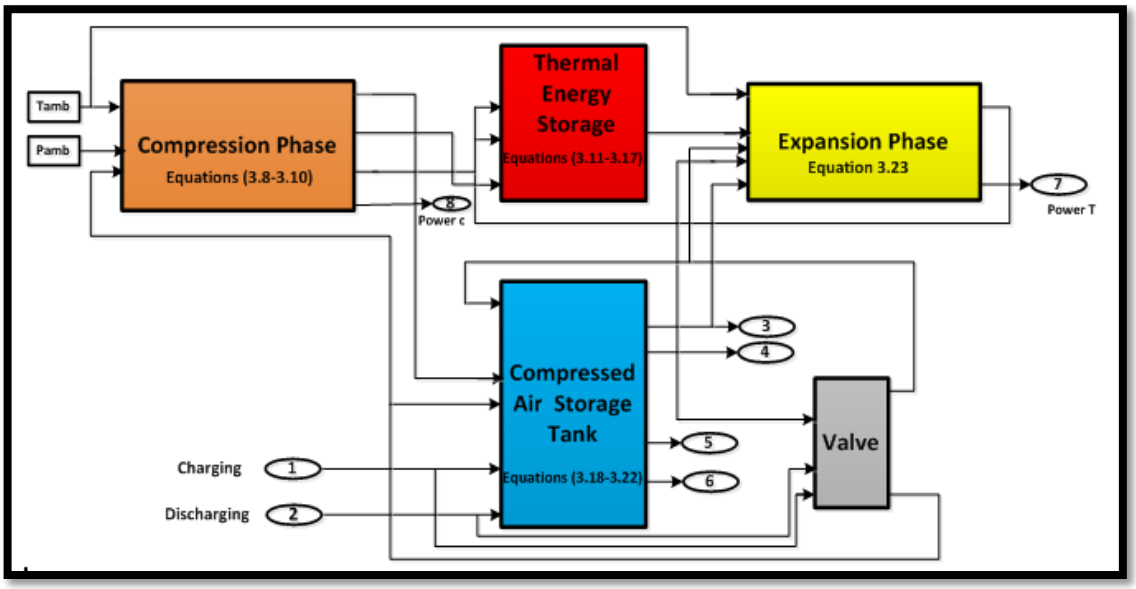

Figure 3.6 Matlab Simulink blocks for D-CAES cycle.

The Matlab/Simulink offers the advantage of using integrators to determine the instantaneous air properties (pressure, temperature and mass) for different cycle operating conditions. For the present study the cycle dynamic modelling aims to identify the operating conditions for the micro turbine under controlled and uncontrolled discharging pressure operation modes. Based on the dynamic modelling results, the turbine was investigated for on and off design conditions to ensure acceptable levels of efficiency and output power for all operating conditions.

Table 3-1 Simulink model parameters

Parameter	Unit	Value
Ambient temperature	K	290
Ambient Pressure	bar	1
Compressor flow rate	kg/s	0.2
Compressor efficiency	[-]	0.86
Turbine mass flow rate	kg/s	0.1
Max tank Pressure	bar	10-40
Air Tank volume	L	200-400-1000

To increase the potential of D-CAES for energy generation applications, the discharge phase (expansion process) needs to be improved for higher system overall efficiency (Safaei and Aziz 2014). From a turbine design point of view, the turbine is designed normally for unique identified operating point for certain output. However, in actual turbine operation, there is a high possibility that the turbine will be operated for a range of operating conditions leading to variations in turbine performance levels (Kim and Ro 1995).

To increase the overall CAES system performance, improving the turbine efficiency during off design operating modes is of paramount importance. In D-CAES, the turbine works extremely in off design conditions as a result of inlet pressure and mass flow rate variations. The inlet pressure can be controlled using pressure regulating valve. However, controlling the discharge pressure leads to change in mass flow rate and cycle performance as obtained by several other researchers (He, et al. 2012, Li, et al. 2012):

$$\dot{m}_{actual} = \dot{m}_{ref}.\frac{p}{p_{ref}}\sqrt{\frac{T_{ref}}{T}} \tag{3.24}$$

$$\eta_{actual} = \eta_{ref}\left[1 - \left(\sqrt{\frac{\Delta h_{ref}}{\Delta h}} - 1\right)^2\right] \tag{3.25}$$

Where $\dot{m}_{ref}$, p_{ref}, and T_{ref} are the design point reference mass flow rate, inlet pressure and temperature respectively.

3.6 CAES Dynamic Modelling Results:

The primary aspect in the development of distributed CAES is the thermodynamic characteristics of CAES in the charging and discharging processes. The thermodynamic analysis of CAES aims to identify the amount of stored energy and the energy required for charging air receiver tank in charging phase and provides detailed information for discharging phase which represent the operating conditions and design specifications for the turbine. In this work, different sizes of compressed air receiver tank were investigated at different compression ratio using thermodynamic relations and system dynamic modelling as described in sections 3.4 and 3.5.

The thermodynamic analysis of CAES can define the energy required for charging the storage tank as well as the amount of energy that can be stored in the system. The energy required for charging the tank was calculated for three tanks 200L, 400L, and 1000L as shown in Figure 3.7. It can be seen that the amount of tank charging energy is dependent upon the charging pressure. For 1000L air receiver, it requires 2.5 kW to achieve a pressure of 40 bars and increasing the tank pressure increases the tank storage capacity.

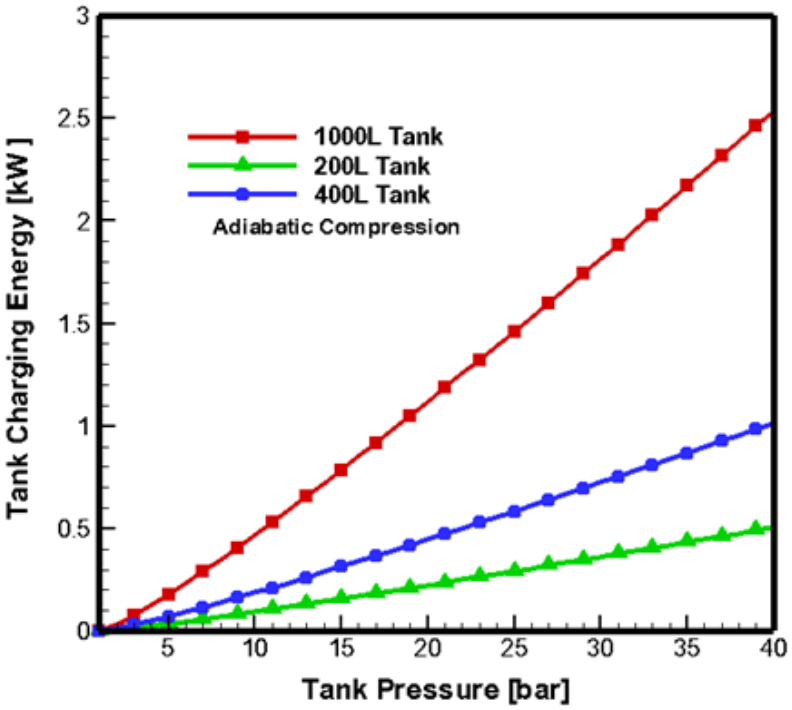

Figure 3.7 Energy required for charging CAES tank

The stored energy in the system is shown in Figures 3.8 and 3.9 in terms of energy density [Whrs/L] and specific energy [J/kg] for both adiabatic and isothermal compression methods for 1000 litter tank volume. As can be seen the calculated energy by isothermal process is higher than adiabatic due to the assumption that the temperature of the air remains constant. The stored energy is calculated for a range of tank pressures (100-5000 kPa) and the maximum stored energy was 4.874 Whrs/L in isothermal charging and 2.109 Whrs/L) in adiabatic process.

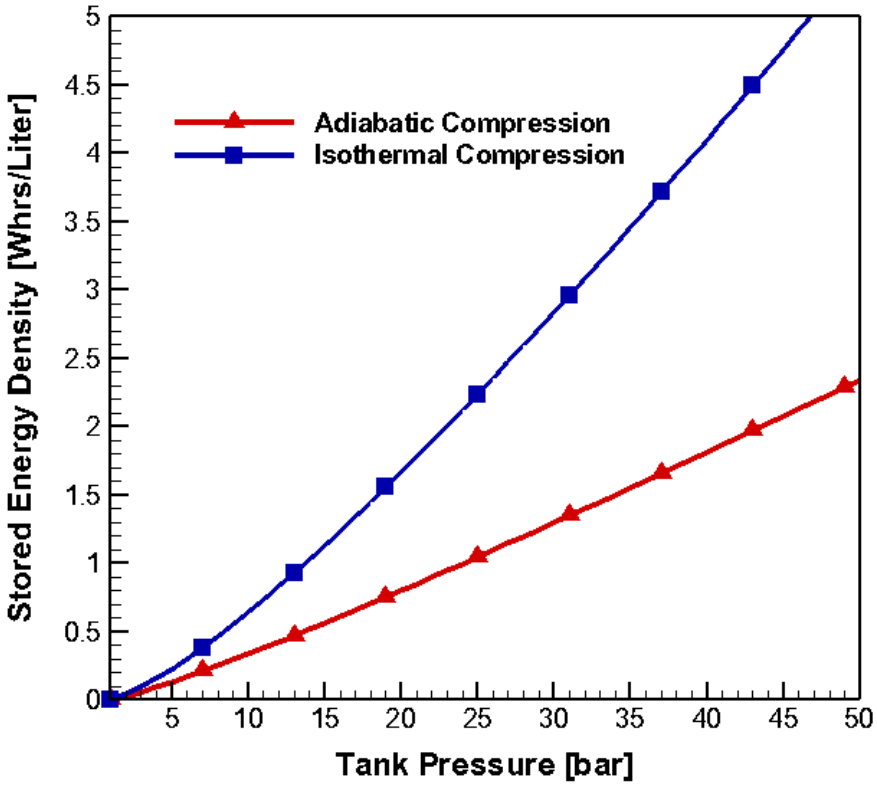

Figure 3.8 Energy density for different Pressure

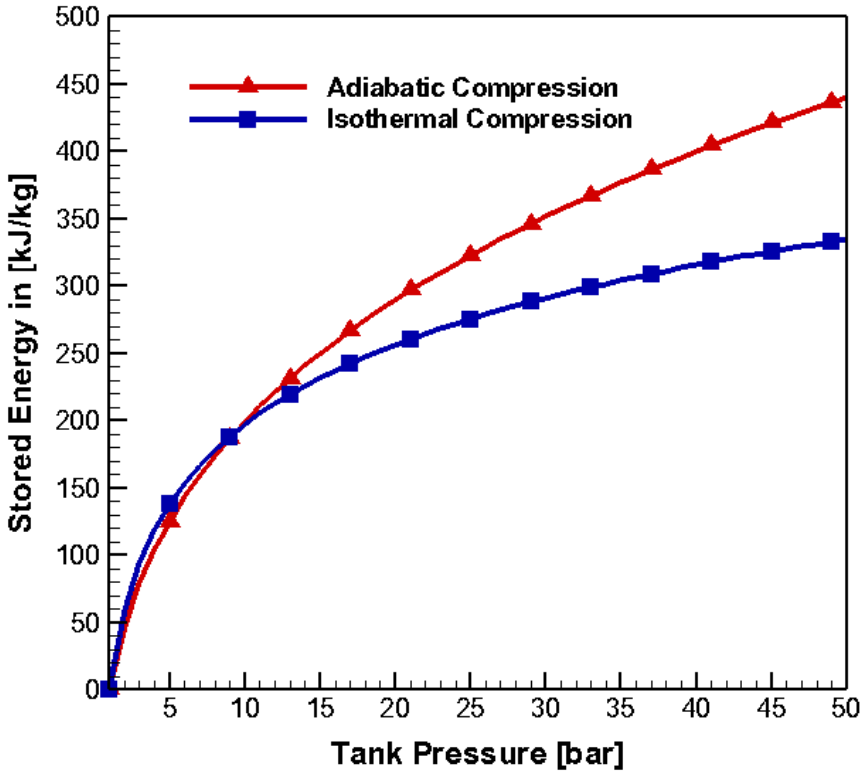

Figure 3.9 Specific energy for different pressure with 1000liter tank

The discharging tank pressure is a key parameter in evaluating the performance of distributed CAES cycle as well as the cycle operation time. Figures 3.10 and 3.11 show the variations in tank pressure for controlled and uncontrolled discharging pressure for different maximum tank pressures. These curves represent the turbine operating map and cycle operation time. The tank discharge time can be increased by discharging at controlled pressure. As a result of fixed pressure discharging, the cycle operation time can be increased by (560 seconds) for 1000 L tank with maximum pressure of 10 bars. This controlled pressure also can provide stable inlet conditions for the small turbine for long time compared to uncontrolled discharge as shown in Figure 3.12.

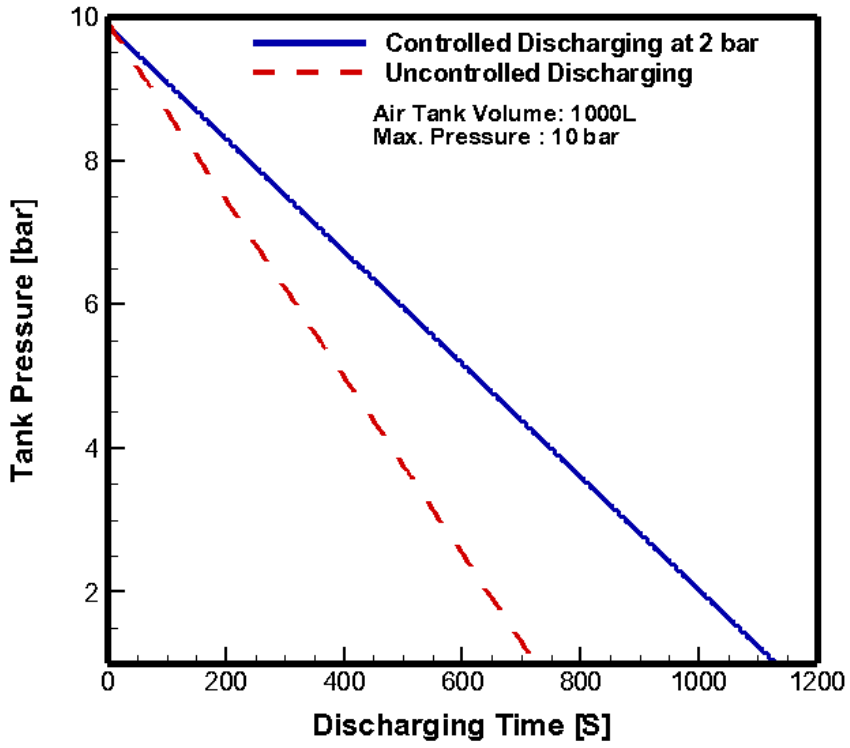

Figure 3.10 Air tank discharging for max. tank pressure 10 bar

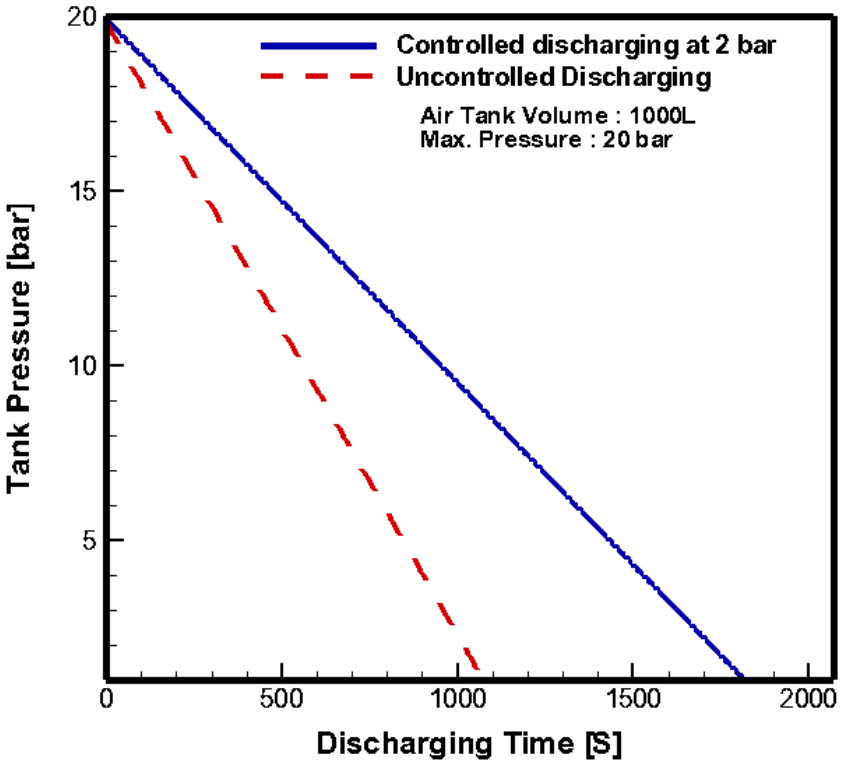

Figure 3.11 Air tank discharging for max. tank pressure 20 bar

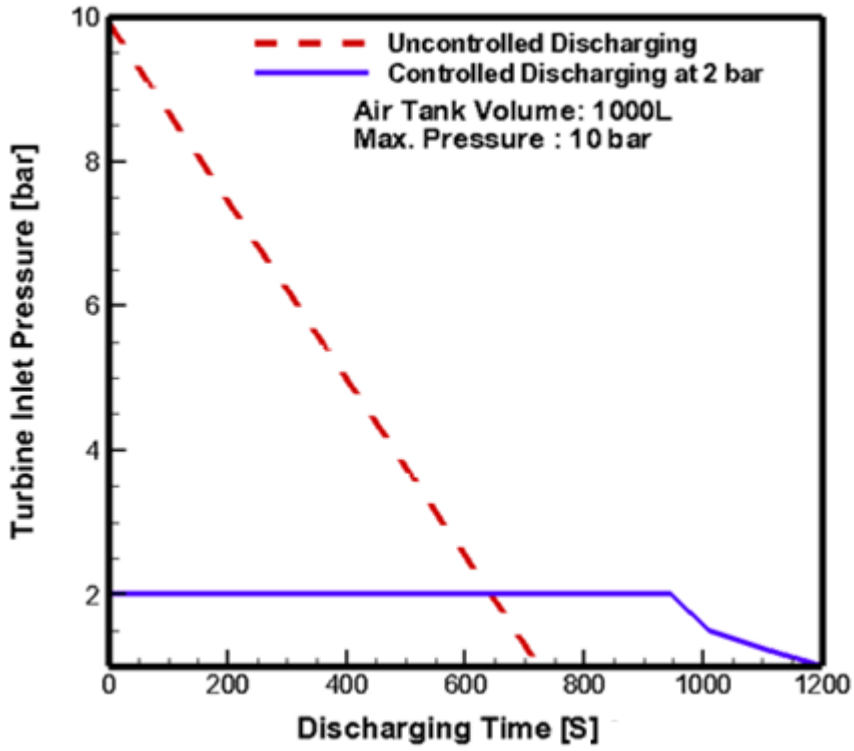

Figure 3.12 Turbine inlet pressure for controlled and uncontrolled discharging pressure

The tank temperature variations with charging time are shown in Figures 3.13 and 3.14 for tank pressure of 10 and 20 bars respectively. The tank temperature can reach 512.09 K at maximum tank pressure 10 bar and 635K for tank pressure of 20bars. This amount of heat needs to be stored using TES system which can be used in expansion phase by reheating the air before entering the turbine.

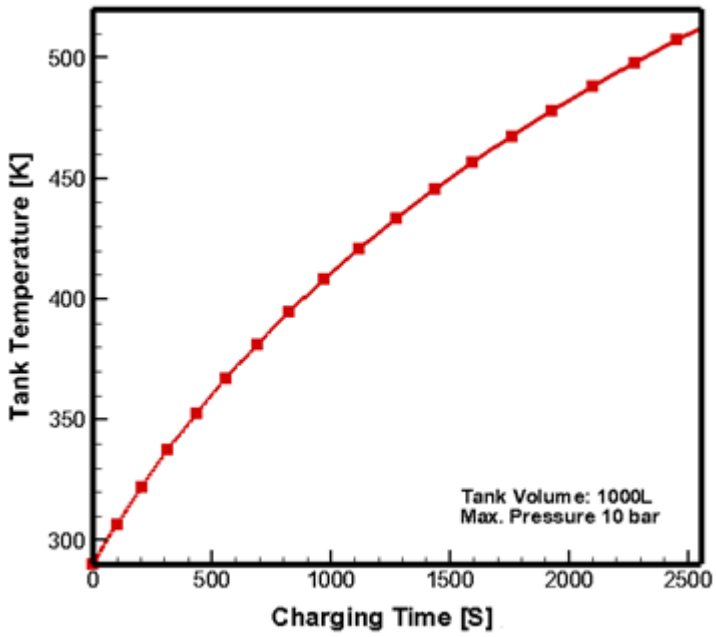

Figure 3.13 Tank temperature for maximum tank pressure 10 bars

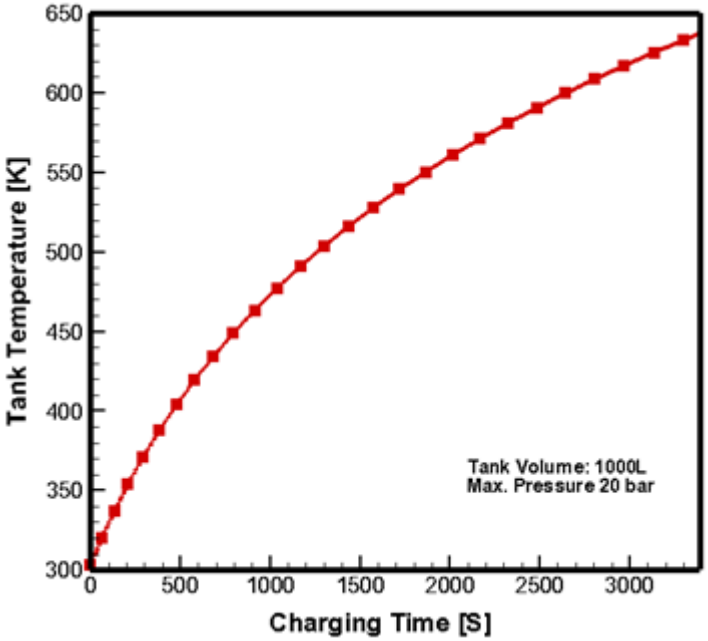

Figure 3.14 Tank temperature for maximum tank pressure 20 bars

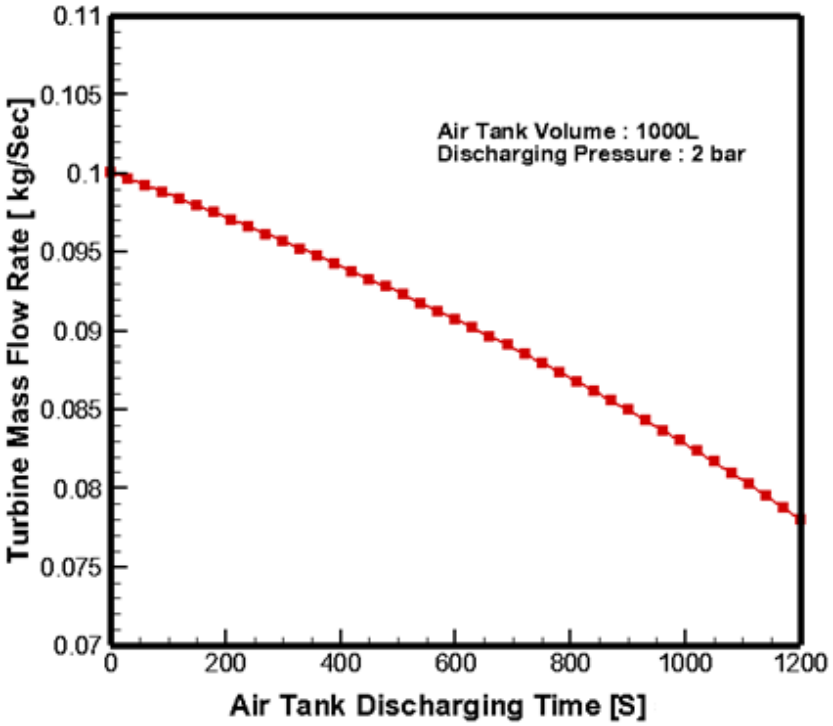

Figure 3.15 Turbine inlet mass flow rate variations for 10 bar maximum tank pressure

Figure 3.15 shows the variation of mass flow rate with discharging time. As can be seen, there is a reduction in mass flow rate which leads to that the turbine will work in off design mode and this leads to decreasing the performance levels like output power which is affected significantly by mass flow rate variations. In order to define the operating conditions for the expansion process in the turbine, the output power of the turbine was calculated for different mass flow rate and total inlet pressure as shown in Figure 3.16.

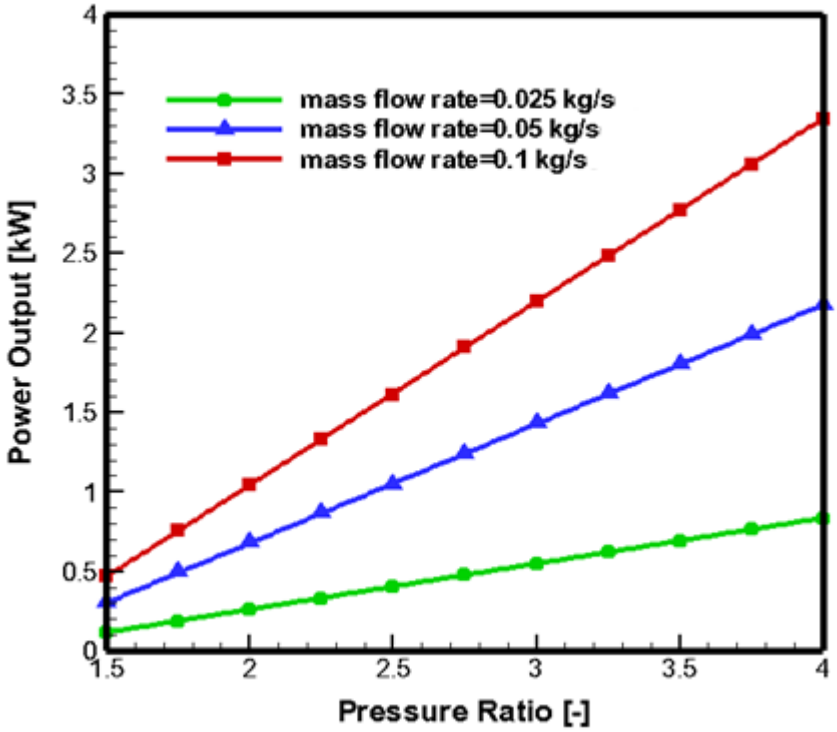

Figure 3.16 Turbine output power for different mass flow rate.

3.7 Turbine Selection Criteria:

The primary aspect in developing the turbine for D-CAES is the thermodynamic characteristics of CAES in the discharging process to identify the operating conditions and performance levels. Based on the cycle modelling results, the main operating conditions and design specifications can be defined in terms of turbine inlet pressure, inlet temperature, inlet mass flow rate, and target output power.

For the proposed D-CAES cycle, the target output power is selected to be 1kW with compressed air receiver volume of 1000 L and maximum pressure of 20 bars. As can be seen from the D-CAES dynamic modelling, the discharging pressure (turbine total inlet pressure) is the key factor which affects turbine performance levels and cycle operation time. In order

to increase the cycle operation time, the discharge pressure was selected to be (1.5-2 bars). Table 3.2 shows the design specification of the turbine expander.

Table 3-2 Turbine design specifications

Parameter	Unit	Value
Target power	kW	1
Turbine inlet pressure	bar	1.5-2
Turbine inlet temperature	K	300-340
Inlet mass flow rate	kg/s	0.05-0.1
Target Efficiency	-	90%

In general, the turbine type is selected based on similarity approach which states that turbines are dynamically similar if they have similar geometry. Using dimensional analysis, the relation between turbine performance and geometrical parameters is defined by a set of non-dimensional parameters as (Dixon and Hall 2013):

$$\eta_{ts} = f\left(\frac{\dot{m}}{\rho_o a_o D^2}, \frac{\rho_o a_o D}{\mu}, \frac{ND}{a_o}, \gamma\right) \tag{3.26}$$

Where $\dot{m}$ is the mass flow rate, D, rotor diameter, N rotational speed, a_o speed of sound, ρ_o fluid density and γ specific heat ratio. Equation (3.26) is normally simplified into other suitable groups as:

$$\eta_{ts} = f(\varphi, \psi, Ma) \tag{3.27}$$

$$\eta_{ts} = f(N_s, d_s, Ma) \tag{3.28}$$

$$\eta_{ts} = f(\varphi, \upsilon, Ma) \tag{3.29}$$

Where φ is the flow coefficient and ψ is loading factors, N_s is characteristic speed, d_s is specific diameter, υ is turbine velocity ratio.

Based on the dimensional analysis, the turbine performance charts were developed by many authors for axial, radial, and mixed turbines as shown in Figure 3. 17 (Wood 1963, Balje 1981, Japikse and Baines 1994). By using the turbine design specifications such as pressure ratio, mass flow rate, rotational speed, and target power, the non-dimensional parameters can be calculated and compared with operating regions on the charts to select turbine type.

The similarity method is acceptable in the case of incompressible flow where the changes in flow density are neglected. However, in the case of compressible flow, the similarity scaling model is influenced by significant variations in some non-dimensional parameters like Reynolds number and Mach number leading to unsuccessful design (Whitfield and Baines 1990, Moustapha 2003). Furthermore, scaling down large scale turbine to achieve miniature turbine leads to unsuccessful prediction of turbine performance due to large differences in power density between large and small turbines (Peirs, et al. 2004).

According to several researchers (Moustapha 2003, Yahya 2010, Dixon and Hall 2013) the key parameters in turbine selection are turbine pressure ratio and inlet mass flow rate. For high pressure ratio with low mass flow rate, the radial turbine is the preferred choice for higher efficiency while the axial turbine is more efficient at low pressure ratio and high flow rate.

Radial turbines can achieve an isentropic efficiency of 85% with at least 65,000 rpm and pressure ratio of (4- 5) (Bao and Zhao 2013). However, for the D-CAES cycle, discharging pressure of 4 bar will decrease the cycle operating time by 340 seconds compared with 2 bar discharging pressure as shown in Figure 3.18. As a result, small axial turbine is selected for the proposed D-CAES to achieve high efficiency at lower discharging pressure (1.5-2 bars) with acceptable cycle operation time.

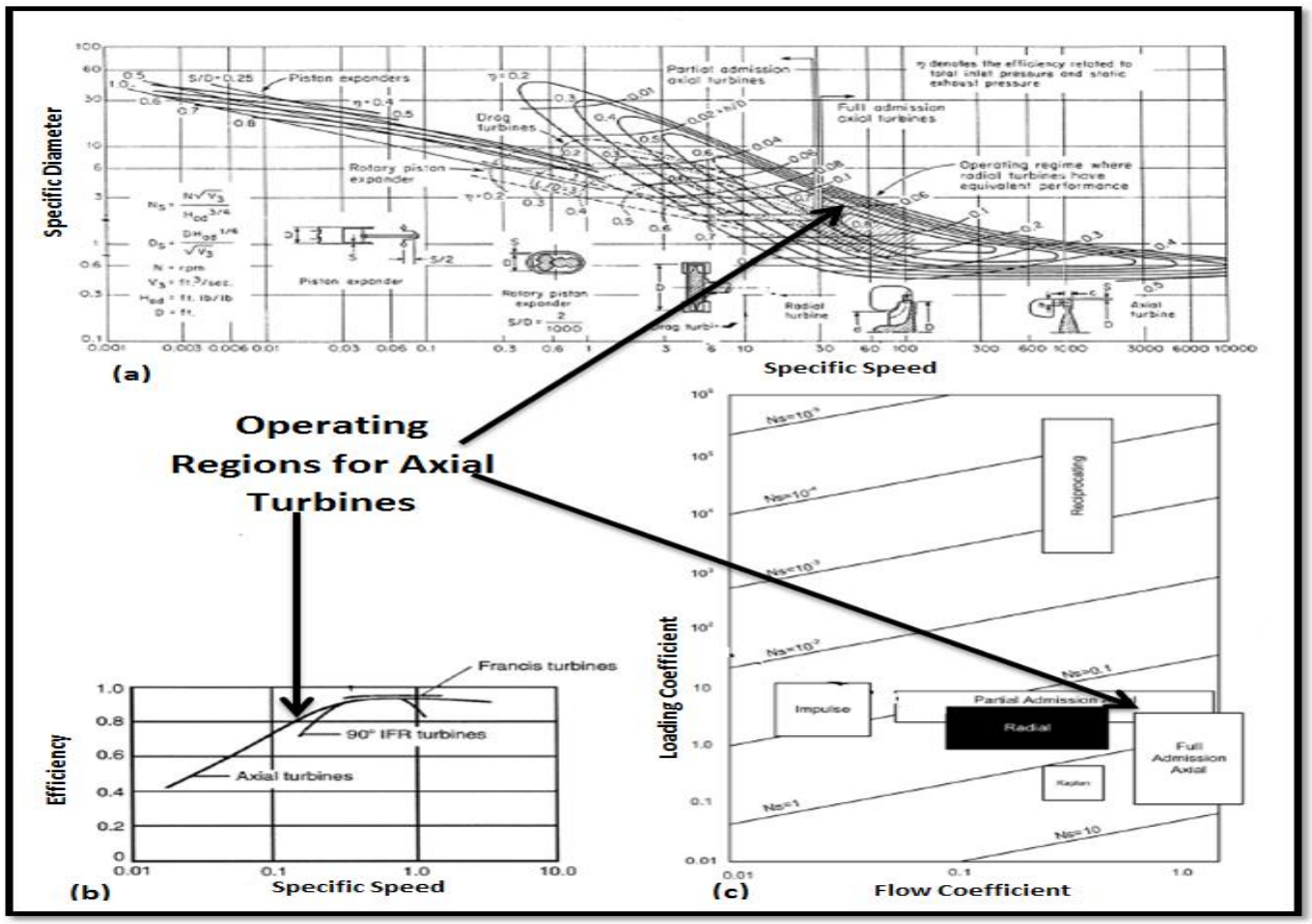

Figure 3.17: Turbine Selection Charts based on non-dimensional parameters (Bao and Zhao 2013).

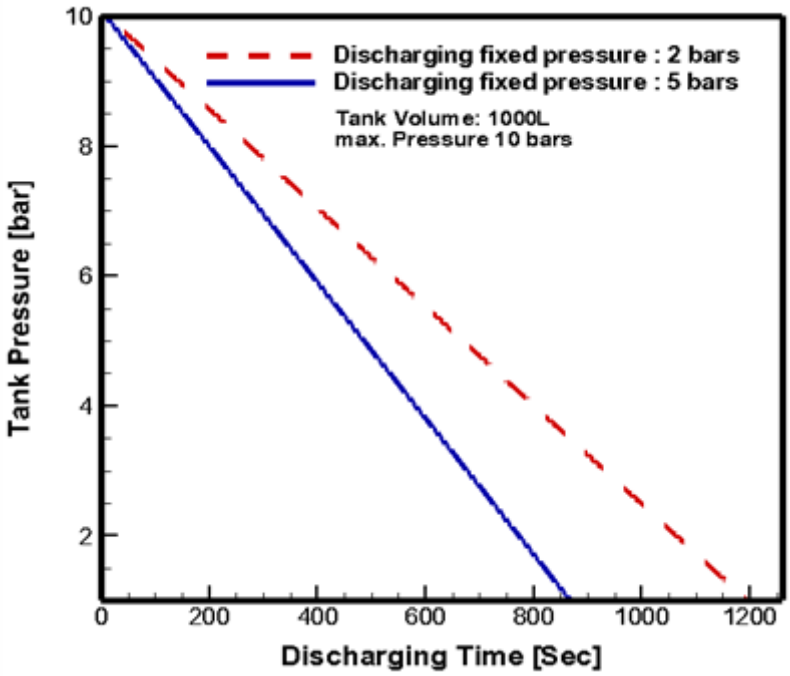

Figure 3.18 CAES tank discharging at different pressures.

3.8 Summary:

- Compressed air storage system is a promising energy storage technology for sustainable environmental friendly energy production based on renewable energy sources.
- For distributed power generation, CAES can be achieved using man made pressure vessels for small and medium applications.
- Small CAES is still not proven and further research is required for developing both compression and expansion phases.
- Based on the D-CAES dynamic modelling, the amount of energy storage depends on air receiver volume and maximum charging pressure.
- Discharging tank pressure and mass flow rate are the key factors which determine the cycle operation time and output power.
- As a result of transient variations of discharging pressure and temperature, the turbine works deeply in off design mode.
- Small axial turbine is selected for the proposed D-CAES to achieve high efficiency at lower discharging pressure (1.5-2 bars) with acceptable cycle operation time.

CHAPTER 4

AXIAL TURBINE DEVELOPMENT METHODOLOGY

4.1 Introduction:

This chapter provides a description of the methodology used to develop a small axial air turbine. A detailed overview of the main design parameters and turbine performance prediction were introduced. The process of developing the axial turbine included: one dimensional mean-line modelling; iterative CFD simulation, finite element analysis, and optimization.

4.2 Axial Turbine Theory:

Axial turbine is an expansion device which extracts the energy from a moving fluid and converts this energy into useful mechanical work. This can be achieved by passing the fluid through axial turbine stage which consists of a fixed row of blades called stator or nozzle guide vanes and a row of rotating blades called rotor. Axial turbine is one of the key components in the power generation systems and aircraft engines (Brayton Cycle). As shown in Figure 4.1, the air enters the compressor at ambient conditions (state2) and is compressed to a certain pressure (state3). This compressed air is used in the combustion chamber to burn the fuel which will raise its temperature (state4). Finally, the combustion gases are expanded through the turbine to the ambient pressure (state5) producing a useful power. This power is used partly to drive the compressor but mainly for electricity generation. In this cycle, the

useful output work which can be used for energy production is the difference between the turbine work and the work required to drive the compressor.

$$w_{net} = w_{turbine} - w_{compressor} = C_p\{(T_{o4} - T_{o5}) - (T_{o3} - T_{o2})\} \quad (4.1)$$

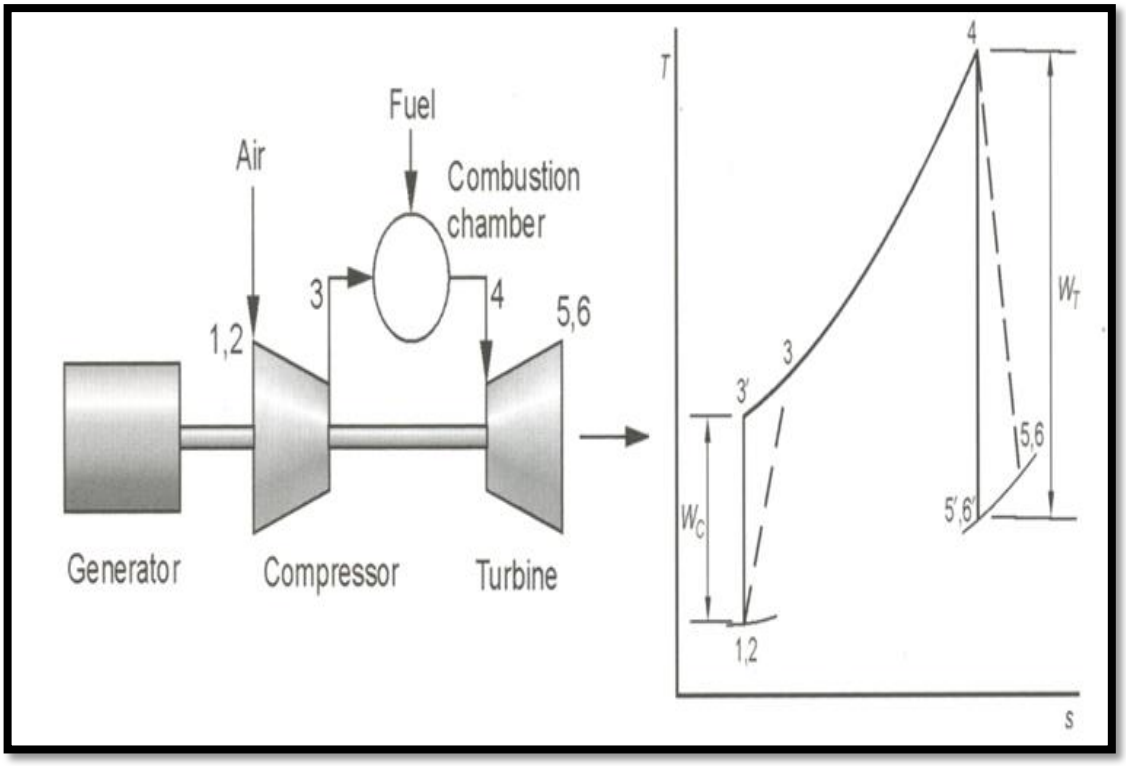

Figure 4.1 Ideal Brayton cycle engine

The thermodynamic cycle efficiency can be expressed as a ratio of useful output work to the heat required for the combustion:

$$\eta_{th} = \frac{w_{net}}{q_{combustion}} = \frac{w_{net}}{C_P(T_{o4} - T_{o3})} \quad (4.2)$$

The ideal thermodynamic cycle efficiency can be also expressed in terms of pressure ratio ($\pi = \frac{P_{o3}}{P_{o2}}$) as:

$$\eta_{th} = 1 - \frac{1}{\pi^{(\frac{\gamma-1}{\gamma})}} \quad (4.3)$$

From equations (4.2) and (4.3) the specific work output can be expressed as a function of temperature and pressure ratios as:

$$\frac{w_{net}}{C_p T_{o1}} = \frac{T_{o4}}{T_{o1}}\left(1 - \frac{1}{\pi^{\left(\frac{\gamma-1}{\gamma}\right)}}\right) - \left(\pi^{\left(\frac{\gamma-1}{\gamma}\right)} - 1\right) \tag{4.4}$$

Equation (4.4) shows clearly that the output work is dependent on the temperature ratio $(^{T_{o4}}/_{T_{o1}})$ while equation (4.3) shows that the cycle efficiency is a function of pressure ratio (π). As a result, the designer needs to optimize both temperature and pressure ratios in early design stages to define the turbine design point operating conditions.

4.3 Expansion through a stage in an axial turbine:

In axial turbine stage, the flow enters the stage and is accelerated and guided by stator towards rotor blades. As shown in Figure 4.2 the moving fluid through the turbine has three components; axial velocity C_x (the component of velocity in axial direction), tangential velocity C_θ (the velocity component in tangential direction), and third component is radial velocity C_r (the velocity component in radial direction) (Moustapha 2003).

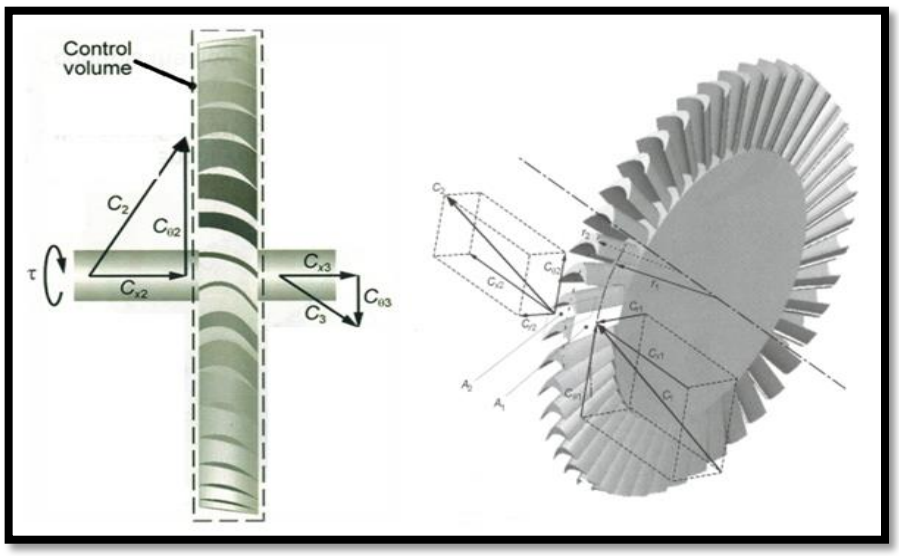

Figure 4.2 Flow through turbine blades

By applying Newton's Second Law, the generated torque is equal to the change in momentum through turbine stage as:

$$\tau = \dot{m}[r_3 C_{\theta 3} - r_2 C_{\theta 2}] \tag{4.5}$$

The turbine output power is:

$$Power = \tau\Omega = \dot{m}[U_3 C_{\theta 3} - U_2 C_{\theta 2}] \tag{4.6}$$

Where Ω is the angular velocity and U is the blade speed ($U = \Omega r$).

The specific work done by the turbine is:

$$\Delta W_t = \frac{Power}{\dot{m}} = \frac{\tau\Omega}{\dot{m}} = U(C_{\theta 2} - C_{\theta 3}) \tag{4.7}$$

Equation (4.7) is a well-known equation which describes the working principles of turbines and known as Euler's Turbine Equation (Dixon and Hall 2013).

The Mollier diagram shown in Figure 4.3 (a) describes the working principles of a turbine stage in terms of thermodynamic characteristics ($h - s$ diagram) including state changes due to irreversibility. The process (1-2) represents the actual flow expansion in the nozzle where the pressure drops from P_1 to P_2 and the process (2-3) describes the expansion through the rotor blades where the pressure drops from P_2 to P_3. The dash line represents the ideal reversible expansion process. Applying the first law of thermodynamics for adiabatic expansion, the output work is equal to the total enthalpy drop through the turbine stage as:

$$\Delta W_t = h_{o1} - h_{o3} \tag{4.8}$$

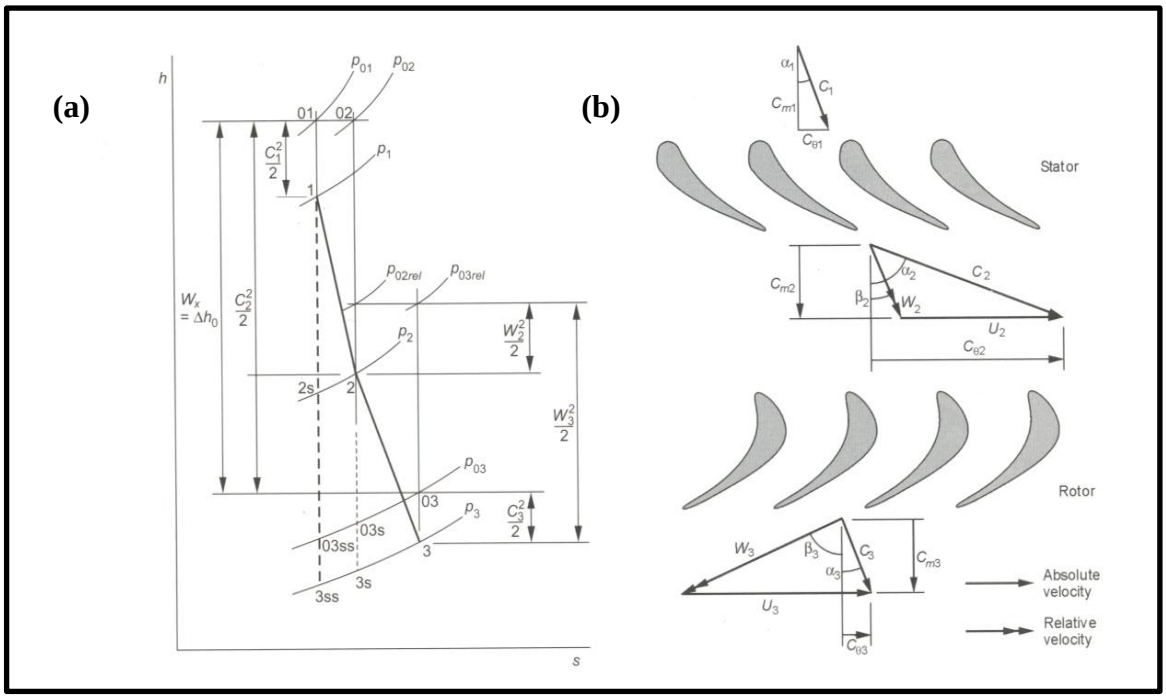

Figure 4.3 (a) Enthalpy-entropy diagram (b) Turbine velocity triangles

The flow development in axial turbine stage (stator and rotor) can be described by velocity triangles at turbine blade mean diameter as shown in Figure 4.3 (b). The flow enters the turbine stator at velocity C_1 and with an angle α_1. The flow is accelerated and exits with C_2 and with an angle α_2. As shown in velocity triangles the flow enters the turbine rotor with relative velocity w_2 and angle β_2. The relative velocity (w) can be determined by subtracting the blade speed U from absolute velocity C. Finally, the flow is accelerated again through the rotor and leaves with relative velocity w_3 and angle β_3 (Dixon and Hall 2013).

From Enthalpy-Entropy $(h-s)$ diagram shown in Figure 4.3 (a), in the case of uncooled turbine blade:

$$h_{o1} = h_{o2} \tag{4.9}$$

The stagnation enthalpy can be written as $(h_o = h + \frac{1}{2}C^2 + \frac{1}{2}C_\theta^2)$ and by using equations (4.7) and (4.9) the total enthalpy drop can be determined as:

$$h_{o2} - h_{o3} = h_2 - h_3 + \frac{1}{2}(C_2^2 - C_3^2) + \frac{1}{2}\left(C_{\theta 2}^2 - C_{\theta 3}^2\right) = U(C_{\theta 3} + C_{\theta 2}) \tag{4.10}$$

From velocity triangles and by assuming constant axial velocity (C_x) and blade speed (U) at turbine inlet and exit then the turbine specific work can be expressed in terms of absolute velocity (C) and relative velocity (w):

$$\Delta W_t = \frac{1}{2}[(w_2^2 - w_3^2) + (C_2^2 - C_3^2)] \tag{4.11}$$

The velocity triangles are connected to the Euler Turbine Equation (4.7) ($w_t = U_3 C_{\theta 3} - U_2 C_{\theta 2}$) which explains that the turbine output work depends on the difference between $C_{\theta 2}$ and $C_{\theta 3}$ and for higher work the designer should keep $C_{\theta 3}$ small and $C_{\theta 2}$ large .The velocity triangles also show that the flow angles are achieved by turning the blade itself to turn the flow in axial direction (Moustapha 2003, Aungier 2006, Dixon and Hall 2013).

4.4 Turbine Blade Terminology:

There is a well-known method for turbine cross section definition published by (Pritchard 1985). In this method the blade aerofoil cross section is defined by eleven parameters as shown in Figure 4.4 (Moustapha 2003). These parameters include aerofoil radius, axial chord, tangential chord, turning angle, inlet blade angle, exit blade angle, inlet wedge angle, leading edge radius, trailing edge thickness, throat and number of blades.

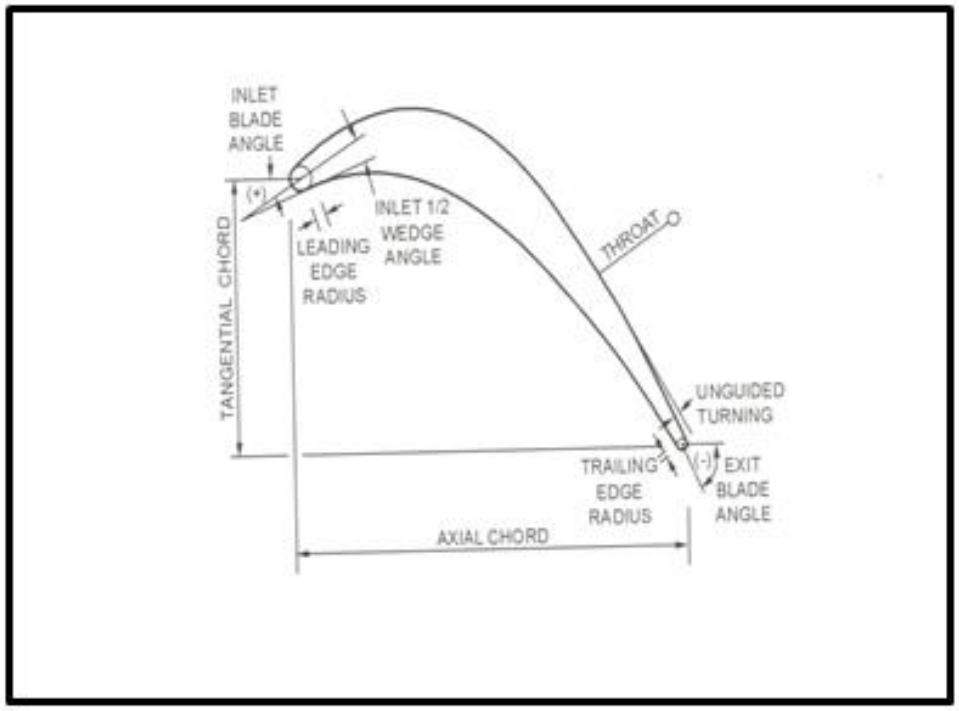

Figure 4.4 Turbine blade cross-section aerofoil (Moustapha 2003)

There are other parameters which are used to define the overall turbine blade geometry and size as shown in Figure 4.5. The blade profile is constructed by means of curved camber line which divides the blade surface into concave and convex sides. The concave is known as pressure side and the convex is known as suction side. As shown in Figure 4.4 and Figure 4.5 the geometrical parameters which are used to characterise the blade passage include (Wilson and Korakianitis 2014):

- Blade pitch (s) which defines the spacing between turbine blades.
- Blade span which represents blade height (h) and is equal to the difference between blade tip and hub radiuses.
- Blade axial chord (c_x) which represents the axial length of the parallel line to the axial blade axis.
- Blade chord (c) which is the true distance between the leading and trailing edges of the blade.
- Throat (o) is the minimum area of the turbine blade passage.

- Incidence angle (i) which equals the difference between inlet flow angle (α_1) and inlet metal angle (α_{m1}).

$$i = \alpha_1 - \alpha_{m1} \tag{4.12}$$

- Deviation angle (δ) which equals the difference between flow exit angle (α_2) and exit blade metal angle (α_{m2}).

$$\delta = \alpha_2 - \alpha_{m2} \tag{4.13}$$

- Deflection angle (ε) which is known as blade turning angle and equals the difference between inlet and exit flow angles.

$$\varepsilon = \alpha_1 - \alpha_2 \tag{4.14}$$

- Camber line which represents blade symmetry line and divides the blade surface into pressure side and suction side.
- Camber angle (θ) the angle between tangents of chord line and camber line and it measures the amount of turning achieved by blade and equals the deference between blade metal angles at inlet and exit.

$$\theta = \alpha_{m1} - \alpha_{m2} \tag{4.15}$$

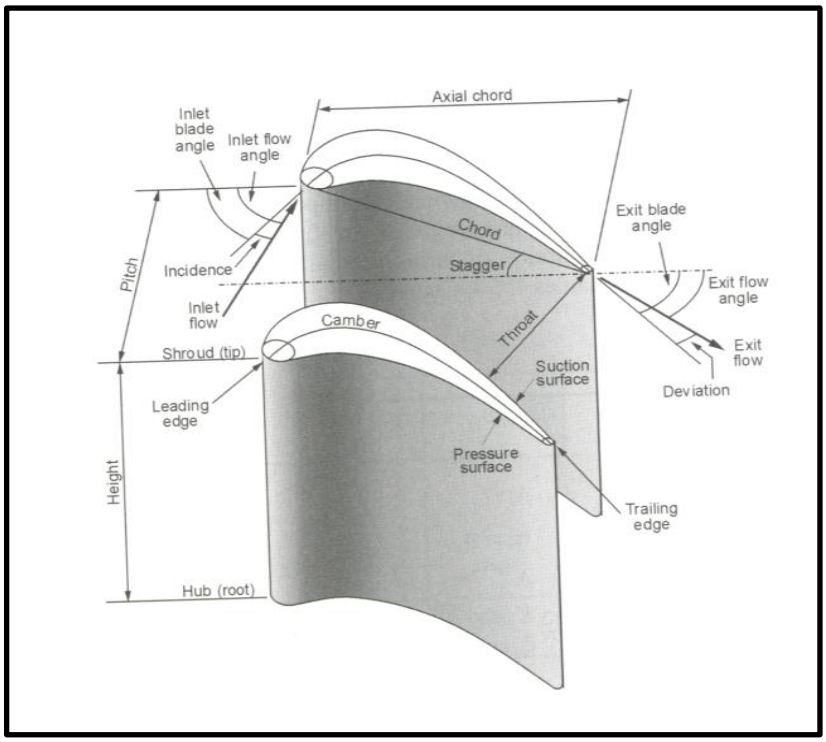

Figure 4.5 Turbine overall geometry (Moustapha 2003)

4.5 Axial turbine design parameters:

There is a set of turbine dimensionless parameters which have significant impact on turbine overall performance. These parameters allow the designer to optimize the design by varying these parameters for different operating conditions. This section provides a brief description of turbine dimensionless parameters.

4.5.1 Total-to-Total Efficiency:

Generally turbine efficiency is the ratio of actual work to ideal work and is the main measure of losses. In case of making use of exhaust kinetic energy, the common useful definition of turbine efficiency is total to total efficiency (Dixon and Hall 2013). From Mollier diagram of enthalpy drop which is shown in Figure 4.3 (a) the total to total efficiency can be expressed as:

$$\eta_{tt} = \frac{h_{o1} - h_{o3}}{h_{o1} - h_{o3ss}} \tag{4.16}$$

Where $(h_{o1} - h_{o3})$ is the total enthalpy drop in the actual irreversible adiabatic process (1-3) and $(h_{o1} - h_{o3ss})$ is the total enthalpy change in the ideal isentropic process (1-3ss).

4.5.2 Total-to-Static Efficiency:

Total to static efficiency is used in the case of flow exit kinetic energy is not included with output useful power. It is defined as:

$$\eta_{ts} = \frac{h_{o1} - h_{o3}}{h_{o1} - h_{3ss}} \tag{4.17}$$

4.5.3 Degree of Reaction:

It is a well-known parameter in turbine design and it defines how the expansion process is divided between nozzle and rotor in the same turbine stage. Mathematically, turbine reaction is expressed as the ratio between enthalpy drop in the rotor to enthalpy drop in the whole stage (stator and rotor):

$$R = \frac{h_2 - h_3}{h_1 - h_3} \tag{4.18}$$

4.5.4 Stage Loading Factor:

Stage loading (ψ) is a measure of work that can be generated by the single stage and based on this parameter and the required amount of work, the number of stages can be determined. Stage loading can be defined mathematically as the ratio of total enthalpy drop in the stage to the square of blade velocity.

$$\psi = \frac{\Delta h_o}{U^2} \tag{4.19}$$

4.5.5 Flow Coefficient:

In axial turbines, flow coefficient is the ratio of axial flow velocity to the velocity of the blade. Its value defines whether the flow angles close to axial or tangential directions.

$$\emptyset = \frac{C_x}{U} \tag{4.20}$$

4.5.6 Turbine Flow Capacity:

It is also known in some references as swallowing capacity and is used to study turbine mass flow rate for different operating conditions.

$$Flow\ capacity = \frac{\dot{m}\sqrt{T_{o1}}}{P_{o1}} \tag{4.21}$$

4.6 Axial Turbine Development Methodology:

This section describes the development process of axial turbine which starts normally with a detailed analysis of the power cycle in order to identify the turbine specifications and operating conditions. At this stage, the researcher can determine the working fluid type, total pressure ratio, total inlet temperature, rotational speed, and mass flow rate or required output power. Figure 4.6 shows the flow chart of the steps used in developing axial turbine which are necessary to be performed to achieve the desired results.

Once the turbine operating conditions are identified based on cycle analysis, the next step is preliminary turbine sizing process which can be performed using one dimensional meanline approach for turbine design. The main goal of meanline modelling is to determine axial turbine overall geometry and the initial performance parameters as output power and turbine efficiency which can be predicted using performance and losses estimation for different operating conditions.

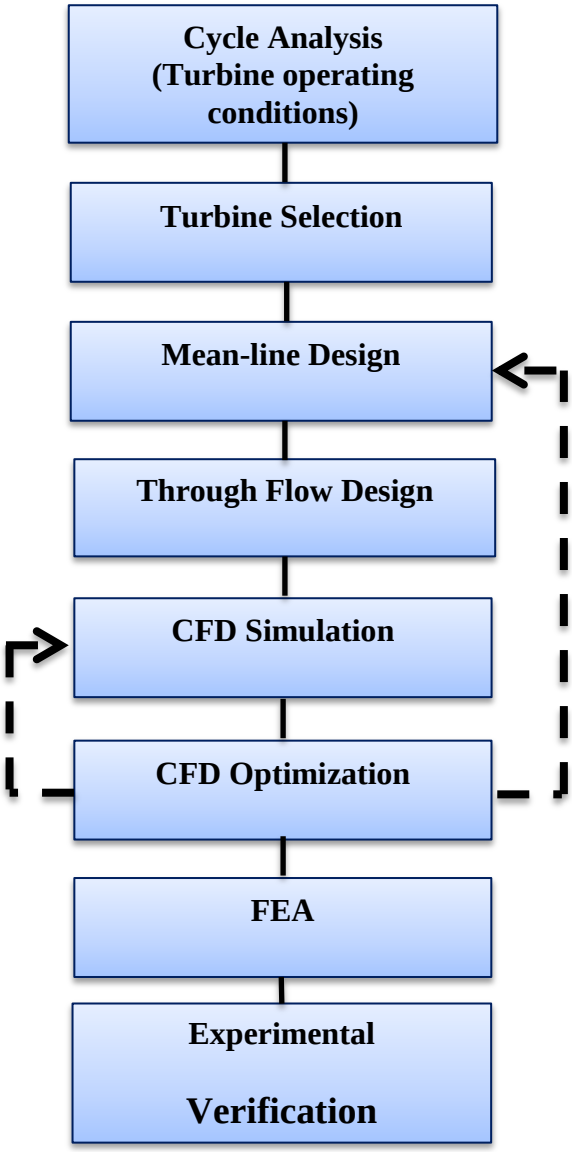

Figure 4.6 Overview of the methodology (adopted from (Moustapha 2003))

In conventional turbine design, the 1D Mean-line modelling is followed by throughflow analysis or 2D design method in which the Mean-line calculations are extended to include flow analysis along blade span from hub to tip to consider the variations in flow along turbine blade span. The throughflow analysis can be conducted in the case of large scale turbines with long blades having hub to tip ratio around 0.4 where the variations in flow are significant (Sieverding 1985, Yahya 2010).

Due to the fact that 1D meanline approach is based on many simplified assumptions, the results of meanline design require significant improvements to capture the complex 3D viscous flow features through turbine passage. Hence, turbine 3D CFD simulation is required to develop aerodynamically efficient turbine blade profile. Using CFD modelling, the turbine efficiency can be improved by varying blade geometry parameters. Furthermore, using CFD the influence of several parameters can be investigated through CFD simulation like number of blades, wedge angle, deflection angle, stator-rotor gap, and other geometry parameters which are not considered in conventional performance prediction schemes. In this research, the CFD analysis was used to predict the loss through turbine stage and the results were compared with conventional loss prediction techniques to identify the most appropriate loss model for preliminary small scale axial turbine sizing.

After the aerodynamic design phase, the designer needs to ensure that the design can mechanically withstand different loads during turbine operations. This can be evaluated using 3D turbine blade finite element analysis (FEA) to identify total stress and deformation levels.

The turbine development process also included the optimization of turbine blade profile for maximum efficiency and minimum loss through CFD simulation using Multi-objective Genetic Algorithm (MOGA) optimization to achieve the required power at high efficiency. A detailed description of axial turbine optimization techniques is provided in chapter 5.

4.6.1 One Dimensional Mean-Line Turbine Design Approach:

Mean-line modelling assumes that the characteristics and parameters of the whole flow through the turbine passage at the mean streamline represent the average of the flow dynamic properties in the turbine passage (Moustapha 2003). For simplicity, this approach neglects the flow variations in both radial and circumferential directions. In mean-line approach, the flow governing equations and Euler turbomachinery equation are solved at mean turbine radius.

The mean radius (r_m) is shown in Figure 4.7 and can be defined mathematically in terms of blade hub and tip radiuses as:

$$r_m = \frac{r_h + r_t}{2} \tag{4.22}$$

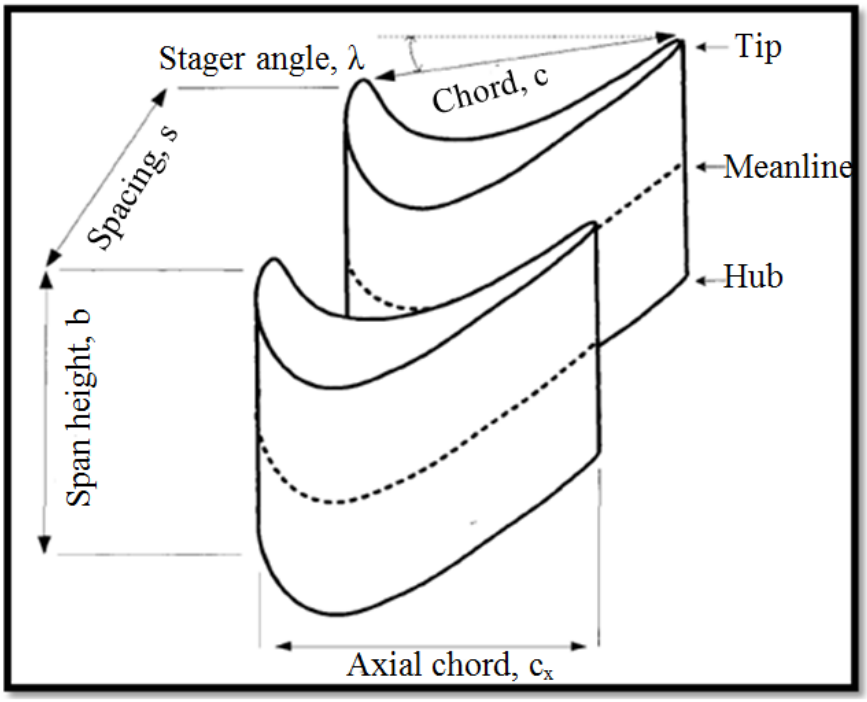

Figure 4.7 Axial turbine mean-line

Meanline modelling is a highly iterative process since it requires comprehensive studies of many different configurations by exploring a large design space created by variation of a large group of input parameters. Inputs to the mean-line model include the operating conditions (turbine inlet total temperature and pressure, mass flow rate and expansion ratio), non-dimensional parameters (velocity ratio, specific speed, loading coefficient) and geometry ratios (ratio of rotor hub to tip) that are either provided as an input file or as an output from another code (i.e. cycle analysis program). With the provided inputs and the initial guess of the turbine isentropic efficiency, the preliminary design of the rotor is carried out.

Using mean-line modelling, the turbine design space is generated by design parameters variation. According to the cycle analysis, there are several parameters which need to be specified as input parameters for mean-line analysis to calculate turbine overall size and for performance prediction. These parameters include: turbine operating conditions (inlet pressure, inlet temperature, pressure ratio, and mass flow rate), non-dimensional design parameters (flow coefficient, blade loading, and velocity ratio), and some geometrical parameters (hub-to-tip ratio). Also, based on the application of axial turbine the designer needs to identify the output power, temperature drop, rotational speed, and target efficiency (Moustapha 2003).

The preliminary design of axial turbine normally starts with the selection of flow coefficient, stage loading, and degree of reaction. This can be achieved at early design stages by using Smith chart which is shown in Figure 4.8. Smith chart is an empirical chart that provides a range of turbine efficiency for different flow coefficient values (0.4-1.2) and stage loading coefficient (0.3-0.5) based on the testing results of 70 turbines of Rolls-Royce aircraft engines (Dixon and Hall 2013).

Using the flow coefficient, stage loading, and degree of reaction, the 1D modelling was performed to determine turbine velocity triangles and working fluid thermodynamic properties can be calculated at the mean-line. The velocity triangles allow the designer to calculate all velocity components, absolute and relative blade angles.

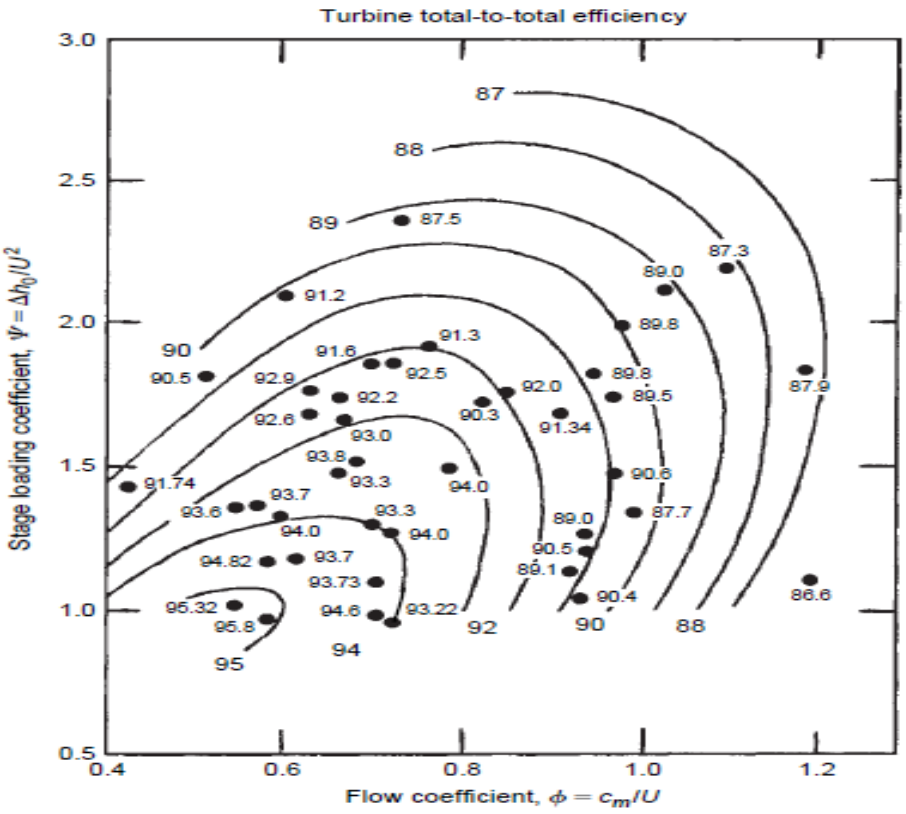

Figure 4.8 Smith chart of axial turbine stage (Smith 1965)

According to (Dixon and Hall 2013) the shape of velocity triangles is connected with three non-dimensional design parameters: degree of reaction, flow coefficient, and loading coefficient as following:

Using the definition of stage reaction:

$$R = \frac{h_2 - h_3}{h_1 - h_3} = 1 - \frac{(h_1 - h_2)}{h_{01} - h_{03}} \tag{4.23}$$

For constant axial velocity:

$$h_1 - h_2 = (h_{o1} - h_{o2}) + \frac{1}{2}(c_2^2 - c_1^2) = \frac{1}{2}c_x^2(tan^2\alpha_2 - tan^2\alpha_1) \tag{4.24}$$

From equation (4.19):

$$h_{o1} - h_{o3} = \psi U^2 \tag{4.25}$$

By substituting equations (4.24) and (4.25) in equation (4.23) the stage reaction can be expressed as:

$$R = 1 - \frac{c_x^2}{2\psi U^2}(tan^2\alpha_2 - tan^2\alpha_1) \tag{4.26}$$

Using flow coefficient definition ($\emptyset = c_x/U$), the stage reaction can be written in terms of loading coefficient, flow coefficient, and flow angles as:

$$R = 1 - \frac{\emptyset^2}{2\psi}(tan^2\alpha_2 - tan^2\alpha_1) \tag{4.27}$$

The stage loading can also be defined in terms of tangential velocity and blade speed as:

$$\psi = \frac{\Delta C_\theta}{U} = \frac{c_x(\tan\alpha_2 + \tan\alpha_3)}{U} = \emptyset(tan\,\alpha_2 + tan\,\alpha_3) \tag{4.28}$$

Using equations (4.27) and (4.28) the stage loading can be expressed in another form as:

$$\psi = 2(1 - R + \emptyset tan\alpha_1) \tag{4.29}$$

Equation (4.29) shows that high stage loading can be achieved using low reaction and high swirl angle. Also for fixed design parameters the designer can determine the flow angles and the velocity triangles can be constructed at mean line. The geometrical relations of velocity triangles can be used to identify absolute and relative angles as detailed by (Yahya 2010):

$$\tan\beta_2 = \tan\alpha_2 - \frac{1}{\emptyset} \tag{4.30}$$

$$\tan\beta_3 = \tan\alpha_3 + \frac{1}{\emptyset} \tag{4.31}$$

The flow angles can also expressed in terms of $\emptyset$ and ψ as:

$$\tan\beta_2 = (\psi - 2R)/2\,\emptyset \tag{4.32}$$

$$\tan\beta_3 = -(\psi + 2R)/2\,\emptyset \tag{4.33}$$

The turbine stage performance can be determined in terms of total to total efficiency or total to static efficiency. Using equation (4.16) and the velocity triangles relations and enthalpy drop, the total to total efficiency can be written as:

$$\eta_{tt} = \frac{h_{o1} - h_{o3}}{h_{o1} - h_{3ss}} = \frac{h_1 - h_3}{h_1 - h_3} + (h_3 - h_{3s}) + (h_{3s} - h_{3ss})] \tag{4.34}$$

From thermodynamic second law and by applying the slope of constant pressure line on enthalpy- entropy diagram ($(\frac{\partial h}{\partial s})_{\,p} = T$), the enthalpy change can be written as:

$$\Delta h = T\Delta s \tag{4.35}$$

Then:

$$h_{3s} - h_{3ss} = T_3(S_{3s} - S_{3ss}) \tag{4.36}$$

$$h_2 - h_{2s} = T_2(S_2 - S_{2s}) \tag{4.37}$$

Mollier diagram (Figure 4.3 a) shows that $(S_{3s} - S_{3ss})$ and $(S_2 - S_{2s})$ are equal and as a result, equations (4.36) and (4.37) can be written in one equation as:

$$h_{3s} - h_{3ss} = (\frac{T_3}{T_2})(h_2 - h_{2s}) \tag{4.38}$$

Due to the flow irreversibility, the change in static enthalpy through the nozzle and rotor can be defined as (Dixon and Hall 2013):

For nozzle: $$h_2 - h_{2s} = \frac{1}{2} c_2^2 \zeta_N \tag{4.39}$$

For rotor: $$h_3 - h_{3s} = \frac{1}{2} w_3^2 \zeta_R \tag{4.40}$$

Where ζ_N and ζ_R are nozzle and rotor loss coefficients.

Finally both total-to-total and total to static efficiencies can be determined as:

$$\eta_{tt} = \left[1 + \frac{\zeta_R w_3^2 + \zeta_N c_2^2 \, T_3/T_2}{2(h_1 - h_3)}\right]^{-1} \tag{4.41}$$

$$\eta_{ts} = \left[1 + \frac{\zeta_R w_3^2 + \zeta_N c_2^2 + c_1^2}{2(h_1 - h_3)}\right]^{-1} \tag{4.42}$$

As can be seen from equation (4.41) and (4.42) the preliminary estimation of turbine efficiency relies on loss prediction. A detailed description of loss mechanism, classification, and prediction models are presented in section 4.10.

For constant axial velocity, the blade height can be determined using mass flow rate through turbine stage:

$$\dot{m} = \rho A_x c_x \tag{4.43}$$

The annulus area A_x can be calculated as:

$$A_x = m/\rho c_x = m/\rho \emptyset U \cong 2\pi r_m b \tag{4.44}$$

Where b is the blade height, and r_m mean radius and they can be determined in terms of blade speed U and rotational speed Ω:

$$r_m = U/\Omega \tag{4.45}$$

Then,

$$b = \frac{\dot{m}\Omega}{2\pi\rho\emptyset U^2} \tag{4.46}$$

Once the blade height is determined, the blade chord length can be derived using the aspect ratio as:

$$Aspect\ Ratio = \frac{b}{C} \tag{4.47}$$

The turbine blade pitch s can be estimated using Zweifel's correlation which defines blade solidity (s/C) for minimum pressure loss.

$$Z = 2(\frac{S}{C})cos^2\beta_3(tan\beta_3 + tan\beta_4) \tag{4.48}$$

According to Mustapha et al. (Moustapha 2003) the optimum value of Zweifel's coefficient is in the range of 0.75-0.85 based on some turbine cascade experiments and due to the recent developments in turbine design optimization this value has increased to 1.0.

Then, the number of blades can be estimated using optimum space to chord ratio as:

$$N = \left[2\pi r/\left(C/\left(\frac{s}{C}\right)_{opt}\right)\right] \tag{4.49}$$

Number of blades is one of the most critical parameters due to its significant impact on flow guidance and boundary layer thickness. For the optimum flow guidance with minimum pressure loss the number of blades needs to be optimized in advanced design stages. The number of turbine stages can also be determined based on stage loading and available output work as:

$$N_{stages} \geq \frac{\dot{W}}{\dot{m}\psi U^2} \tag{4.50}$$

Equation (4.50) shows clearly that the number of stages decreases with increasing the stage loading and the blade speed. Increasing stage loading and rotational speed to decrease the number of stages is restricted by stresses on the blade, material properties, and maximum Mach number.

For effective aerodynamic design of blade aerofoil geometry, the matching between blade angles and flow angles are required. This can be achieved by calculating the required blade incidence angle. According to (Moustapha 2003), due to the turning of flow stream lines, the zero incidences cannot be achieved and there is an induced incidence angle instead. The induced incidence angle is estimated using some empirical data and there are few existing empirical correlations for incidence angle (i) calculations. One of these correlations is introduced by (Moustapha 2003) as a function of inlet flow angle (α_{in}) :

$$i = 0.175.\alpha_{in} - 5.5deg. \tag{4.51}$$

Equation (4.51) is used as starting point and the designer must consider the incidence angle variations at off design conditions. The turbine performance is also affected by flow deviation which occurs as a result of the differences between metal and flow angles at blade exit. The flow deviation leads to change in turbine torque due to change in tangential velocity. The flow

deviation occurs as a result of boundary layer and the difference in stream lines pressure on both blade surfaces.

Based on 1D mean line approach for axial turbine design, a Matlab programme was developed. In this code all design equations were employed to calculate all turbine geometric parameters and the turbine performance was predicted based on loss correlations. Figure 4.9 shows the flow chart of the computer code developed for axial turbine design.

Using this design code and in order to identify the output power and efficiency levels, the preliminary design was explored for a wide range of design parameters such as loading coefficient, flow coefficient, stage reaction, and hub/tip ratio to determine the final input parameters values for turbine sizing. In this code, the air was assumed as an ideal gas and the performance was predicted based on turbine loss models approach. The parametric study was also carried out based on thermodynamic analysis of compressed air storage system for the proposed distributed power cycle, the specification and operating conditions of small axial turbine are specified. The target output power is around $1-5\text{kW}$ with mass flow rate of 0.05-0.2 kg/s. The total inlet pressure and temperature ranges are specified as 2-5 bar and 300-350K. Using the previous specifications, the design aims to determine the rotational speed and detailed turbine geometry based on air as working fluid. Table (4.1) shows the design input parameters and the range of operating conditions which are based on low grade heat sources (Zhai, et al. 2009, Kang 2012, Tempesti, et al. 2012).

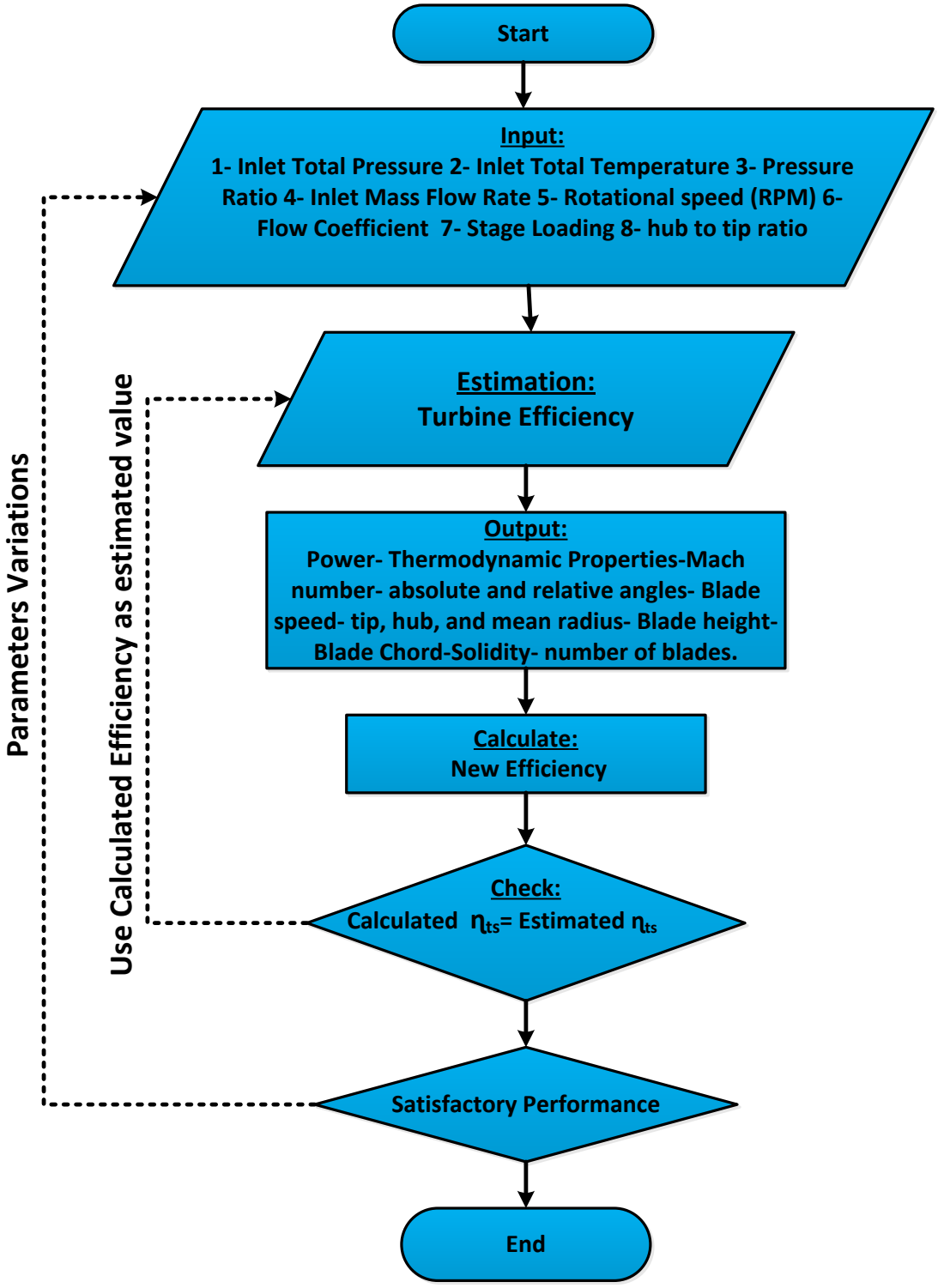

Figure 4.9 Meanline modelling code flow chart

Table 4-1 Turbine design input parameters

Parameter	Unit	Range
Total Inlet Pressure	[bar]	2-6
Total Inlet Temperature	[K]	300-360
Mass Flow Rate	[kg/s]	0.05-0.2
Flow Coefficient	-	0.1-0.8
Loading Coefficient	-	0.1-1.4
Hub –to- tip ratio	-	0.2-0.7
Reaction	-	0.3-0.8
Target Power	kW	1-5
Target Efficiency	-	0.9

4.6.2 Throughflow Design:

In Throughflow design or 2D design method, the flow analysis is performed for both axial and radial directions. In this method, the velocity triangles are constructed at hub and tip to achieve optimum blade loading distribution along blade span. Throughflow analysis is carried out to overcome the impacts of flow properties variation along blade span-wise by varying velocity triangles at mean, hub, and tip to achieve twisted blade. The twisted blade is designed in case of long blades with low hub to tip ratio (around 0.4) where the flow properties variations are significant (Yahya 2010). The twisted blade design is called vortex blading or vortex theory for changing flow angles along the blade. Figure 4.10 shows the variations in pressure and velocity through turbine annulus (Cohen, et al. 1987)

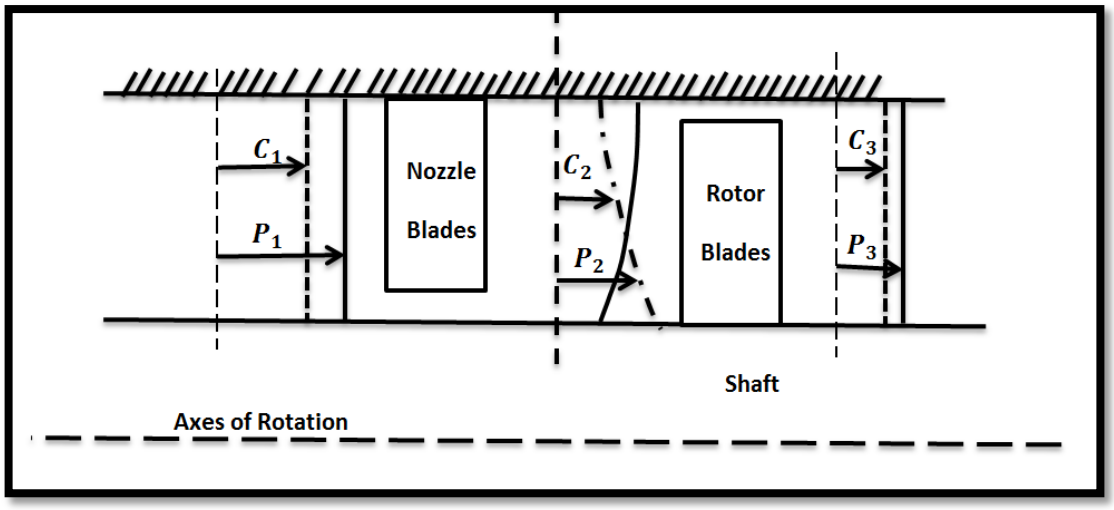

Figure 4.10 Variations in pressure and velocity through turbine stage (Cohen, et al. 1987)

For free vortex designs (zero vorticity) and by applying radial theory of fluid elements and for constant enthalpy drop and axial velocity, the flow along radial direction is governed by:

$$rC_\theta = Constat \tag{4.52}$$

By applying equation (4.54) at hub, tip, and mean for rotor inlet and exit:

$$r_h C_{\theta 2h} = r_t C_{\theta 2t} = r_m C_{\theta 2m} = C_2 \tag{4.53}$$

$$r_h C_{\theta 3h} = r_t C_{\theta 3t} = r_m C_{\theta 3m} = C_3 \tag{4.54}$$

For constant axial velocityc_x:

$$c_{xm} = c_{xh} = c_{xt} = c_x \tag{4.55}$$

Then, the absolute and relative flow angles can be calculated using velocity triangles relations as (Yahya 2010):

At blade hub:

$$tan\alpha_{2h} = \frac{C_{\theta 2h}}{c_x} = \frac{C_2}{r_h c_x} \tag{4.56}$$

$$tan\alpha_{3h} = \frac{C_{\theta 3h}}{c_x} = \frac{C_3}{r_h c_x} \tag{4.57}$$

$$tan\beta_{2h} = \frac{C_2}{r_h c_x} - \frac{U_h}{c_x} \tag{4.58}$$

$$tan\beta_{3h} = \frac{C_3}{r_h c_x} + \frac{U_h}{c_x} \tag{4.59}$$

At blade tip:

$$tan\alpha_{2t} = \frac{C_{\theta 2t}}{c_x} = \frac{C_2}{r_t c_x} \tag{4.60}$$

$$tan\alpha_{3t} = \frac{C_{\theta 3t}}{c_x} = \frac{C_3}{r_t c_x} \tag{4.61}$$

$$tan\beta_{2t} = \frac{C_2}{r_t c_x} - \frac{U_t}{c_x} \tag{4.62}$$

$$tan\beta_{3t} = \frac{C_3}{r_t c_x} + \frac{U_t}{c_x} \tag{4.63}$$

4.6.3 CFD Turbine Modelling:

Due to the internal flow complexity through axial turbine, computational fluid dynamics (CFD) modelling is performed for turbines. CFD simulation has become an effective tool for modern turbomachinery design and optimization with considerable improvements in performance levels and reduction of design time (Denton and Dawes 1998).

The CFD is defined as numerical methodology for solving flow field partial differential equations (Navier-Stokes N-S) using computer simulation based on finite difference and finite volume approaches (Hirsch 2007).

Today, with the increase of computing power, CFD plays a major role in turbine aerodynamic design with high accuracy levels. Using CFD, the turbine can be modelled with single or multi-stage for both steady and transient flow. The importance of CFD modelling is that the designer can understand the complex flow through turbine passage and the design can be improved by studying the influence of geometry variation on turbine overall performance. This section explains the theory of computational fluid dynamics (CFD) as a powerful numerical tool for turbine design.

4.6.3.1 Flow Governing Equations:

In turbine CFD modelling, the flow is described by three governing equations which are known as conservation laws of physics (Elder, et al. 2003). These equations include:

- Continuity Equation: $$\frac{\partial \rho}{\partial t} + \nabla.\left(\rho \vec{U}\right) = 0 \quad (4.64)$$
- Momentum Equation: $$\frac{\partial (\rho \vec{U})}{\partial t} + \nabla.\left(\rho \vec{U} \otimes \vec{U}\right) = -\nabla P + \nabla.\vec{\tau} + \overrightarrow{S_M} \quad (4.65)$$
- Energy Equation: $$\frac{\partial (\rho h_o)}{\partial t} - \frac{\partial P}{\partial t} + \nabla.\left(\rho \vec{U} h_o\right) = -\nabla.(\lambda \nabla T) + \nabla.\left(\overrightarrow{U}.\vec{\tau}\right) \quad (4.66)$$

Where τ is the stress tensor and S_M is the momentum source.

4.6.3.2 Turbulence Modelling:

Turbulence is the fluctuations in flow due to significant fluid inertia compared with flow viscosity. To enable considering the impact of turbulence on mean flow, an accurate turbulent model is required. The majority of turbulence models rely on eddy viscosity approach in which the turbulence solution is correlated with turbulent viscosity (Ansys 2009).

$$-\overline{\rho v_x v_y} = \mu_t \frac{\partial v_x}{\partial y} \tag{4.67}$$

Where μ_t is the turbulent viscosity which needs to be predicted.

- **K-ε Turbulence Model:**

This model is the most commonly used model for turbulent flow modelling in many CFD applications. This Model defines the turbulence viscosity in terms of turbulent kinetic energy (k) and turbulence dissipation rate (ε) as (Ansys 2009):

$$\mu_t = C_\mu \rho . \frac{k^2}{\varepsilon} \tag{4.68}$$

Where C_μ is the turbulence constant and the transport equations for k and ε are:

$$\frac{\partial(\partial k)}{\partial t} + \nabla(\rho \vec{U} k) = \nabla\left[\left(\mu + \frac{\mu_t}{\sigma_k}\right)\nabla k\right] + p_k + p_{kb} - \rho\varepsilon \tag{4.69}$$

$$\frac{\partial(\partial \varepsilon)}{\partial t} + \nabla(\rho \vec{U} \varepsilon) = \nabla\left[\left(\mu + \frac{\mu_t}{\sigma_\varepsilon}\right)\nabla \varepsilon\right] + \frac{\varepsilon}{k}[C_{\varepsilon 1}(p_k + p_{kb}) - C_{\varepsilon 2}\rho\varepsilon] \tag{4.70}$$

Where C_ε and σ are constants, p_k is the turbulence production due to viscosity and can be calculated as:

$$p_k = \mu_t \nabla \vec{U} . \left(\nabla \vec{U} + \nabla \vec{U}^T\right) - \frac{2}{3}\nabla . \vec{U}(3\mu_t \nabla . \vec{U} + \rho k) \tag{4.71}$$

And $(p_{kb}, p_{\varepsilon b})$ are factors of buoyancy force and can be estimated as (Ansys 2009):

For full buoyancy model:

$$p_k = \frac{\mu_t}{\rho \sigma_P} g . \nabla \rho \tag{4.72}$$

And for Boussinesq buoyancy:

$$p_k = \frac{\mu_t}{\rho \sigma_P} \beta . g . \nabla \rho \tag{4.73}$$

$p_{\varepsilon b}$ is expressed as a function of p_{kb} as:

$$p_{\varepsilon b} = C_3 max(0, p_{kb}) \tag{4.74}$$

Where C_3 is the dissipation coefficient.

- **K-ω Turbulence Model:**

K-ω model was developed by (Wilcox 1998) and in this model the turbulence viscosity is calculated based on kinetic energy (k) and turbulent frequency (ω) as:

$$\mu_t = \rho \frac{k}{\omega} \tag{4.75}$$

The K and ω transport equations are:

$$\frac{\partial(\partial k)}{\partial t} + \nabla(\rho \vec{U} k) = \nabla \left[\left(\mu + \frac{\mu_t}{\sigma_k} \right) \nabla k \right] + P_k + P_{kb} - \beta' \rho \omega \tag{4.76}$$

$$\frac{\partial(\partial \omega)}{\partial t} + \nabla(\rho \vec{U} \omega) = \nabla \left[\left(\mu + \frac{\mu_t}{\sigma_\omega} \right) \nabla \omega \right] + \alpha \frac{\omega}{k} P_k + P_{\omega b}) - \beta \rho k \omega] \tag{4.77}$$

In equation (4.78) $P_{\omega b}$ is determined by:

$$P_{\omega b} = \frac{\omega}{k} [(\alpha + 1) C_3 . \max(0, P_{kb}) - P_{kb}] \tag{4.78}$$

- **Shear Stress Transport (SST) Model:**

This model is developed for more accurate prediction of the flow separation due to adverse pressure gradient. This model is recommended for good near wall treatment. The SST turbulence model combines both $k - \varepsilon$ and $k - \omega$ elements with an implementation of

blending function (Fl) for transition region treatment (Ansys 2009). As a result of combining two turbulent models, SST model is considered as reliable, accurate, and stable turbulence model and as a result this model was used in turbine CFD modelling. A new dissipation term is generated from the combination of $k-\varepsilon$ and $k-\omega$ as:

$$2(1-Fl)\sigma_{\omega 2}\frac{1}{\omega}\frac{\partial k}{\partial x_j}\frac{\partial \omega}{\partial x_j} \tag{4.79}$$

4.7 CFD Axial Turbine Modelling Using ANSYS CFX16.2:

The main goal of turbine CFD modelling is to improve 1D mean line design output through simulating different turbine designs. Turbine performance map can be generated to predict the efficiency and output power for different operating conditions. In this research 3D CFD simulation of axial turbine was conducted using ANSYS CFX 16.2 and Figure 4.11 describes the general procedure used for axial turbine CFD modelling using.

Using ANSYS both aerodynamic and structural analysis were performed. The detailed geometry of turbine blade is defined through CFX-BladeGen for both stator and rotor. Once the turbine blade geometry is defined, the fluid domain is discretised using CFX TurboGrid into cells. The flow is solved as 3D steady, compressible, and adiabatic using CFX solver. This section explains the methodology of axial turbine CFD modelling using ANSYS CFX 16.

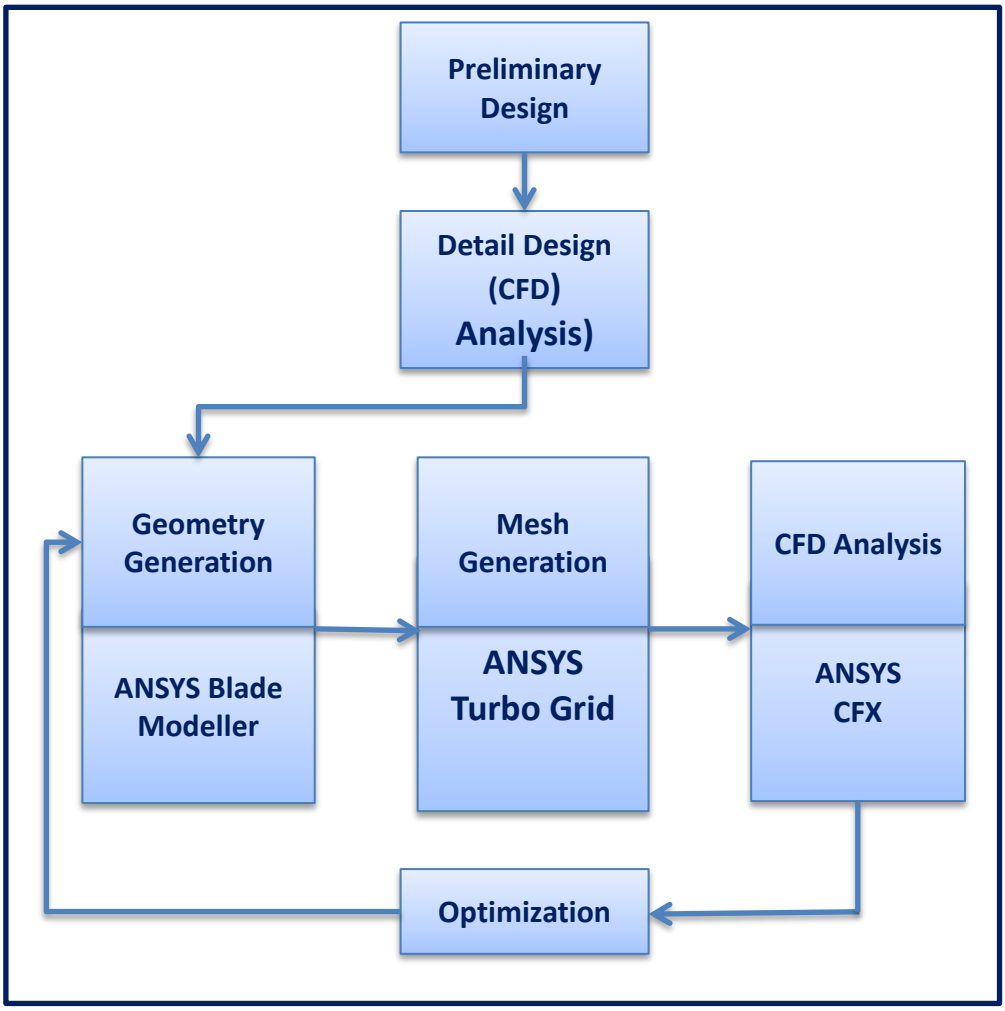

Figure 4.11 Procedures of axial Turbine CFD modelling using ANSYS CFX 16

4.7.1 CFX BladeGen:

Based on 1D mean line modelling, the initial geometry parameters are defined. These parameters include blade metal angles, stagger angle, chord, tip radius, hub radius, and leading and trailing edge radii. Using these parameters, the blade geometry can be generated in CFX- BladeGen model. Figure 4.12 shows the turbine stage generated using CFX-BladeGen.

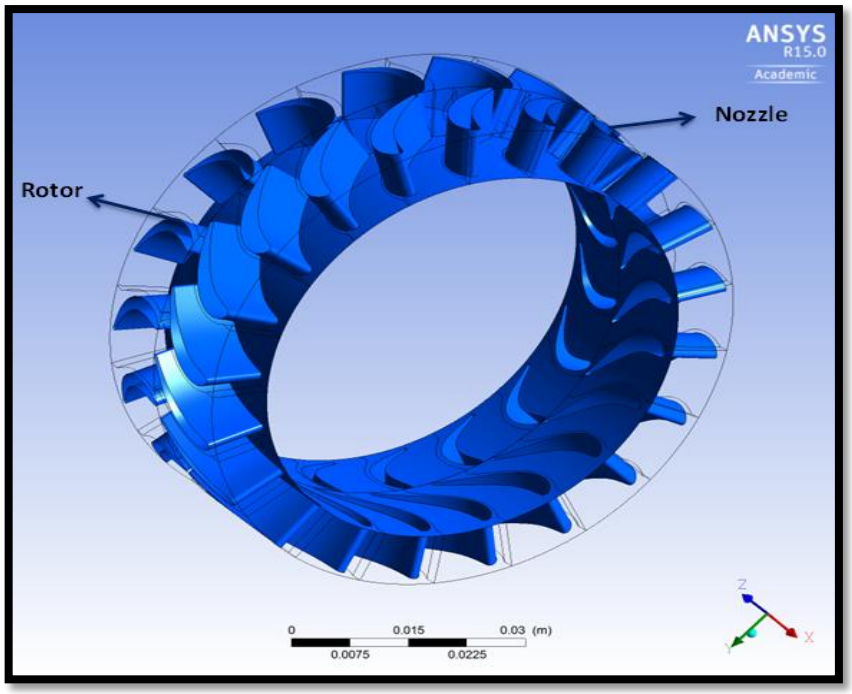

Figure 4.12 Axial turbine stage generated using BladeGen.

4.7.2 CFX-TurboGrid:

Once the blade profile is generated using BladeGen, the blade was exported to CFX-TurboGrid for domain meshing. In TurboGrid the Optimized Automatic Topology was selected and structured hexahedral cell mesh was generated. The blade Reynolds number was calculated at design point in order to check the y^+ values (y^+ =1) to ensure the proper size of the mesh near walls (Ansys 2009). Figure 4.13 shows the generated mesh for both stator and rotor. Also the mesh sensitivity analysis was conducted to check mesh independency of flow solution as shown in Figure 4.14. As can be seen the mesh sensitivity analysis shows the turbine total efficiency remains constant when the number of grid cells exceeds 650000 indicating that the solution is not affected by the number of mesh cells.

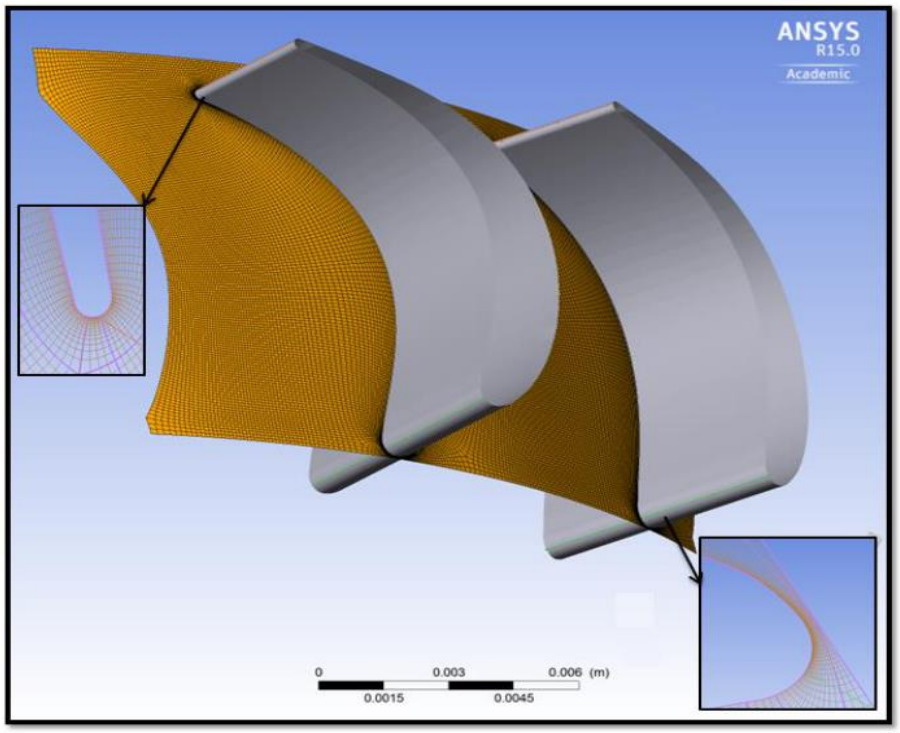

Figure 4.13 Mesh generation (Fine 650,000 cells)

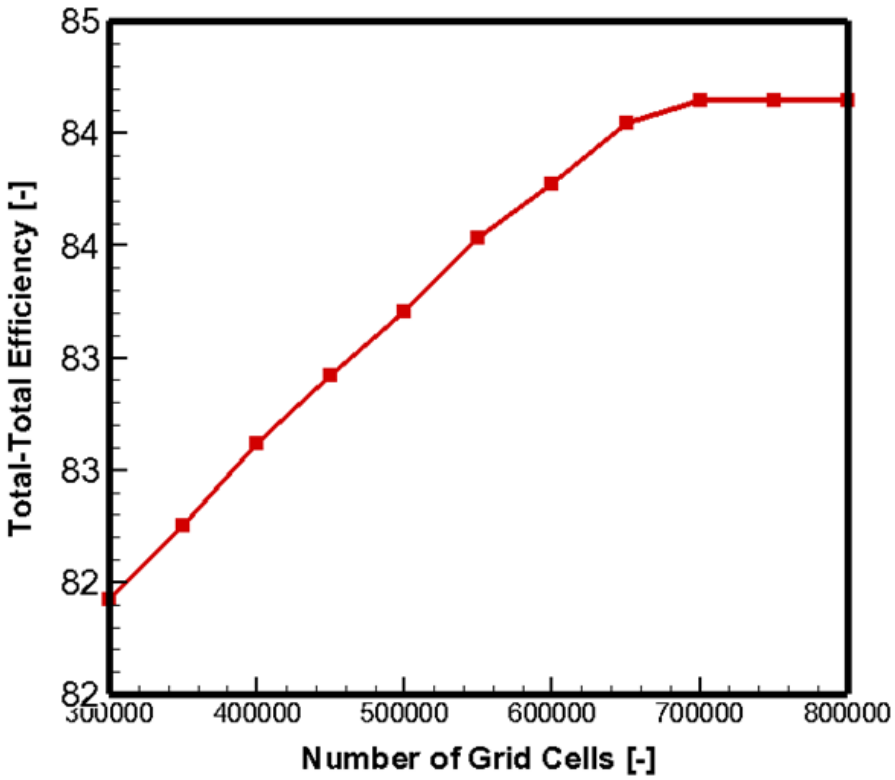

Figure 4.14 Grid sensitivity analysis based on total-total efficiency

4.7.3 CFX-Pre:

CFX-Pre is the tool for simulation setup where turbine boundary conditions for inlet and outlet, working fluid properties and turbulence model are defined. Once the boundary conditions are setup, the different interferences and periodic boundaries are defined using Turbo-Mode tool. The boundary conditions of axial turbine stage are shown in Figure 4.15. The boundary conditions are set as total pressure at inlet and static pressure at turbine outlet. The blade surfaces of both stator and rotor are set as no wall slip condition and the rotor blade wall is treated as rotating wall. The interactions between stationary domain and rotating domain are modelled using stage interference. Shear Stress Transport (SST) turbulent model was chosen for the simulation due to its capability of near-wall treatment and it is recommended for turbomachinery modelling (Rhie and Chow 1983, ANSYS 2014, Rahbar, Mahmoud et al. 2014). The inlet and outlet computational domains were reduced from -35 mm to -20 mm for the inlet and from 45 mm to 30 mm for the outlet to save the computational time with a reduction in total to static efficiency by only 0.12% and for more precise results longer domains are recommended.

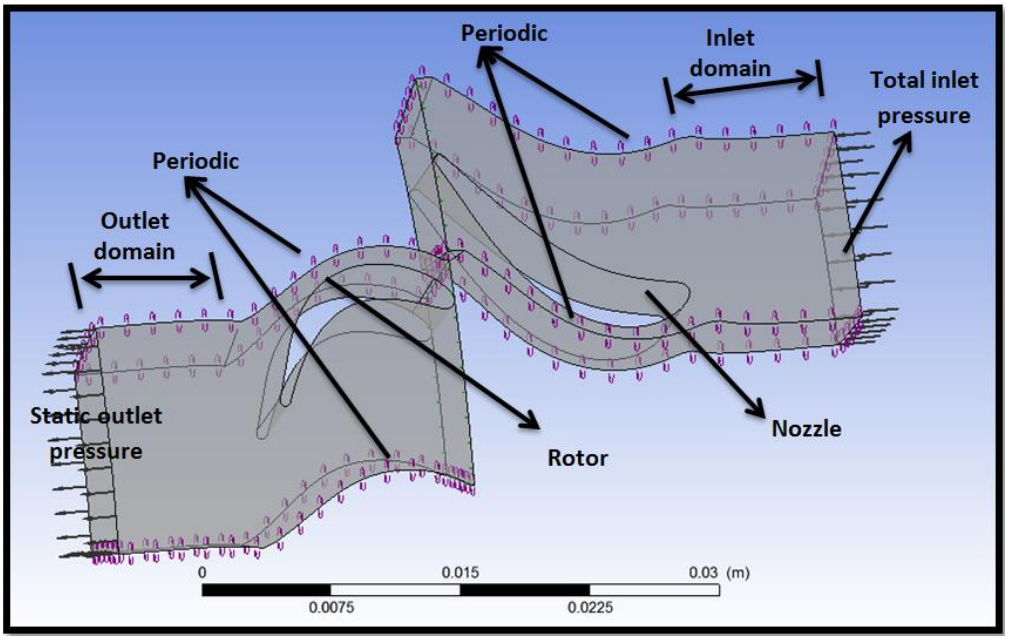

Figure 4.15 CFD axial turbine stage boundary conditions

4.7.4 CFX-Solver:

Once all solver parameters are specified in CFX-Pre, a detailed definition file was created and this file contains all the information required for starting the solution. Using CFX-Solver, the user can start/stop the solution, performing parallel calculation, and monitoring solution progress. CFX-Solver allows the designer to initialize the solution and start solving flow governing equations. For solution convergence, CFX-Solver plots the residuals in solver window and the solution finishes when the residuals are converged to target convergence limit. For all solutions in this thesis the convergence residual value was 10^{-5}.

4.4.5 CFX-Post:

This module is a graphical tool for presenting the simulation results. In CFX-Solver all simulation results are written in a special file and this file is used by CFX-Post to present the simulation results. Using the Turbo-Mode in CFX-Post, the axial turbine simulation results can be generated in a variety of charts, graphs, and contours like blade loading, Mach number distribution, velocity vectors, pressure contours, and blade to blade plot. Furthermore, the detailed axial turbine performance report can be generated using Turbo- Mode templates.

4.8 Turbine Mechanical Design:

The design aspects of turbine blade include two phases: Blade aerodynamic design and blade structural design. The structural analysis aims to ensure that the aerodynamic design can withstand the different loads generated during turbine operation. These loads include centrifugal loads and gas bending loads which cause stresses acting on turbine rotor (Gorla and Khan 2003). There are also stresses due to rotor vibration which are responsible for failures in some cases. These stresses are considered as limiting factors for turbine aerodynamic design where the centrifugal stresses are correlated to the rotational speed and

annulus area whereas the gas bending stresses are connected to number of blades, blade height, and specific work (Cohen, et al. 1987).

4.8.1 Turbine Blade Stress:

The axial turbine rotor experiences three main stresses which include:

- **Centrifugal Tensile Stress:** this stress arises due to rotational speed and it is considered as the largest.
- **Gas Bending Stress:** this type of stress arises as a result of change in gas angular momentum which causes bending moment around axial axis (Cohen, Rogers et al. 1987).

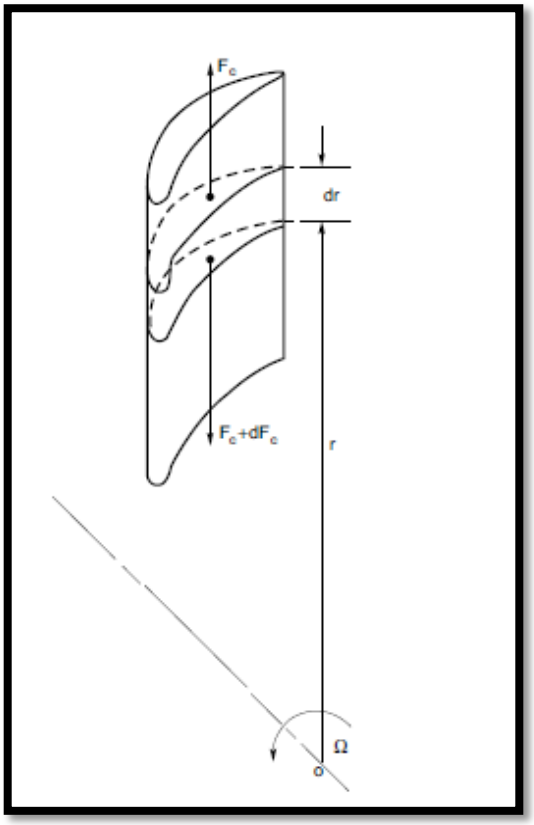

Figure 4.16 turbine rotor blade element

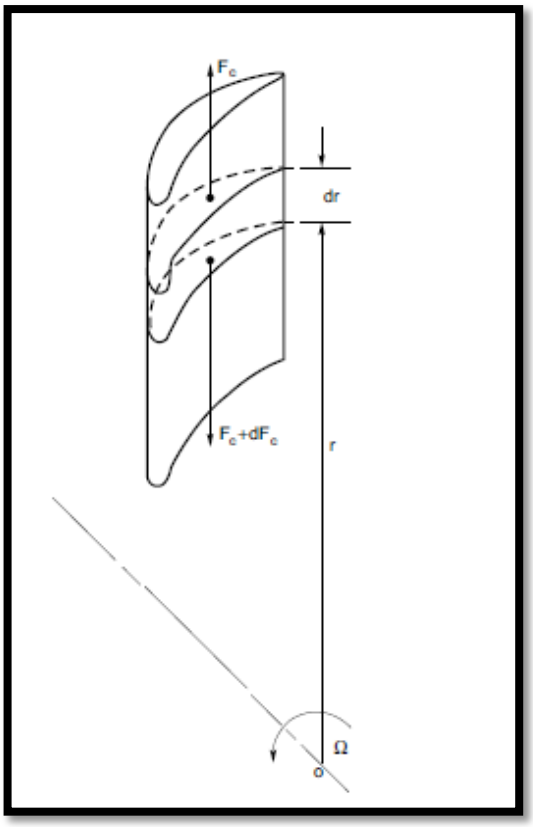

For the blade element shown in Figure **4.16**, the change in centrifugal force is given by (Cohen, Rogers et al. 1987):

$$\mathrm{dF_c} = -\Omega^2 \mathrm{rdm} \tag{4.80}$$

$$dm = \rho_m A dr \tag{4.81}$$

$$\frac{d\sigma_c}{\rho_m} = \frac{dF_c}{\rho_m A} = \frac{-\Omega^2 r dm}{\rho_m A} = -\Omega^2 r dr \tag{4.82}$$

Then,

$$\frac{d\sigma_c}{\rho_m} = \Omega^2 \int_{r_h}^{r_t} r dr = \frac{U_t^2}{2}\left[1 - \left(\frac{r_h}{r_t}\right)^2\right] \tag{4.83}$$

For tapered blades:

$$\frac{d\sigma_c}{\rho_m} = \frac{kU_t^2}{2}\left[1 - \left(\frac{r_h}{r_t}\right)^2\right] \tag{4.84}$$

Where k is the blade taper ratio and it is a ratio between the stress of tapered blade at root to the stress of un-tapered blade at root.

The gas bending stress is calculated as a function of axial pressure force which causes bending moment in axial direction.

$$F_x = \frac{(P_2 - P_3).2\pi.h}{N} \tag{4.85}$$

According to (Cohen, Rogers et al. 1987) the maximum approximation value of gas bending stress is:

$$(\sigma_{gb})_{max} = \frac{m(C_{w2m} + C_{w3m})}{N} \times \frac{b}{2} \times \frac{1}{zc^3} \tag{4.86}$$

Where N is the number of blades, z is blade section modulus and b blade height.

For blade section modulus z calculation, there is a general approximation rule developed by Ainely and published by (Cohen, Rogers et al. 1987) for zero incidence as shown in Figure 4.17.

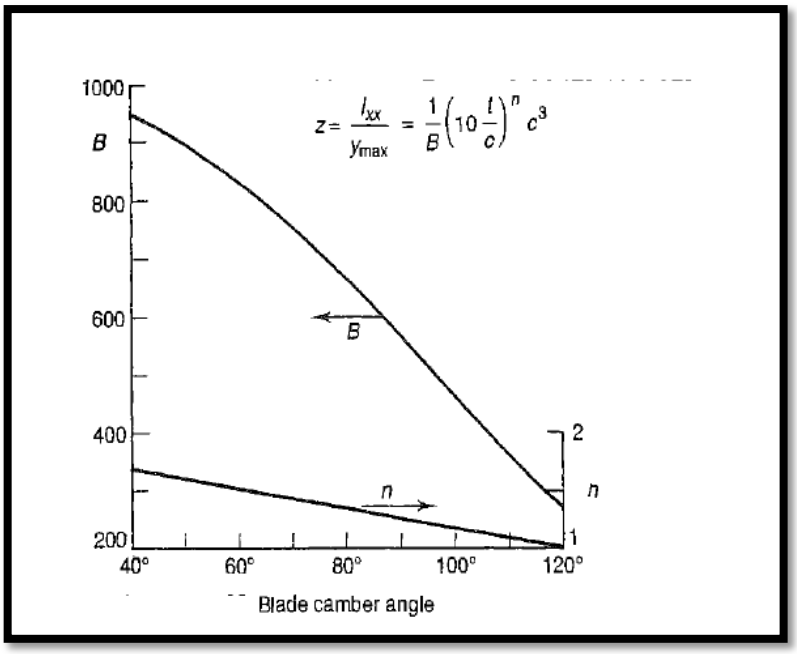

Figure 4.17 Approximation rule for section modulus (Cohen, et al. 1987)

4.8.2 Rotor Disk Stresses:

The stresses on rotor disk are estimated based on the stresses generated by rotor blades. The total forces which are created by rotor blades can be calculated using estimated stress by (Cohen, et al. 1987):

$$F_{blades} = N\ \sigma_c\ [c_h . t_{max}] \tag{4.87}$$

$$\sigma_{disk} = \frac{F_{blades}}{2\pi\ r_h c_h} \tag{4.88}$$

Where N is the number of blades, c_h is the blade chord at hup, and t_{max} is the blade maximum thickness.

4.8.3 Shaft Design:

The shaft is a round bar which carries the rotating turbine blades. It is supported by rolling bearings to carry the loads at the desired shaft speed. The shaft end is connected with flanges for torque transmission by coupling. The initial shaft diameter is estimated based on transmitted torque and material strength of the shaft as described by (Klebanov, et al. 2007):

$$d \cong (5\ to\ 6)\sqrt[3]{\frac{T}{S_u}} \tag{4.89}$$

Where T is the transmitted torque and S_u is the tensile strength of shaft material.

Then the bending vibration of the shaft can be estimated as:

$$f_n = \frac{\pi n^2}{2L^2}\sqrt{\frac{EIg}{A\gamma}} \tag{4.90}$$

Where n is the number of mode shapes, L is the distance between bearings, A is the shaft cross section area, γ is material specific weight, and I is shaft moment of inertia.

4.9 FEA Modelling Using ANSYS 16.2:

In axial turbines, the rotor experiences mechanical and aerodynamic loads. Rotor structural analysis is required to ensure that the rotor can withstand these loads during turbine operation. The static structure analysis of the turbine rotor was conducted using finite element method (FEM) in ANSYS16.2. This analysis aims to identify the limits of blade tip deformation and total Von-Mises stresses at blade root to ensure that these values are within materials yields limits.

4.9.1 Structural Model Geometry:

In the structural model, the blade geometry is generated in BladeGen and then the geometry is transferred to ANSYS mechanical model to define material properties and to mesh turbine domain as shown in Figure 4.18.

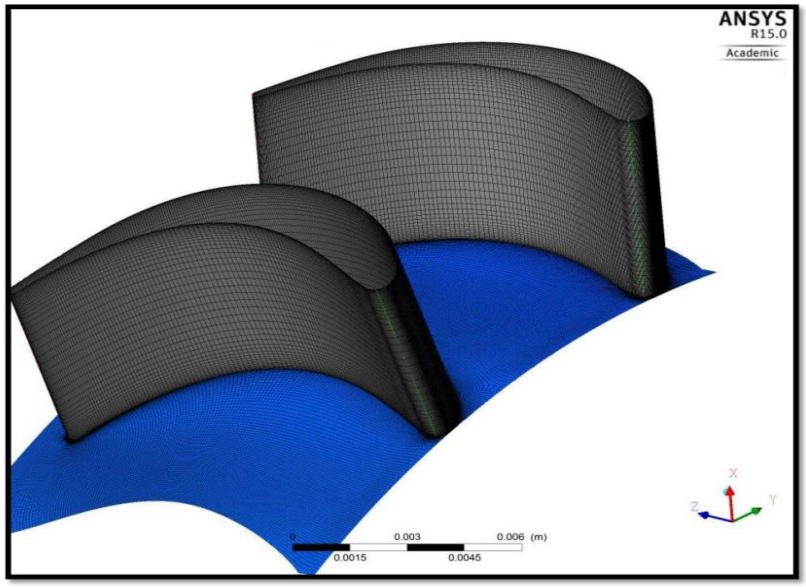

Figure 4.18 Blade mesh for FEA

4.9.2 Properties of Turbine Materials:

In ANSYS mechanical model, Engineering Data cell is used to define the material properties. The main properties required for structural analysis include material density, coefficient of thermal expansion, modulus of elasticity, Poisson's ratio, yield strength, and tensile ultimate strength.

4.9.3 Rotor Turbine Loads:

Axial Turbine rotor is subjected to many loads during turbine operation mode. These loads are caused by temperature, pressure, and rotational speed. In static structure, these loads are modelled based on CFX simulation results where the aerodynamic pressure force on blade and thermal loads due to increase in temperature are transferred to static structural model and solved for equivalent Von-Mises stress and total deformation. Next the effects of rotational speed on turbine rotor blades are simulated by duplicating static structural model and specifying the magnitude and direction of rotational speed then the total deformation and stresses are determined.

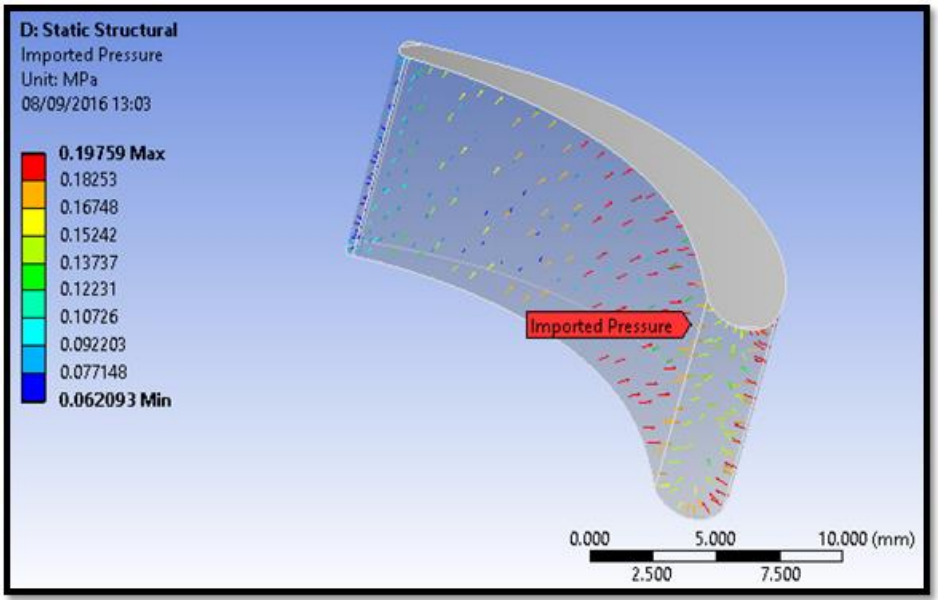

Figure 4.19 Loads on turbine Blade

4.10 Fullcure 720 Experimental Testing:

The 3D printing material Fullcure 720 (multipurpose Polymer) is selected as cost effective, fast, and efficient way for turbine manufacturing. Table 4-2 provides the properties of Fullcure720 materials.

Table 4-2 Fullcure 720 material properties

Properties	Unit	Value
Tensile Strength	MPa	60.3
Elongation at break	%	15-25
Modulus of Elasticity	MPa	2,870
Flexural Strength	MPa	75.8
Flexural Modulus	MPa	1,718
Compression Strength	MPa	84.3
T	°C	48.7

In order to ensure the material can be used for functional applications, tensile testing was carried out using Instron machine for the Fullcure 720 specimen as shown in Figure 4.20. The Fullcure720 specimen was pulled in the tensile machine with displacement rate of 1mm/min and load of 1kN at ambient temperature. The specimen dimensions are specified based on D638-03 Standard Test Method with dog-bone shape as shown in Figure 4.21. Based on tensile test results, the stress-strain curve of Fullcure 720 was obtained as shown in Figure 4.22 and the maximum tensile strength was 55.47 MPa.

Figure 4.20 Fullcure720 tensile testing

Figure 4.21 Photograph of tensile testing specimen

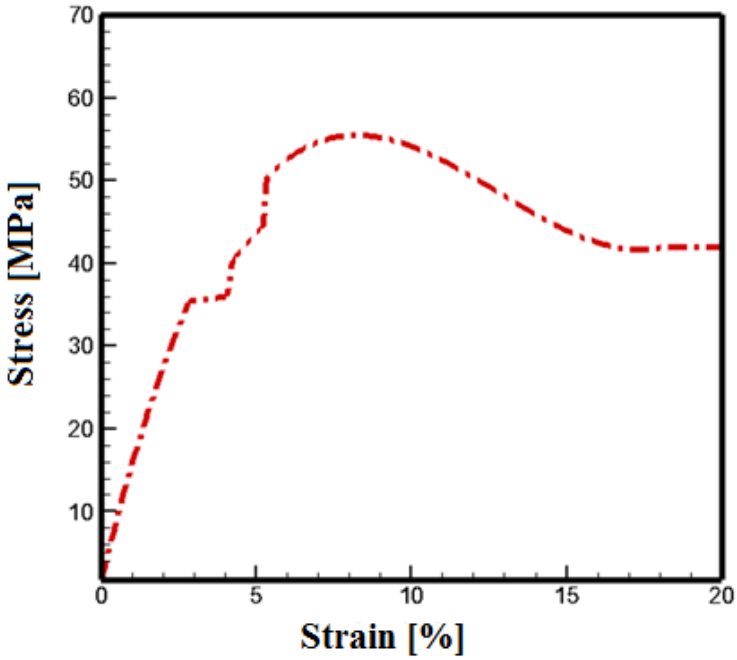

Figure 4.22 Stress-strain curve for Fullcure720 material

4.11 Axial Turbine Performance Estimation using Loss Models:

There are numerous preliminary approaches for axial turbine performance estimation. The well-known method for axial turbine performance estimation was introduced by Ainely and Mathieson (Ainley and Mathieson 1951). This method relies on loss prediction for the determination of axial turbine efficiency. Ainely and Mathieson method for efficiency prediction was improved by many researchers through considering the impacts of some parameters which were not included in this method like Mach number, Reynolds number, and blade aspect ratio (Dunham and Came 1970).

Smith (1965) and Balje et al. (1968) developed different methods which can be used in early design stage for axial turbine performance prediction. These methods were based on overall design parameters like stage loading and flow coefficient.

According to (Craig and Cox 1970) and (Dunham and Came 1970), the use of traditional performance estimation methods in steam turbine design leads to unsuccessful results and improvements for loss predictions is required. These methods have been developed for large scale turbines, but as turbine sizes become smaller the effect of aerodynamic losses becomes more significant, therefore, the development of more accurate loss prediction models is required for small scale turbines (Bullock 1964, Benner, et al. 1997). Furthermore, small scale turbines are working with small amount of mass flow rate which leads to small blade height leading to higher rotational speed and aerodynamic losses (Klonowicz, et al. 2014).

In this study the losses were predicted using conventional approach in early design stage then CFD axial turbine modelling was used to predict the losses through turbine stage. The CFD predicted losses were compared to the results of conventional prediction methods in order to decide which loss model is applicable for small scale axial turbines.

4.11.1 Axial Turbine Losses:

Axial turbine designer needs to understand the mechanism of losses, and loss prediction models in order to refine turbine design using CFD modelling and optimization tools. This section explains in detail the loss developments in axial turbines. Efficient axial turbine design requires understanding of the aerodynamic losses generated due to the complex 3-D viscous flow through the turbine. These losses are illustrated in Figure 4.23 and their breakdown is shown in Figure 4.24. The various losses are described in the following sections.

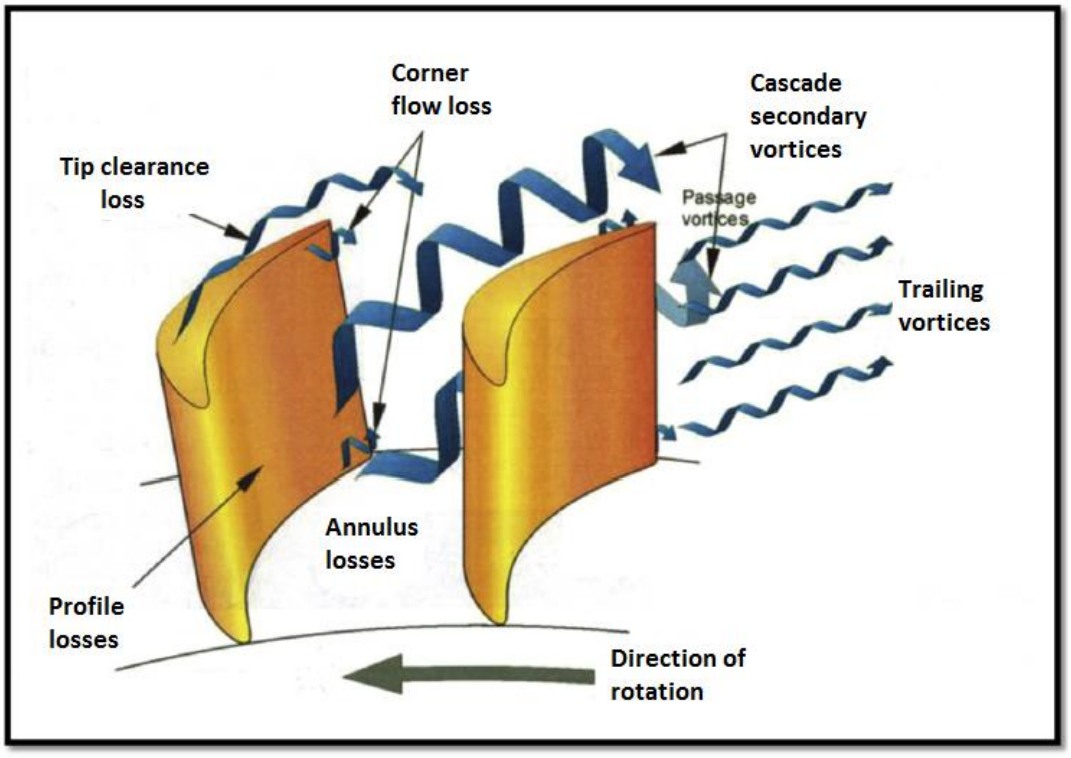

Figure 4.23 Loss sources in axial turbine (Moustapha 2003)

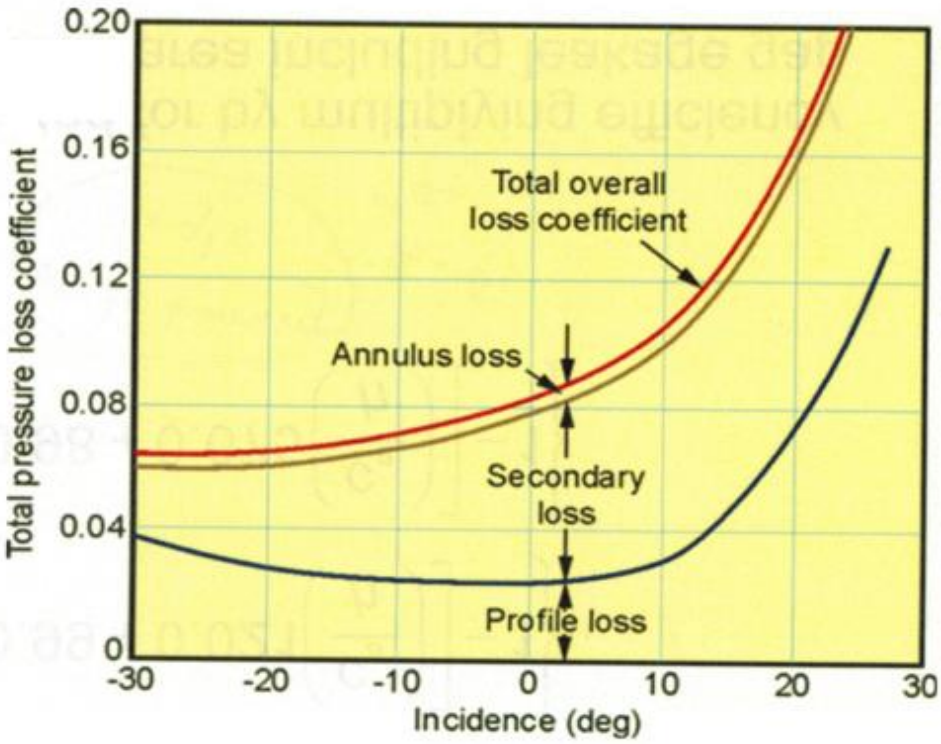

Figure 4.24 Axial turbine loss breakdown (Horlock 1966)

4.11.1.1 Profile Loss:

This loss is generated due to skin friction of the viscos flow along turbine passage and depends on flow velocity, contact surface area, surface roughness, Reynolds and Mach numbers. Profile losses are usually referred to entropy generation inside inner part of boundary layer which depends on the geometry of turbine blade itself (Hummel, et al. 2005).

4.11.1.2 Secondary Loss:

This type of loss occurs near the end walls boundary layer where the flow is turned due to pressure gradient and flow vortices are generated as a result of mixing secondary flow and main flow. These vortices are located in a region lower than main flow and lead to boundary layer rolling up as shown in Figure 4.25. The secondary flow also affects the flow on blade suction side where the vortices are generated at leading edge and developed along blade span. A detailed description of secondary flow and boundary layer rolling up was provided by (Klein 1966).

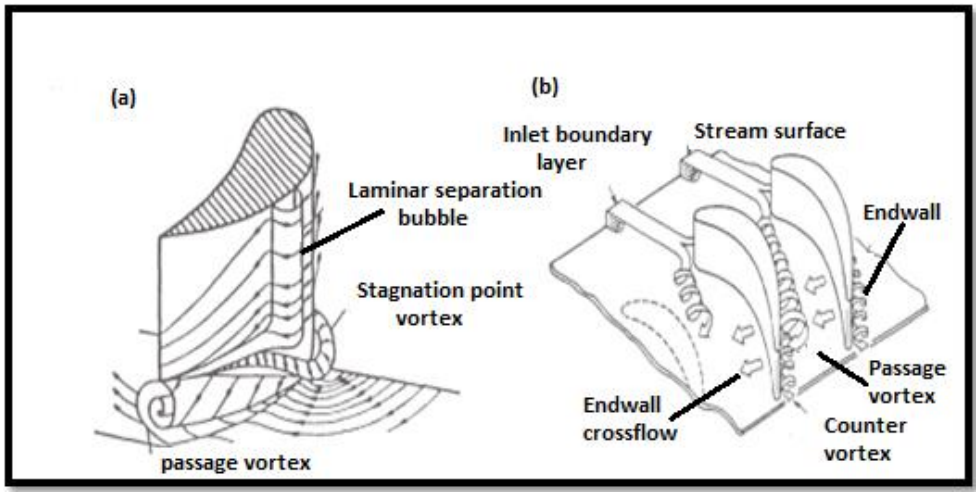

Figure 4.25 (a) Klein end wall flow model (Langston, et al. 1977) (b) Langston flow model (Klein 1966).

4.11.1.3 Tip Clearance Loss:

This loss occurs due to the gap between turbine casing and moving blade and as a result of pressure difference the fluid leaks from the pressure side to the suction side. In tip clearance regions, the leakage flow mixes with secondary flow generating vortices at blade tip. In the case of shrouded blades, there is no flow path between pressure and suction sides of the blade but the flow leaks from leading edge to trailing edge. Figure 4.26 shows a comparison between shrouded and unshrouded blades. This typical comparison shows that in shrouded turbines an increase of 1% of clearance-span ratio leads to a reduction in efficiency by 2% but in the case of shrouded blades the reduction in turbine efficiency is 1%. However, the shroud increases the blade weight and stresses. As a result, shrouds are not applicable in small scale turbines (Moustapha 2003).

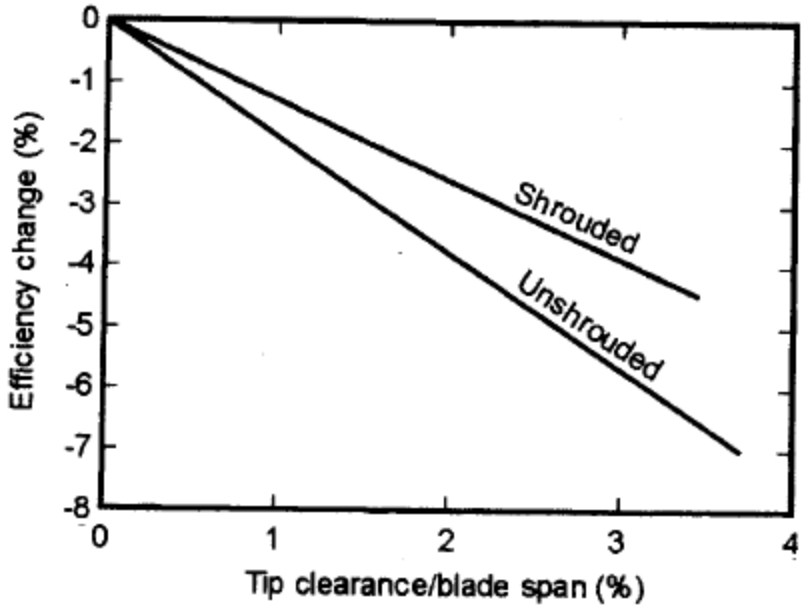

Figure 4.26 Efficiency variations with tip clearance (Moustapha 2003).

4.11.2 Axial Turbine Loss Coefficients:

In order to assess the losses occurring during expansion through the turbine (Figure 4.27), there are loss coefficients which are related to the reduction in flow enthalpy compared with isentropic enthalpy (Wei 2000). These loss coefficients include pressure, energy, and entropy and are described in the following subsections.

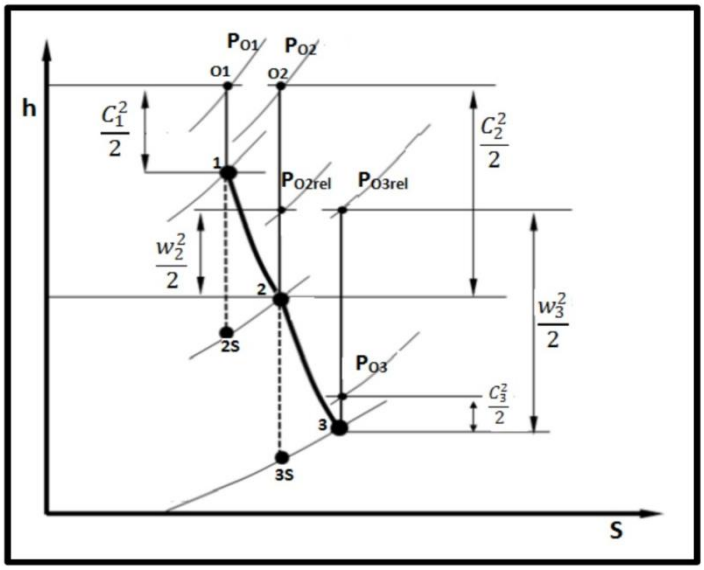

Figure 4.27 Enthalpy-entropy diagram for turbine expansion process

4.11.2.1 Pressure Loss Coefficient:

This loss coefficient is used to estimate the losses using stagnation pressure through turbine passage. It is the most common loss coefficient due to the fact that pressure loss can be calculated directly from the data obtained from cascade test using the following relations (Wei 2000):

For stator: $$Y_{Stator} = \frac{(P_{o1} - P_{o2})}{(P_{o2} - P_2)} \quad (4.91)$$

For rotor: $$Y_{Rotor} = \frac{(P_{o2\,rel} - P_{o3\,rel})}{(P_{o1\,rel} - P_3)} \quad (4.92)$$

4.11.2.2 Energy Loss Coefficient:

Based on 1st law of thermodynamics this coefficient defines the amount of energy that does not contribute to the generated work. This loss coefficient is another method for defining turbine efficiency.

For stator: $$Y_{Stator} = \frac{h_2 - h_{2S}}{h_{o1} - h_2} \quad (4.93)$$

For rotor: $$Y_{Rotor} = \frac{h_3 - h_{3S}}{h_{o2,rel} - h_3} \quad (4.94)$$

Using Enthalpy- entropy diagram shown in Figure 4.27:

$$h_{o1} - h_2 = h_2 + \frac{1}{2}C_2^2 - h_2 = \frac{1}{2}C_2^2 \quad (4.95)$$

$$h_{o2rel} - h_3 = h_3 + \frac{1}{2}w_3^2 - h_3 = \frac{1}{2}w_2^2 \quad (4.96)$$

Using equations (4.95) and (4.96), Y_{Stator} and Y_{Rotor} can be expressed as:

$$Y_{Stator} = \frac{(h_2 - h_{2S})}{\frac{1}{2}C_{2s}^2} \quad (4.97)$$

$$Y_{Rotor} = \frac{(h_3 - h_{3S})}{\frac{1}{2}W_{3s}^2} \tag{4.98}$$

4.11.2.3 Entropy Loss Coefficient:

This coefficient is another method for defining isentropic efficiency and it is expressed in terms of entropy change instead of enthalpy change based on second law of thermodynamics.

$$Y_{Stator} = \frac{(S_2 - S_1).T_3}{\frac{1}{2}C_2^2} \tag{4.99}$$

$$Y_{Rotor} = \frac{(S_3 - S_2).T_3}{\frac{1}{2}W_3^2} \tag{4.100}$$

According to (Denton 1993) the energy and pressure losses are satisfactory in the case of cascade tests, but in rotating blades the pressure and enthalpy vary along blade span and as a result the entropy generation is the effective approach for loss measurement.

The total loss coefficient (Y_{total}) can be converted into kinetic energy loss as (Moustapha, et al. 1990):

$$\boldsymbol{Y_{total}} = \frac{\left[\mathbf{1} - \frac{\gamma-1}{2}M^2(\frac{1}{\emptyset^2} - \mathbf{1})\right]^{-(\frac{\gamma}{\gamma-1})} - \mathbf{1}}{\mathbf{1} - (\mathbf{1} + \frac{\gamma-1}{2}M^2)^{-(\frac{\gamma}{\gamma-1})}} \tag{4.101}$$

Also, the total loss can be expressed in terms of blade aerodynamic characteristics as following (Fielding 2000):

$$Y_{total} = \frac{C_D.\left(\frac{C}{S}\right).Cos^2(\alpha_2)}{Cos^3(\alpha_m)} \tag{4.102}$$

$$C_L = \frac{L}{\frac{1}{2}\rho V_\infty^2 C} \tag{4.103}$$

$$C_D = \frac{D}{\frac{1}{2}\rho V_\infty^2 C} \tag{4.104}$$

4.11.3 Existing Loss Prediction Correlations:

Due to the importance of turbine efficiency, there are significant efforts carried out to improve turbine efficiency. The efficiency improvements are related to the developments in numerical and experimental techniques for turbine design and testing. Axial turbine efficiency is affected by losses generation due to 3D complicated flow through the turbine passage, tip leakage, boundary layer, and secondary flow.

The estimation of turbine efficiency is correlated with the losses prediction models. There are several losses prediction correlations which are developed based on cascade tests of conventional turbines (Denton 1993). These empirical correlations for losses prediction can be used in 1D mean line modelling to optimize the design by varying the turbine's geometric parameters. For further minimization of turbine losses 3D CFD simulation with design optimization can be effective for efficient turbine design. The common loss prediction methods in axial turbine are described in the following subsections.

4.11.3.1 Soderberg Model:

Soderberg (1949) developed a correlation for quick losses prediction in early design stage for total profile and secondary losses. The profile losses were given as a function of blade deflection and secondary losses were given as a function of blade aspect ratio. The total loss coefficients of the turbine stage are expressed as:

For nozzle: $$Y_{Stator} = \left(\frac{10^5}{Re}\right)^{1/4}\left[(1+\zeta^*)\left(0.993+0.075\frac{l}{H}\right)-1\right] \quad (4.105)$$

For rotor: $$Y_{Rotor} = \left(\frac{10^5}{Re}\right)^{1/4}\left[(1+\zeta^*)\left(0.975+0.075\frac{l}{H}\right)-1\right] \quad (4.106)$$

Where ζ^* is the nominal loss factor given as function of blade deflection (ε):

$$\zeta^* = 0.04 + 0.06\left(\frac{\varepsilon}{100}\right)^2 \quad (4.107)$$

The tip leakage loss is not considered in this Soderberg's correlation and as a result this approach was criticized by many turbine researchers (Wei 2000).

4.11.3.2 Ainely& Mathieson Model:

This model was developed by (Ainley and Mathieson 1951) and it is considered as the most common approach for loss prediction in axial turbines. This method was based on simplified assumptions and tests of typical gas turbine blades developed in the 50's with large cross sections (Sieverding 1985). For simplicity, this method neglected the impacts of Mach number and flow outlet angles on turbine performance. The total losses are equal to the sum of profile, secondary, and tip clearance losses as:

$$Y_{total} = (Y_P + Y_S + Y_{Tl})\chi_{Te} \quad (4.108)$$

Where χ_{Te} is the trailing edge correction factor and can be estimated using charts which is provided by Ainely and Mathieson (Ainley and Mathieson 1951).

The profile losses Y_P can be calculated using an empirical correlation which is based on charts provided by Ainely and Mathieson for different pitch to chord ratios. The profile losses at zero incidence angles can be calculated as:

$$Y_{P(i=0)} = \left\{ Y_{P(\alpha'_{in}=0)} + \left(\frac{\alpha'_{in}}{\alpha_{out}}\right)^2 \left[Y_{P(\alpha'_{in}=\alpha_{out})} - Y_{P(\alpha'_{in}=0)} \right] \right\} \left(\frac{t_{max}/l}{0.2} \right)^{\frac{\alpha'_{in}}{\alpha_{out}}} \quad (4.109)$$

Where $Y_{P(i=0)}$ represents the profile losses at zero incidence (design point) and final total profile losses can be calculated as:

$$Y_P = X_i * Y_{P(i=0)} \quad (4.110)$$

Where X_i is incidence correction factor and it can be estimated using charts provided by Ainely and Mathieson (Ainley and Mathieson 1951).

For secondary losses (Y_S) estimation, Ainley and Mathieson (1951) developed a correlation which expresses the secondary losses as a function of blade turning as:

$$Y_s = \lambda \left(\frac{C_L}{t/l} \right)^2 \left(\frac{cos^2 \alpha_{out}}{cos^3 \alpha_m} \right) \quad (4.111)$$

λ in this equation is a parameter which measures the flow acceleration through turbine blades and can be estimated using charts. C_L is the lift coefficient and according to (Xiao, et al. 2001) it can be calculated by:

$$C_L = 2\frac{t}{l}(tan\alpha_{in} - tan\alpha_{out})cos\alpha_m \quad (4.112)$$

The α_m is the flow mean angle and can be calculated as:

$$\alpha_m = \tan^{-1}[(tan\alpha_{in} + tan\alpha_{out})] \quad (4.113)$$

The tip leakage losses Y_{Tl} can be estimated using the following correlation (Ainley and Mathieson 1951):

$$Y_{Tl} = 4B\frac{\tau}{h}\,[tan\alpha_{in} - tan\alpha_{out}]^2\left[\frac{cos^2\alpha_{out}}{cos\alpha_m}\right] \quad (4.114)$$

Where τ represents the clearance gap, h is the annulus height, and B is a constant equals to 0.25 for shrouded blades and 0.5 for unshrouded blades.

4.11.3.3 Dunham & Came Model:

The Ainely & Mathieson approach was refined by (Dunham and Came 1970) by considering the influence of Reynolds number on turbine losses generation. This model was developed based on a comparison between new test data for 25 turbines against Ainely and Mathieson method. This comparison showed that the results of Ainely and Mathieson model were acceptable for large scale turbines and unsuccessful in the case of smaller turbines (Wei 2000). Dunham and Came (1970) defined the total losses as:

$$Y_{total} = \left((Y_P + Y_S)\left(\frac{Re}{2\times 10^5}\right)^{-0.2} + Y_{Tl}\right)\chi_{Te} \quad (4.115)$$

The profile loss (Y_P) was improved in this approach by considering the Mach number impact as:

$$Y_P = [1 + 60(M_{out} - 1)^2]\chi_i Y_{P(i=0)} \quad (4.116)$$

The secondary losses estimation was also modified for better aspect ratio consideration into:

$$Y_s = 0.0334(\frac{l}{H})[4(tan\alpha_{in} - tan\alpha_{out})^2]\left(\frac{cos^2\alpha_{out}}{cos\alpha_m}\right)\left(\frac{cos\alpha_{out}}{cos\alpha'_{in}}\right) \quad (4.117)$$

In this method, the tip leakage losses was expressed as power function instead of the Ainely & Mathieson linear function as:

$$Y_{Tl} = B\frac{l}{h}\left(\frac{\tau}{l}\right)^{0.78} 4(tan\alpha_{in} - tan\alpha_{out})^2\left(\frac{cos^2\alpha_{out}}{cos\alpha_m}\right) \quad (4.118)$$

Using this correlation the constant B equals 0.47 for unshrouded blade and 0.37 for shrouded blade.

4.11.3.4 Kacker & Okapuu Model:

In this model the Ainely and Mathieson losses model was updated by (Kacker and Okapuu 1982) by considering the influence of compressibility and shock. Furthermore, the trailing edge effect was developed as a separate loss component in their total loss model as:

$$Y_{total} = \chi_{Re}Y_P + Y_s + Y_{TI} + Y_{Te} \quad (4.119)$$

χ_{Re} is a correction factor and can be calculated using the following equation:

$$\chi_{Re} = \begin{cases} \left(\frac{R_e}{2\times10^5}\right)^{-0.4} & R_e \le 2\times10^5 \\ 1.0 & 2\times10^5 > R_e < 10^6 \\ \left(\frac{R_e}{10^6}\right)^{-0.2} & R_e > 10^6 \end{cases} \quad (4.120)$$

The profile losses in this scheme are calculated as:

$$Y_P = 0.914\left(\frac{2}{3}K_P\chi_i Y_{P(i=0)} + Y_{shock}\right) \quad (4.121)$$

Where K_P represents Mach number factor and estimated as:

$$K_P = 1 - 1.25(M_{out} - 0.2)\left(\frac{M_{in}}{M_{out}}\right)^2 \tag{4.122}$$

Y_{shock} is the loss due to shocks calculated using the following correlation:

$$Y_{shock} = 0.75\left(M_{in,H} - 0.4\right)^{1.75}\left(\frac{r_H}{r_T}\right)\left(\frac{P_{in}}{P_{out}}\right)\frac{1 - \left(1 + \frac{\gamma-1}{2}M_{in}^2\right)^{\frac{\gamma}{\gamma-1}}}{1 - \left(1 + \frac{\gamma-1}{2}M_{out}^2\right)^{\frac{\gamma}{\gamma-1}}} \tag{4.123}$$

Where $M_{in,H}$ is the inlet Mach number at blade hub and can be calculated as:

$$M_{in,H} = M_{in}\left(1 + K\left|\frac{r_H}{r_T} - 1\right|^{2.2}\right) \tag{4.124}$$

Where K is constant equals to 1.8 for nozzle and 5.2 for rotor.

The secondary losses prediction using Dunham & Came system was refined by Kacker and Okapuu by considering the influences of flow compressibility and aspect ratio as:

$$Y_s = 0.04\left(\frac{l}{H}\right)\chi_{AR}[4(tan\alpha_{in} - tan\alpha_{out})^2]\left(\frac{cos^2\alpha_{out}}{cos\alpha_m}\right)\left(\frac{cos\alpha_{out}}{cos\alpha'_{in}}\right)\left[1 - \left(\frac{l_x}{H}\right)^2(1 - K_P)\right] \tag{4.125}$$

Where χ_{AR} is aspect ratio coefficient and estimated as:

$$\chi_{AR} = \begin{cases} 1 - 0.25\sqrt{2 - {}^{H}/_{l}} \\ 1 \end{cases} \tag{4.126}$$

The trailing edge loss coefficient can be calculated as:

$$Y_{Te} = \frac{\left[1 + \frac{\gamma-1}{2} M_{out}^2 \left(\frac{1}{1-\Delta E_{Te}} - 1\right)\right]^{-\gamma/\gamma-1} - 1}{1 - \left(1 + \frac{\gamma-1}{2} M_{out}^2\right)^{-\gamma/\gamma-1}} \quad (4.127)$$

Where ΔE_{Te} is the energy loss coefficient at trailing edge.

For unshrouded blade the tip leakage effect is calculated in terms of total to total efficiency variation as:

$$\Delta\eta_{tt} = 0.93 \left(\frac{r_T}{r_m}\right)\left(\frac{1}{H cos\alpha_{out}}\right)\eta_o \Delta\tau \quad (4.128)$$

Where $\Delta\tau$ is the variation of tip clearance, and η_o is turbine efficiency with zero-clearance.

For the shrouded blades the leakage losses can be calculated using the following equation:

$$\mathrm{Y_k} = 0.37 \frac{c}{h}\left(\frac{k'}{c}\right)^{0.78} 4(tan\alpha_{in} - tan\alpha_{out})^2 \left(\frac{cos^2\alpha_{out}}{cos^3\alpha_m}\right) \quad (4.129)$$

Where k' = the effective tip clearance value.

4.12 Summary and conclusions:

- Small axial turbine design methodology follows similar procedure of large axial turbines which include: 1D meanline modeling for initial turbine sizing, CFD simulation for detailed design, and FEA for mechanical design.
- The performance prediction methods were based on many simplified assumptions and some tests of blade loss prediction for large scale gas turbine engines. However, as the turbine sizes become smaller the effect of aerodynamic losses becomes more significant, therefore, the development of more accurate losses prediction models is

required for small scale turbines (Bullock 1964, Benner, et al. 1997). Furthermore, small scale turbines are working with small amount of mass flow rate which leads to small blade height (low aspect ratio) leading to higher rotational speed and aerodynamic losses.

- Limited studies have been conducted to develop means for loss prediction in small scale axial turbines (Macchi and Perdichizzi 1981, Macchi and Lozza 1985, Klonowicz, et al. 2014). Therefore this work aims to develop a systematic approach to predict the losses in a small scale axial air turbine using computational fluid dynamics (CFD) simulations.

- Efficient small axial turbine design requires precise loss estimation and geometry optimization of turbine blade profile for maximum performance.

CHAPTER 5

AXIAL TURBINE DESIGN OPTIMIZATION

5.1 Introduction:

Turbine efficiency has a significant impact on cycle overall performance. Numerical optimization techniques are important tools for increasing turbine efficiency. Due to complicated flow features through turbine passage, the turbine blade design is a challenging iterative process. CFD simulation and design optimization based on 3D turbine modelling can achieve efficient blade profile with high performance levels and minimum losses. This chapter provides an overview of the design optimization techniques and a detailed description of the turbine optimization based on 3D CFD modelling.

5.2 Design Optimization Problem Formulation:

In engineering applications, the optimization process aims to maximize or minimize a specific parameter. For axial turbine design the designer is looking for maximizing the efficiency and minimizing the losses and stresses. As a result, to design efficient turbine, the engineer requires knowledge about optimization techniques and the problem formulation.

In order to specify the optimal turbine design, there is a need to compare different turbine geometries to adopt the best turbine design for certain goals and conditions. The process of setting up the optimization requirements is known as problem formulation which aims to identify design variables, constraints, variable bounds, objective function, and optimization

algorithm. Figure 5.1 shows the flow chart of design optimization steps which are described in detail in the following subsections.

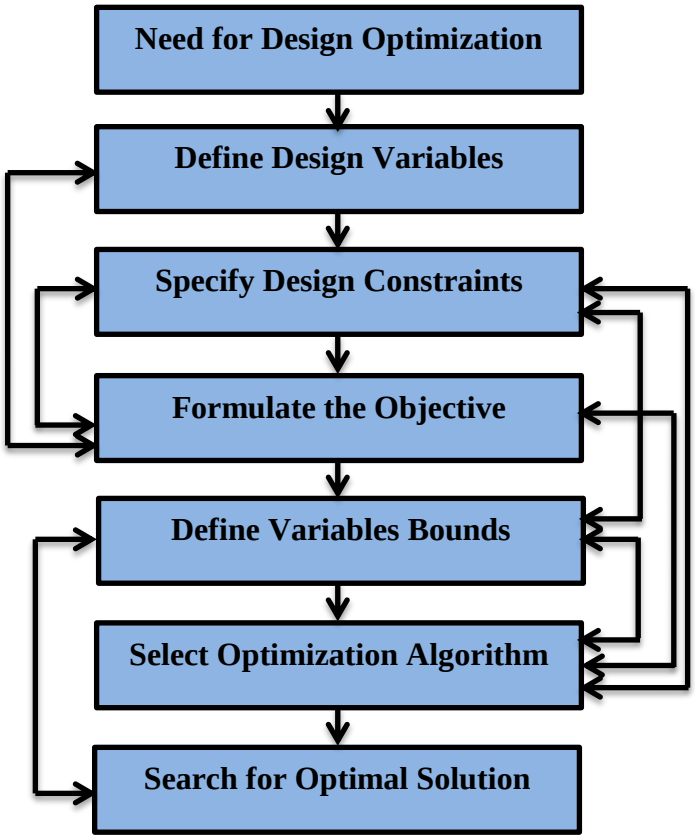

Figure 5.1 Design optimization procedures

5.2.1 Design Variables:

Design optimization process start normally by defining the design variables which are varied to generate different designs during the optimization. The selection of the design variables depends on the designer and the number of these variables which affect the optimization solution speed and efficiency. As a result, it is often recommended to choose a small number of design parameters in optimization problem formulation.

5.2.2 Constraints:

Once the design variables are identified, the designer needs to specify the optimization constraints. These constraints represent design limitations and the functional relations of design parameters. In the case of turbine design optimization the constraints are to satisfy the manufacturing ability, stress limitations and output power or mass flow rate.

5.2.3 Objective Function:

The design optimization is performed by varying the design variables to satisfy the maximum or minimum of a certain function which is known as objective function. This objective function is formulated in terms of design variables and specified to be maximum or minimum. However, in many engineering designs there is multi-objective optimization which includes both minimization and maximization objective functions.

5.2.4 Variable Bounds:

In optimization problem formulation, it is necessary to identify the upper and lower bounds of design variables. In some optimization algorithms the upper and lower parameters values are created automatically based on design constraints. In this case if the optimal value of design variable is close to the lower or upper bound, then the variable bounds needs to be adapted and the optimization can be performed again for more efficient and accurate solution.

5.3 Design Optimization Methods:

The efficient aerodynamic design of axial turbine blades can be achieved using two conventional strategies: inverse design method and design optimization method. The inverse design method is applied in the case where the detailed performance levels of the turbine are known and the corresponding blade geometry is determined based on the solution of the governing equations (Mengistu 2005). The inverse method aims to identify the geometry of

turbine blade based on target pressure distribution. Despite the fact that the inverse method is simple, the selection of target performance levels is challenging and fully depends on trial and error approach and designer experience (Arabnia 2012).

In design optimization method, the turbine performance is defined by a set of geometrical parameters and the blade geometry is optimized for maximum efficiency. This method is flexible in choosing optimization functions and design constrains. This method is applicable for multi-point design optimization such as the turbine design which is a multidisciplinary optimization problem. Broadly, the design optimization methods can be classified into two groups. The first group is direct search optimization and the second group is gradient based optimization (Deb 2012).

5.3.1 Gradient Optimization Method:

This method is a fast optimization scheme for local optimal where the objective function derivatives are computed at initial design point and the new design points are calculated in the gradient direction till the local optimal is reached after small number of iterations (Sasaki, et al. 2001). Gradient based method is not applicable for optimization problems with discrete design variables. During the optimization, this method stops at the first local optimal point and as a result it cannot be used for global multi-objective optimization. The sequential quadratic programing (SQP) is a clear example for the gradient based algorithms. The SQP is used for local single optimization problems but it can be coupled with direct optimization algorithms for multi-objective optimization (Chen 2011, Piegl and Tiller 2012).

5.3.2 Direct Optimization Method:

In real optimization problems where the objective function is computed based on simulation packages, direct search optimization is the most effective technique for computing objective function derivatives. The direct search method can be performed for single and multi-

objective functions. In single point optimization the variables are varied in positive or negative x-axis and for multi-objective optimization the design variable are modified in both positive and negative x-axis. The optimization algorithms which are based on this method is known as one- variable at a time approach. The common direct search based algorithm is genetic algorithm (GA). GA technique is a computerized global optimization algorithm which can perform robust effective optimization but with large cycle time. The computing time in the design optimization using GA can be reduced by combining response surface approximation (RSA) with direct optimization.

5.3.2.1 Genetic Algorithm:

Genetic algorithm is a computerized optimization approach which is based on search optimization method. In this algorithm the solution is obtained by natural selection evolution mechanism. The GA is a common optimization approach for aerodynamic design optimization and it is proven as effective optimization technique for finding the optimal global solution for the problems which have many local optimal points (Zhu and Chan 1998, Gen and Cheng 2000). GA scheme is used in the case of maximization design problems and for minimization goals the objective function is modified to be maximized by applying appropriate transformation to the fitness function. The fitness function F(x) is a non-negative function that is derived from the objective function and used in genetic operations. In the case of maximization problems, the fitness function is equal to the objective function ($F(x) = f(x)$). However, in minimization problems the fitness function is transformed to become a maximization problem as described by (Deb 2012):

$$F(x) = 1/(1 + f(x)) \quad (5.1)$$

The GA optimization starts normally by generating random population of design points. This population is evaluated by applying four basic operations to find the optimum solution. As shown in

Figure 5.2 the main GA operators include selection, crossover, mutation, and estimation which are described below (Deb 2012).

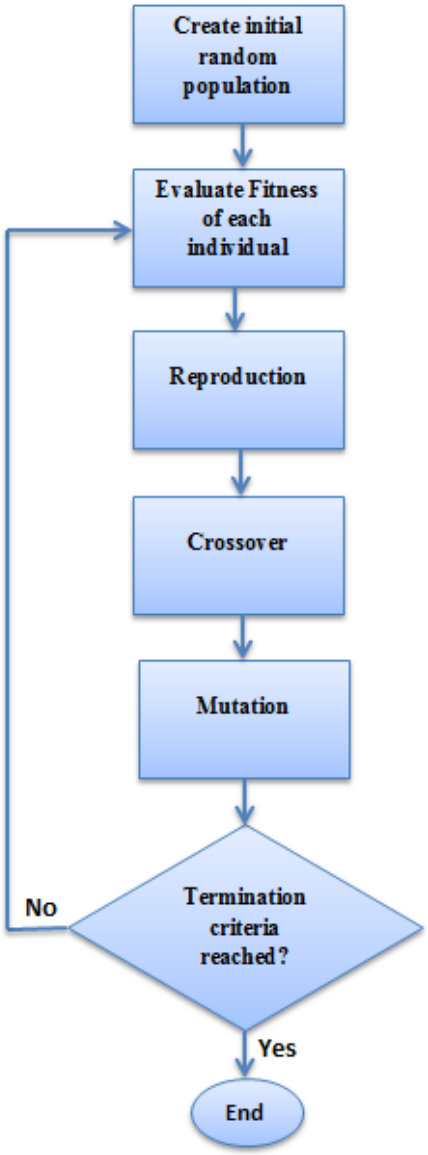

Figure 5.2 Genetic algorithm working principles.

- **Selection Operator:**

This operator is also known as reproduction operator which is applied to generate new candidates (Children) using good candidates in current population (parents) in order to produce a mating pool.

- **Crossover Operator:**

This operator is used to generate a new solution by creating a new chromosome which is compared to parent candidates. There are two types of crossover operators: Arithmetic and Heuristic. In Arithmetic crossover, the two parent candidates are combined to create new children candidates as:

$$\text{Child1} = \lambda\,(\text{parent1}) + (1-\lambda)\text{parent2}$$

$$\text{Child2} = (1-\lambda)(\text{parent1}) + \lambda(\text{parent2})$$

Where λ is crossover probability between 0 and 1.

The Heuristic operator works based on the fitness between the best and worst individuals to create a new candidate as:

$$\text{Child1} = \text{Best Parent} + \lambda[\text{Best Parent} - \text{Worst Parent}]$$

$$\text{Child2} = \text{Best Parent}$$

- **Mutation Operator:**

This operator is the key operator in GA scheme which is used to alter the genes in the chromosome to create a new good string which can be added to the population. This new gene helps the GA search around the obtained solution for local optimum in short time. The mutation is performed using mutation probability (P_m) which is normally set at 10% of the population size.

- **Elitism Operator:**

In order to ensure that the best performed solution will be considered, elitism operator copies two best candidates to be included in the next generation.

5.3.2.2 Multi-objective Genetic Algorithm:

In turbine development, the designer needs to optimize the blade profile with more than one objective function which makes the optimization of turbine design a multi-objective problem. Multi-objective genetic algorithm (MOGA) is well known as one of the most powerful optimization techniques in turbomachinery design optimization which can be applied for non-linear continuous and discrete parameters in both response surface and direct optimization with more than one option (Obayashi, et al. 2000, Yang and Xiao 2014).

Multi- objective genetic algorithm is a normal GA with multi-objective function (min/max) subjected to inequality and equality constrains. According to (Coello, et al. 2002) MOGA can be mathematically formulated in a vector form as:

The objective function vector: $F(X) = [f_1(X), f_2(X), \dots \dots f_k(X)]^n$

Subject to: $g_i(X) \leq 0 \quad i = \{1, \dots . m\}$

$$h_j(X) = 0 \quad j = \{1, \dots . p\}$$

Where k is the dimensional space of the objective functions $g_i(X)$ is the inequality constrains, and $h_j(X)$ is the equality constrains.

In MOGA technique the solution trade-offs are divided into dominated and non-dominated solutions based on Pareto-Optimal population ranking (Fonseca and Fleming 1993). The dominated solution group is considered as the efficient population and the optimum candidate is chosen with respect to one function without worsening the rest of objective functions.

The objective functions in this MOGA are in conflict together and as a result the objective functions are combined in one scalar fitness function. As shown in Figure 5.3 the solution in MOGA optimization is found by searching in the multi-dimensional space (Murata and Ishibuchi 1995).

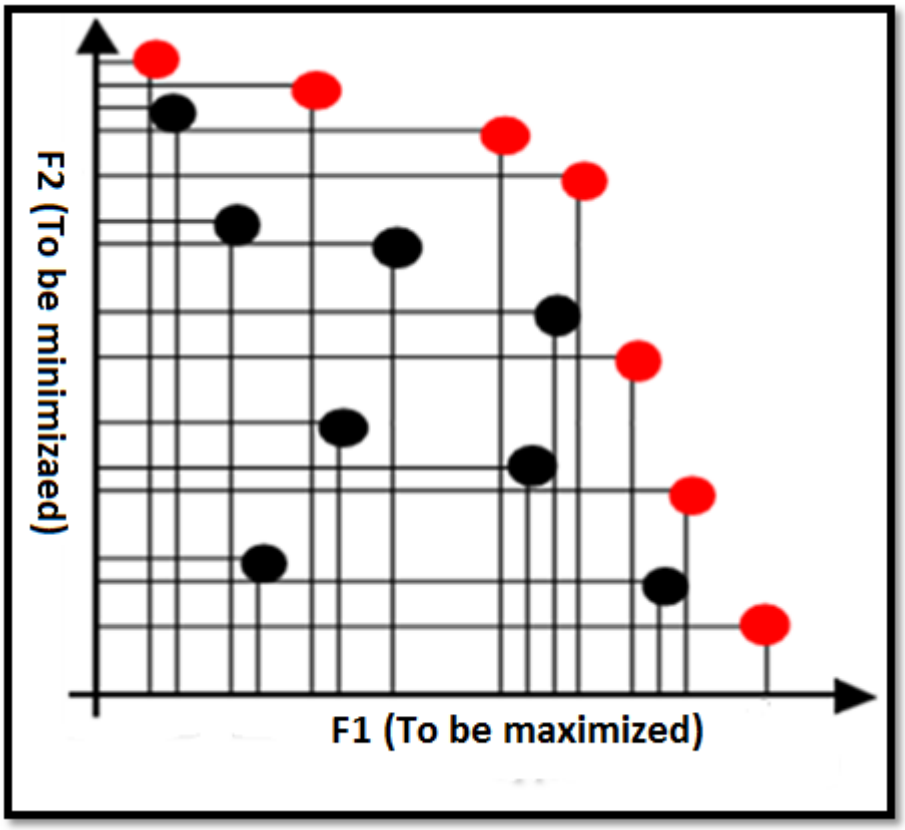

Figure 5.3 MOGA optimization solution(Murata and Ishibuchi 1995).

5.4 Turbine Two- Level Optimization Approach:

The design optimization based on GA for maximization or minimization of the objective function requires large number of iterations to calculate the objective function through expensive running of Navier Stokes (NS) solver. Two-level optimization is one of the developed approaches which aim to reduce the design cycle time and cost of objective function computing based on NS or FEA. This approach is developed by Von Karman Institute for Fluid Dynamics as effective automated optimization tool for turbine blade

geometry optimization (Pierret and Van den Braembussche 1998). The main idea of the two-level optimization is to perform the calculation in two different levels. In the first level, an approximation function is used to predict the objective function near to the optimum blade geometry. Then this approximated solution is refined for higher accuracy by using actual runs of CFD modelling or FEA. The approximation function is known as meta-function prediction (den Braembussche 2008). The common type of meta-function based optimization is Response Surface Method (RSM) which uses the information in a data base generated by design of experiments (DOE) to build correlations between turbine performance and geometric parameters.

5.4.1 Response Surface Method:

Response surface method (RSM) is an approximation function based on a set of mathematical techniques (Cornell 1990). RSM is used in design optimization as a tool to build a relationship between independent design variables (input parameters) and the output response (output parameter). The new approximated function is used to predict the objective function based on small number of runs which replaces long computational time of actual system analysis. As a result RSM is an inexpensive design optimization tool which can be applied to reduce the analysis cost of CFD modelling and FEA. In design optimization the RSM aims to minimize or maximize the response using the relation between the output response (y) and design parameters (x_1, x_2) (Anderson and Whitcomb 2005).

$$y = f(x_1, x_2) + \epsilon \tag{5.2}$$

Where f(x) represents the elements function and ϵ is the approximation error.

In RSM the designer can identify the sensitivity of output response due to design variables variations in design space which is a set of design points created by applying design of experiments (DOE) approach. The response surface can be represented graphically in terms of

3D plot or contour lines as shown in Figure 5.4 which shows the functional mapping of design variables to output response.

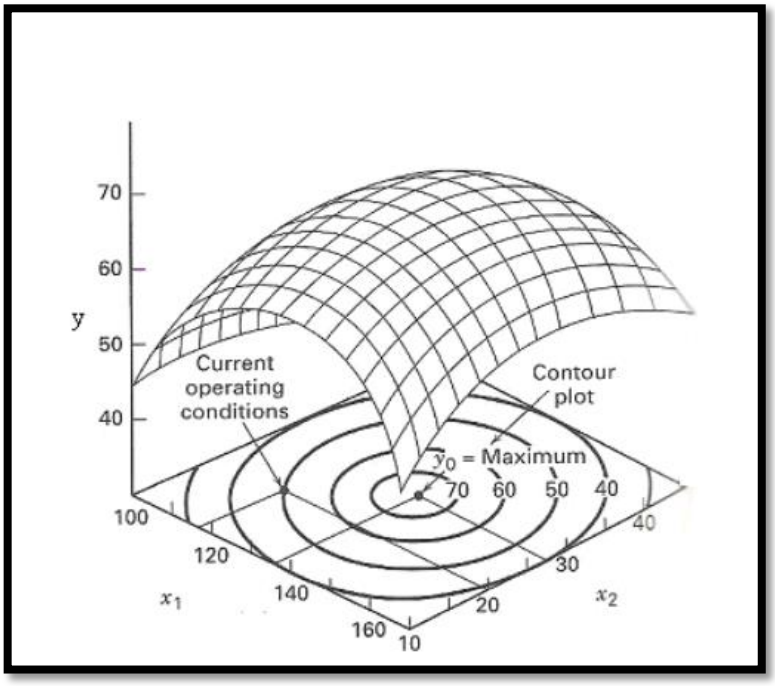

Figure 5.4 Response surface 3D contours (Anderson and Whitcomb 2005).

Due to the fact that the relation between the output response and design parameters is unknown, the response surface method uses an approximation model known as Meta-model or Meta-function to define this relation. In order to guarantee that the approximation function is able to predict the output response with high accuracy, the fitting between this function and actual engineering model needs to check the Goodness of Fit. The Goodness of Fit criteria compares between the predicted values of output function using RSM and DOE as shown in Figure 5.5 to ensure that all response surface results fit the DOE results and close to the diagonal line (Lawrence 2012).

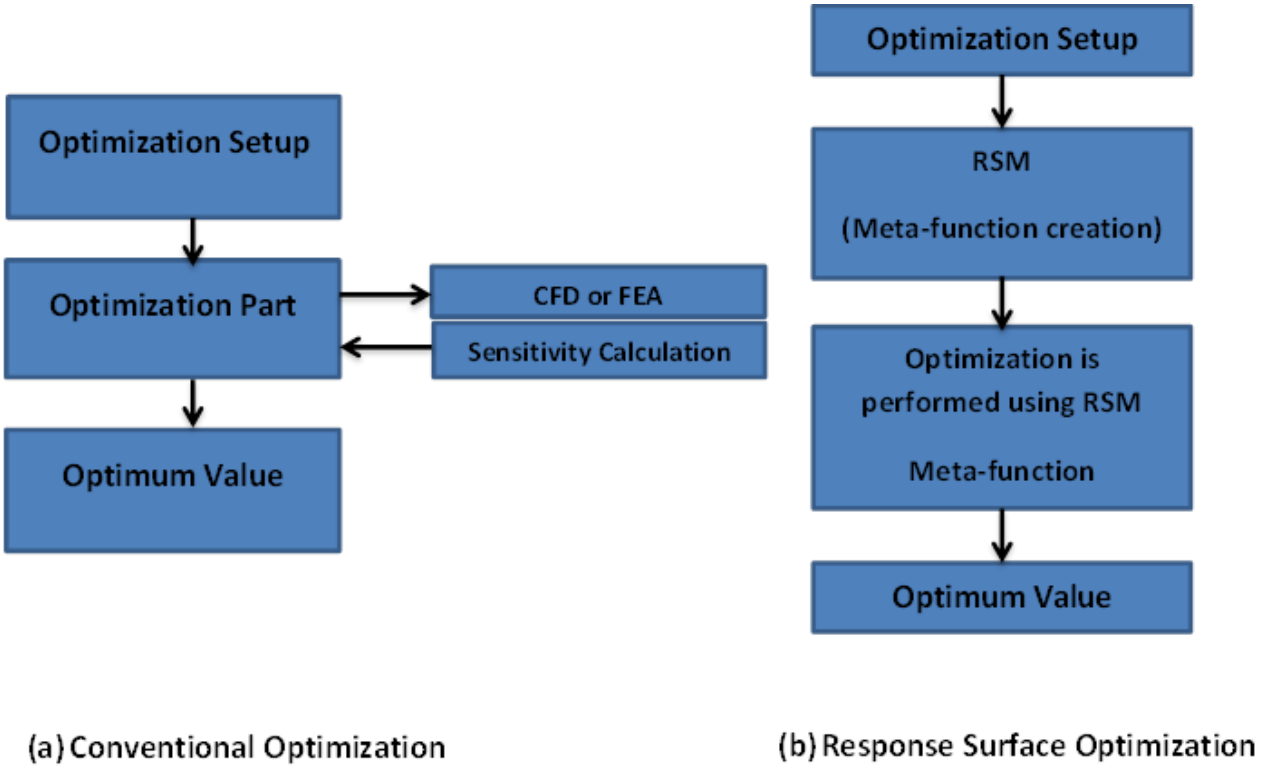

Figure 5.5 Comparison between conventional and RSM optimization

RSM uses different regression analysis approaches to create the response function. The commonly used RSM approximation Meta-models are described in the following subsections.

5.4.1.1 Standard Response Surface Model:

In this model the RSM uses first order or second order polynomial to predict the output function. The first order model is a screening tool of linear independent parameters function applicable only for flat surface with least squares. It is also known as low order polynomial and mathematically can be expressed as:

$$y = B_o + \sum_{i=1}^{k} B_i x_i + \epsilon \qquad (5.3)$$

The second order model is known as higher degree polynomial which is used when there is a curve in the response surface.

$$y = B_o + \sum_{i=1}^{k} B_i x_i + \sum_{i=1}^{k} B_{ii}\, x_i^2 + \sum \sum_{i<j} B_{ij} x_i x_j + \epsilon \qquad (5.4)$$

In some engineering designs, the polynomial models are unlikely to be fitted with the actual system especially for nonlinear problems and it is recommended only when there is a smooth variation in the output response like in FEA for stresses and deformation approximations (Van den Braembussche 2008, Lawrence 2012). However, in other design optimization problems, the 2nd order polynomial approximation quality needs to be improved where the Goodness of Fit is significantly bad.

5.4.1.2 Kriging Model:

In this model, the meta-function uses higher order polynomial equations to determine the relation between output function and input parameters. The Kriging model can interpolate all points in DoE to refine all input parameters with internal error estimation. In this model the relative error in all design space can be predicted as:

$$\text{Predicted Relative Error} = \frac{100 \times \text{Predicted relative error for output Parameter}}{\text{Out}_{\max} - \text{Out}_{\min}} \quad (5.5)$$

Where the $\text{Out}_{\max}$ and $\text{Out}_{\min}$ are maximum and minimum output values.

The main disadvantage of Kriging Meta-model is that this model supports only continuous input parameters and it is not applicable for discrete parameters.

5.4.1.3 Sparse Grid Model:

This meta-model works based on grid adaptive algorithm which is used to build a matrix of design points in a repeated process to meet the desired quality. In this model, the refinement for input parameters is performed automatically to identify the significant parameters levels. The application of this model is limited only for continuous type parameters (Lawrence 2012).

5.4.1.4 Artificial Neural Network (ANN):

Artificial Neural Network (ANN) is a robust mathematical approximation technique that can be used in design optimization to build a non-linear relationship between input and output parameters (Thevenin and Janiga 2008). In turbine design optimization the ANN is used to predict the turbine performance for different new geometries. Using the information in the database, the ANN model can build a relationship between n input parameters of turbine geometry and m output parameters of turbine performance like efficiency, power, etc. (Cravero and Macelloni 2010).

The working principles of ANN are similar to the human brain nervous system. The ANN consists of neurons or nodes which are collections of elementary processing units. These nodes are wired in layers and joined together with special connections called Synapses with different weights (W). Each node has two operations which are the summation and transformation through the activation function. The simple ANN is organized as shown in Figure 5.6 in three layers; input layer, hidden layer, and output layer (Li 1994). The ANN Meta-model is recommended for turbomachinery optimization due to its ability of fast aerodynamic geometry optimization based on GA with less computational time compared with NS solver (Thevenin and Janiga 2008, Hamzaoui, et al. 2015).

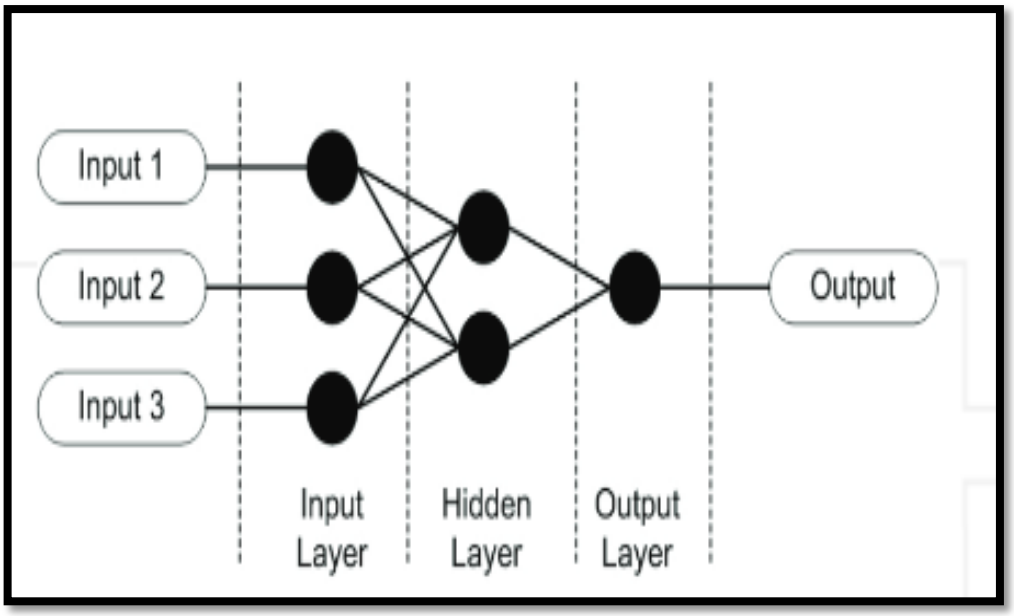

Figure 5.6 Simple artificial neural network (Thevenin and Janiga 2008).

5.5 Design of Experiments:

In turbine design process, there are different design variables which affect the overall turbine performance. The design of experiments (DoE) approach is a statistical technique that can be used to identify the critical design parameters and specify the relationship between these parameters and output response. In design optimization problems, the DoE is a powerful tool which can generate sufficient data (design points) to identify the interaction between design variables by testing the cause and effects relationships for higher and lower design variables levels. The DoE approach can be applied for both physical and numerical modelling systems to predict the output response as a function of design parameters which can be optimized for maximum or minimum output response.

The optimal DoE is generally achieved based on polynomial mathematical model with different methodologies which include: Factorial Design, Central Design, and D-optimal Design. The most common method is factorial design which investigates the output response for 2^k runs or experiments for two levels of k design variables. The main advantage of

factorial method is that it is capable to identify design variables interaction impacts by including the combinations of design variables in the design space (Lundstedt, et al. 1998).

In turbine design optimization, the DoE is an essential aspect that provides the input information to the RSM. This information represents the optimization database which can be used to build relations between turbine geometrical parameters and output performance. The objective function in design optimization is predicted based on DoE database information without running NS solver and as a result the computational efforts and time can be reduced. To ensure the accuracy of the DoE for 2^k runs the global error can be estimated based on actual NS simulation as (Van den Braembussche 2008):

$$Global\ Error = \sum_{i=1}^{2^k} \frac{Exact\ Value - Predicted\ Value}{Exact\ Value} \times 100 \quad (5.6)$$

5.6 Turbine Multidisciplinary Optimization:

The optimization techniques can be used in design optimization to specify the optimal solution but not for all disciplines. In the case of axial turbine, the design process involves two phases: the aerodynamic design which can be achieved by CFD analysis of the complex flow through turbine blades, and the mechanical design which can be conducted using finite element analysis (FEA) to identify the maximum stress levels due to aerodynamic loads. Turbine design optimization is performed to maximize turbine efficiency. This requires stress prediction at the same time to guarantee turbine mechanical reliability. As a result, efficient turbine design is challenging multi-objective multidisciplinary task (Korte, et al. 2001).

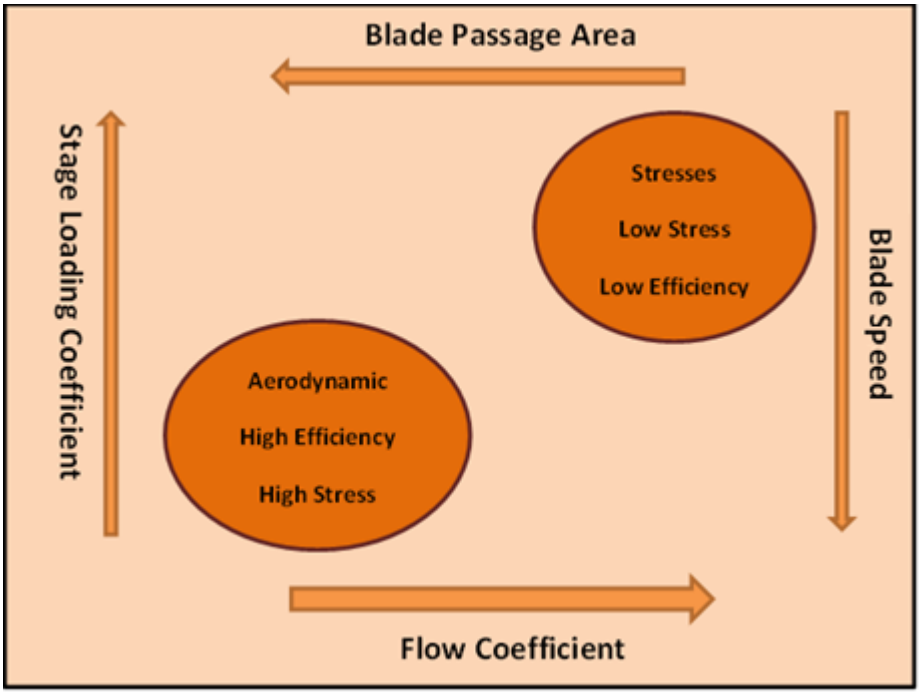

Figure 5.7 Aerodynamic and mechanical designs interactions (adapted from (Moustapha 2003)).

Multidisciplinary optimization is a design optimization approach which combines CFD modelling with FEA at the same time in order to compromise between high turbine efficiency requirements and stress limitations. In this optimization technique, the optimal aerodynamic blade profile can be mechanically guaranteed based on FEA for total deformation and maximum stresses on turbine blades and all the design conflicts shown in Figure 5.7 can be avoided (Janiga and Thévenin 2008). This can be achieved based on GA optimization using the input data from both Navier Stokes (NS) calculations and FEA as shown in Figure 5.8. This optimization approach offers some advantages which are:

- In this approach, the geometry is defined using design variables in GA. This can reduce the error of geometry transmission from discipline to another.
- In multidisciplinary optimization, the global objective function is determined for all design aspects with small number of iterations.
- Parallel calculations can be conducted in the case of independent disciplines.

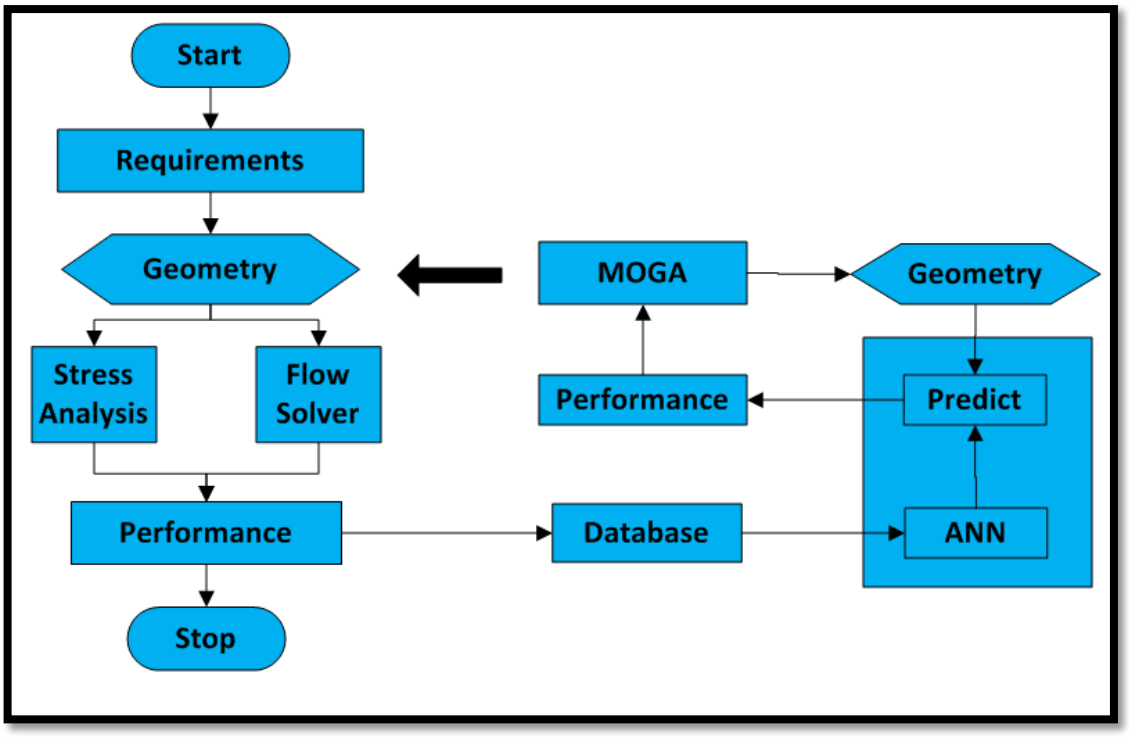

Figure 5.8 Multidisciplinary optimization flowchart (Thevenin and Janiga 2008)

5.7 Multi-point Turbine Optimization:

In general, turbine design optimization is conducted by redesigning blade profile for a certain operating condition (design point) and this approach is known as single point optimization. However, in real applications, the turbine is characterised by a wide range of operating conditions and in other applications the turbine works deeply in off design conditions for long time.

A multi-point optimization is an optimization approach which is performed for a range of operating conditions to ensure that the turbine has acceptable performance levels at this operation range. This can be achieved by using the interaction between GA, ANN and design points database generated by DoE. Multi-point optimization is a proven technique for turbine rotor optimization through redesigning the rotor profile for different inlet conditions (Demeulenaere, et al. 2004).

The multi-point optimization approach aims to stabilize turbine mass flow rate (avoiding stall region) which can be achieved by solidity (chord to pitch ratio), and blade curvature variations to predict turbine performance for different inlet conditions (Thevenin and Janiga 2008).

5.8 Geometry Parameterisation:

Turbine geometry parameterisation is an essential step in design optimization. There is a well-known method for turbine blade aerofoil cross section definition as published by (Pritchard 1985). This method is known as an eleven parameter method and it is considered as the simplest way for blade profile representation with less data compared with other conventional methods like numerically defined blade thickness, inverse method, and polynomial blade profile.

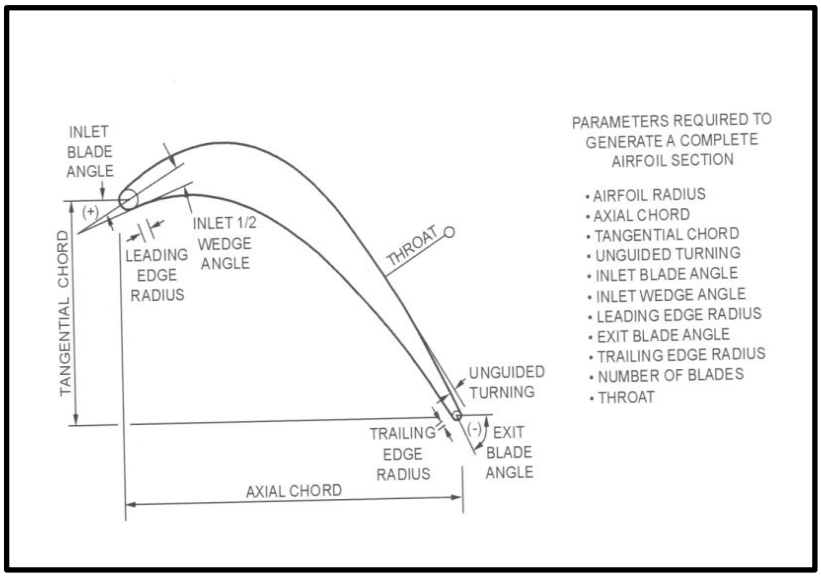

Figure 5.9 Turbine blade cross section defined by 11 parameters (Moustapha 2003)

In turbine design optimization, it is recommended that all geometry parameters are sufficiently defined and limited to the number required for good blade profile representation. For complex blade profile the turbine is normally parameterized using Bezier polynomials to generate flexible curve with control points (x, y). In this geometry definition method, both

pressure and suction sides of turbine are defined with respect to the camber line which is defined as shown in Figure 5.9 by using three main points: the first point matches the leading edge, second point is for the trailing edge, and the third one which results from LE and TE tangents intersection. These points are correlated with blade chord, and stagger angle (Moustapha 2003, Thevenin and Janiga 2008).

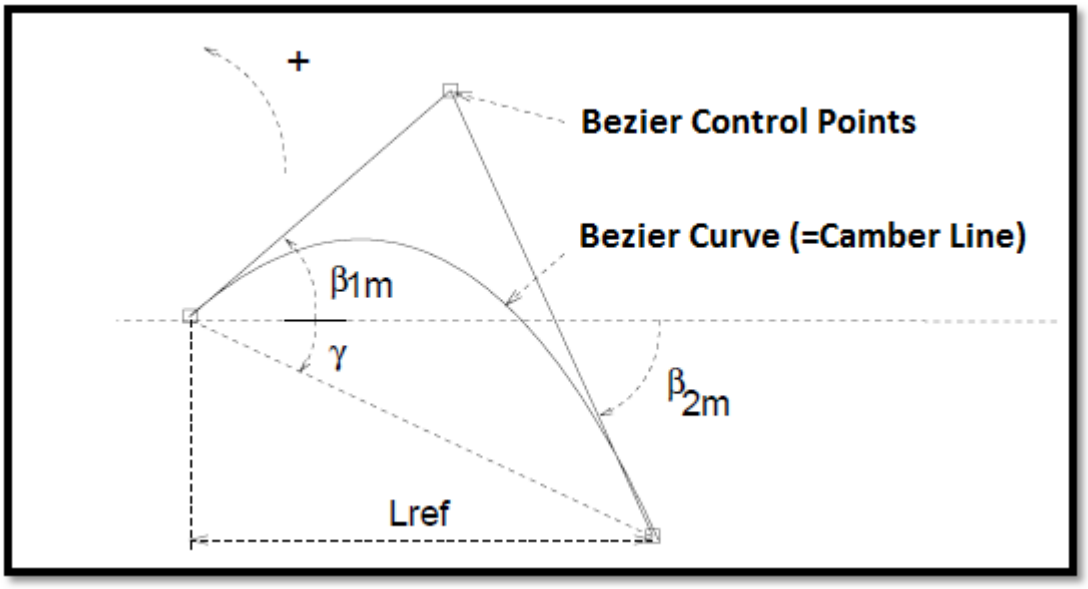

Figure 5.9 blade camber line definition by control points (Thevenin and Janiga 2008)

In this research, the eleven parameters method was chosen for blade parameterisation due to its simplicity with lower input variables. However, the optimization based on Bezier curve parameterisation is time consuming due to the large number of input parameters (for each control point (x,y) x represents parameter and y represents another parameter) and decreasing the number of parameters leads to unsuccessful blade representation in the optimization algorithm.

5.9 CFD Based Optimization Using ANSYS Design Exploration:

Turbine optimization based on CFD modelling coupled with optimization algorithms is an effective approach which can achieve efficient novel blade profile without the need to conduct complex expensive tests of various blade profiles to determine the optimum design. In this optimization system, the aerodynamic turbine blade can be optimized by integrating NS solver with advanced optimization algorithms to achieve higher efficiency. Modern CFD packages have been integrated with several advanced optimisation techniques which can be used to perform an effective design process (Sasaki, et al. 2001, Janjua, et al. 2013).

In ANSYS CFX the designer can use design explorer for turbine optimization with large amount of data about the design. The advantage of using design explorer in optimization is that the impact of geometry parameters variations on performance levels can be investigated. Also, the effect of any changes in design constrains can be studied and the designer can take the right decision based on available large amount of information (Manual 2000).

The design exploration can use the design candidates which are generated by design of experiments method to optimize the design with a high flexibility in choosing design parameters levels for both direct and RSM optimization (Tveit and Fogelholm 2006).

The main components of design exploration include:

- **Design Modeller**: in which the turbine geometry is generated for both nozzle and rotor and all geometrical parameters are set as design variables (parameterization) before running NS solver.
- **Design of Experiments (DoE):** This technique is used to generate sufficient design space (design space matrix) based on the number of input and output parameters including the interactions between design variables. The DoE is used also to identify parameters levels (upper and lower bounds).

- **Response Surface Method (RSM)**: RSM is used in design exploration to build a relationship between independent design variables (input parameters) and the output response (output parameter) for the design matrix generated by DoE to study local and global output sensitivity to input parameters variations. RSM is integrated with different regression approaches to predict the objective function based on small number of runs which replaces long computational time of actual system analysis. (Myers, et al. 1989).
- **Optimization part**: in the optimizer, optimization constrains, objectives, and convergence criteria are defined. In this component the optimization is performed using different techniques which include: MOGA, NLPQL, Screening, and MISQP.

In this research, three-dimensional steady flow simulation using ANSYS CFX16.2 was created for blade profile optimization and design explorer was used for nozzle and rotor optimization based on RSM and MOGA optimization technique. The general optimizations strategy using ANSYS CFX is described by the flowchart shown in Figure 5.10.

In this research, there are two objective functions considered in multiobjective optimisation algorithm. The first objective function (to be maximized) is turbine total to total efficiency (η_{tt}), and the second objective function (to be minimized) is total pressure loss through turbine rotor (Y_R).

Maximize:
$$OF_1 = \eta_{tt} = \frac{h_{o1} - h_{o3}}{h_{o1} - h_{o3ss}} \tag{5.7}$$

Minimize:
$$OF_2 = Y_R = \frac{(P_{o2\,rel} - P_{o3\,rel})}{(P_{o1\,rel} - P_3)} \tag{5.8}$$

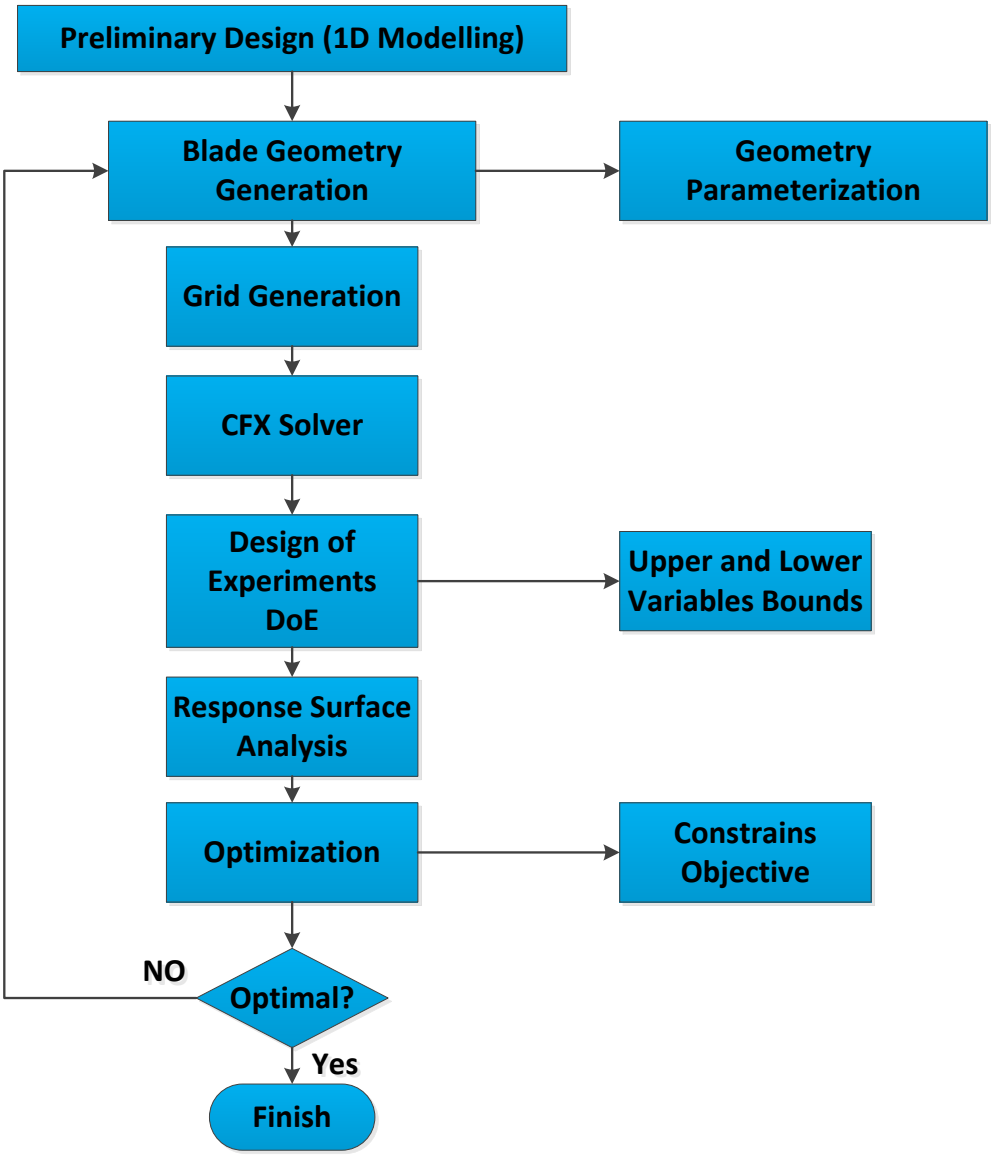

Figure 5.10 Optimizations strategy using ANSYS CFX design exploration

CHAPTER 6

AXIAL TURBINE TEST RIG FACILITY

6.1 Introduction:

This chapter describes the developed axial air turbine test rig facility with detailed description of test rig components and measuring instruments. The main objectives of this experimental work were to evaluate the overall performance of the developed turbine and to validate turbine design methodology (1D modelling- CFD simulation- Design optimization) using experimental results.

6.2 Test Facility Layout:

In order to validate the design and CFD modelling of the developed small axial air turbine, a complete compressed air system was built as shown in Figure 6.1 which represents a detailed schematic diagram of the test facility. The experimental test rig shown pictorially in Figure 6.2 consists of the compressed air storage tank for air supply, developed axial turbine with all components (inlet cone, nozzle guide vanes, and rotor with shaft), flow meter to measure and control the inlet air flow rate, torque meter to measure the output power and turbine rpm, filter and valves to regulate the inlet turbine pressure, pressure transducer for measuring the pressure, and thermocouples for measuring air temperature.

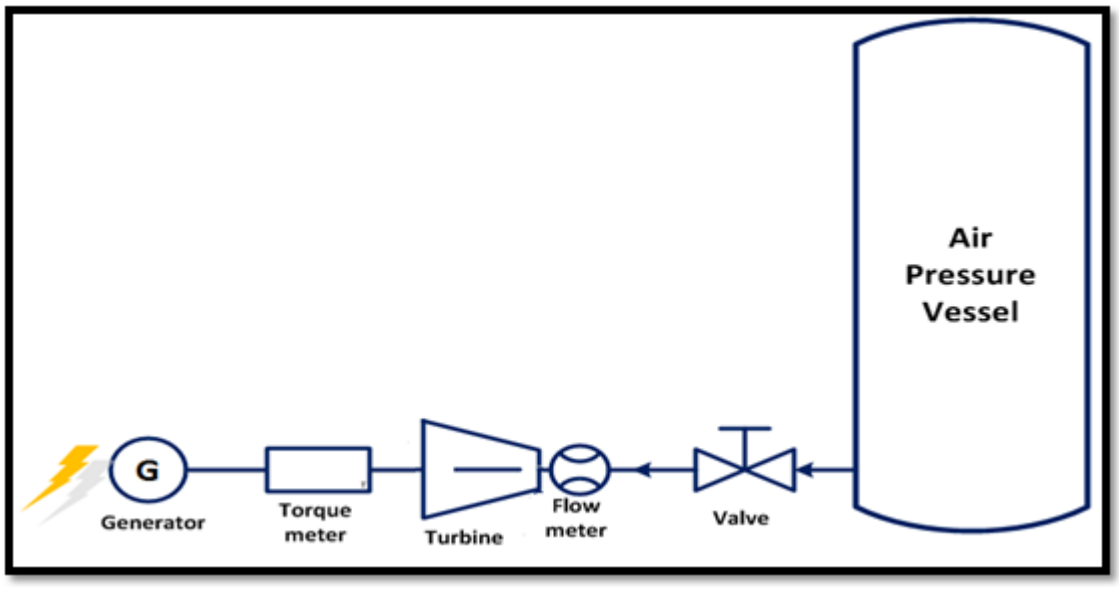

Figure 6.1 Schematic diagram of axial turbine test rig

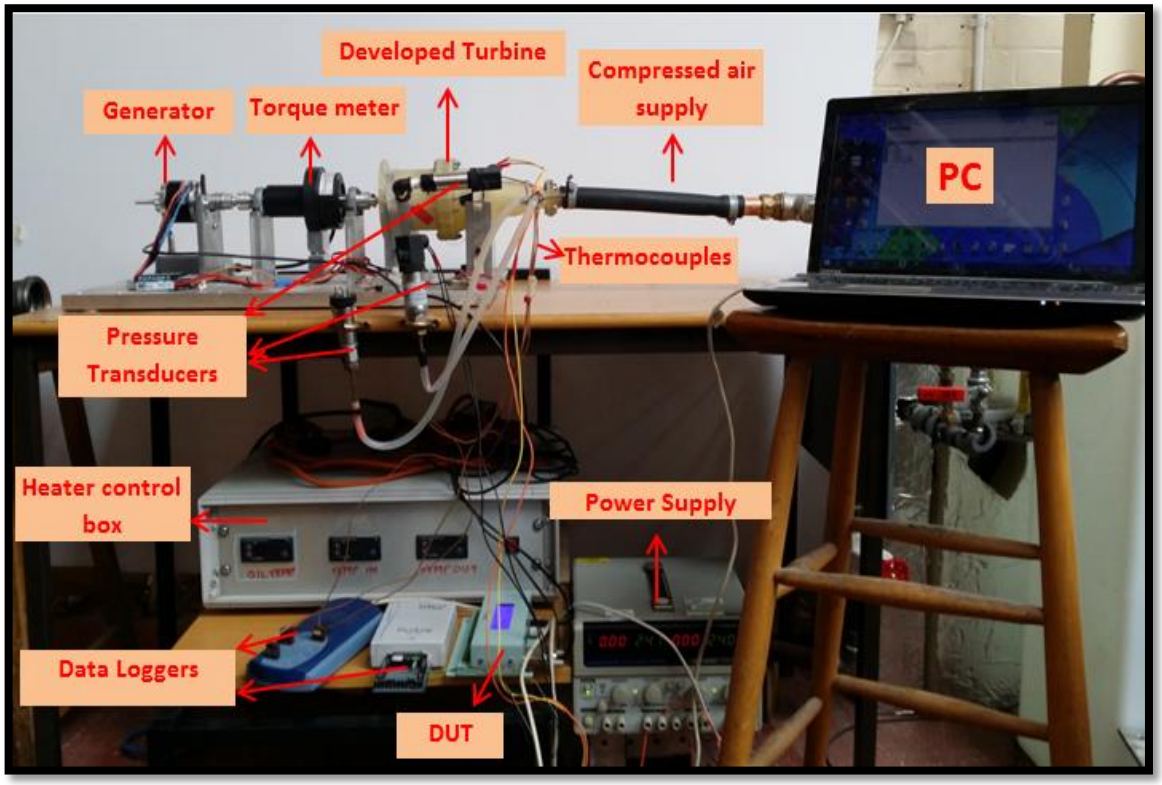

Figure 6.2 Axial air turbine test facility

In this test rig, the air is drawn from the compressed air tank and passed through a regulation valve to set the pressure at certain value. To heat up the air entering the turbine a special

heater tape was used with temperature control box in order to perform the test at different turbine inlet temperatures. By setting the heater thermocouples at the turbine inlet, the air temperature entering the turbine can be adjusted using the heater control box. Pressure transducers and thermocouples were fitted at both the turbine inlet and exit to measure the pressure and the temperature of the air entering and leaving the turbine. For recording all data, the measuring instruments were connected to data loggers which in turn were connected to a personal computer. In order to measure the output power, the turbine shaft was coupled with a torque meter and DC generator to apply different loads.

6.3 Developed Turbine Components:

Based on turbine 1D modelling and CFD optimization results, the final design model of a 1kW axial air turbine was manufactured using 3D printing facility. As shown in Figures 6.3 and 6.4 the main components of the developed axial air turbine are: inlet cone for guiding the airflow with minimum pressure loss, nozzle row vanes to direct the flow towards rotor blades, turbine rotor which is connected to a metal shaft for coupling with the torque meter and rotor casing and bearing housing. This axial air turbine was connected directly to the air supply pipe and measuring instruments to record the air properties at turbine inlet and exit. The inlet cone was simulated to select the optimum cone design that can achieve good flow guidance with minimum pressure and shock losses as shown in (Appendix A).

Figure 6.3 Developed turbine components

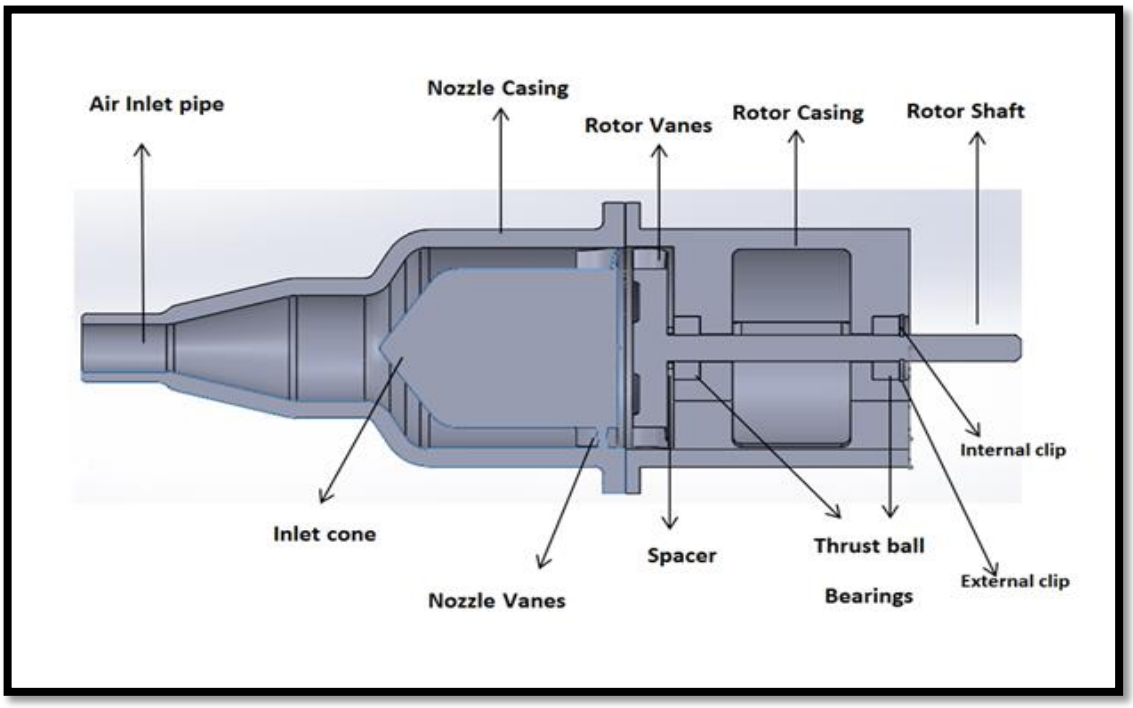

Figure 6.4 Cross section of developed turbine assembly.

6.4 Measuring Devices:

To determine the turbine overall performance at different inlet conditions, several instruments were installed in the test rig to enable measuring all air flow properties at both turbine inlet and exit. These measuring instruments include pressure transducers, thermocouples, flow meter and torque meter which are described in the following sections.

6.4.1 Pressure Transducers:

Pressure transducers were fitted at both the turbine inlet and exit to measure air pressure. At the turbine inlet, a pitot - static tube was installed at the inlet cone and connected to (1-10 bars) a GE 5000 pressure transducer to allow measuring both total and static pressure at the turbine inlet with an accuracy of ±0.05% based on manufacturer specifications. A PTX 1400 pressure transducer (1-6 bars) was installed at the turbine rotor exit to measure the exit static pressure. All pressure transducers were connected to the data logger and DC power supply for pressure data recording as shown in Figure 6.5.

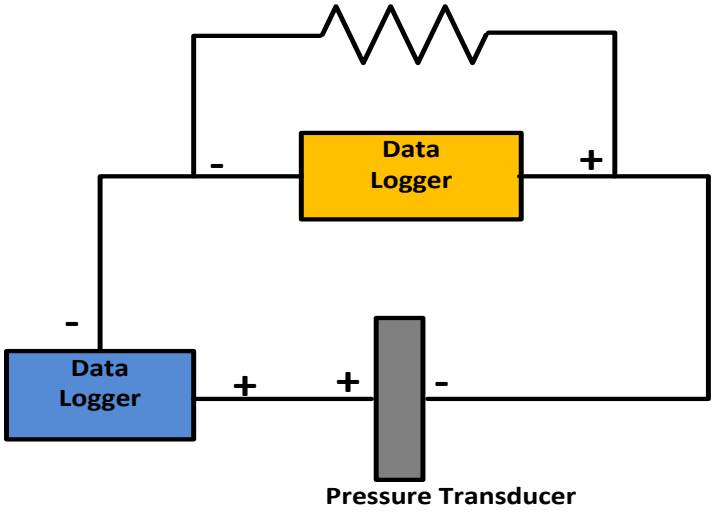

Figure 6.5 Pressure transduce electrical wiring

6.4.2 Thermocouples:

For direct air temperature measurements, T-type thermocouples with 0.75 mm diameter, 150 mm length, and accuracy of ±0.5^{o}C were installed at different locations in the test rig facility. Two thermocouples were located at turbine inlet cone, two located between the nozzle vanes and rotor and two placed at turbine rotor exit. The measurements of turbine inlet and exit temperatures allow calculating turbine efficiency.

6.4.3 Flow Meter:

To measure the inlet air flow rate a variable area flow meter with capacity up to 4000Liter/min and accuracy of ±0.02 L/min was installed at the turbine inlet. This flow meter was also used for air mass flow rate variations at fixed inlet pressure to evaluate the turbine performance at different inlet mass flow rate.

6.4.4 Torque Meter:

The torque meter was coupled with the turbine shaft to allow measuring turbine rotation speed up to 20,000 rpm, torque up to 10Nm and the output power with an accuracy of ±0.1Nm according to Datum Electronics specifications. This torque meter was connected to the PC to display the output power for different turbine torque and rotational speed. Figure 6.6 shows the torque meter components.

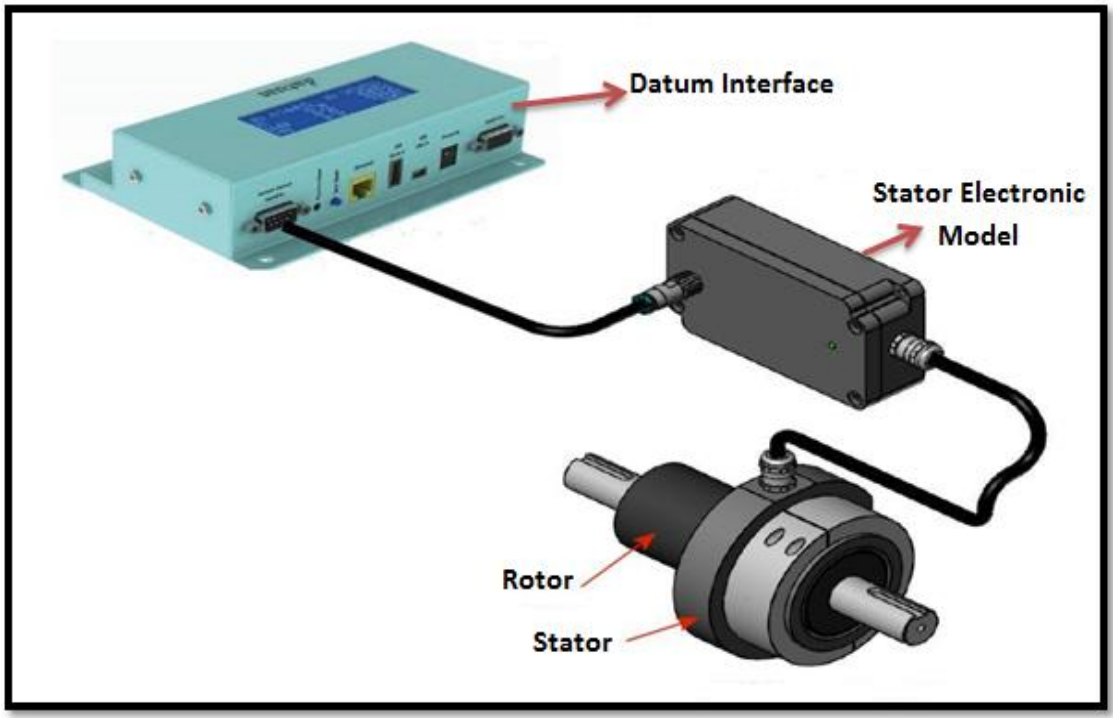

Figure 6.6 Torque meter components

6.4.5 Data acquisition System:

All measuring instruments were connected to data loggers connected directly to a PC to display and record all measured data. For the thermocouples, Pico TC-8 data logger was used to measure all temperature readings which will be monitored using PC. The pressure transducers were connected directly to Pico 1012 data logger to convert the voltage signal to readable pressure value using a PC. For the rpm and output power, the torque meter was connected to the data logger incorporated with a torque meter datum interface which can be connected to the PC to display and record the power, rpm, and the torque.

6.5 Measuring Instruments Calibration:

For accurate evaluation of turbine performance, the measuring instruments for both pressure and temperature need to be calibrated to ensure the accuracy of the recorded data. The calibration process aims to define the relation between measured parameter value and the true

value. This can be achieved by comparing the measured value against standard instrument measurements.

6.5.1 Pressure Transducers Calibration:

The calibration of all used pressure transducers were conducted against standard pressure gage with an accuracy of ±0.04 bar. To calibrate the pressure transducers, each one was connected to a water cylinder to measure water pressure as shown in Figure 6.7 and the output voltage of the pressure transducer was compared to the corresponding standard gage pressure reading. Using a rotating shaft, the pressure inside the cylinder was varied in order to determine the correlation between pressure transducers output signals and the gauge pressure readings as shown in Figure 6.8.

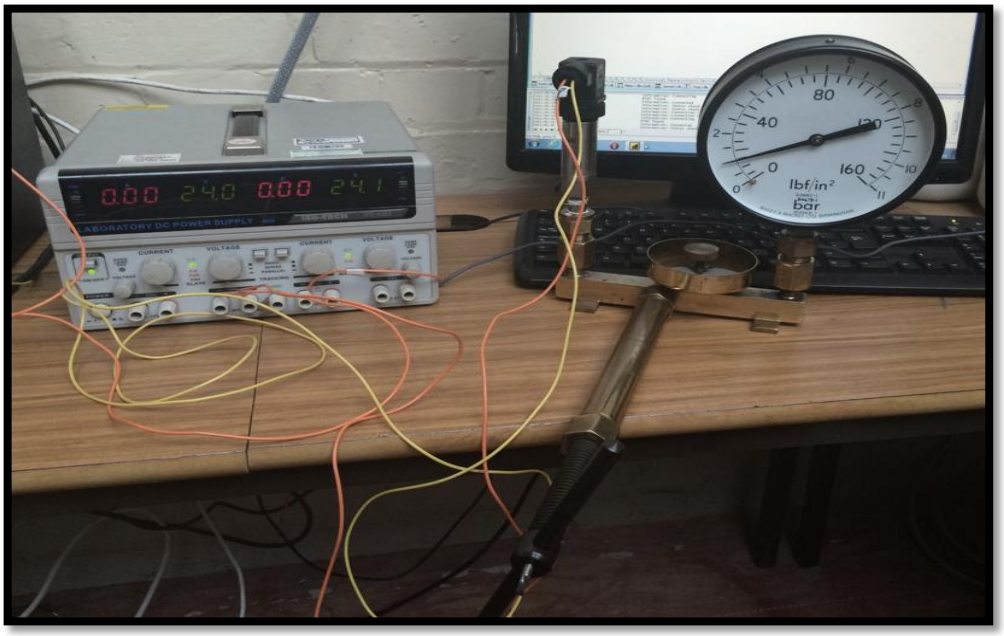

Figure 6.7 Pressure transducer calibration

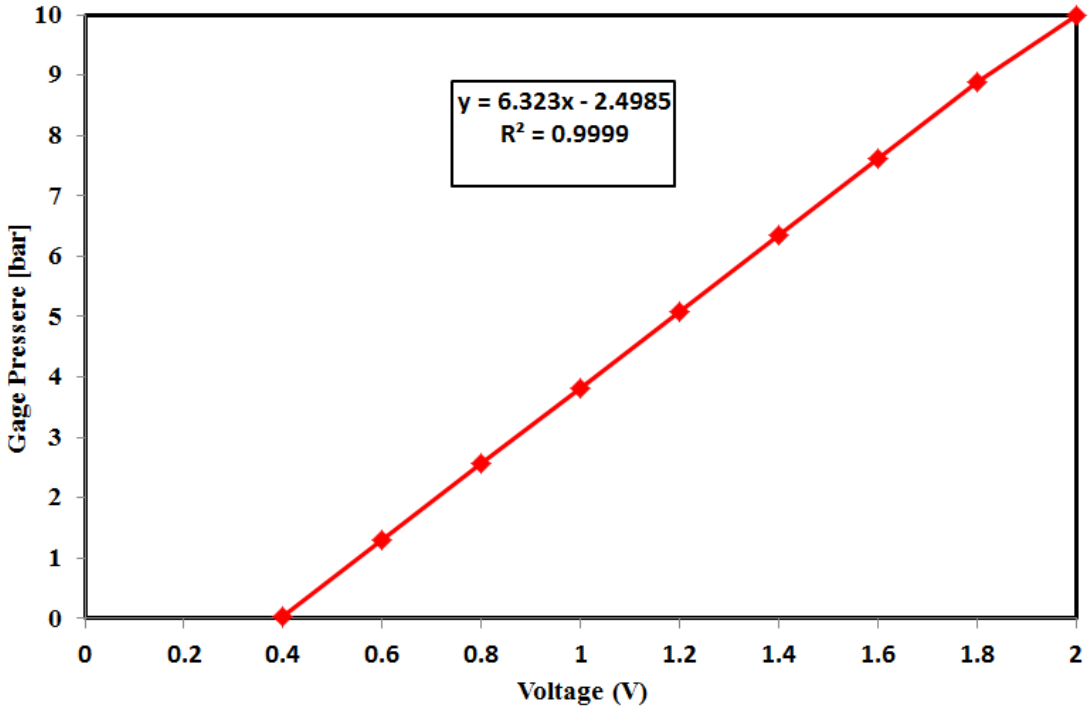

Figure 6.8 Pressure transducer calibration curve (GE UNIK 5000-1)

6.5.2 Thermocouple Calibration:

For measuring the air temperature at both turbine inlet and exit, T-type thermocouples were installed. These thermocouples were calibrated against standard RTD type thermocouple using water container as shown in Figure 6.9. The T-type thermocouples and the standard RTD were fitted at the same height in the water container to measure water temperature. The heat was added to the water using thermostat that can be set at different temperatures in a repeated process. All thermocouples were connected to TC-08 data logger and PC to display the temperature readings. Figure 6.10 shows the calibration results of T-type thermocouple against the standard RTD thermocouple readings.

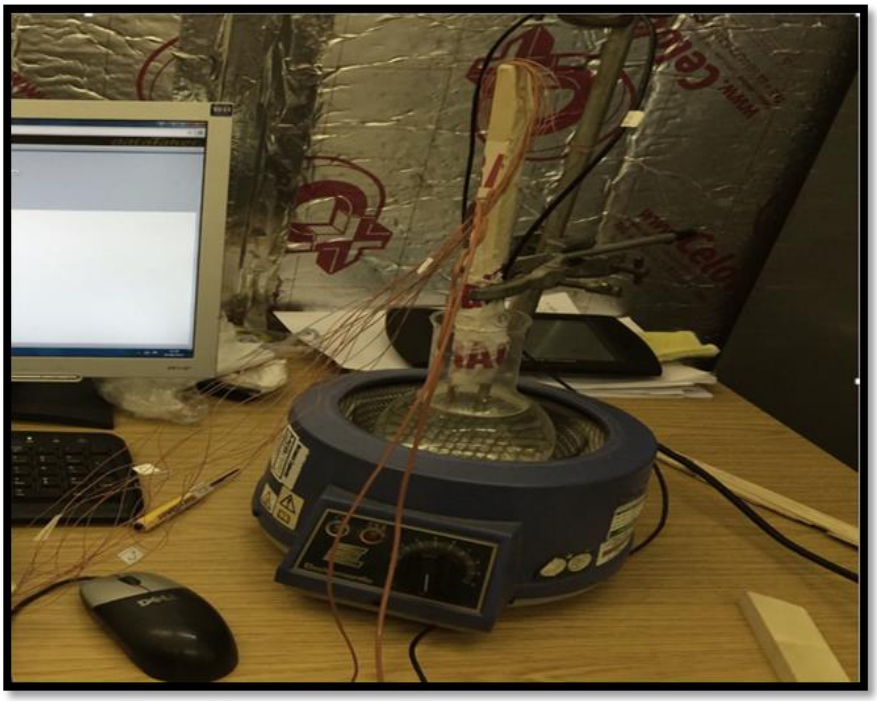

Figure 6.9 Thermocouple calibration process

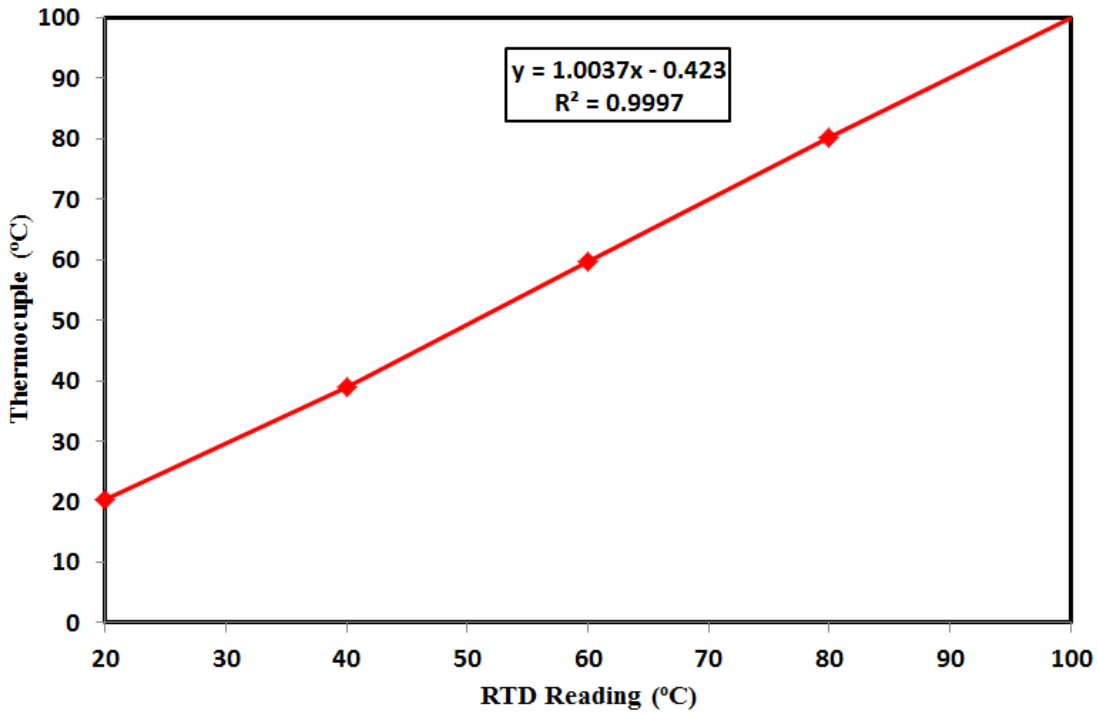

Figure 6.10 Calibration curve of thermocouple1

6.6 Accuracy and Uncertainty Analysis:

In any real experimental work, the measuring instruments are used to determine a result R as a function of combined individual parameters X_i.

$$R=R(X_1,X_2,X_3,\ldots..Xn) \qquad (6.1)$$

The measurement process of each individual parameter (X_i) is affected by the developments of errors during actual experiment leading to the deviation of the result R from the expected true value. In experimental work, there are two types of errors namely fixed error (bias) and random error (precision). The fixed or systematic errors are related to poor measurement accuracy due to poor instrument calibration, faulty instrument installation, and user faults in taking measurements. The systematic errors can be removed by careful calibration and installation of measuring devices (Moffat 1982). The random errors are the errors which are described as fluctuations in the result above and below actual values. This type of errors can be analysed statistically using mean square deviation approach with 95% confidence level (Elsayed 2011). Figure 6.11 shows the effect of errors in measuring variable X.

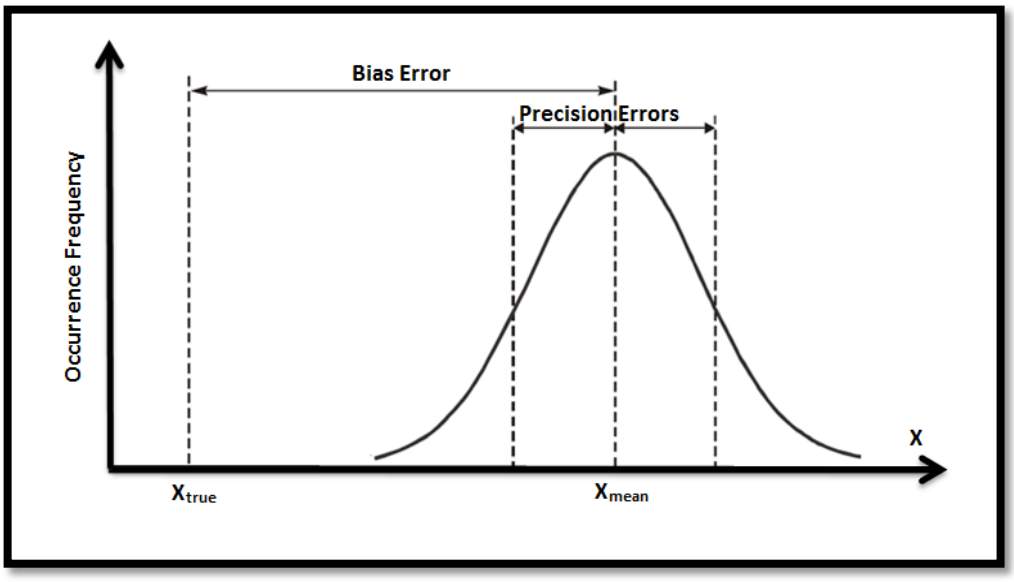

Figure 6.11 Measurements error sources

In actual experimental work, it is difficult to decide the exact true value of any measured variable and there is a need to estimate the error value to define the exact value interval (±U) based on uncertainty analysis. The overall deviation or uncertainty in all measured parameters was estimated using the commonly used standard mean square approach in terms of fixed (U_{sys}) and random (U_{random}) errors as:

$$U_{Overall} = \pm\sqrt{U_{Sys}^2 + U_{random}^2} \tag{6.2}$$

The random error U_{random} can be estimated using standard mean deviation approach with 95% confidence level as:

$$U_{random} = t_{N-1,95\%}\sigma_{\bar{S}} \tag{6.3}$$

Where: N is the number of samples, t is student distribution coefficient with N-1 degree of freedom, and $\sigma_{\bar{S}}$ is the mean deviation calculated as:

$$\sigma_{\bar{S}} = \frac{1}{\sqrt{N}}\sqrt{\frac{\sum_{i=1}^{N}(X_i-\bar{X})^2}{N-1}} \tag{6.4}$$

The systematic error for a number M of fixed error sources can be estimated as:

$$U_{Sys} = \sqrt{\sum_{i=1}^{M} U_{i,Sys}^2} \tag{6.5}$$

6.7 Uncertainty Propagation:

For each measured individual parameter (temperature and pressure) X_i, both systematic and random errors propagate in the overall experimental result R as in equation (6.1). Figure 6.12 shows the impact of errors in measuring X_i on the calculated result R. As can be seen any small deviation (σ_X) in measuring X_i leads to a considerable deviation (σ_R) in the calculated result R (power and efficiency). The deviation in result (R) due to the errors in measured parameter X_i, is approximated as the product of sensitivity factor ($\frac{dR}{dX_i}$) and the error in X_i value (Stern, et al. 1999).

$$U_{R,X_i} = \left[\frac{dR}{dX_i}\right] U_{X_i} \tag{6.6}$$

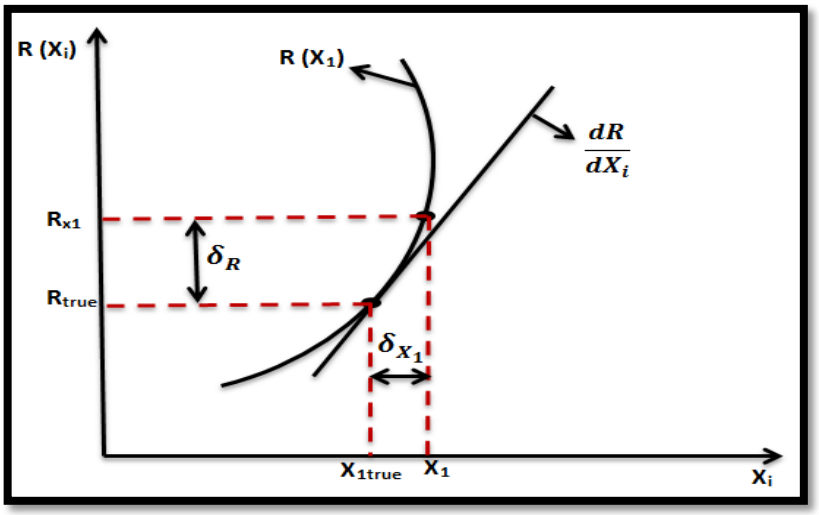

Figure 6.12 Error propagation in R from parameter X1(Stern, et al. 1999)

The overall uncertainty of experimental result (R) due to errors in all measured individual variables can be expressed as (Stern, et al. 1999):

$$U_R = \sqrt{\left(\left[\frac{dR}{dX_1}\right] U_{X_1}\right)^2 + \left(\left[\frac{dR}{dX_2}\right] U_{X_2}\right)^2 + \cdots + \left(\left[\frac{dR}{dX_k}\right] U_{X_k}\right)^2} \tag{6.7}$$

6.7.1 Uncertainty in Temperature measurement:

In the air turbine test facility, T-type thermocouples have been installed to measure the air temperature at turbine inlet and exit. As mentioned before, these thermocouples were calibrated against standard RTD thermocouple with an accuracy of ±0.04^{o}C. The thermocouples calibration curves and related uncertainty are summarized in Table 6.1 while the detailed process of calculating the uncertainty is described in Appendix B.

Table 6-1 Calibration and uncertainty of thermocouples

Thermocouple	Location	Curve fit formula	Uncertainty (˚C)
Thermocouple-1	Inlet Cone	1.0037T - 0.423	±0.7544
Thermocouple-2	Stator inlet	1.0118×T-0.9277	±0.6899
Thermocouple-3	Between Stator and rotor	1.0124×T-0.8724	±0.7168
Thermocouple-4	Between Stator and rotor	1.0121×T-0.2993	±0.7204
Thermocouple-5	Rotor exit	1.01×T-0.3848	±0.6512
Thermocouple-6	Rotor exit	1.0105×T+0.2354	±0.7114

6.7.2 Uncertainty in Pressure measurement:

There are two 10 bar pressure transducers installed at turbine inlet through a pitot-static tube to measure total and static inlet pressure. A 6 bar pressure transducer was fitted at turbine exit to measure exit static pressure. Table 6-2 summarizes the pressure transducers calibration formulas and the related uncertainty.

Table 6-2 Summary of the calibration and uncertainty of pressure transducers

Transducer	Location	Curve fit formula	Uncertainty (Bar)
GE UNIK 5000-1	Pitot Total Pressure Port	6.323× volt-2.4985	±0.0411
GE UNIK 5000-2	Pitot Static Pressure Port	6.299× volt-2.4663	±0.0422
Druck PTX 1400	Rotor Exit	3.688× volt -1.4877	±0.0418

6.7.3 Uncertainty in power and efficiency:

Using the uncertainty analysis of thermocouples, pressure transducers and torque meter, the propagated uncertainty was calculated for both the power output and efficiency. Using all measured data the turbine efficiency was calculated as:

$$\eta_{ts} = \frac{T_{o1} - T_{o2}}{T_{o1}\left(1 - (P_r)^{\frac{\gamma-1}{\gamma}}\right)} \quad (6.8)$$

The output power was recorded directly from the torque meter data logger or can be calculated using turbine torque (τ) and rotational speed (ω) as:

$$Power\ output = \tau\omega \quad (6.9)$$

An excel sheet was used to estimate the uncertainty propagation in both efficiency and power output using overall uncertainty (equation 6.7) and the equations (6.8) and (6.9). Table 6-3 shows typical results of uncertainty analysis for the power and efficiency. As can be seen, the uncertainty in efficiency calculation is higher than the power output indicating that the turbine efficiency is more sensitive to the uncertainty in temperature and pressure measurements compared to the power output.

Table 6-3 Uncertainty propagation in efficiency and power output

	Turbine total to static efficiency				
point	Inlet temperature	Average temp.	Inlet pressure	Average press.	Uncertainty
1	25	24.46	1.2	1.21	0.5133
2	30	28.82	1.4	1.345	0.7001
3	35	34.12	1.6	1.613	0.7231
	Turbine output power				
1	25	24.46	1.2	1.21	0.0522
2	30	28.82	1.4	1.345	0.0447
3	35	34.12	1.6	1.613	0.0771

6.8 Test Procedure:

The test facility aims to determine the overall performance of the developed turbine in order to generate a detailed operational map of the turbine and to validate the design methodology. The axial air turbine was tested for a range of operating conditions (total inlet pressure, inlet

mass flow rate, and turbine inlet temperature). The compressed air was drawn from the storage tank through a pressure regulator to control the inlet pressure value. In order to increase the turbine inlet temperature, the air was heated using special heater tape to the required temperature. Then the air was expanded through the turbine and the air pressure and temperature at turbine inlet and exit were measured to determine the turbine performance.

The first set of experiments was carried out while maintaining turbine inlet temperature constant and varying the inlet total pressure and inlet mass flow rate. The second set of experiments was carried out by varying turbine inlet temperature at fixed inlet total pressure and inlet mass flow rate. These two sets allowed generating the turbine performance map for a range of operating conditions.

CHAPTER 7

TURBINE DESIGN RESULTS AND DISCUSSION

7.1 Introduction:

This chapter provides a detailed discussion of the small-scale axial air turbine design methodology results. A detailed parametric study has been presented in meanline modelling section for different turbine operating conditions. The detailed design results of selected turbine geometry have been presented in terms of meanline modelling, CFD simulation, design optimization, FEA modelling, and experimental validation results.

7.2 Meanline Modelling Results:

This section describes the results of the parametric study carried out to develop small scale axial air turbine using 1D meanline approach as described in chapter 4. This parametric study aims to investigate the axial turbine performance at different operating conditions and turbine design parameters in order to select the most efficient turbine geometry.

The turbine performance was determined using the developed 1D modelling code and the results were presented in terms of output power and efficiency of the turbine at different operating conditions and design parameters including total inlet pressure, temperature, rotational speed, mass flow rate, loading coefficient, flow factor, and the degree of reaction.

This parametric study is beneficial for the selection of operating conditions and design parameters which can achieve the best performance and initial design can be determined.

Figure 7.1 shows the output power of the small axial turbine at different pressure ratios and turbine inlet temperature (TIT). The turbine output power increases with the increase in both turbine inlet temperature and pressure ratio. However, the effect of the pressure ratio is more significant than the temperature. For example, increasing the pressure ratio from 2 to 3 at temperature 300K will increase the turbine output power from 0.8 to 1.7 kW while increasing the temperature from 300K to 340K at pressure ratio of 2 increases the turbine output power from 0.8kW to 1.25kW. The turbine efficiency increases with the increase in pressure ratio up to 2 and then it drops gradually as shown in Figure 7.2. The increase in turbine pressure ratio from 2 to 2.5 leads to an increase in turbine output power by 11% and drop in turbine efficiency by 4.4%. This reduction in turbine efficiency indicates to the effect of the effect of off design operation on turbine efficiency.

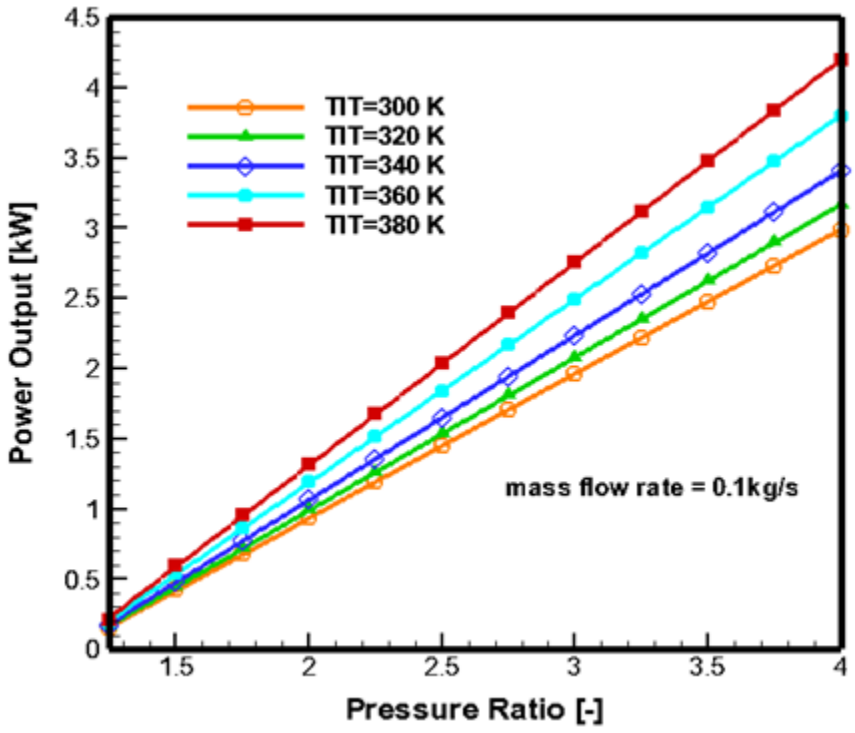

Figure 7.1 Turbine output power for different pressure ratio and TIT

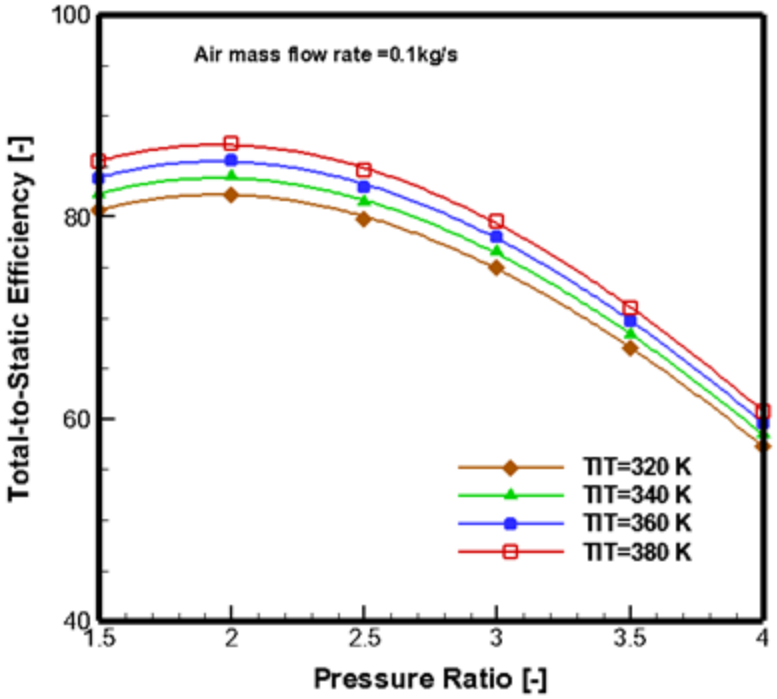

Figure 7.2 Turbine total-to-static efficiency for different pressure ratio and TIT

Figure 7.3 shows the effect of mass flow rate on the turbine power output using pressure ratio ranging from 1.5 to 4 and fixed rotational speed of 18,000 RPM. This can be related to Euler's turbomachinery equation (4.11) which defines the relationship between output power and turbine inlet mass flow rate. The variations of turbine total to static (η_{ts}) and total to total (η_{tt}) isentropic efficiencies with air mass flow rate are shown in Figures 7.4 and 7.5 respectively. The results show a significant increase in turbine efficiency with mass flow rate due to the increase in temperature drop through the turbine at the same pressure ratio. It can be seen as the mass flow rate increases, the power output increases significantly where at pressure ratio of 2, the power output increases from 0.6 to 1kW as the flow rate increases from 0.05 to 1kg/s. For low mass flow rate levels the effects of turbine size and rotational speed on turbine performance need to be considered for preliminary turbine sizing.

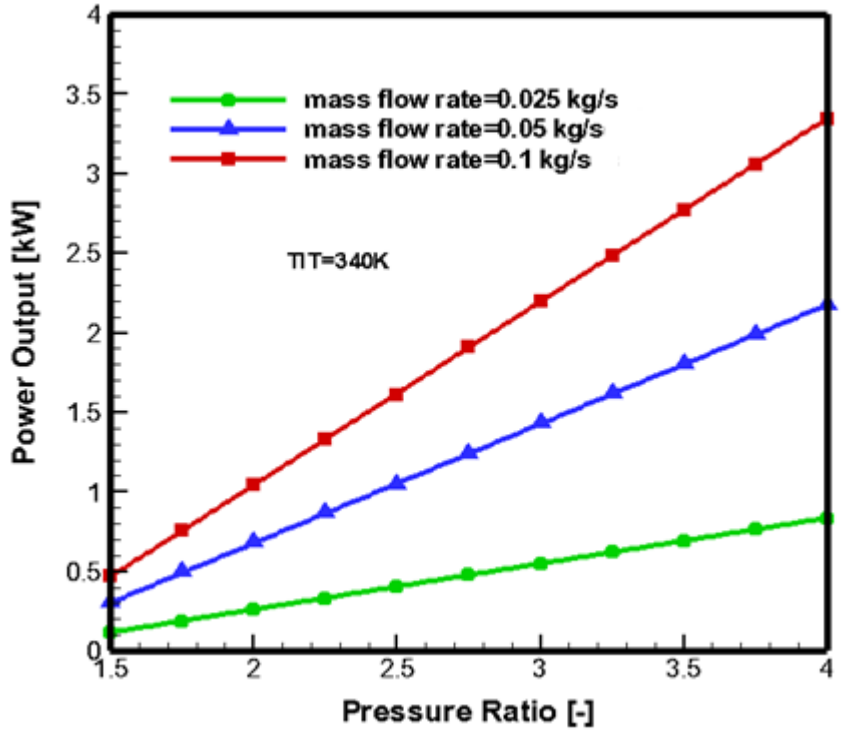

Figure 7.3 Turbine output power for different pressure ratio and mass flow rate

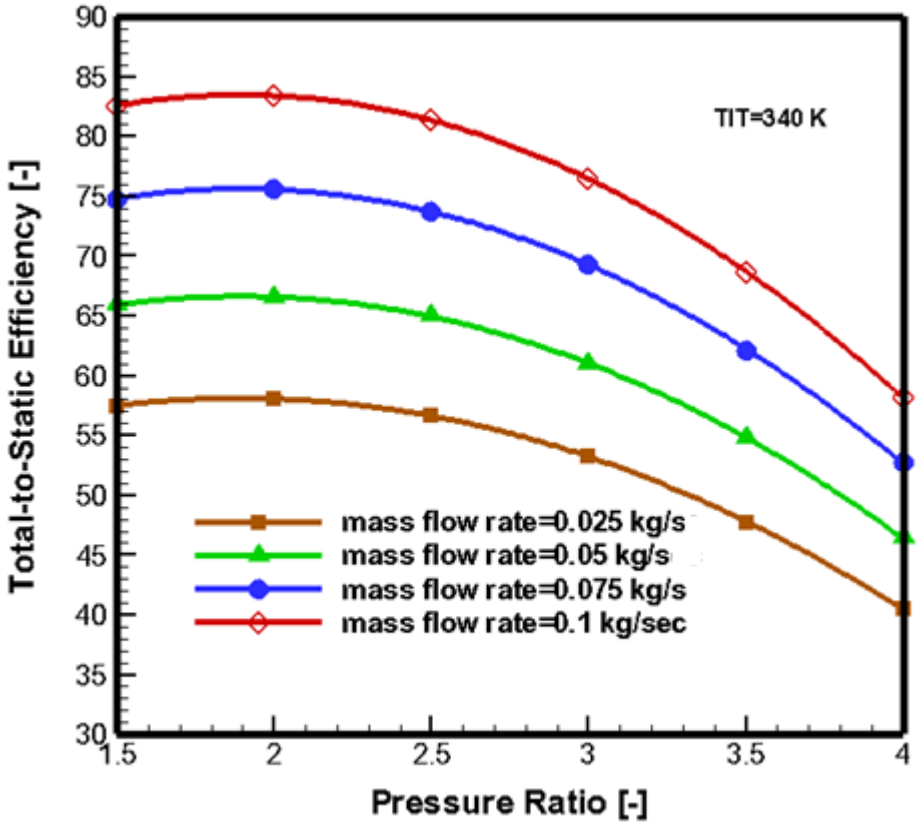

Figure 7.4 Turbine total-to-static efficiency at different Pressure ratio and mass flow rate

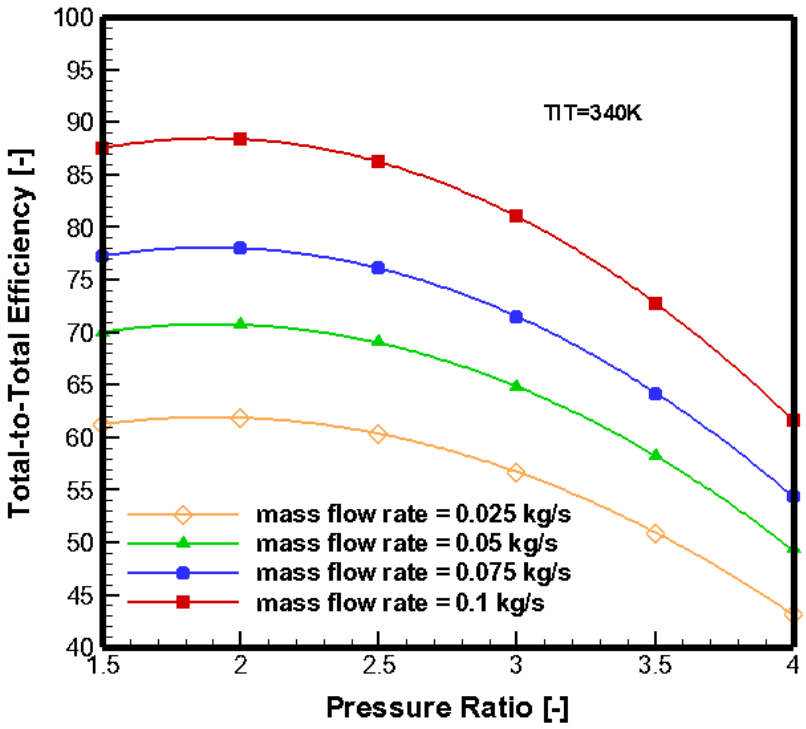

Figure 7.5 Turbine total-to-total efficiency for different Pressure ratio and mass flow rate.

The turbine output power and efficiency are also plotted at different rotational speeds (5,000-30,000 RPM) as shown in Figures 7.6 and 7.7 respectively for the pressure ratio of 2.0. The power increases as RPM increases due to the increase in blade speed (U) while the efficiency increases slowly to reach a maximum at rotational speed of 18,000 RPM then it starts decreasing gradually for all the turbine inlet temperature used. The impact of turbine size on the performance was studied by varying the hub to tip ratio. Figures 7.8 and 7.9 show the change in turbine output power and efficiency at various hub to tip ratio. The value of hub to tip ratio is usually selected based on designer's experience and the value of output power decreases with any increase in hub to tip ratio (decrease in turbine blade height). As can be seen higher power and efficiency can be achieved at low hub to tip ratio (higher blade height) and from the efficiency trend it is noticeable that as the turbine size decreases the efficiency drops indicating that the turbine experiences higher losses.

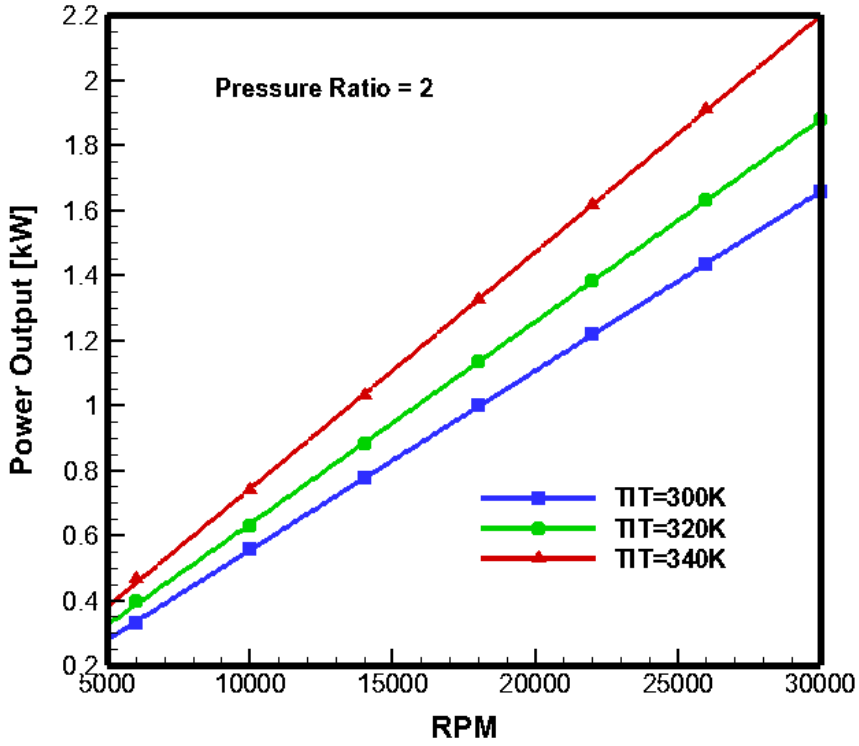

Figure 7.6 turbine output power for different RPM and TIT

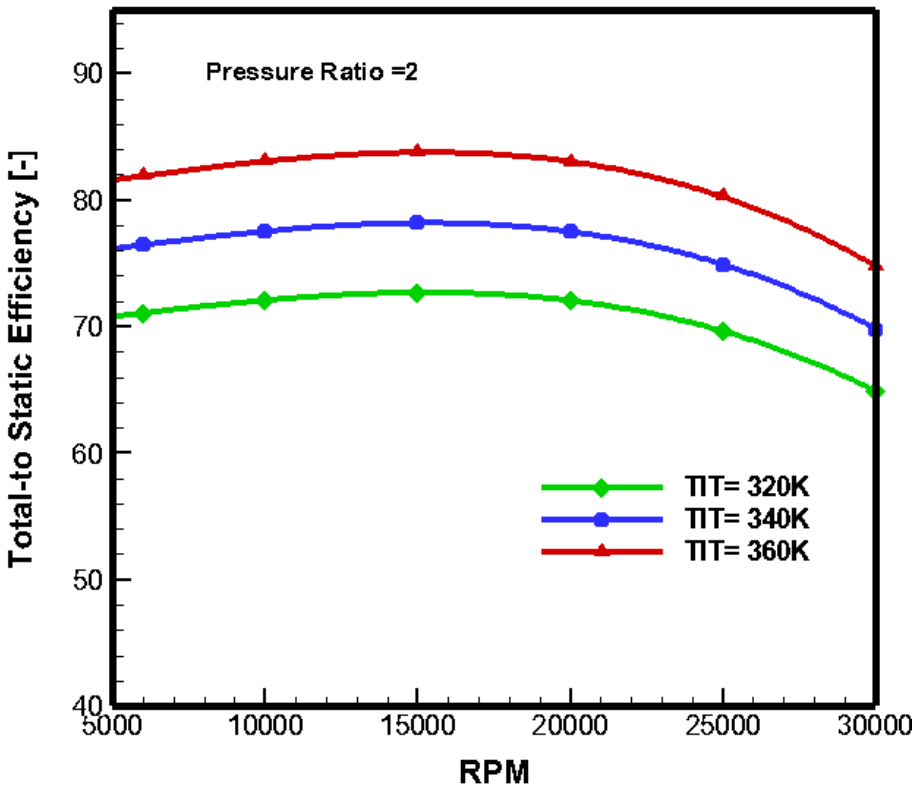

Figure 7.7 Turbine total-to-static efficiency for different RPM and TIT

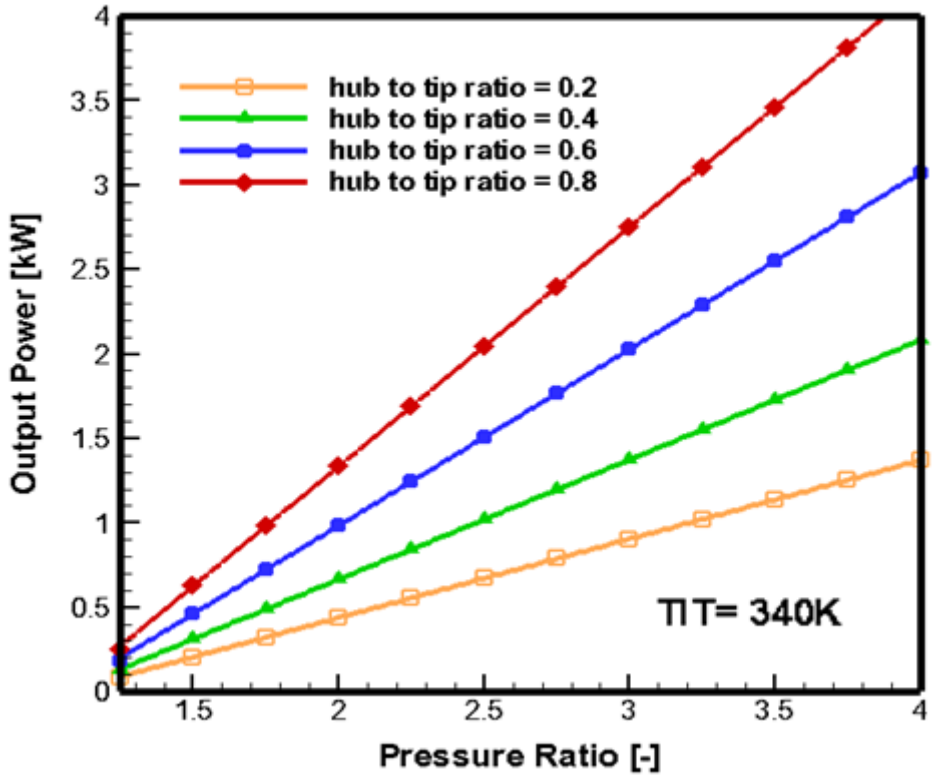

Figure 7.8 Turbine output power for different hub to tip ratio

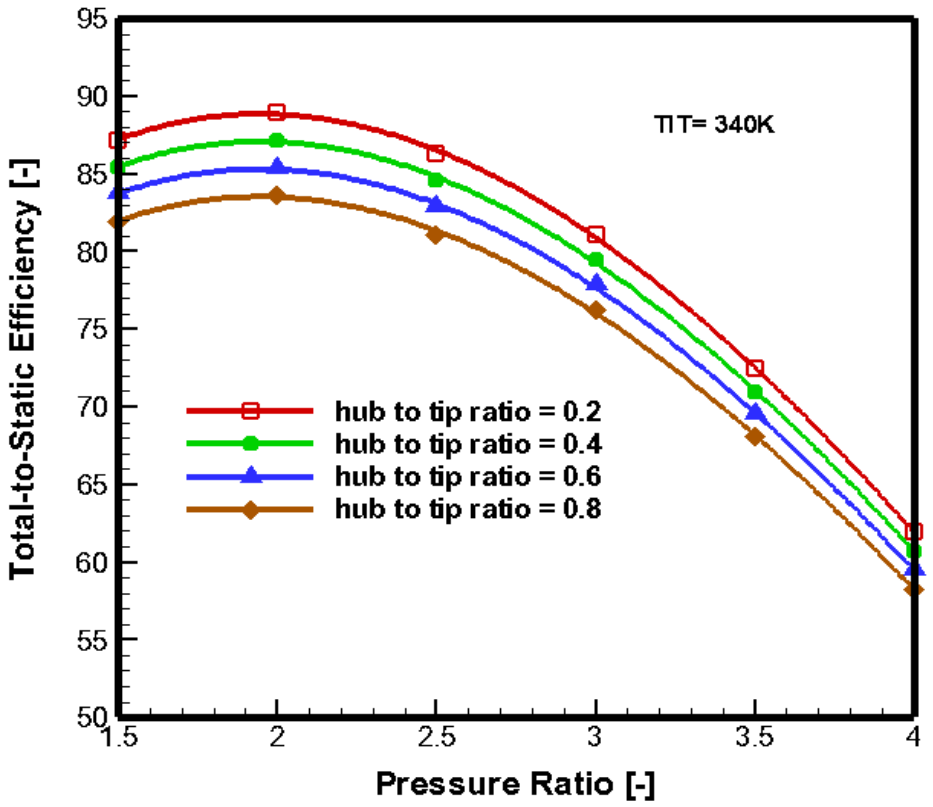

Figure 7.9 Turbine total-to-static efficiency for different hub to tip ratio

The parametric study was performed at different axial turbine design parameters including loading factor, flow coefficient and the degree of reaction to identify the impact of these parameters on turbine output and efficiency. These are the most crucial parameters in the determination of velocity triangles shape and axial turbine overall size. Figure 7.10 shows the variations in turbine output with the loading coefficient for different rotational speeds. For 18,000 RPM the increase in turbine loading coefficient (defined in equation 4.20) from 1 to 1.6 leads to increasing the turbine output power by 26% for the same turbine size. This result indicates that higher output power can be achieved using small axial turbine with higher loading coefficient values. Figures 7.11-13 show the change in turbine efficiency with variations in loading and flow coefficients for different degree of reaction (50%, 70% and 100%). As can be seen the turbine total to static efficiency increases with the increase in blade loading coefficient for all turbine degree of reaction values. However, the increase of flow coefficient (defined in equation 4.21) leads to a reduction in total to static efficiency where a noticeable drop can be noticed as a result of the increase in flow coefficient from 0.2 to 0.8 for a reaction ratio of 50% and loading coefficient of 1.2. This can be explained as increasing the flow coefficient increases the air exit speed (C_3) leading to reduction in enthalpy drop through the turbine stage.

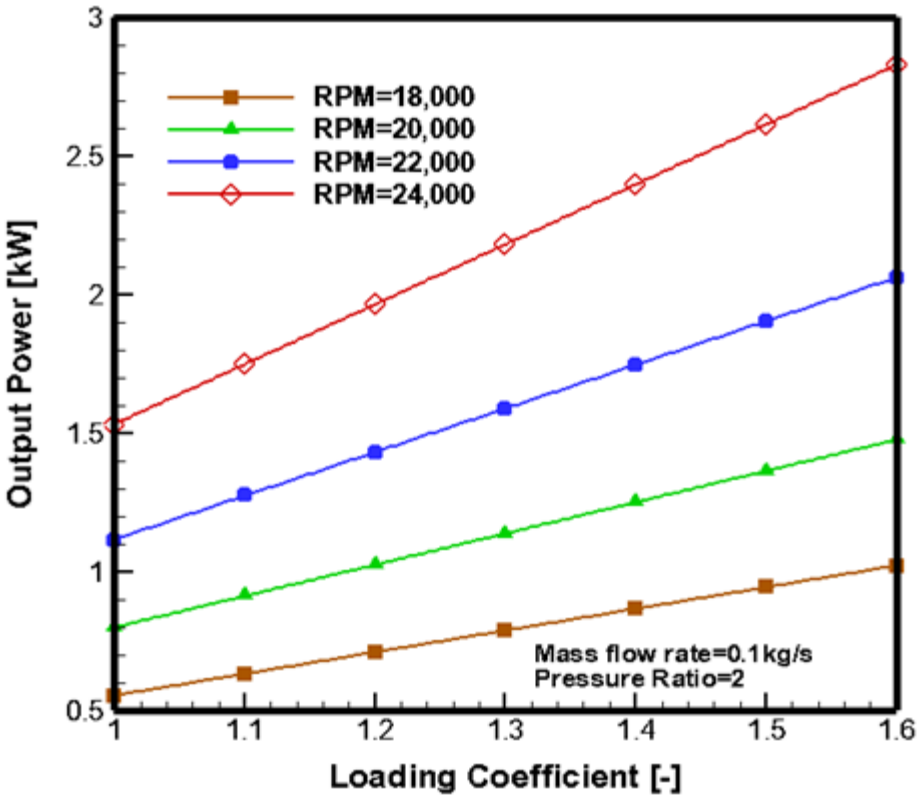

Figure 7.10 Turbine output power for different blade loading coefficient

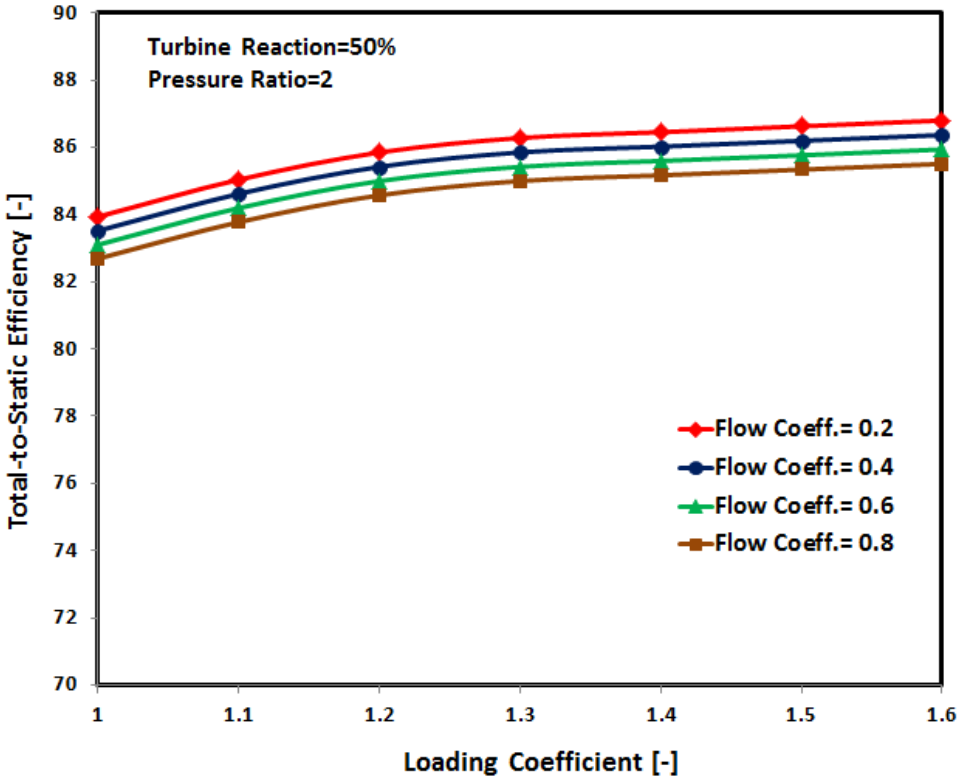

Figure 7.11 Turbine η_{ts} for blade loading coefficient (R=50%)

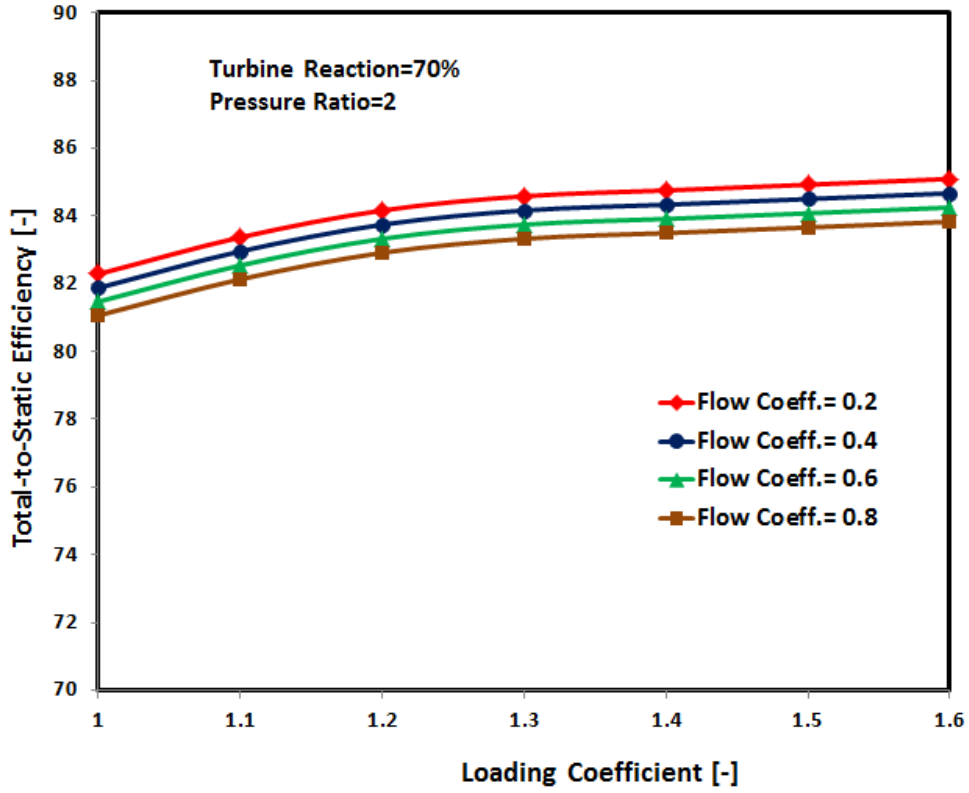

Figure 7.12 Turbine η_{ts} for different blade loading coefficient (R=70%)

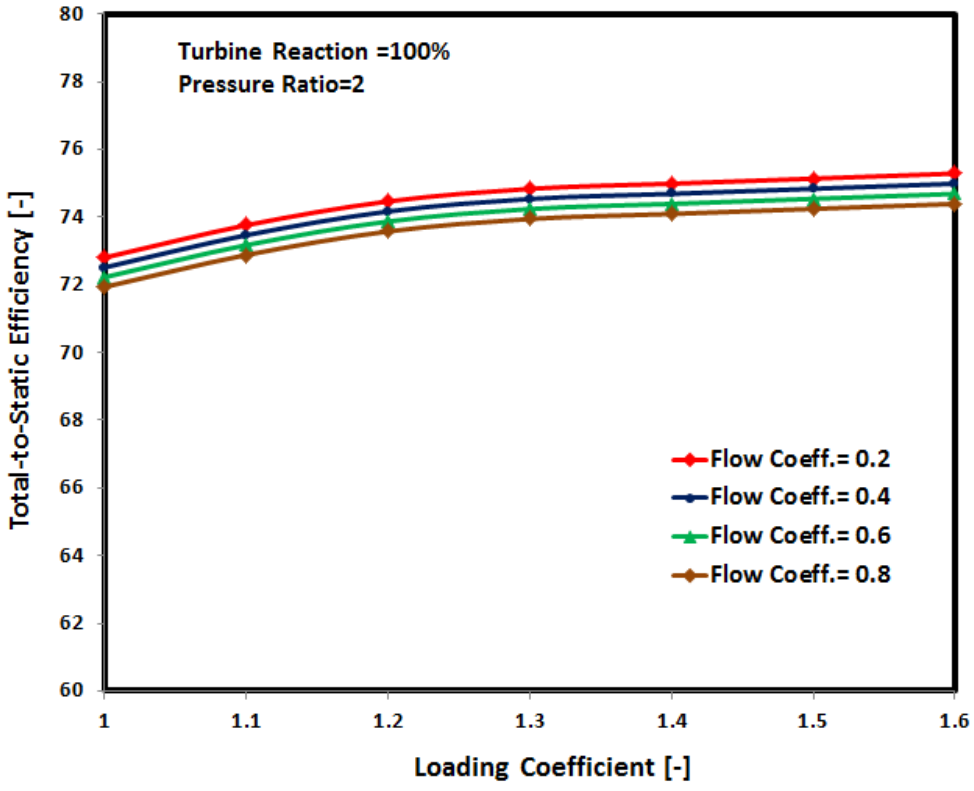

Figure 7.13 Turbine η_{ts} for different blade loading coefficient (R=100%)

The variations of total to static axial turbine efficiency for different blade to air speed ratio (U/C) for 50 and 70% reaction ratios are shown in Figure 7.14. These curves show that 70% reaction value can achieve higher efficiency levels for a wide range of blade to air speed ratios (off design conditions) compared to 50% reaction turbine.

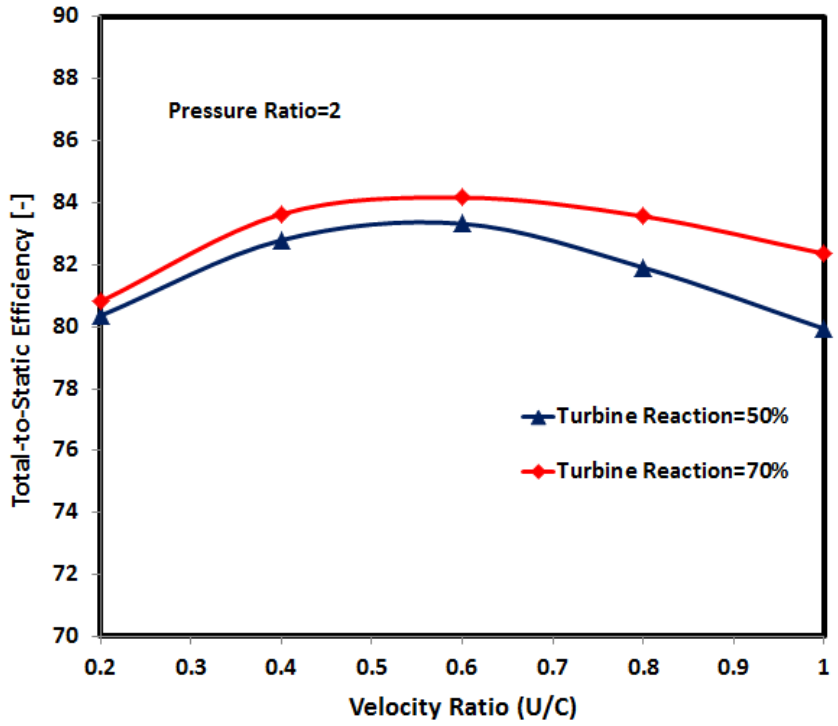

Figure 7.14 Turbine η_{ts} for different velocity ratio for R=50% and R=70%

Table 7-1 shows the detailed results of the preliminary design analysis based on selected design parameters and operating conditions that produces the best performance. The parametric study can be considered as an effective tool for examining the turbine design input parameters and identifying an initial design of the turbine. However, the selection of design parameters depends on designer experience and for more efficient turbine design CFD modelling integrated with an optimization approach is required to improve turbine design for maximum efficiency levels for both on and off design conditions.

Table 7-1 Turbine preliminary design modelling results

Selected Parameter	**Unit**	**value**
Total inlet pressure	kPa	200
Total inlet temperature	K	340
Exit static pressure	kPa	100
Mass flow rate	kg/s	0.1
Rotational Speed	RPM	20,000
Hub to tip ratio	-	0.75
Flow coefficient	-	0.6
Loading coefficient	-	1.2
Reaction	-	0.7
Stator number of blades	-	23
Rotor number of blades	-	22
Stator aspect ratio	-	0.5922
Rotor aspect ratio	-	0.9524
Stator chord	mm	13.32
Rotor chord	mm	10.45
Stator Solidity	-	1.6875
Rotor Solidity	-	1.5224
Stator inlet metal angle	degree	59.13
Stator outlet metal angle	degree	68.39
Rotor inlet metal angle	degree	53.32
Rotor outlet metal angle	degree	63.23
Stator stagger angle	degree	31.05

Rotor stager angle	degree	21.31
Stator Wedge angle	degree	23.11
Rotor Wedge angle	degree	19.07
Stator LE radius	mm	0.533
Rotor LE radius	mm	0.3477
Stator TE radius	mm	0.255
Rotor TE radius	mm	0.0544
Turbine Output power	kW	1.122
Total to Static Efficiency	-	83.26

7.3 CFD Simulation Results:

For more effective turbine blade aerodynamic design, comprehensive CFD simulation has been carried out using the preliminary turbine geometry which was generated by the 1D Meanline modelling. ANSYS CFX 16.2 was used for CFD simulation where 3D axial turbine blade profile was generated in BladeGen model and the results of CFD simulation are presented in terms of velocity vectors, Mach number contours, and blade loading at 50% of blade span. Figure 7.15 shows the velocity vectors through the axial turbine stage showing that there are significant secondary flows and flow separation on the rotor blade pressure suction side near trailing edge region. The velocity streams in 3D rotor blades are shown in Figure 7.16 illustrating the detailed flow characteristic like flow circulation and tip leakage flow. As a result, the rotor blade profile needs to be improved in terms of blade thickness distribution and modifying flow turning angle. As can be observed from Figure 7.16 the flow leakage starts from the leading edge and mix with the main flow leading to vortex formation on the blade suction side. These results indicate the impacts of blade geometry on loss developments and turbine overall performance. The CFD simulation of the developed turbine

shows that the flow leakage increases with the increase of tip clearance value leading to drop in turbine efficiency by 2.4% and 4.12% for 0.5mm and 1mm clearance values compared with zero tip case due to significant pressure loss development due to leakage flow.

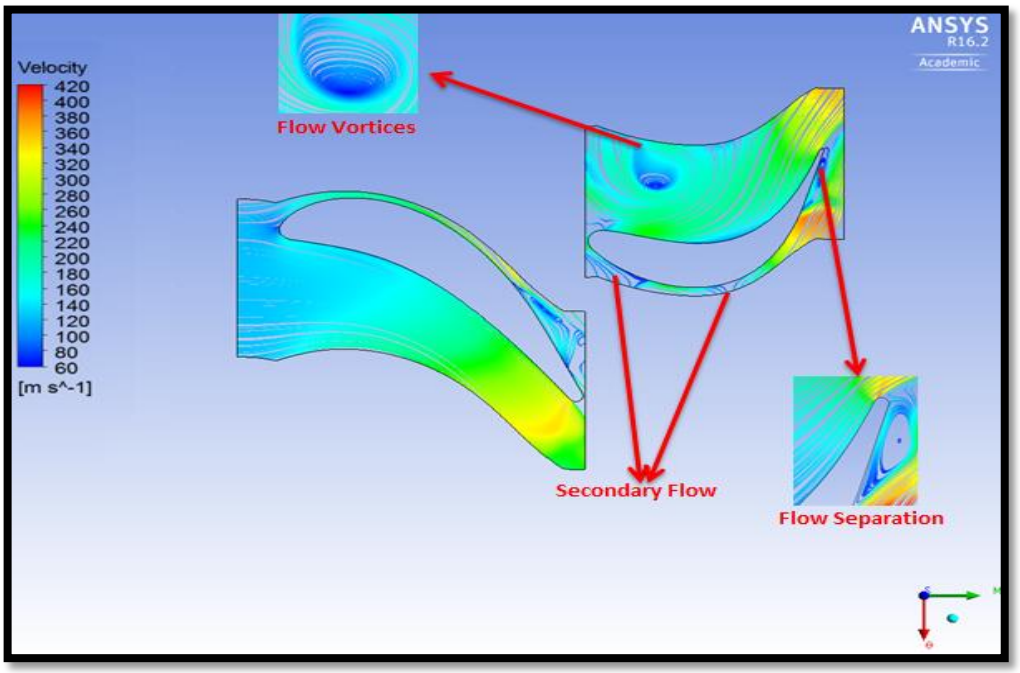

Figure 7.15 Velocity vectors through axial air turbine stage

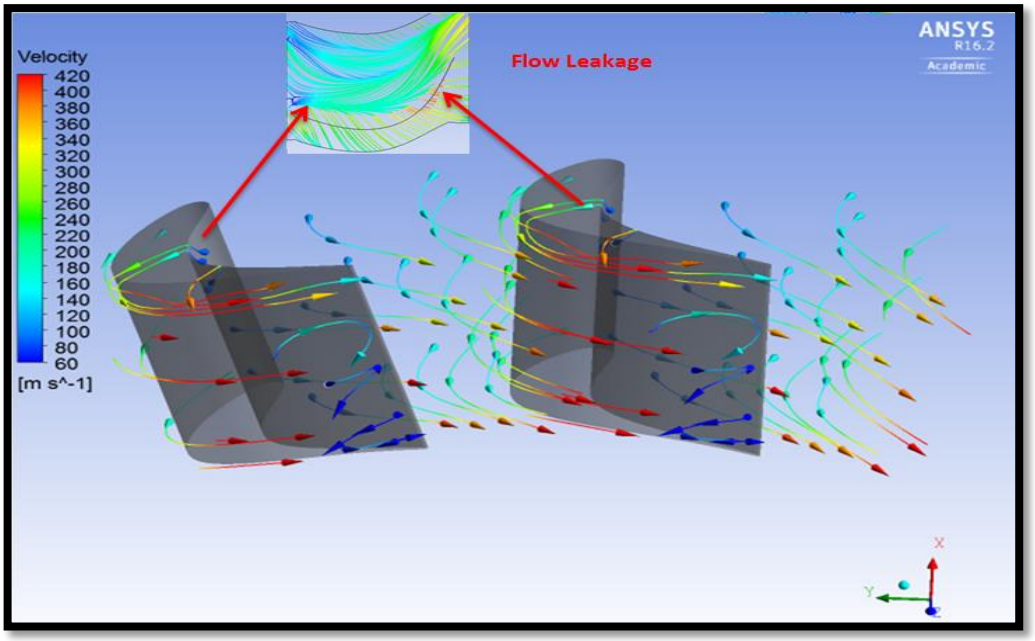

Figure 7.16 Velocity streams through rotor blades

Figure 7.17 shows the Mach number distribution along the axial turbine stage which indicates that the turbine is working in the sonic region and the maximum Mach number values were at the suction surface near to the stator and rotor throat. Figures 7.18 and 7.19 show the CFD predicted turbine blade loading for both stator and rotor blades. The area bounded by the pressure lines represents the amount of work produced by turbine shaft. On the pressure side of the rotor there is uniform distribution of the flow pressure along the blade chord. However, the flow pressure on the suction side of the blade decreases sharply near the throat area and starts to increase as a result of adverse pressure gradient in the trailing edge region due to boundary layer separation. This reduction in flow pressure leads to flow acceleration and as a result flow vortices are generated which increases the aerodynamic losses. From the blade loading and velocity distribution, the initial blade design can be improved by modifying the blade thickness distribution and the flow turning angle. This can be achieved by 2D blade to blade visualization which allows identifying secondary flow regions.

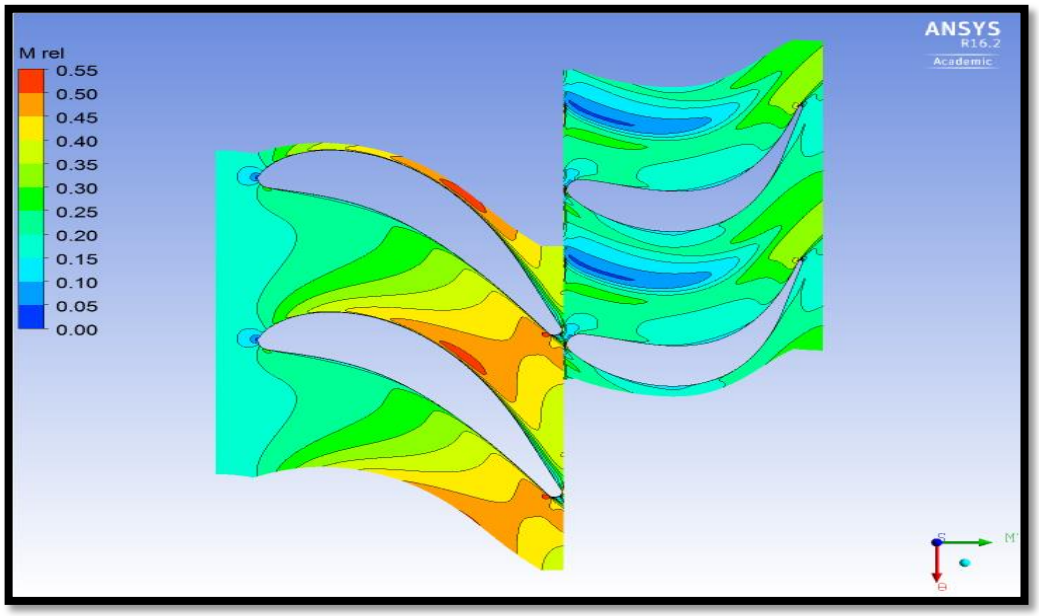

Figure 7.17 Mach number contours through turbine stage

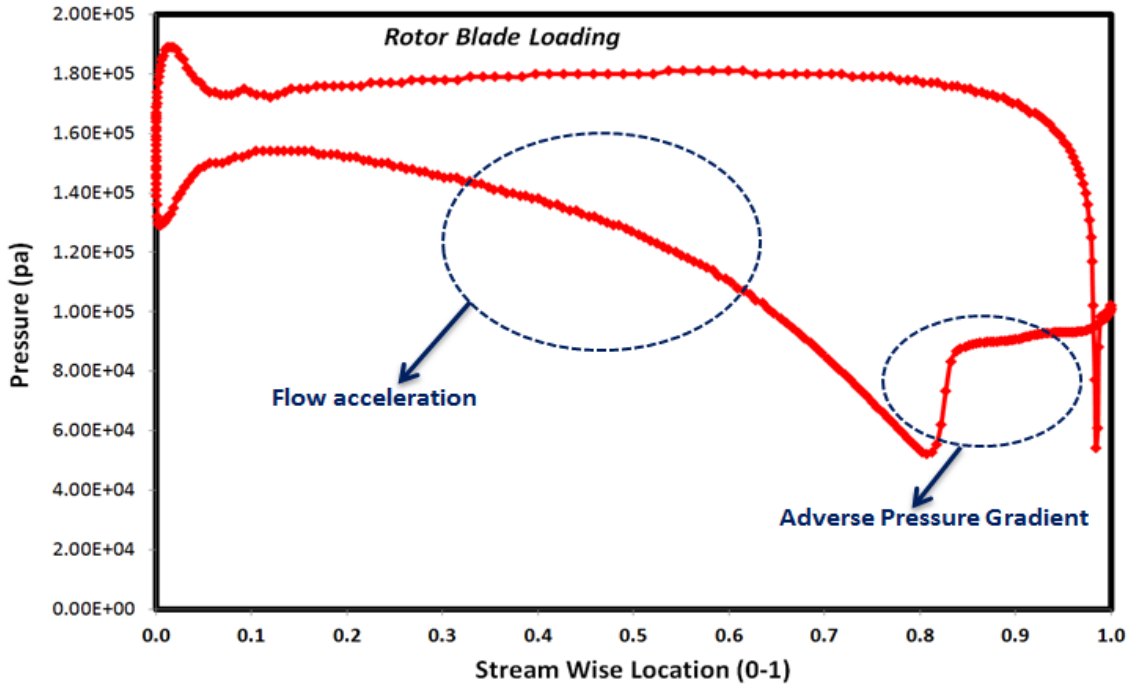

Figure 7.18 Turbine rotor blade loading at mid-span

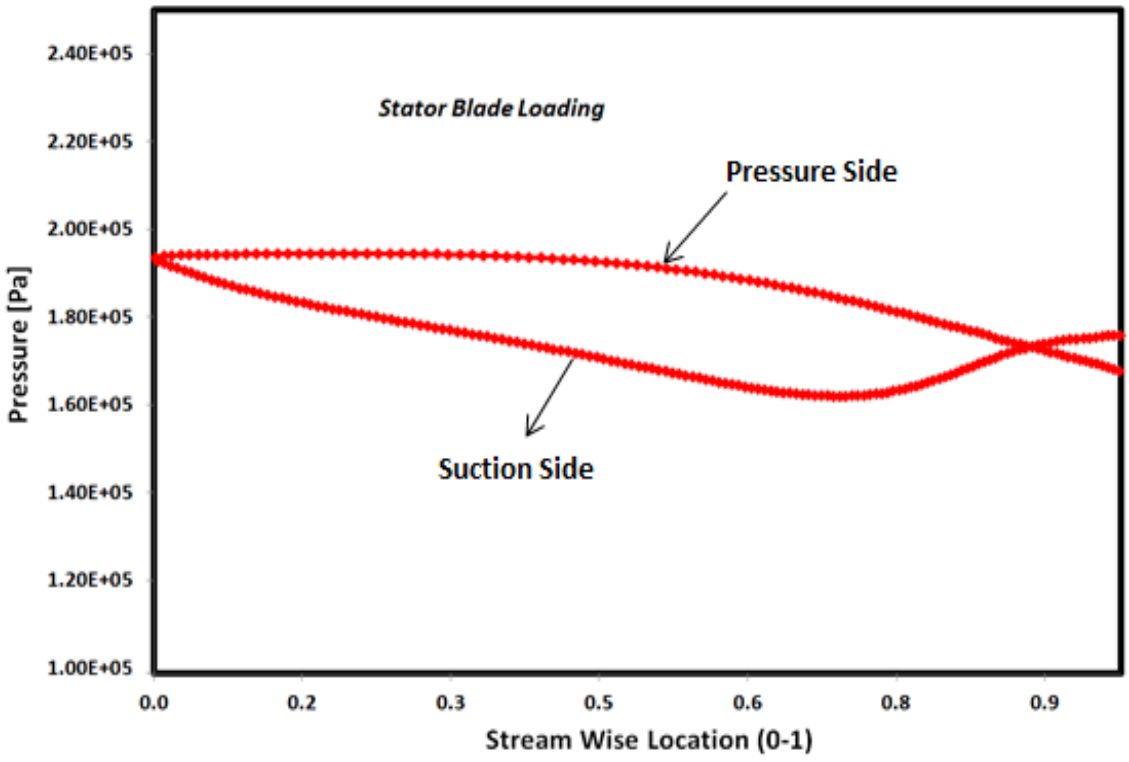

Figure 7.19 Turbine stator blade loading at mid-span

A detailed comparison between 1D meanline modelling and 3D CFD simulations is provided in Table 7.2. To improve the turbine blade aerodynamic performance as the flow moves from the stator to the rotor blades, the blade profile was modified to reduce secondary flow regions and flow separation at the leading and trailing edges. The modification was carried out by varying the thickness distribution of rotor profiles through adjusting Bezier curve control points as shown in Figure 7.20.

Table 7-2 Comparison of 1D modelling and CFD simulation of developed turbine

Parameter	**1DMeanline Results**	**CFD Simulation Results**
To1(K)	340	340
Po1(kpa)	200	200
P_{exit} (kpa)	100	104.63
α_2(degree)	59.13	55.08
β_2(degree)	68.39	67.68
α_3(degree)	53.32	52.08
β_3(degree)	63.23	61.12
C_2(m/sec)	134.19	143.22
C_3(m/sec)	66.99	69.47
W_2(m/sec)	58.24	63.14
W_3(m/sec)	198.56	204.06
C_x(m/sec)	80.63	82.47
$\dot{m_{air}}$ (kg/sec)	0.1122	0.109
Power output(kW)	1.122	0.98705
Total to static efficiency	83.26	78.06

Figure 7.21 shows the velocity vectors and the formation of flow vortex due to variations in blade thickness distribution indicating the significant impact of turbine blade profile on flow characteristics and turbine overall performance. For the blade profile with the best thickness distribution (profile B), the impact of number of blades on flow behaviour was investigated as shown in Figure 7.22.

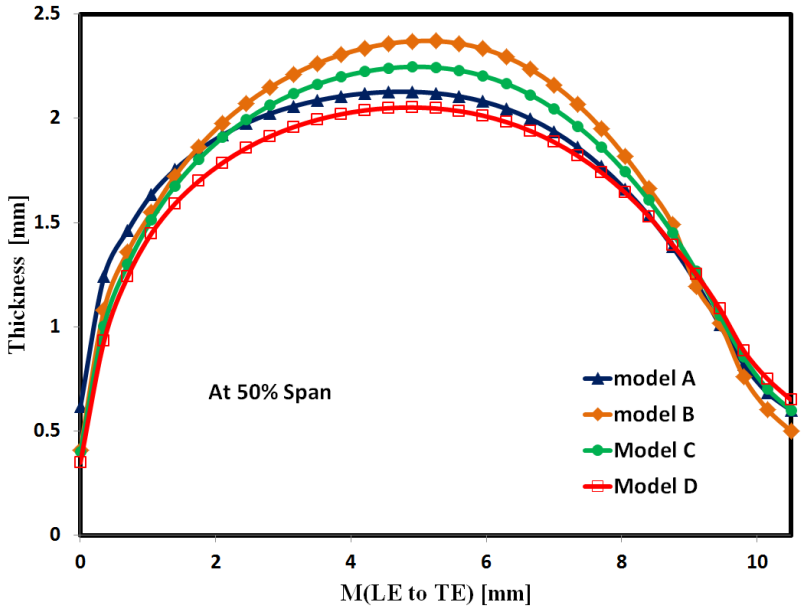

Figure 7.20 Blade thickness distribution for different leading and trailing edges geometry

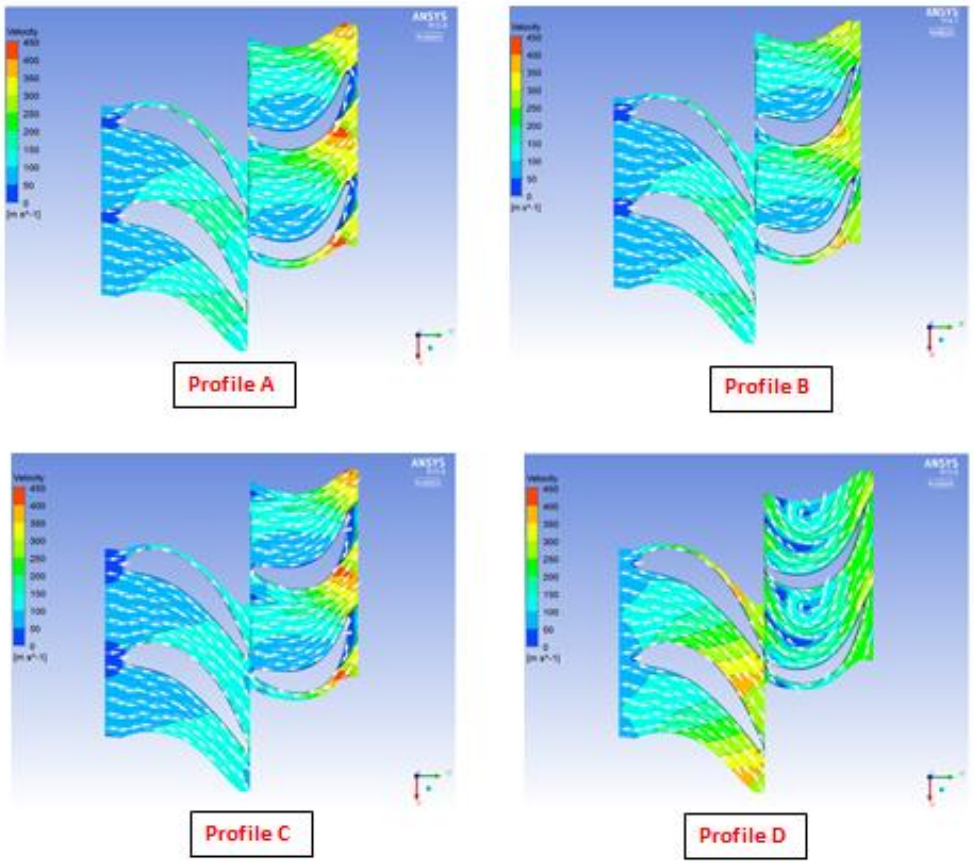

Figure 7.21 Velocity vectors for different blade thickness distributions

The number of blades was estimated using Zweifel's correlation (equation4.50) but for more precise estimation this number needs to be investigated using CFD simulation in order to decrease the boundary layer effect and achieve good flow guidance with less secondary flow formation. The best flow characteristics and the maximum turbine efficiency of 77.42% was achieved at number of blades of 20 indicating that there is an optimum blade number value for maximum turbine performance.

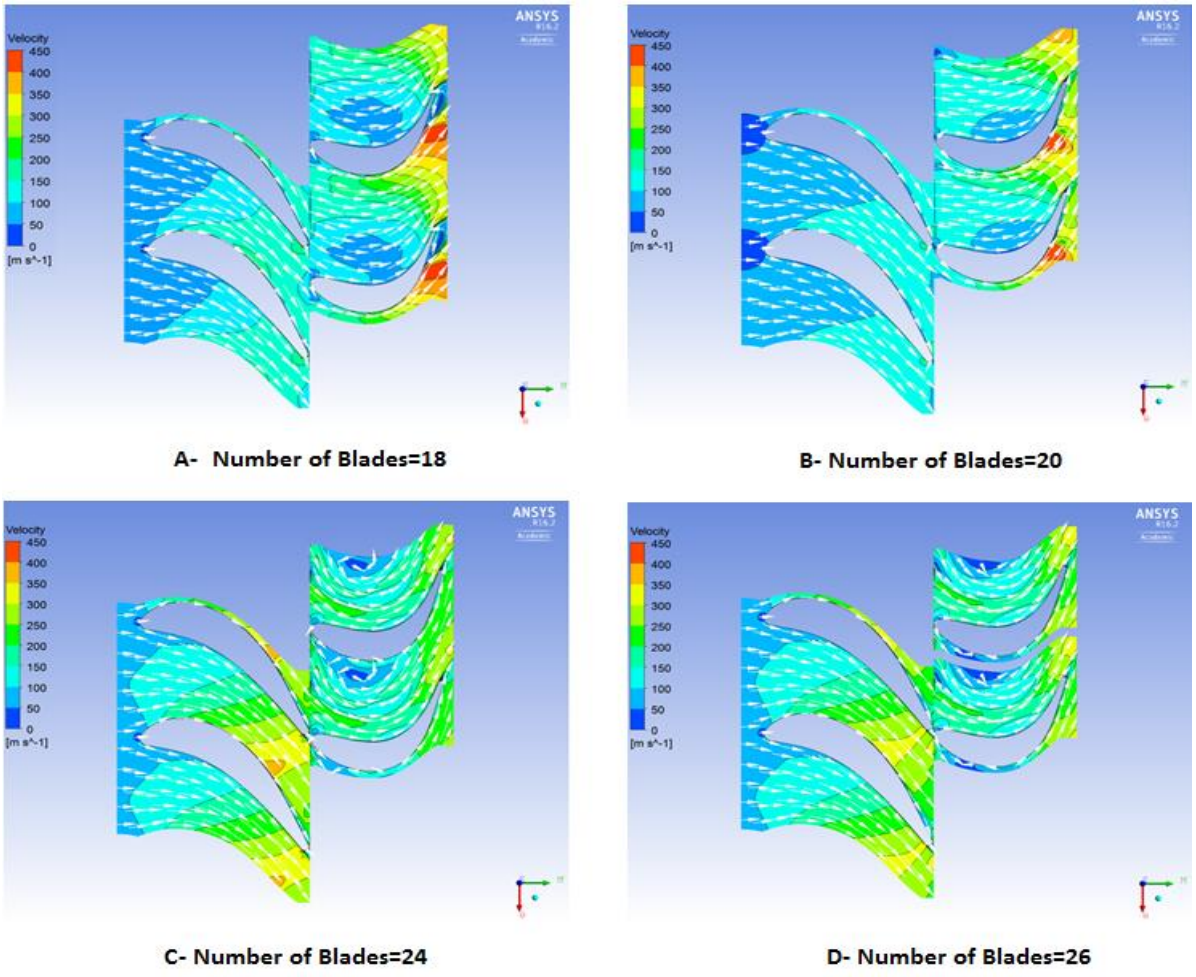

Figure 7.22 Velocity vectors for different number of blades

A comprehensive steady state CFD simulation using ANSYS CFX was carried out for different operating conditions to predict the performance characteristics of the developed axial

air turbine with improved blade profile B. Figure 7.23 shows the turbine isentropic total to static efficiency at different pressure ratios where the maximum turbine efficiency of 77.78% was achieved at pressure ratio of 1.75 which is close to the design point pressure ratio of 2. These results show also that the turbine efficiency at off design conditions above and below the design point decreases as can be observed at pressure ratio of 2.25 which can be explained by turbine chocking near to this pressure ratio value. The turbine output power is shown in Figure 7.24 for different pressure ratio and speeds of 18,000, 20,000 and 22,000. It can be observed that the design power value of 1kW can be obtained at 2 pressure ratio at the design rotational speed of 20,000 RPM.

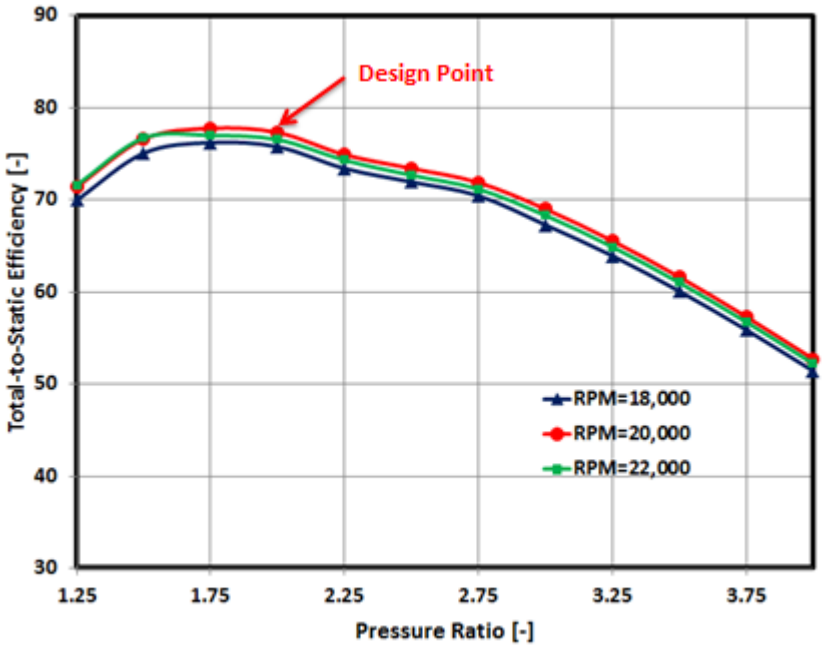

Figure 7.23 CFD results of turbine efficiency for different RPM

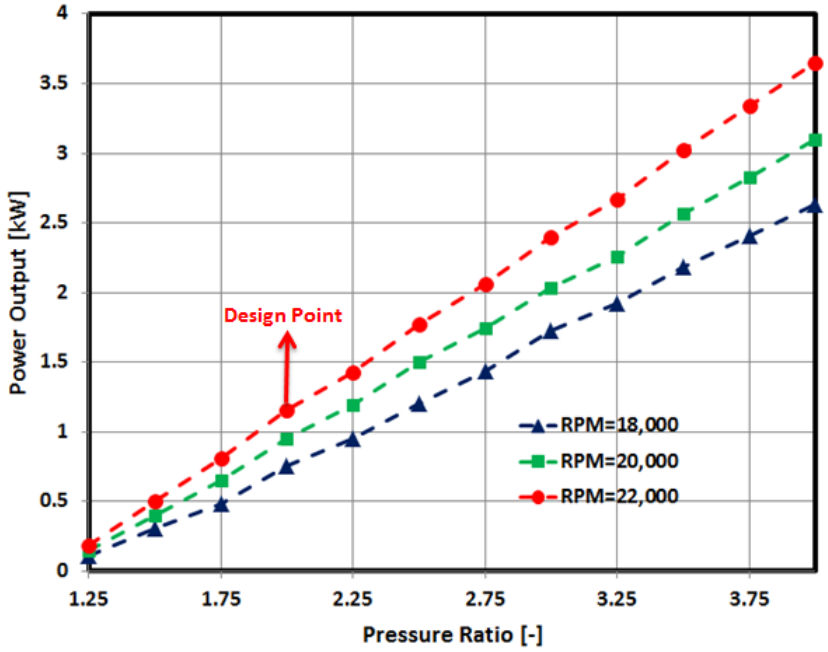

Figure 7.24 CFD results of turbine output power for different RPM

The results of 3D CFD simulation of the modified small axial air turbine was compared with the 1D meanline design code in terms of turbine total to static efficiency, power output, and mass flow rate for different pressure ratio. As shown in Figure 7.25, there is a noticeable difference between the efficiency values of the meanline modelling and CFD simulation. This difference can be attributed to the empirical correlations used for losses prediction in the meanline modelling which under estimated the losses. However, the comparisons of output power and mass flow rate variations with the pressure ratio show very good agreement between the 1D meanline modelling and CFD simulation results as shown in Figures 7.26 and 7.27 for the power and mass flow rate respectively.

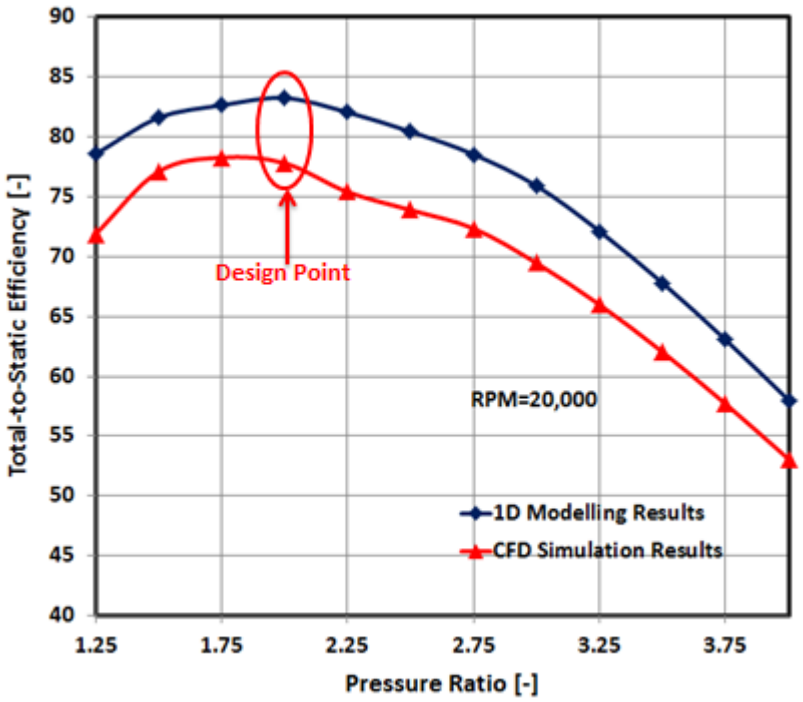

Figure 7.25 Turbine total to static efficiency based on 1D modelling and CFD simulation

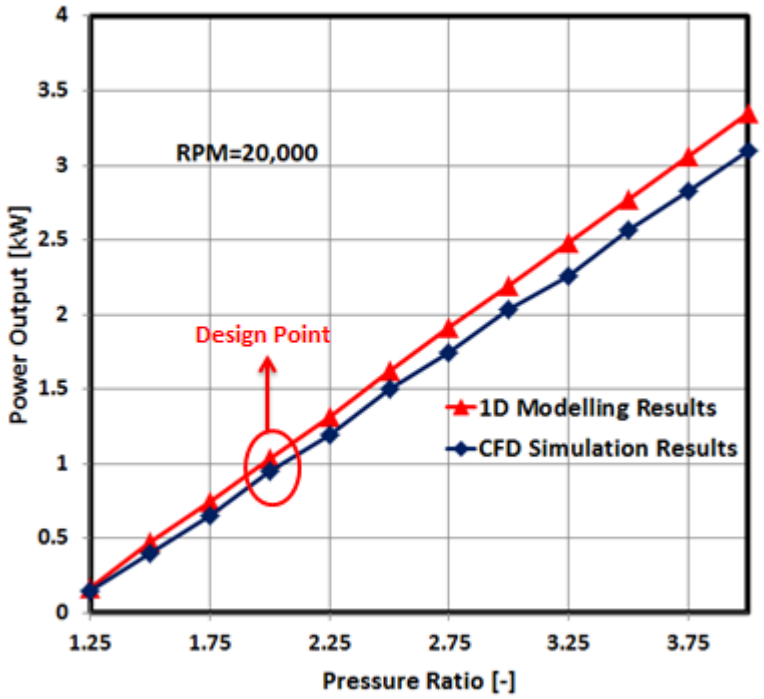

Figure 7.26 Turbine output power based on 1D modelling and CFD simulation

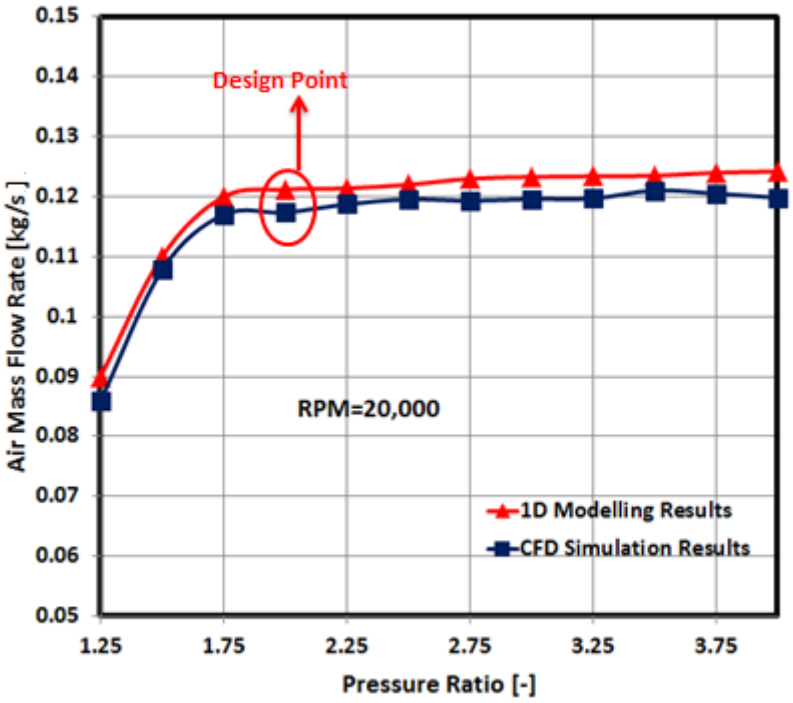

Figure 7.27 Turbine mass flow rate based on 1D modelling and CFD simulation

7.4 Performance Prediction based on CFD Modelling:

The difference between 1D Meanline modelling and CFD simulation results indicated that the turbine efficiency is sensitive to loss prediction correlations which have been developed for large gas turbines. This section presents the results of total pressure losses in small axial turbine using ANSYS CFX 16.2 and published correlations to identify the most accurate correlation to predict losses in small axial turbines. The comparison between the losses prediction results using conventional correlations and CFD simulation is provided for both stator and rotor blades. The total pressure losses for the turbine rotor are shown in Figure 7.28 and 7.29 for different turbine pressure ratios (1.25-3.5) and different RPMs (5,000-30,000). The results of losses prediction using ANSYS CFX were compared to the losses prediction using Ainely, Came & Dunham, and Kacker& Okapuu loss models. This comparison shows that there is a good agreement between the Kacker & Okapuu loss model and the CFD results especially near to the design point (Pr=2, RPM=20000) while the correlations of Ainely and

Came & Dunham produced lower values of losses. This can be explained as that the Kacker & Okapuu correlation has taken into account the effect of Mach number, Reynolds number and shock waves which have significant effect in small scale turbines. However, the difference between Kacker & Okapuu correlation and the CFD modelling increases at off design operating conditions indicating the importance of using CFD simulation to predict turbine performance at off design operating conditions.

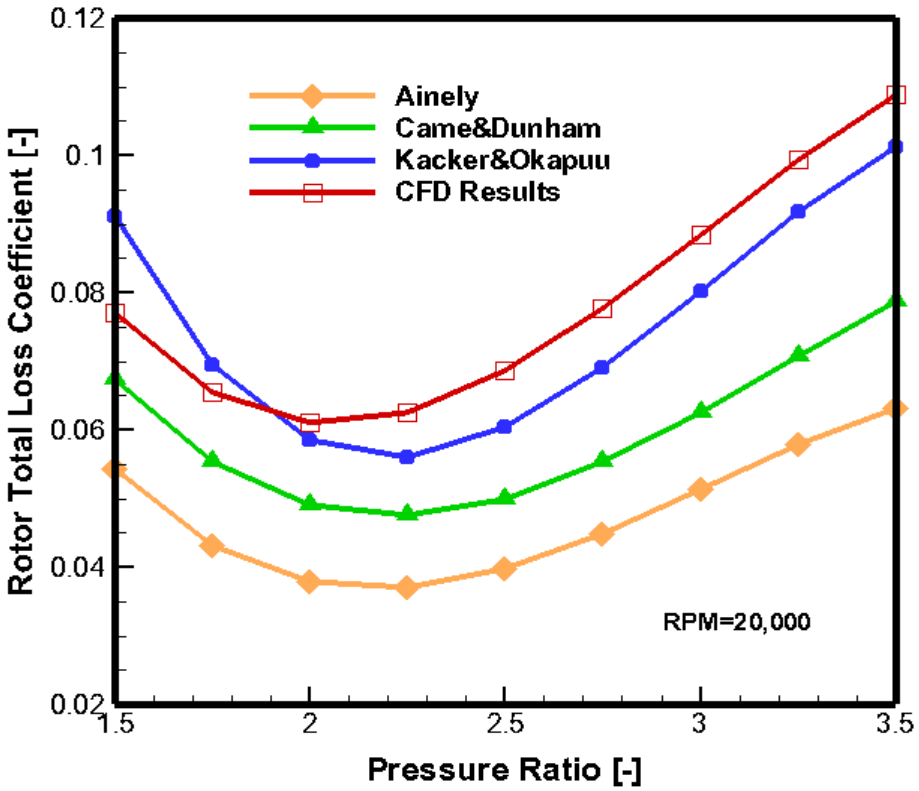

Figure 7.28 Rotor total loss coefficient for different pressure ratio

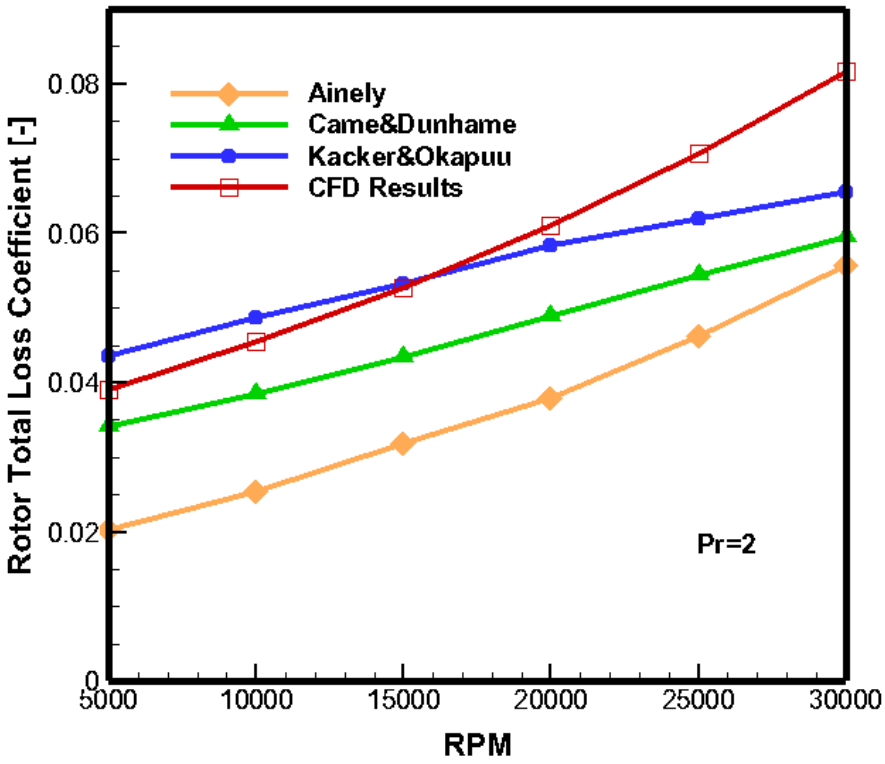

Figure 7.29 Rotor total loss coefficient for different RPM

The total pressure losses for the turbine stator are shown in Figures 7.30 and 7.31 for different turbine pressure ratios (1.25-3.5) and different RPMs (5,000-30,000). The results of loss prediction for stator blades shows similar trend as the rotor loss but the values of loss coefficients in stator were very low compared to those of the rotor. The high loss factors in rotor blades can be explained by the rotational effect on boundary layer development as well as the tip clearance flow leakage.

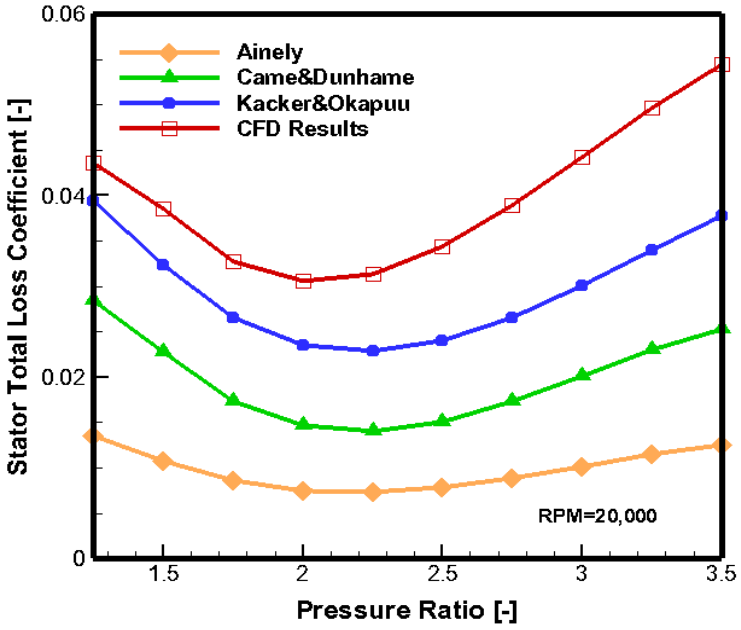

Figure 7.30 Stator total loss coefficient for different pressure ratio

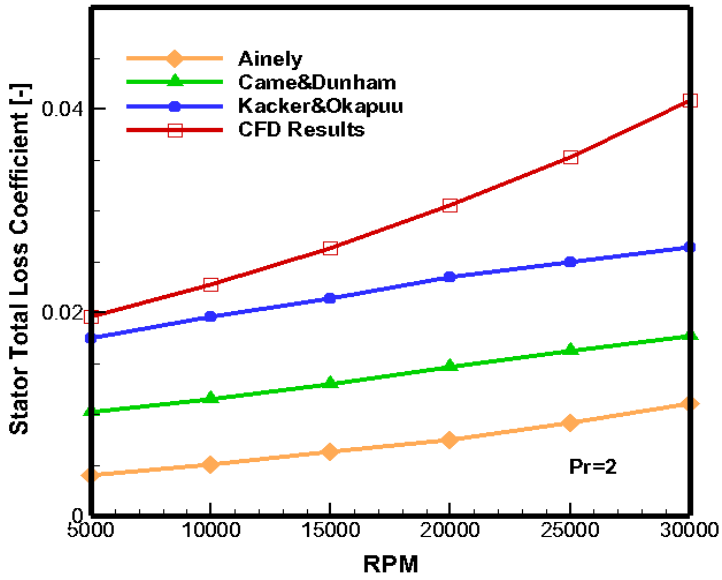

Figure 7.31 Stator total loss coefficient for different RPM

Table 7-3 compares the loss and total to static turbine efficiency with different prediction schemes for the design point. The difference in results can prove that the conventional loss prediction models are not appropriate for small scale turbines and for the preliminary design phase the Kacker and Okapuu scheme is recommended. Then the design can be improved using CFD modelling. The losses are related to the flow characteristics, pressure gradient and

boundary layer development through turbine passage. The effect of blade geometrical parameters on loss generation was studied to improve the aerodynamic performance of the blade profile and to define the parameters upper and lower limits needed for the optimization process.

Table 7-3 Losses prediction at design point

	Ainely&Mathieson Loss Model		**Came&Dunham Loss Model**		**Kacker&Okapuu Loss Model**		**Loss Prediction using CFD**	
(Y_{total})	**Stator**	**Rotor**	**Stator**	**Rotor**	**Stator**	**Rotor**	**Stator**	**Rotor**
	0.00750	0.03791	0.01461	0.04898	0.02351	0.05845	0.03054	0.06108
(η_{ts})	87.47		84.92		80.00		77.32	

The influence of the incidence angle (i) on the rotor loss factor was investigated using ANSYS CFX turbine simulation for both positive (0 to $+15^o$) and negative (0 to -15^o) incidence angles as shown in Figure 7.32. The results show that the minimum loss value was achieved at zero incidence and the loss increased with any incidence angle change from zero in both positive and negative directions. The incidence is affected by leading edge geometry which is defined by two main parameters namely leading edge (L.E) radius and wedge angle. As a result the loss was studied for different leading edge geometries. Figure 7.33 shows the variations of rotor total loss coefficient with leading edge radius for different L.E shapes (circular and elliptical) and the general variation trend indicates that there is an optimum value of L.E radius that can achieve minimum loss. Compared to circular leading edge shape the elliptical configuration has lower loss coefficients. For the L.E radius of 0.5 mm the loss can be reduced by 7.28% using elliptical shape. The loss variations with L.E wedge angle are shown in Figure 7.34 and the minimum total loss coefficient of 0.0614 was achieved at 18^o wedge angle.

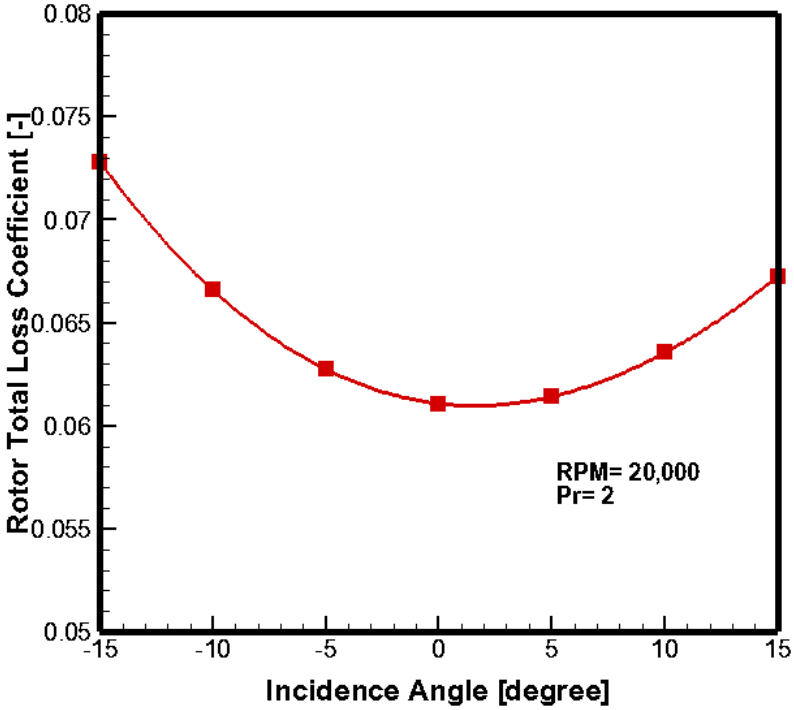

Figure 7.32 Rotor total loss coefficient vs. incidence angle

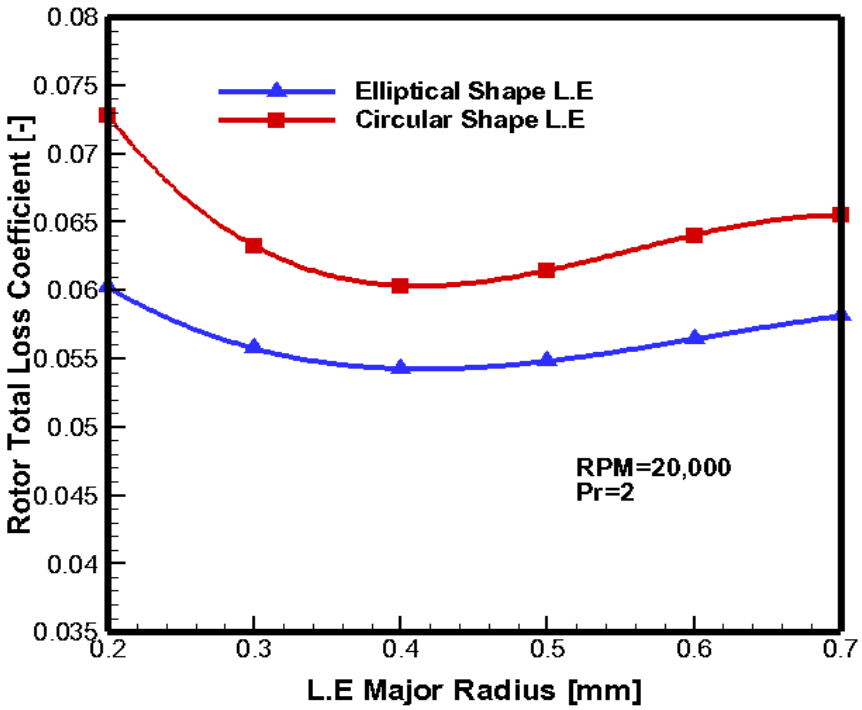

Figure 7.33 Rotor total loss coefficient vs. leading edge radius

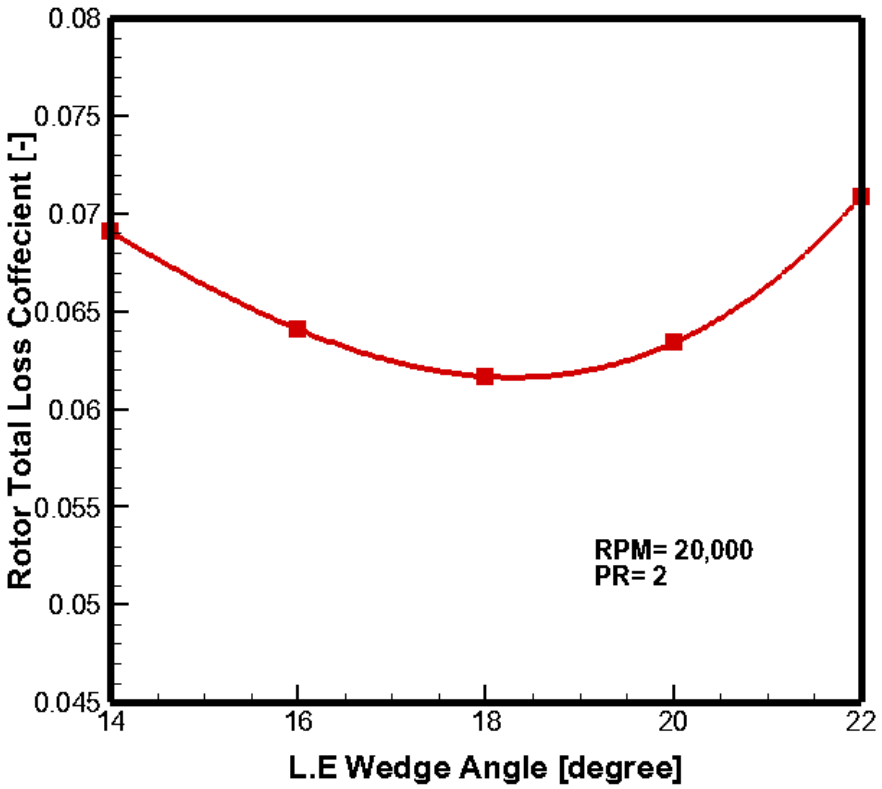

Figure 7.34 Rotor total loss coefficient vs. leading edge wedge angle

The estimation of losses based on CFD modelling was also conducted for other turbine blade geometrical parameters like stagger angle, number of blades, and axial spacing between stator and rotor. Figure 7.35 shows the rotor total loss for different stagger angle and the results indicate the significant effect of blade stagger angle on flow behaviour and the minimum pressure loss coefficient value of 0.06011 was obtained at 23.46^{o}. Figure 7.36 shows the rotor total loss factor variation with the trailing edge thickness. It can be seen that the loss increases with increasing the trailing edge thickness and this can conflict with the stress and manufacturing requirements.

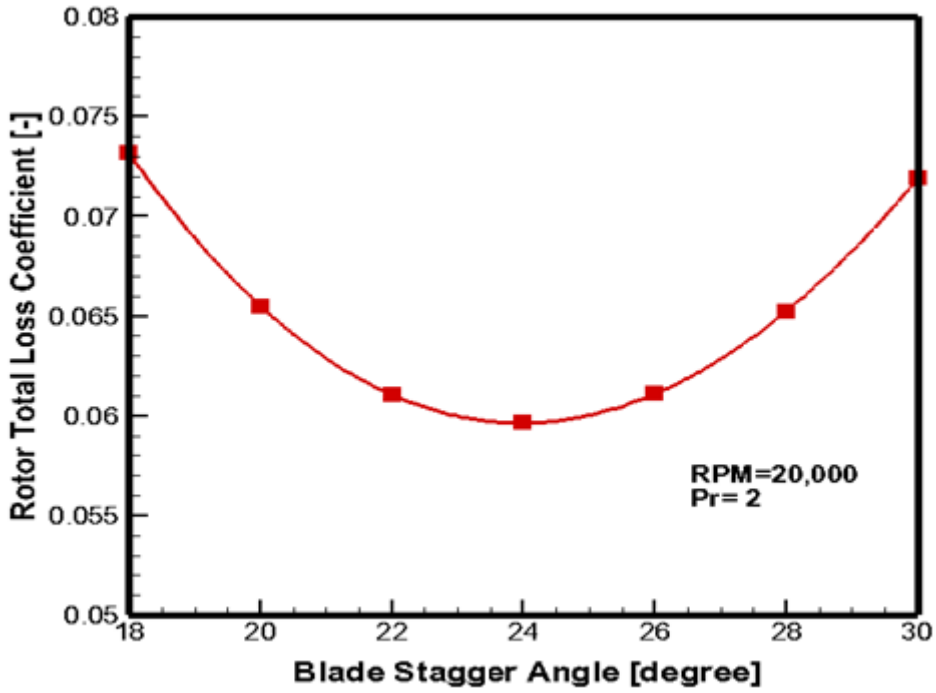

Figure 7.35 Rotor total loss coefficient vs. Stagger angle

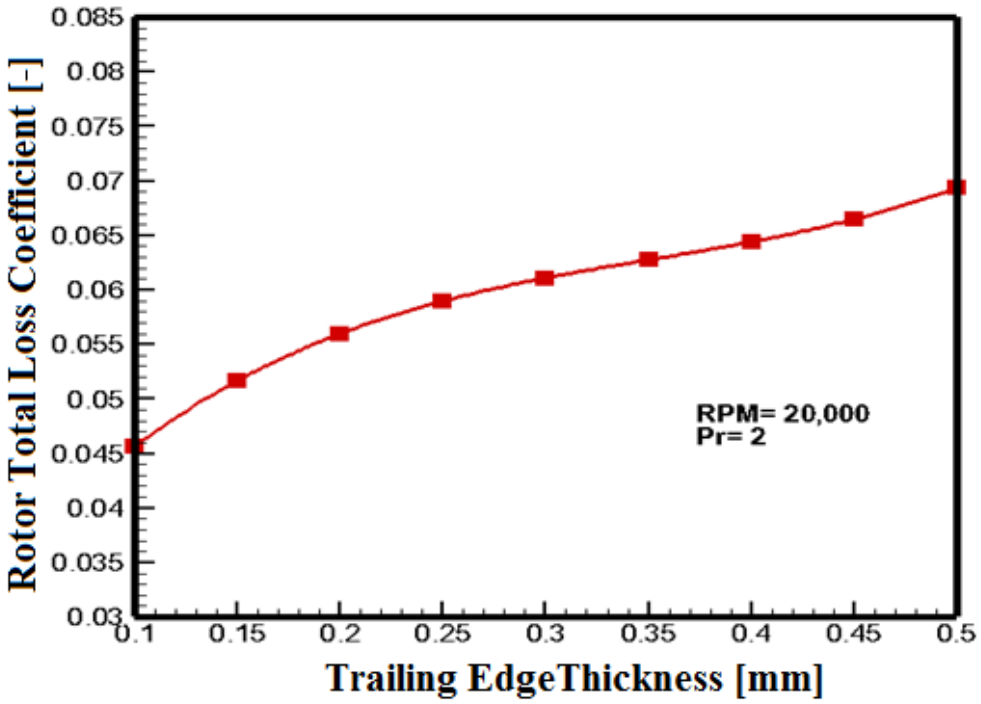

Figure 7.36 Rotor total loss coefficient vs. trailing edge thickness

Also the rotor loss factor is influenced by the number of blades as can be seen in Figure 7.37 where the total loss coefficient varies significantly with the number of blades as a result of the considerable change in boundary layer thickness through the turbine passage. The increase in number of rotor blades from 18 to 22 leads to an increase in total pressure loss by 6.35% indicating the importance of this parameter on turbine overall performance.

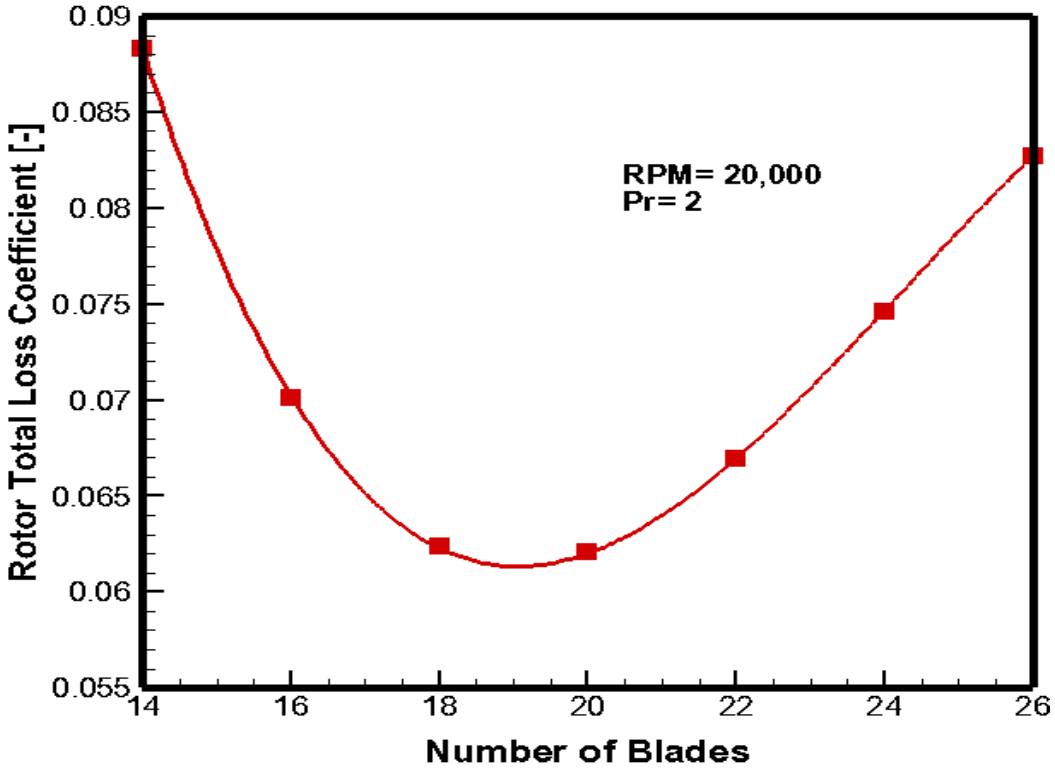

Figure 7.37 Rotor total loss coefficient vs. number of blades

Unlike radial turbine there is no correlation to estimate the axial spacing between stator and rotor blades in axial turbine. In large gas turbines, the axial gap between stator and rotor is around 20-30% of the axial chord length to avoid the interaction effect. Figure 7.38 shows the CFD predicted total pressure loss for the turbine rotor at various axial spacing. The rotor total loss coefficient decreases by increasing the axial gap up to a value of 4.5mm axial gap where the minimum loss amount occur. This gap represents around 35% of the stator axial chord slightly higher than the gap typically used in large turbines.

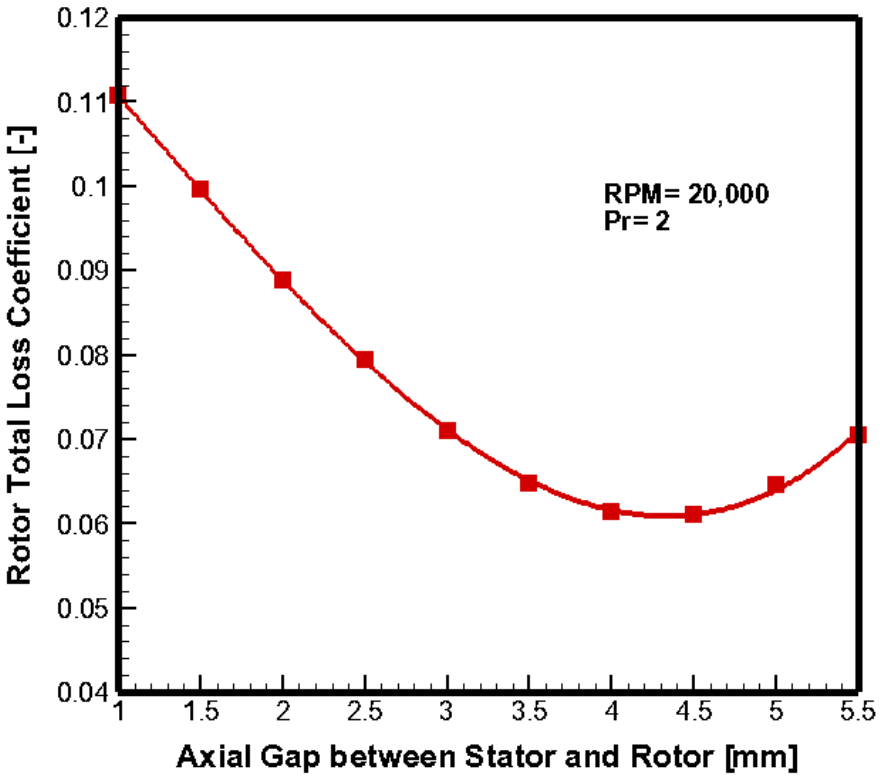

Figure 7.38 Rotor total loss coefficient for different axial spacing.

The total losses were predicted for both the stator and rotor and presented in terms of dimensionless parameters (pitch to chord ratio and exit Mach number) as shown in Figures 7.39 and 7.40. These results show that the variations in the total losses are more significant in the rotor compared to the stator and the initial design pitch to chord ratio of 0.9 has high loss values and the more realistic range is 0.2-0.7. These results can be used for more accurate loss estimation in small axial turbines at the preliminary design phase.

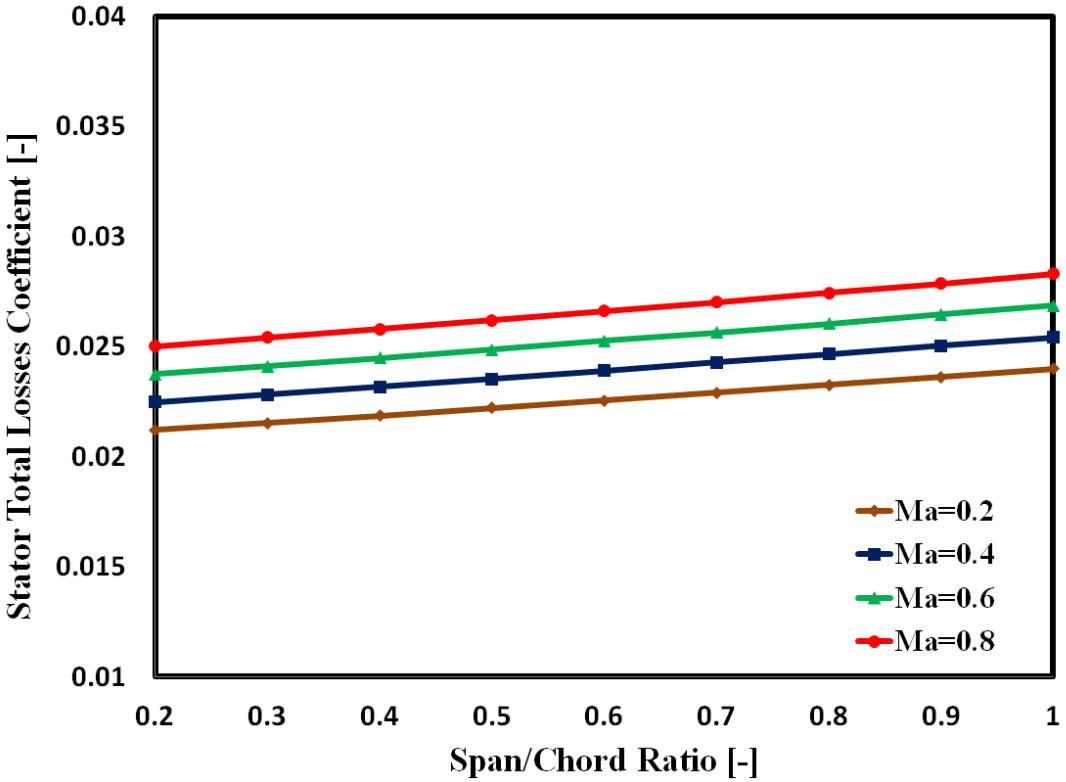

Figure 7.39 Turbine stator total loss for different aspect ratio

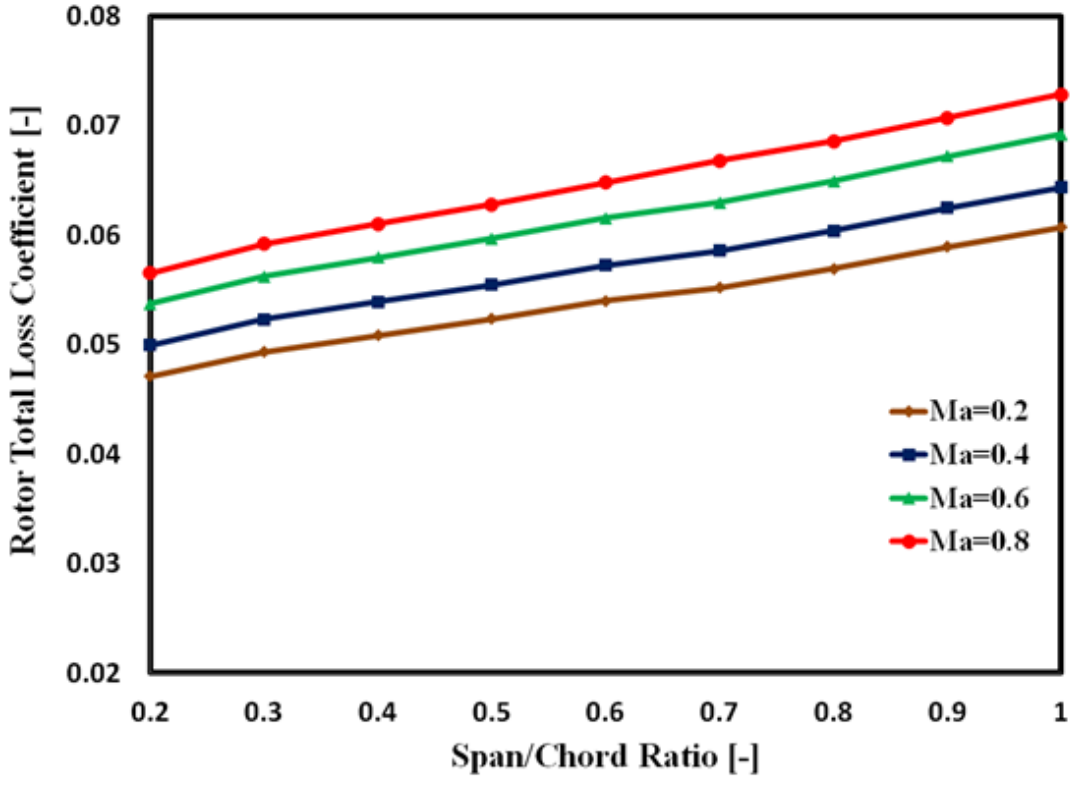

Figure 7.40 Turbine rotor total loss for different aspect ratio

7.5 Turbine Aerodynamic Design Optimization:

It is clear from the results of the CFD parametric study and loss prediction that the performance of axial turbine is affected significantly by the aerodynamic characteristics of the turbine blade profile. The variations of each blade geometry parameter lead to considerable change in the total pressure losses through the turbine stage and there is an optimum value for each parameter that achieves minimum losses. These parameters need to be optimized simultaneously to achieve the optimum blade profile with highest turbine efficiency while delivering the required power. In order to develop an efficient aerodynamic turbine design and achieve reliable prediction of the complex flow features through turbine passage, 3D CFD modelling coupled with an optimization technique is an efficient method for higher turbine performance. In this research, the aerodynamic blade profile optimization was performed using the multi objective genetic algorithm (MOGA) technique for on and off design conditions as shown in Figure 7.41.

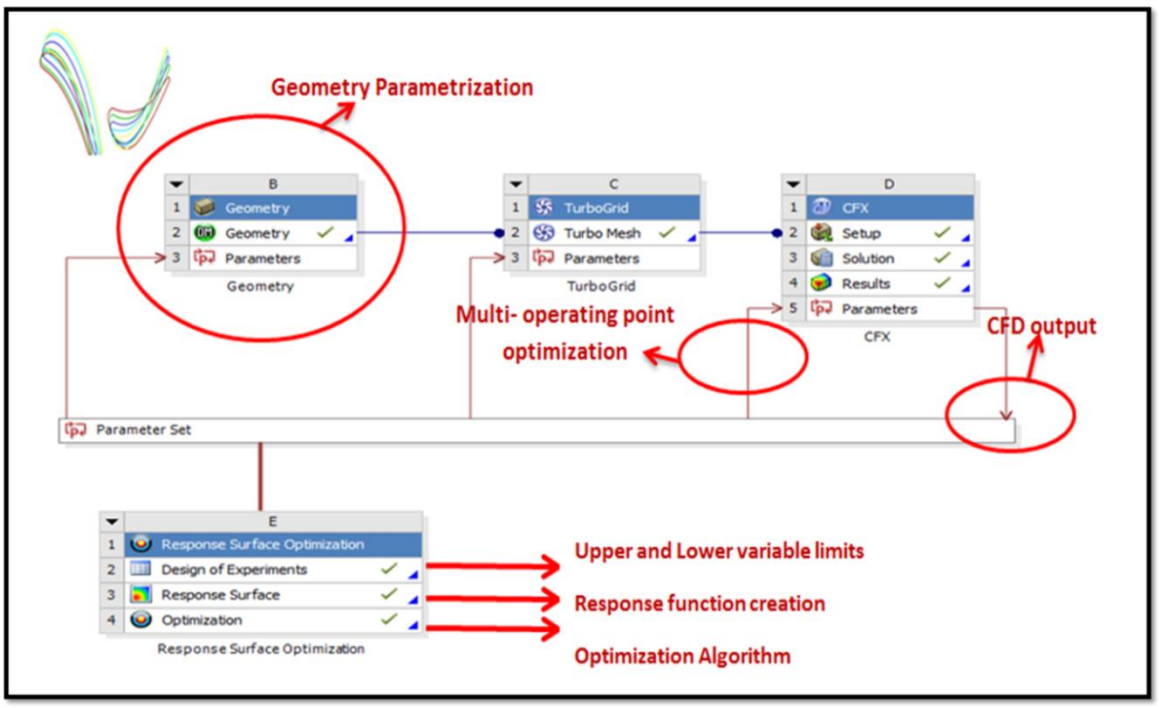

Figure 7.41 Single and multi-operating point in ANSYS workbench.

7.5.1 Single-point optimization:

In the single point optimization, the turbine blade profile was optimized for a single operating point (the design operating conditions). The 3D turbine blade single point optimization was conducted using the following strategy:

- The operating condition in ANSYS CFX Solver was set to be the same design point values (P_{o1}=2, RPM=20,000, T_{o1}=340K).
- Using CFD simulation parametric study and loss analysis, the upper and lower limits of the turbine blade geometrical parameters were selected as shown in Table 7-4.
- Defining the optimization objective functions and constrains.
- Studying the local sensitivity of the output function to the geometry parameters variations.
- Checking the Goodness of Fit of the meta-model function and actual CFX solver results.
- Applying the MOGA to identify the optimum blade geometry parameters combination which satisfy the objective functions and constrains.

In order to reduce the computational time, the dimensional space of the optimization problem is reduced by including only the independent geometry parameters and parallel computing was used for 100 iterations.

Table 7-4 Geometry parameters range

Parameter	**Unit**	**range**
Number blades	-	16-26
Stagger angle	degree	22-28
L.E Major radius	mm	0.3-0.6
L.E Minor radius	mm	0.2-0.5
L.E Wedge Angle	degree	16-20
T.E Minor radius	mm	0.2-0.5
T.E Wedge Angle	degree	10-15
Stator-rotor Spacing	mm	3-5

The Neural Network Meta model was used for response prediction due to its very good fitting with the actual solver runs compared to the 2nd polynomial and Kriging models (Cravero and Macelloni 2010). Figure 7.42 shows the Goodness of Fit in the prediction of both turbine output power and total to static efficiency. This fitness proves the ability of Neural Network model in predicting the response function with relative absolute error of 0.0036. The local sensitivity of the output response to the geometric parameters variations is shown in Figure 7.43. It can be seen that the stagger angle and the numbers of blades are the most significant factors compared to other parameters.

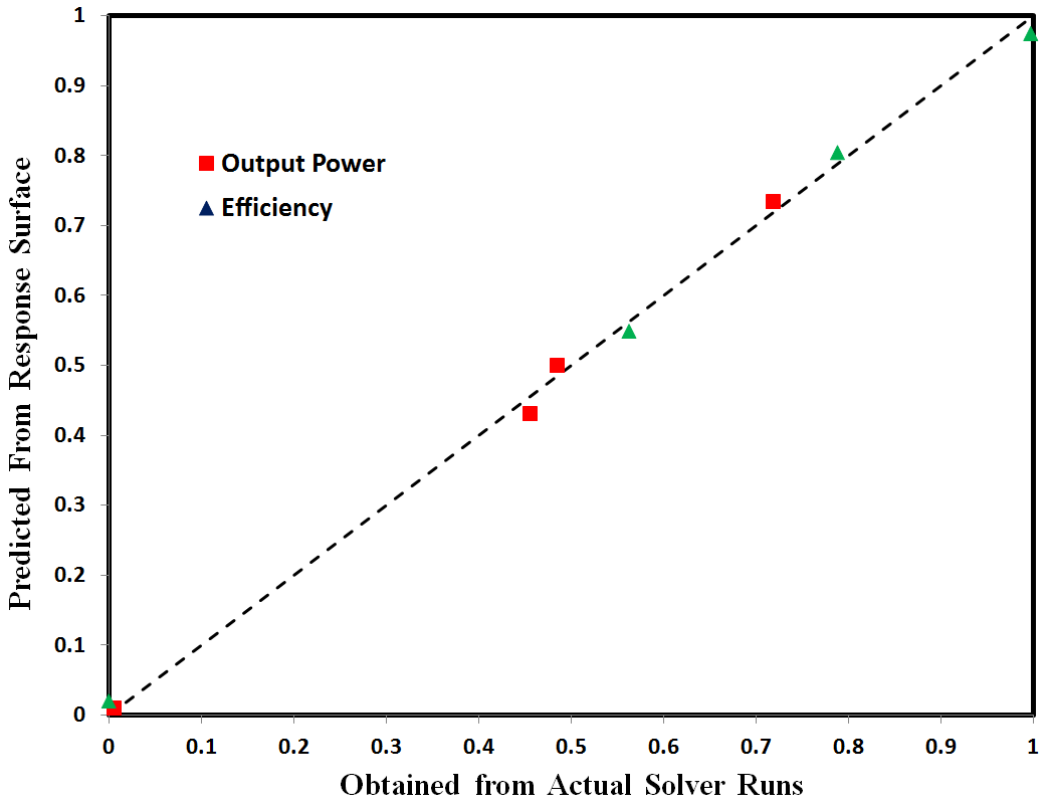

Figure 7.42 Goodness of fit between meta-model and CFX solver results

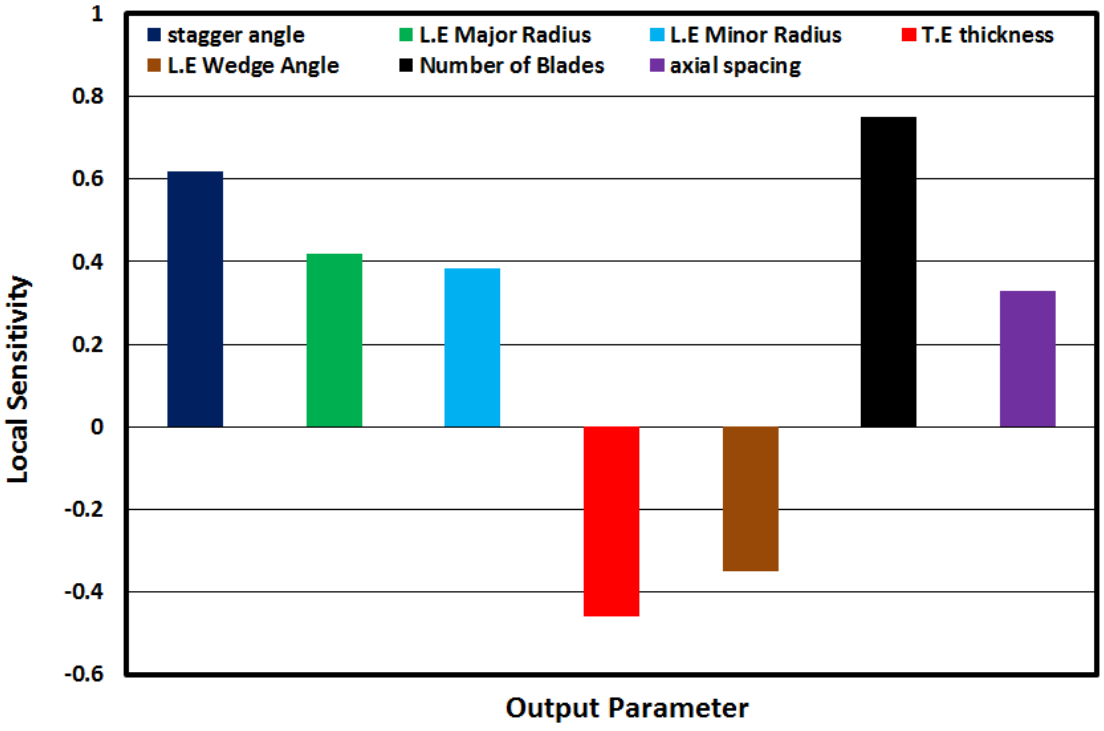

Figure 7.43 Local sensitivity analysis of design parameters.

The optimization was carried out using the initial axial turbine design based on CFD modelling as detailed in Table 7.4 and maintaining the same operating conditions. In the problem formulation, three objective functions were set in MOGA namely the maximization of the total to static efficiency, maximization of the output power and minimization of the total pressure losses. Also the turbine optimization was subjected to the following constrains:

- The allowable maximum change in air mass flow rate is 1% of the design point value of 0.1 kg/sec.
- $\beta_3 \leq 72^o$. This is the maximum value for axial turbine blade manufacturing requirements for rotor relative angle.
- $M_e < 1$. This condition was set to ensure that turbine is in sonic region.
- Tip clearance > 0.5mm. This value was set as a minimum value for manufacturing requirements.

The stator and rotor optimization were performed with initial 100 samples and with 100 maximum iterations as recommended by ANSYS User Guide. The results of single point optimization process for both stator and rotor blade profiles showed an increase in turbine stage total to static efficiency by 7.56% compared to the baseline efficiency indicating the ability of CFD based optimization as a powerful optimization technique to achieve higher turbine performance. The detailed comparison between baseline and optimized design is illustrated in Table 7.5.

Figure 7.44 compares the optimized and baseline rotor blades in terms of pressure distribution which shows that the optimization approach could reduce secondary flow in the rotor passage and adverse pressure was improved by reducing the exit stream velocity by 2.6% and 17.23% at stator and rotor exit respectively. The improvements in blade loading due to the optimization can be explained by the increase in stagger angle from 21.31^o to 25.07^o and as a result the blade thickness distribution is improved with optimized stagger angle value. The

noticeable enhancements in turbine performance are due to rotor blade optimization which could achieve a reduction of 8.23% in total loss compared to stator optimization which could reduce the loss by only 1.42%. A comparison between optimized blade profiles and baseline design is shown in Figures 7.45 and 7.46 for the rotor and stator respectively.

Table 7-5 CFD-MOGA optimization results

Minimize P4;Pressure Loss	Goal, Minimize Mize P4 (Default importance); Strict Constraint	
Seek P5 = 1000 W	Goal, Seek P5 = (Default Importance)	
Optimization Method	The MOGA method (Multi-Objective Genetic Algorithm)	
Configuration	100 samples per iteration	
	Baseline Design	**Optimized Design**
Stagger angle (degree)	21.31	25.07
Number blades	22	18
Tip Clearance (m)	0.001	0.00088821
Leading. Major radius (m)	0.000227	0.000386
Leading. Minor radius (m)	0.0001274	0.0001133
Trailing. Major radius (m)	0.0003	0.00021
Trailing. Minor radius (m)	0.0002	0.00013
Wedge Angle (degree)	19.07	17.23
Stator-Rotor Gap (mm)	5.0	3.78
Throat (m)	0.002077	0.0026628
Rotor Pressure Loss Coeff.	0.06108	0.05474
η_{ts}(Total-to-static)	78.064	84.457
Output Power (W)	987.05	993.48

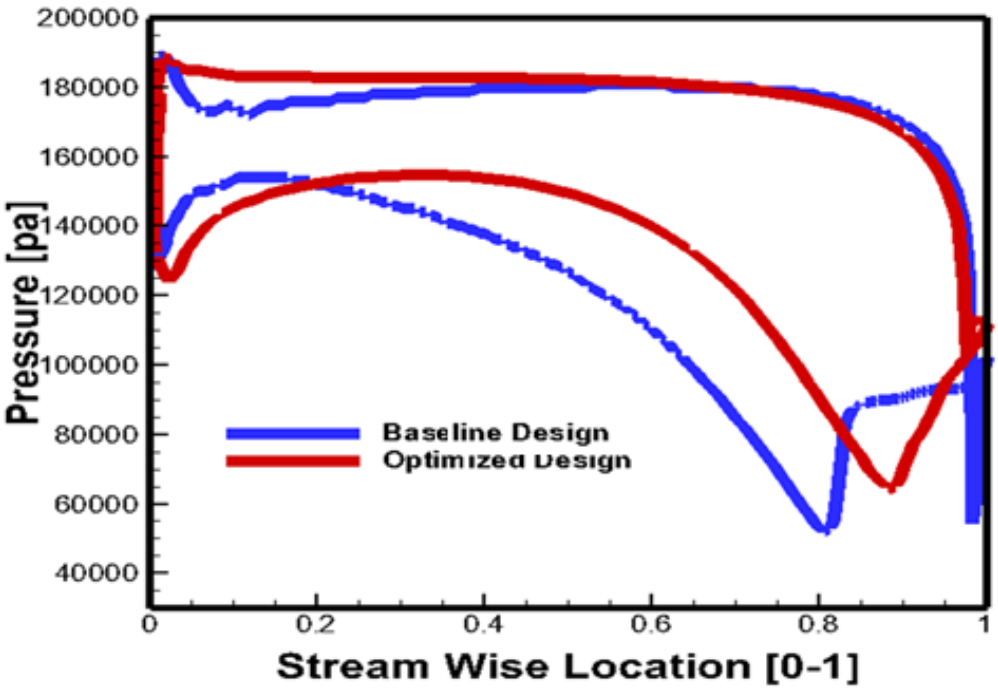

Figure 7.44 Rotor blade loading for baseline and optimized design

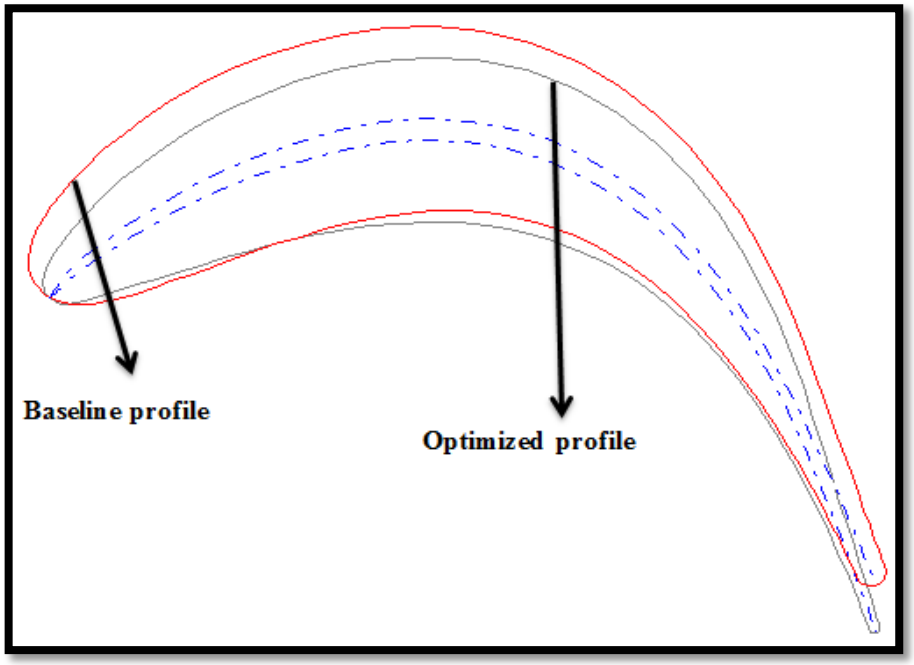

Figure 7.45 Rotor blade profiles for baseline and optimized designs

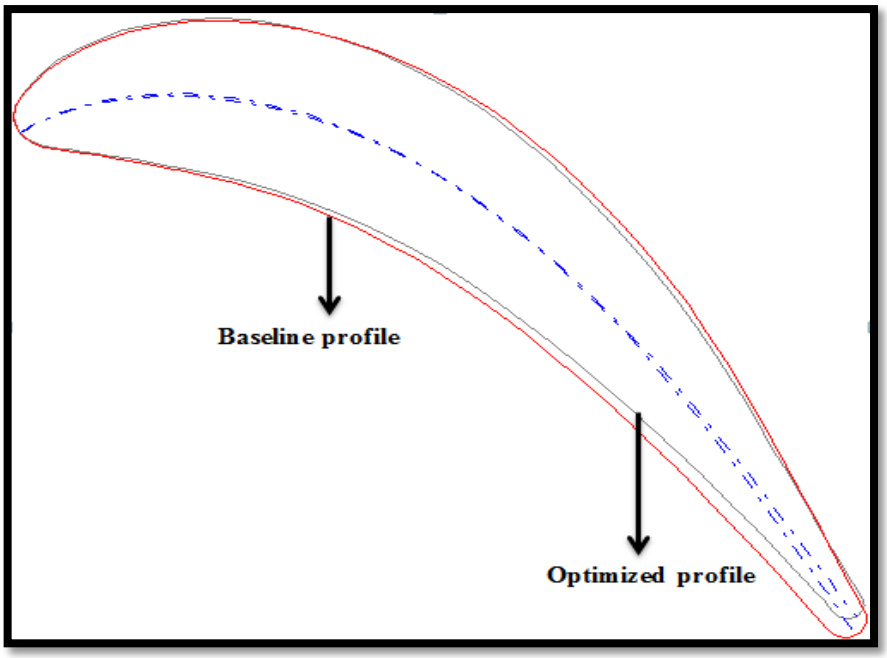

Figure 7.46 Stator blade profiles for baseline and optimized designs

The initial baseline design and optimized blades were simulated in ANSYS CFX and the results were compared in terms of velocity vector and entropy contours. The velocity streams show the improvements in flow behaviour and the reduction in secondary flow due to blade profile optimization. Also the entropy generation is a common parameter that can measure the losses. Figure 7.47 compares the entropy generation contours for the baseline and the optimized turbine blades. It can be seen that the entropy values in the optimized design were reduced compared to those associated with the baseline thus the optimization approach was effective in reducing the entropy generation from 158.43 up to 98.61 J/kg.K. Figure 7.48 compares the velocity streamlines for the baseline and optimized blade profiles show that the flow vortices and secondary flow through blades passage can be reduced using this optimization approach.

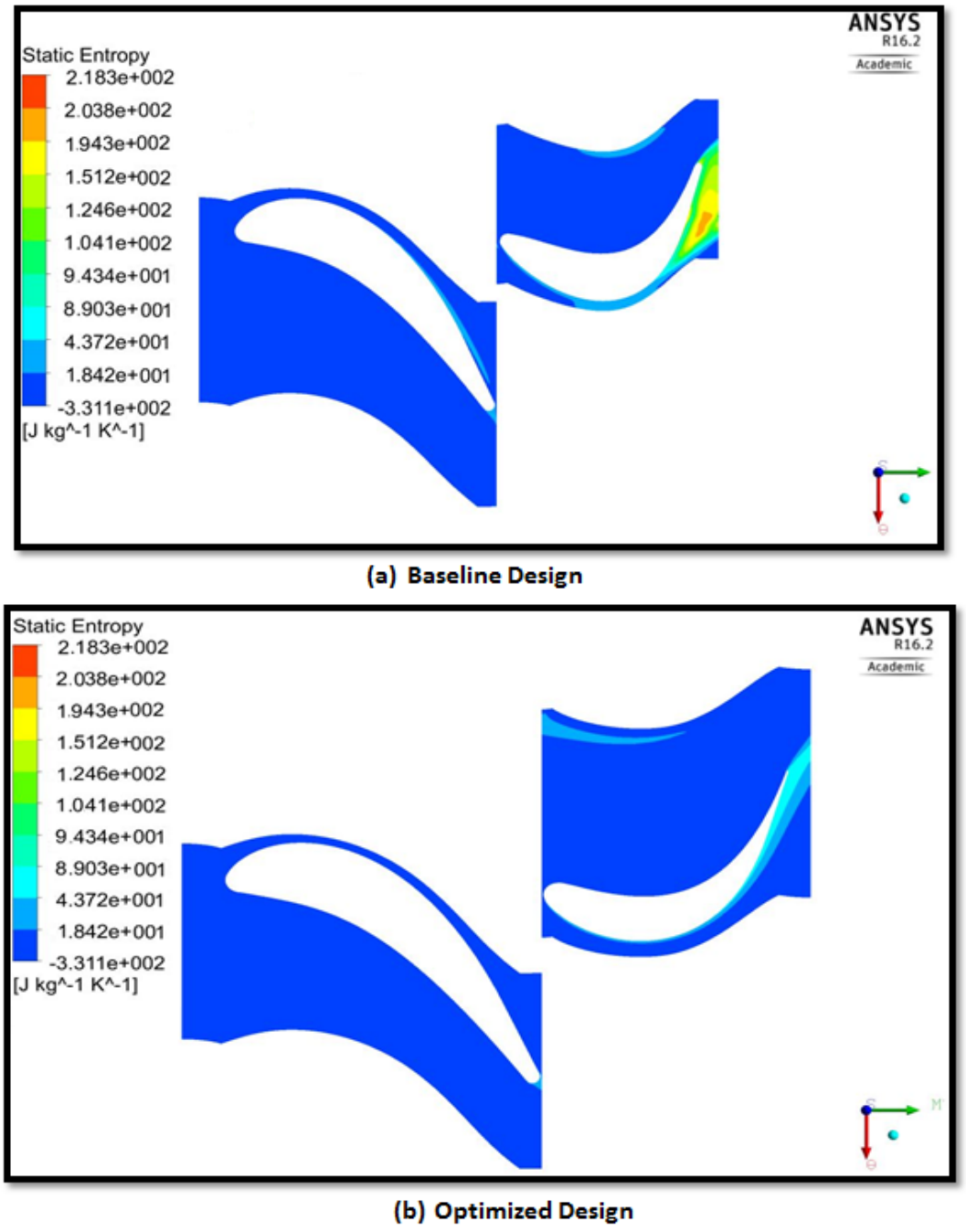

Figure 7.47 Entropy generation contours: (a) baseline design (b) optimized design

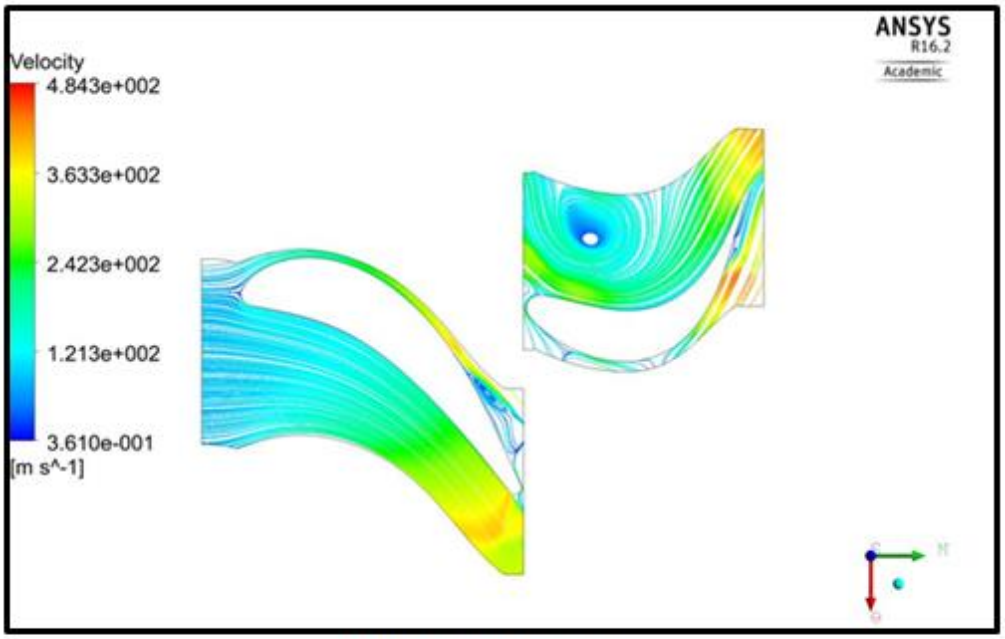

(a) Baseline Design

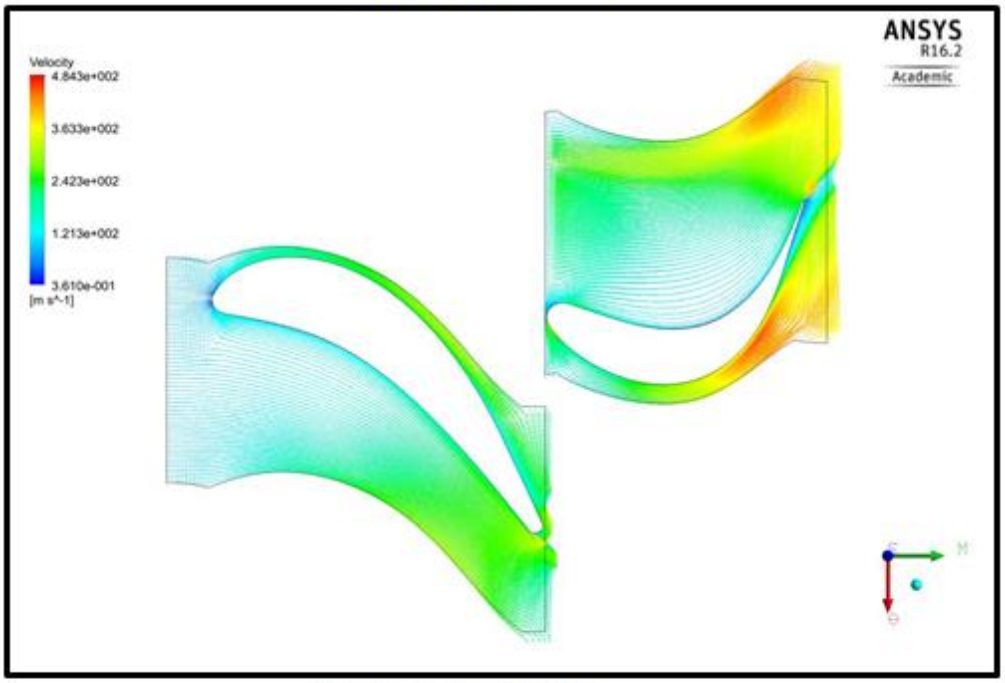

(b) Optimized Design

Figure 7.48 Velocity vectors: (a) baseline design (b) optimized design

7.5.2 Multi-operating point optimization:

In single point optimization the turbine blade profile is redesigned to achieve high efficiency at certain operating condition which represents the turbine design point. However, in actual operation, the turbine may work at off design mode for significant period of time. In D-CAES, as a result of transient operating conditions the turbine works at inlet pressure and mass flow rates higher and lower than the design point value. The discharging pressure can be controlled at 2 bars but that will lead to a reduction in mass flow rate due to variations in air density. As a result, the axial turbine blade profiles for the stator and rotor were optimized for a range of inlet mass flow rate (0.025-0.1kg/sec) to achieve higher power and efficiency levels during cycle discharging phase. Table 7.6 provides detailed comparison between single and multi-operating point optimization results. Also Figure 7.49 compares the rotor blade profiles as obtained from both single and multi-operating point optimization and it is observed that the multi-point optimization leads to noticeable change in rotor solidity as a result of multi operating conditions. Compared to single operating point, the multi-operating point optimization approach can improve the turbine cycle performance in both on and off design modes with higher overall cycle efficiency.

Figure 7.50 shows the D-CAES overall efficiency with the turbine designs obtained by the two optimization approaches where an improvement of 8.07% was achieved by multi point optimization compared to single point optimization. However, the computational time needed for multi operating point optimization is excessively long compared to that needed for single point optimization and this is why in this approach the inlet pressure was set as constant at 2 bar and only variations in inlet mass flow rate was used to save the computational time.

Table 7-6 Single and multi-point optimization results

Minimize P4;Pressure Loss	Goal, Minimize Mize P4 (Default importance); Strict Constraint	
Seek P5 = 1000 W	Goal, Seek P5 = (Default Importance)	
Optimization Method	The MOGA method (Multi-Objective Genetic Algorithm)	
Configuration	100 samples per iteration	
	Single point optimization	**Multi-point optimization**
Stagger angle (degree)	25.07	23.14
Number blades	18	18
Tip Clearance (m)	0.00088821	0.000754412
Leading. Major radius (m)	0.000386	0.000406
Leading. Minor radius (m)	0.0001133	0.0001228
Trailing. Major radius (m)	0.00021	0.000114
Trailing. Minor radius (m)	0.00013	0.000087
Wedge Angle (degree)	17.23	20.07
Stator-Rotor Gap (mm)	3.78	3.43
Throat (m)	0.0026628	0.00258817
Blade Solidity	1.5224	1.7332
Rotor Pressure Loss Coeff.	0.05474	0.055118
η_{ts}(Total-to-static)	84.457	82.767 %
Output Power (W)	993.48	989.12

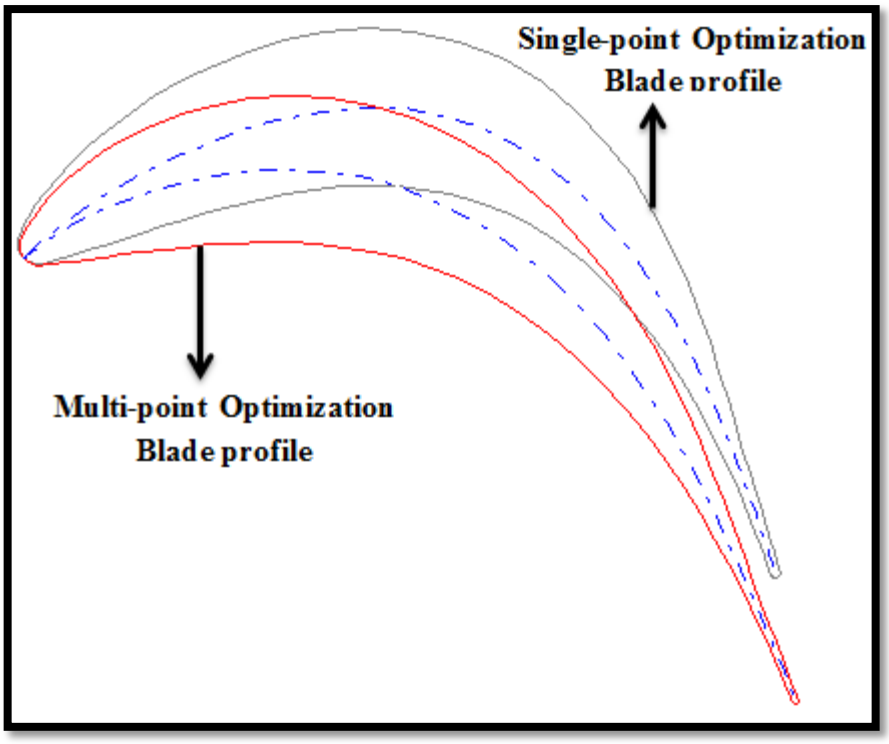

Figure 7.49 Rotor blade profiles for single and multi-point optimization

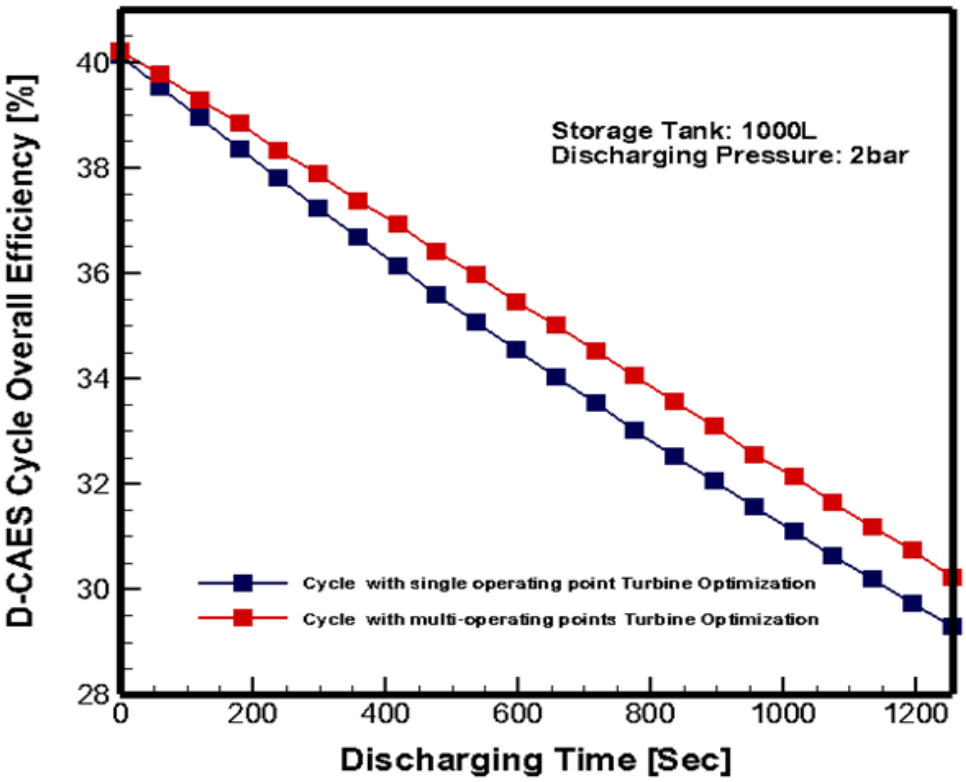

Figure 7.50 D-CAES efficiency based on single and multi-point turbine optimization

7.6 Multidisciplinary Optimization:

The aerodynamic design optimization of the turbine blade profile is performed to improve the turbine efficiency through geometry variations. However, the optimum aerodynamic design is usually in conflict with the structural requirements. In order to ensure that the optimum aerodynamic design is compatible with structural design limitations, the multidisciplinary automatic optimization was conducted in ANSYS Workbench for both the aerodynamic and mechanical blade designs simultaneously as shown in Figure 7.51. The coupling of the CFD solver with the mechanical structure solver allows transferring the loads (Pressure and rotational speed) from CFX fluid solver to the finite element model in which the Von Mises stress and total deformation can be predicted. The optimization problem was formulated with Multiobjective functions which included maximization of the turbine efficiency with minimization of Von Mises stress and minimization of total deformation. As can be seen in Figure 7.52 the sensitivity analysis of the rotor blade stresses to the blade geometry variations indicates that the Von Mises stress is more sensitive to the geometry of both L.E and T.E compared to other parameters.

Using the multidisciplinary optimization based on 3D printing material (Fullcure720) the maximum total blade deformation was reduced from 0.11506 mm to 0.077578 mm as shown in Figure 7.53 which compares the FEA results for the rotor blade profiles based on aerodynamic optimization and multidisciplinary optimization. Also the maximum total equivalent Von Mises stresses were reduced from 49.715 MPa to 41.729 MPa as shown in Figure 7.54. This optimization approach could reduce the stresses while maintaining the turbine efficiency high around 82.95% with only a reduction of only 1.8% compared to the optimum efficiency based on aerodynamic blade optimization. This reduction in turbine efficiency is due to the change in rotor blade geometry to meet the structural requirements. Table 7-7 provides a detailed comparison between aerodynamic and multidisciplinary

optimisation results. Figure 7.55 shows the rotor blade profiles for more clear comparison between aerodynamic based optimization and multidisciplinary optimization.

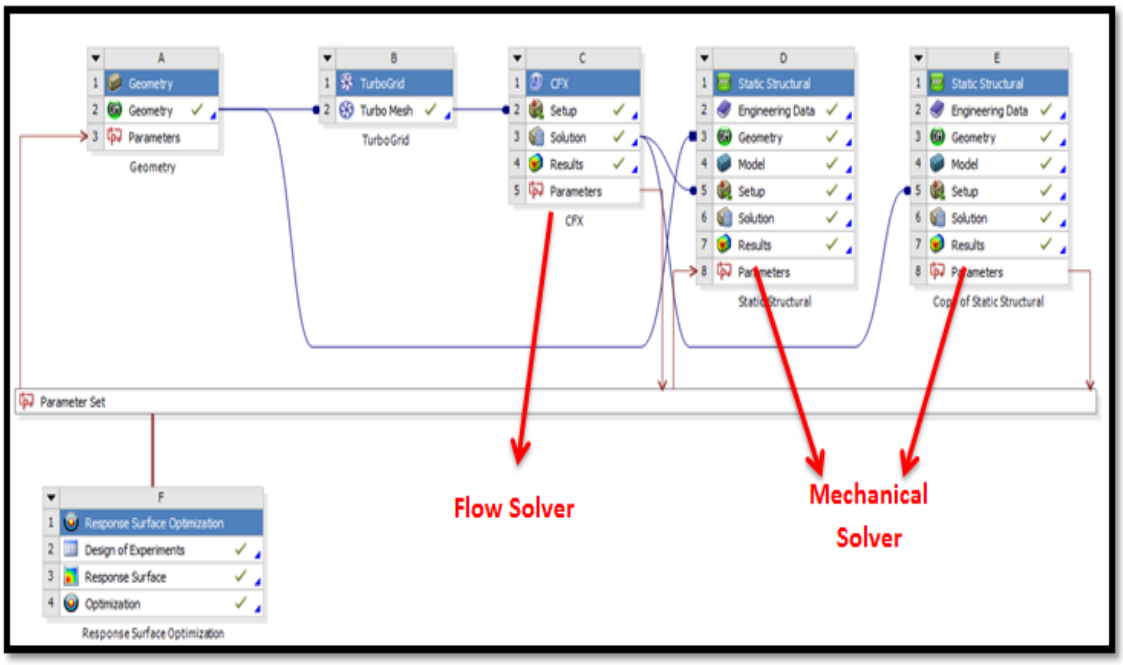

Figure 7.51 Multidisciplinary optimization in ANSYS workbench.

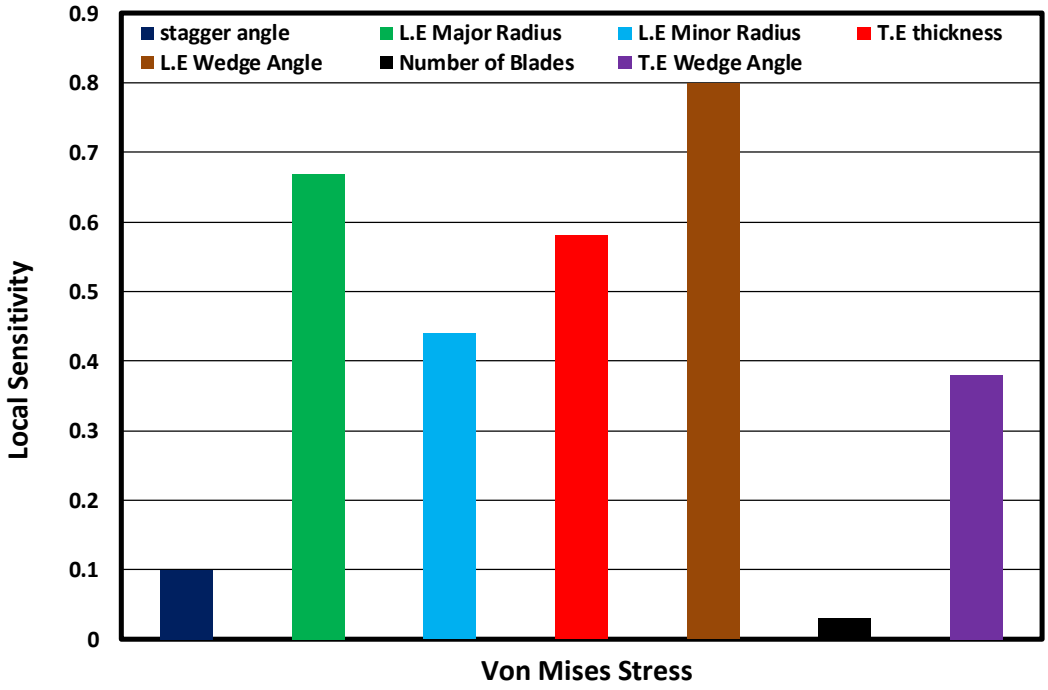

Figure 7.52 Sensitivity analysis of geometry variations on total stresses

Table 7-7 Aerodynamic and multidisciplinary optimization results

Minimize P4;Pressure Loss	Goal, Minimize Mize P4 (Default importance); Strict Constraint	
Seek P5 = 1000 W	Goal, Seek P5 = (Default Importance)	
Optimization Method	The MOGA method (Multi-Objective Genetic Algorithm)	
Configuration	100 samples per iteration	
	Aerodynamic optimization	**Multidisciplinary optimization**
Stagger angle (degree)	25.07	22.14
Number blades	18	18
Leading. Major radius (m)	0.000386	0.000944
Leading. Minor radius (m)	0.0001133	0.0006221
Trailing. Major radius (m)	0.00021	0.000436
Trailing. Minor radius (m)	0.00013	0.000707
L.E Wedge Angle (degree)	17.23	22.34
Stator-Rotor Gap (mm)	3.78	3.78
Blade Solidity	1.5224	1.5224
η_{ts}(Total-to-static)	84.457	80.95
Output Power (W)	993.48	990.27

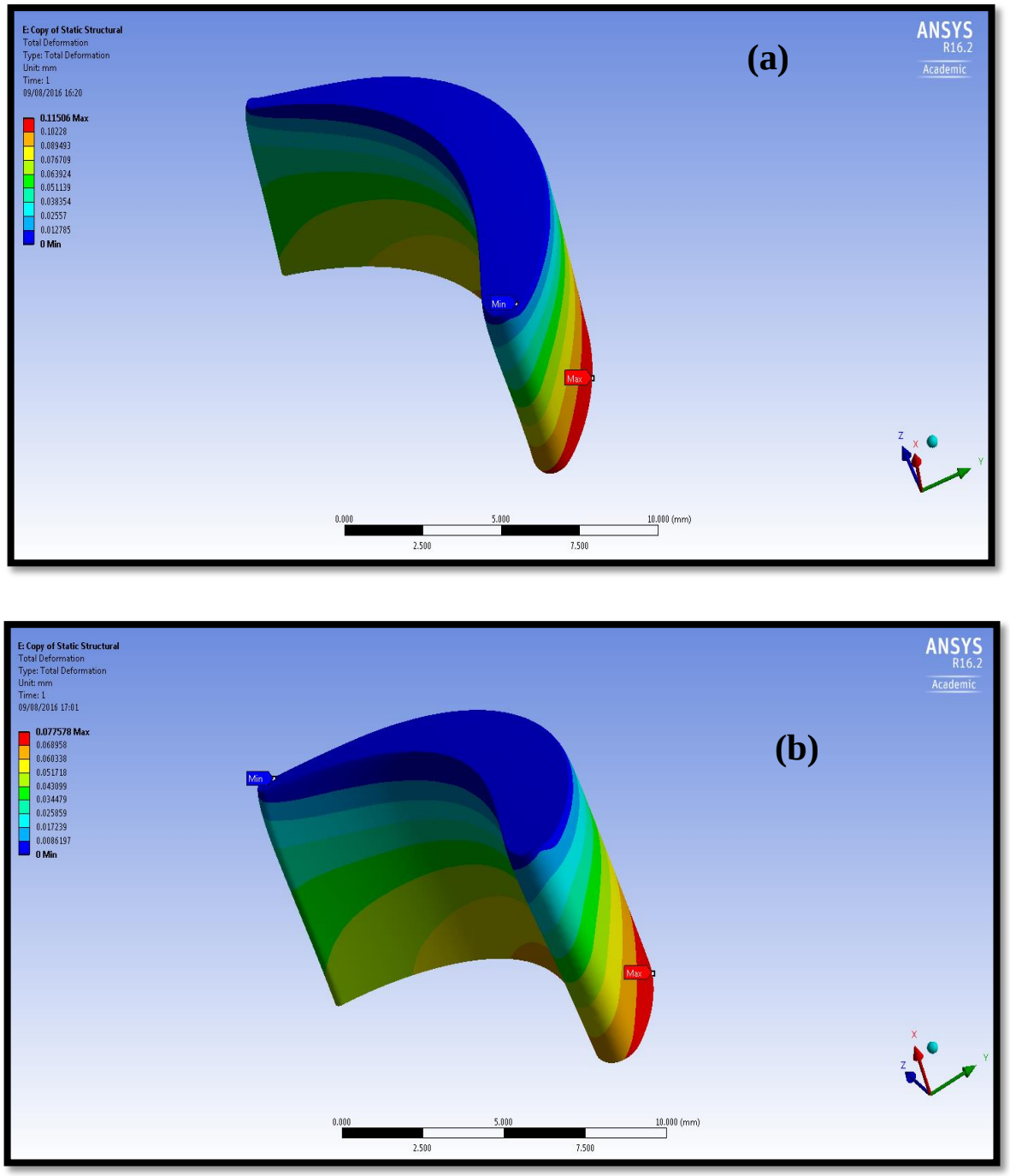

Figure 7.53 Total deformation (a) aerodynamic optimized profile (b) Multidisciplinary optimized profile

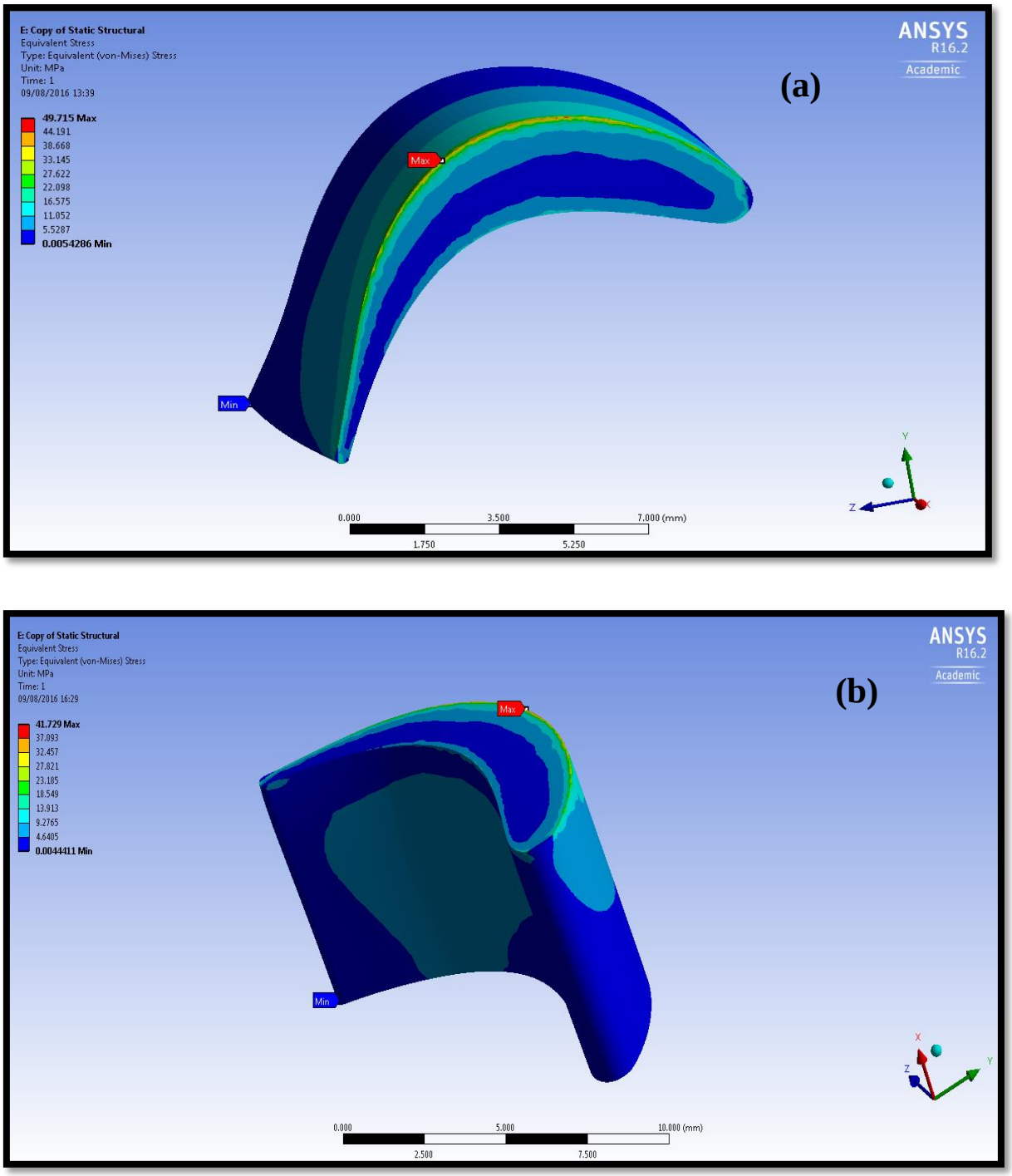

Figure 7.54 Total stresses (a) aerodynamic optimized profile (b) Multidisciplinary optimized profile

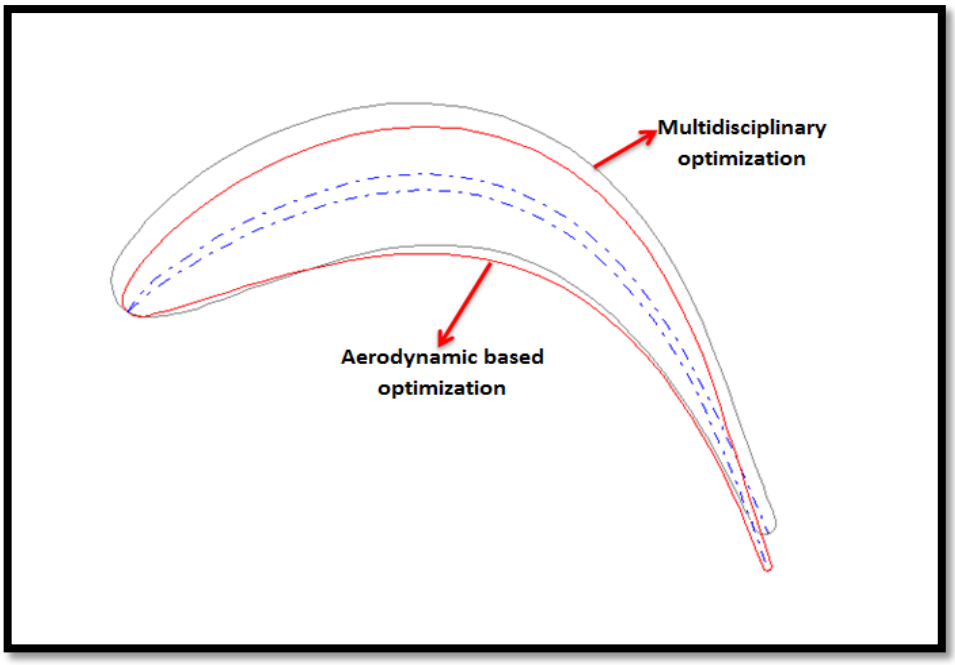

Figure 7.55 Comparison between rotor blade profiles for aerodynamic and multidisciplinary optimization

7.7 Experimental Validation:

In order to validate the methodology used to develop small scale axial air turbine for solar powered compressed air energy storage system, the developed turbine was manufactured and tested using compressed air. The developed axial turbine was tested at different inlet pressure, temperature, mass flow rate, and RPM. The maximum inlet pressure that could be achieved from the compressed air supply was 1.6 bar. For the inlet temperature, a heating tape was fixed near the turbine inlet to heat the inlet air from ambient temperature of 20^oC up to 34^oC. A 3D CFD turbine simulation was conducted with the same operating conditions of the experimental test for different rotational speed starting from 6,000 RPM up to 18,000 RPM for different inlet pressures (1.2-1.6bar).

The experimental results were compared to the CFD simulation results at different rotational speed (6,000-18,000 RPM) and turbine inlet temperature (20^oC - 34^oC).

Figure 7.56 compares the turbine output power obtained by both CFD simulation and experimental testing for different pressure ratios and rotational speeds at fixed inlet temperature of 34^oC. For more precise power prediction, the uncertainty propagation was included and represented by error bars for each experimental result. Figure 7.57 compares the total to static efficiency of CFD simulation and experimental results with including the uncertainty propagation for measuring instruments. Both power output and efficiency comparisons show good agreement between CFD simulation and experimental results. The turbine efficiency and power increase with the RPM due to the increase in enthalpy drop through the turbine stage. Also the increase in turbine inlet temperature TIT from 20^oC to 34^oC leads to observed increase in turbine power and efficiency. The maximum output power was 701.87 W at 1.6 bars and 18,000 RPM with an efficiency of 59.26 %.

Figures 7.56- 7.59 show that the CFD simulation results were over predicted compared to the experimental results for both turbine output power and efficiency. These differences between experimental and CFD simulation can be explained due to:

- In CFD simulation of the turbine stage, the surface roughness of the blade was assumed to be smooth unlike the actual manufactured model. Decreasing the surface roughness can improve the turbine efficiency significantly. Figure 7.62 shows the comparison between the experimental and CFD results by including the effect of surface roughness of 3D printing material (Fullcure720). The surface roughness of Fullcure 720 was obtained using Alicona Infinite Focus optical scanner for 3D turbine blade profile and the average surface roughness was 10.23µm. The comparison shows that the difference between CFD and experimental results was reduced by 2.5% by considering the effect of surface roughness in CFD simulation.
- The CFD modelling was conducted based on steady state flow condition. However, the actual test had transient flow characteristics.

- In actual turbine testing, there are significant mechanical losses in shaft bearings leading to a reduction in turbine output power. These mechanical losses were not considered in CFD modelling of the turbine stage.

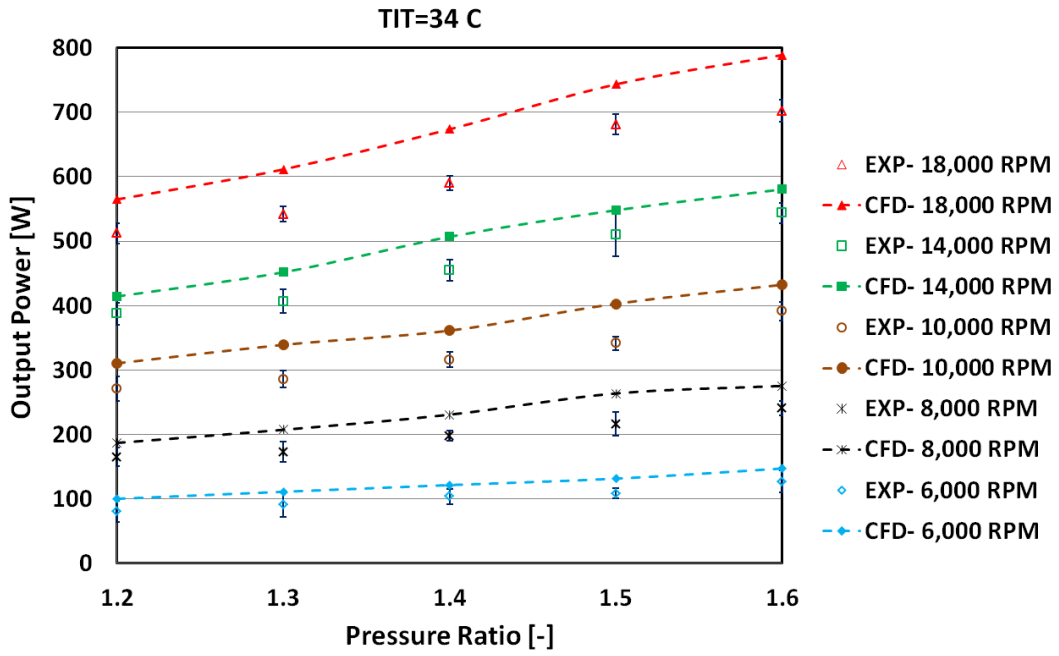

Figure 7.56 CFD modelling validation with experimental for turbine power ($\mathbf{34^oC}$)

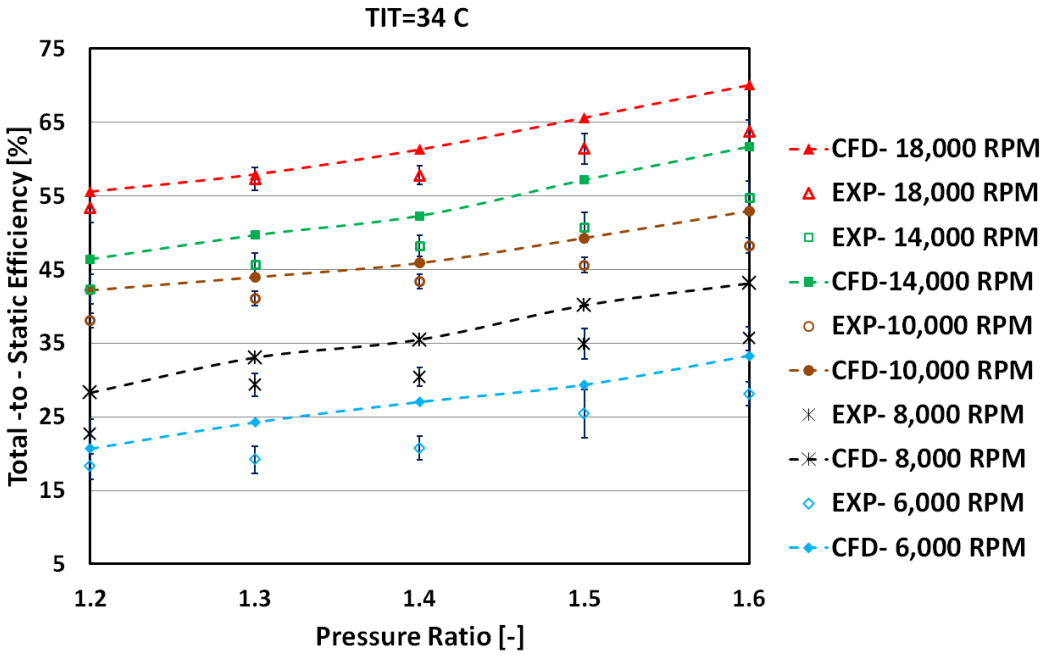

Figure 7.57 CFD modelling validation with experimental for turbine efficiency ($\mathbf{34^oC}$)

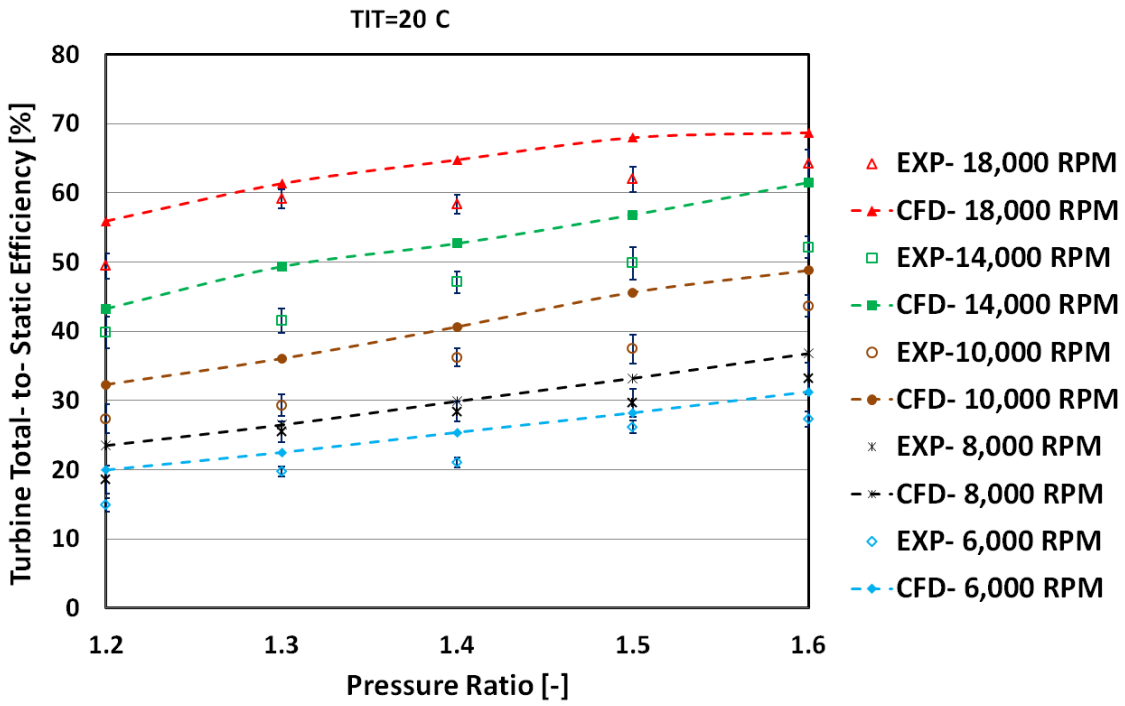

Figure 7.58 CFD modelling validation with experimental for turbine efficiency ($\boldsymbol{20^oC}$)

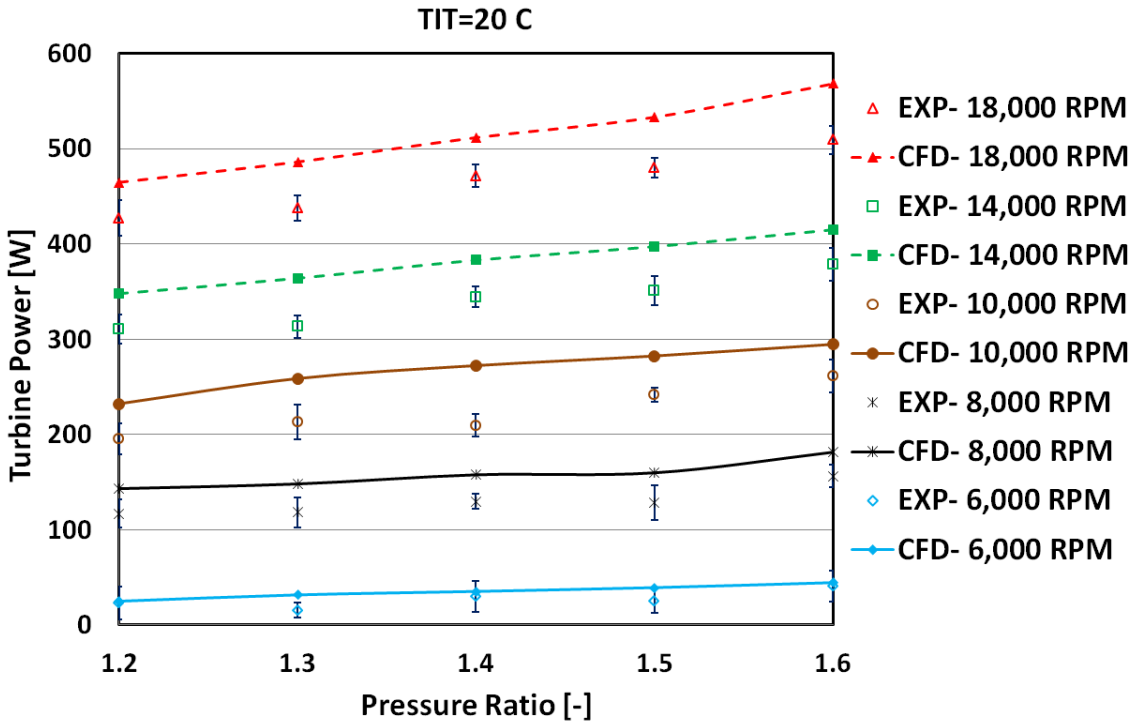

Figure 7.59 CFD modelling validation with experimental for turbine output power ($\boldsymbol{20^oC}$)

Figures 7.60 and 7.61 show the CFD predicted turbine efficiency and power output versus the experimental results. On Figure 7.60, lines presenting percentage deviation of ±16.50 % between the CFD and experimental results while in Figure 7.61 lines presenting percentage deviation of ±12.5 % were indicated.

The percentage deviation between the CFD modelling and experimental results were calculated using relative error equation as:

$$\text{Relative Error } (\%) = \frac{|CFD - EXP.|}{CFD} \times 100 \tag{7.1}$$

This comparison gives clear boundaries for the CFD simulation against the experimental data. As shown in Figure 7.60 and Figure 7.61 the predicted CFD values were within ±16.50 % for the total to static efficiency and ±12.5 % for the output power indicating acceptable agreement between experimental and CFD results. The comparison shows that the relative error in power prediction using CFD is lower than that of the efficiency prediction due to the uncertainty in efficiency calculations being higher than the uncertainty in the power which was measured directly with the torque meter with high accuracy. The effect of surface roughness on turbine CFD simulation is shown in Figure 7.62.

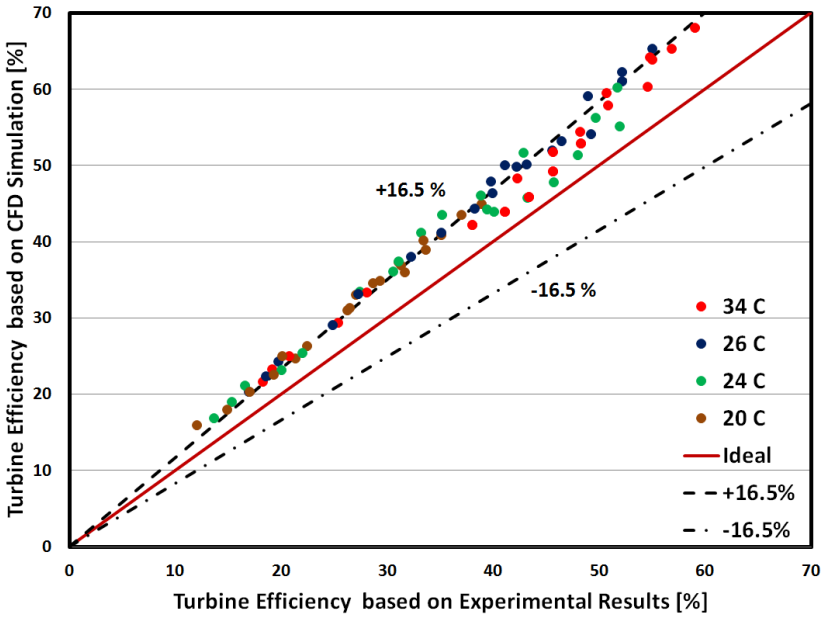

Figure 7.60 Turbine efficiency based on CFD modelling and experimental testing

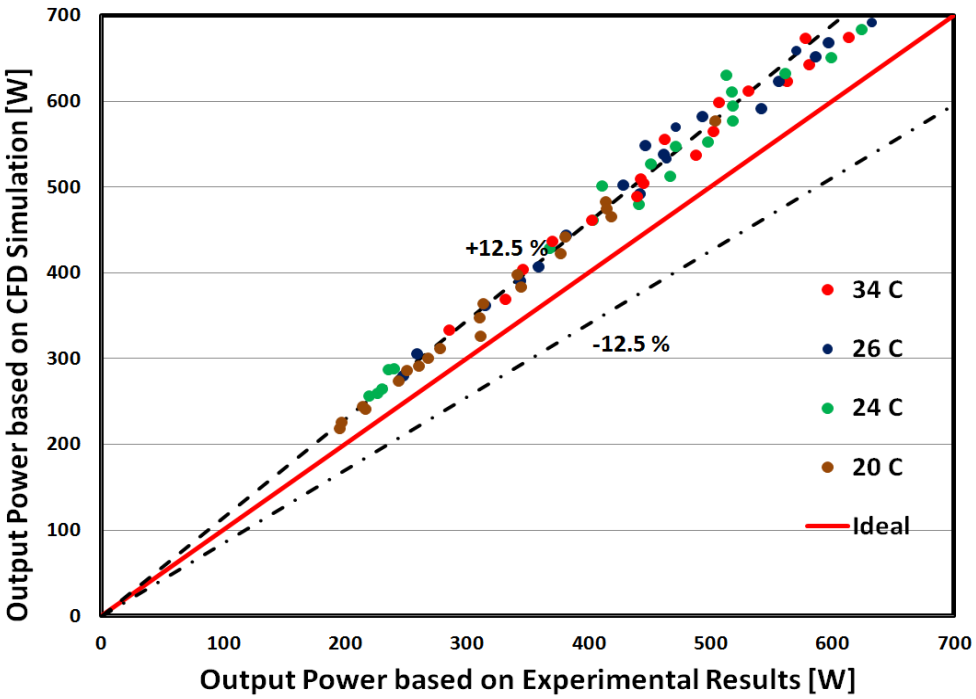

Figure 7.61 Turbine power based on CFD modelling and experimental testing

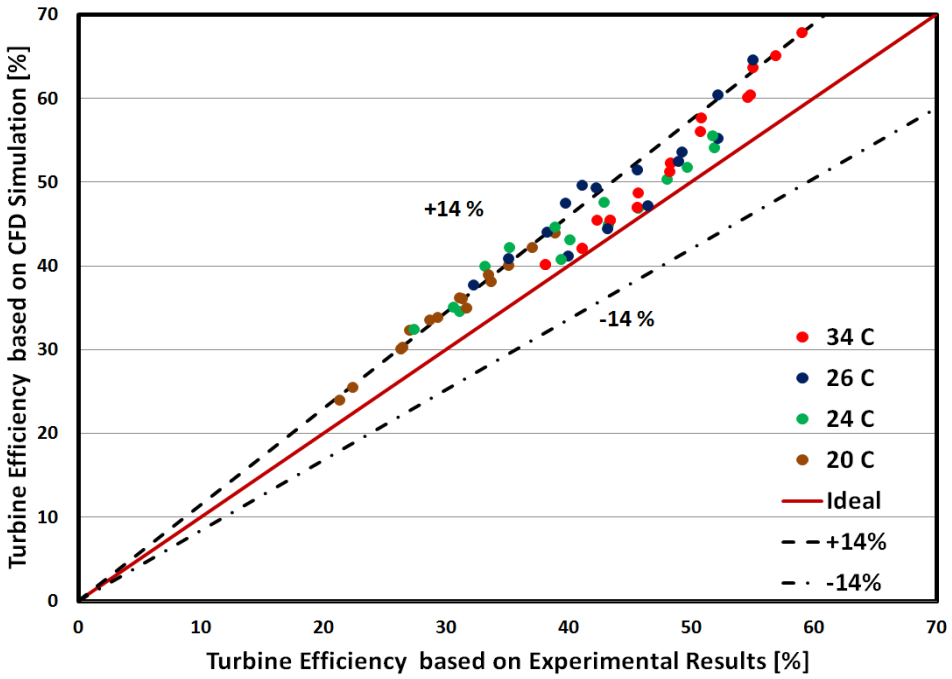

Figure 7.62 Turbine efficiency based on CFD modelling and experimental testing by considering the surface roughness effect.

CHAPTER 8

CONCLUSIONS AND RECOMMENDATIONS

8.1 Introduction:

Distributed power generation systems can play a major role for cost effective environmental friendly electricity generation. The implementation of DPG systems based on renewable energy source requires developing energy storage technology to store the excess renewable energy at peak times and then recover the stored energy efficiently for usage where needed. Compressed air as a storage technology is one of the competitive solutions for more developments in energy production using renewable energy sources like solar and wind energies which has been implemented in large scale applications. However, small scale D-CAES is still new and further research is required for enhancing the charging and discharging phases to increase the overall efficiency of the cycle. In the discharging phase, the compressed air is expanded in small turbine with a rotating shaft to operate an electrical generator. This small turbine is the key component in the D-CAES and the system overall efficiency is dependent on the small turbine performance.

8.2 Conclusions:

In D-CAES system, the small turbine works deeply at off design mode due to the transient behaviour of the discharging process of the compressed air. This research developed a methodology for the design and optimization of a small axial turbine applicable for D-CAES system with an output power of 1kW suitable for domestic applications. The strategy of the research aims to improve the overall performance of the D-CAES system through developing an efficient small scale axial air turbine to achieve higher efficiency levels in both on and off design modes. The main conclusions from this research can be drawn in the following points:

- A systematic comprehensive methodology for developing a small scale axial turbine for compressed air energy storage system was developed. The methodology consists of : (i) developing an initial turbine design using mean line analysis; (ii) use 3D-CFD modelling with single and multi-operating point optimization to achieve the best performance over wide range of operating conditions and (iii) use of multi-disciplinary optimization to modify the optimum aerodynamic design to enable low cost 3D printing material withstanding the mechanical stresses occurring in the turbine and demonstrate the potential of such material for real functional applications.
- Small scale turbines experience high losses and precise losses prediction for small scale turbines is needed. The comparison between losses prediction using conventional losses schemes and losses prediction based on 3D CFD modelling was conducted. This comparison showed that the losses prediction were under predicted by Ainely, Came&Dunham correlations and Kacker & Okapuu losses model is more appropriate for performance prediction in small axial turbines at the preliminary design phase compared to other losses models. Kacker & Okapuu losses prediction model was within ±1.87% from the CFD results at the design point and for more accurate performance prediction, the CFD modelling can be effective tool for reducing

the losses through improving the blade thickness distribution for better velocity vectors distribution and blade loading.

- The results of total loss prediction based on 3D CFD modelling for different blade aspect ratios were presented for different exit Mach number. These results provide the guidelines for the total loss prediction in small axial turbines at early design stages in terms of dimensionless parameters which can be used directly for more precise performance prediction of small scale axial turbines with aspect ratio range of 0.2 to1.
- The 3D CFD turbine simulation coupled with MOGA optimization was proven as an effective inexpensive design approach for minimizing the losses through the turbine stage leading to an optimum blade profile. The single operating point optimization approach based on 3D CFD modelling could improve the turbine total to static efficiency by 7.56% highlighting the potential of this optimization approach in developing turbine design for higher efficiency levels.
- In D-CAES system, there are significant variations in the turbine inlet pressure and mass flow rate leading to considerable drop in turbine performance. Multi-operating point optimization approach could improve the turbine efficiency for a wide range of off design operating conditions and increase by 8.07% in D-CAES overall efficiency was achieved indicating the ability of Multi-point optimization technique to reach acceptable turbine efficiency levels compared to normal baseline design in off design operation mode.
- The aerodynamic turbine optimization leads to high efficiency value with a novel blade profile geometry. However, this optimum profile conflicts with the mechanical design constrains. In this regard and to ensure the optimum design can withstand mechanical loads, multidisciplinary optimization approach was used to optimize the blade profile for maximum efficiency, minimum stress, and minimum deformation at

the same time. This optimization technique was proven as new design tool for simultaneous optimization of both aerodynamic and mechanical designs optimization. This optimization approach could reduce the equivalent Von Mises Stress from 49.715 MPa to 41.729 MPa while maintaining the turbine total to static efficiency high at 80.95% which is 4.89% higher than efficiency obtained using 1D meanline modelling.

- The developed design methodology for the small axial turbine has been proven as a powerful design tool by experimental testing of the developed turbine. The comparison between experimental and CFD results showed deviations of 16.5% and 12% in efficiency and power output respectively which can be reduced by considering the surface roughness in turbine CFD simulation.
- The use of 3D printing materials (Fullcure 720) in turbine manufacturing and testing can highlight the potential role of this material as cost effective material that can be used not only for prototyping but for real functional applications like manufacturing turbine inlet cone, stator vanes, and rotor blades.

8.3 Recommendations:

Based on the work that has been conducted in this research for developing small axial air turbine, the turbine efficiency is sensitive to blade profile geometry and for more enhancements in small axial turbine performance the design requires considering the following:

- Improving the losses prediction schemes for on and off design condition by including the turbulent and boundary layer transition effects in small and micro turbines.
- Transient CFD modelling of small axial turbine to investigate the impact of stator-rotor interactions on turbine performance.

- Vibration in small axial turbines is another parameter that requires deep research particularly for high rotational speed levels.
- For more improvements in D-CAES expansion phase, the thermal energy storage design needs to be optimized for maximum heat storage capacity with minimum pressure loss in heat exchanger system.

REFERENCES

Abdelfattah, S. and Schobeiri, M. (2012). "Experimental and numerical investigations of aerodynamic behavior of a three-stage high-pressure turbine at different operation conditions." Proceedings of the Institution of Mechanical Engineers, Part C: Journal of Mechanical Engineering Science 226(6): 1535-1549.

Ackermann, T., Andersson, G. and Soder, L. (2000). Electricity market regulations and their impact on distributed generation. Electric Utility Deregulation and Restructuring and Power Technologies, 2000. Proceedings. DRPT 2000. International Conference on, IEEE.

Ackermann, T., Andersson, G. and Soder, L. (2001). "Distributed generation: a definition." Electric power systems research 57(3): 195-204.

International Energy Agency (2014). "Energy Technology Perspectives−ETP2014." Harnessing electricity's potential.

Ainley, D. and Mathieson G. (1951). An examination of the flow and pressure losses in blade rows of axial-flow turbines, HM Stationery Office.

Ainley, D. and Mathieson G. (1951). A method of performance estimation for axial-flow turbines, Citeseer.

Anderson, M. J. and Whitcomb, P. J. (2005). RSM simplified: optimizing processes using response surface methods for design of experiments, Productivity Press.

Angelino, G., Luca, L. De and Sirignano, W. A. (2012). Modern Research Topics in Aerospace Propulsion: In Honor of Corrado Casci, Springer Science & Business Media.

Ansys, C. (2009). "ANSYS CFX-solver theory guide." ANSYS CFX Release 11: 69-118.

ANSYS Guid (2014). "Design Exploration User's Guide." Canonsburg.

Aoun, B. and Clodic D. F. (2008). "Theoretical and experimental study of an oil-free scroll vapor expander."

Arabnia, M. (2012). Aerodynamic shape optimization of axial turbines in three dimensional flow, Concordia University.

Energy Association (2016). "Distributed Energy Resources: Guide."

Ataer, O. E. (2006). "Storage of thermal energy." Encyclopedia of Life Support.

Aungier, R. H. (2006). Preliminary Aerodynamic Design of Axial-Flow Turbine Stages, ASME press.

Balje, O. and Binsley R. (1968). "Axial Turbine Performance Evaluation. Part A—Loss-Geometry Relationships." Journal of Engineering for Power 90(4): 341-348.

Balje, O. E. (1981). Turbomachines : a guide to design selection and theory. New York, Wiley.

Bao, J. and Zhao L. (2013). "A review of working fluid and expander selections for organic Rankine cycle." Renewable and Sustainable Energy Reviews 24: 325-342.

Benner, M., Sjolander S.and Moustapha S. (1997). "Influence of leading-edge geometry on profile losses in turbines at off-design incidence: experimental results and an improved correlation." Journal of turbomachinery 119(2): 193-200.

Benner, M., Sjolander S.and Moustapha S. (2006). "An empirical prediction method for secondary losses in turbines—part I: a new loss breakdown scheme and penetration depth correlation." Journal of Turbomachinery 128(2): 273-280.

Benner, M., Sjolander S.and Moustapha S. (2006). "An empirical prediction method for secondary losses in turbines—part II: a new secondary loss correlation." Journal of Turbomachinery 128(2): 281-291.

Bhadoria, V. S., Pal N. S. and Shrivastava V. "A Review on Distributed Generation Definitions and DG Impacts on Distribution System."

Bloch, H. P. and Godse A. (2006). Compressors and modern process applications, John Wiley & Sons.

Bollinger, B. R. (2010). System and method for rapid isothermal gas expansion and compression for energy storage, Google Patents.

Brandon, N. E., Aunedi, J. S., Barbour, M., Bruce, E. R., Chakrabarti, P. G., Esterle, Ding, J. W., and Fu, Y. L. "UK RESEARCH NEEDS IN GRID SCALE ENERGY STORAGE TECHNOLOGIES."

Bullock, R. (1964). "Analysis of Reynolds number and scale effects on performance of turbomachinery." Journal of Engineering for Gas Turbines and Power 86(3): 247-256.

Bullough, C. G., Christoph J., Christoph K., Martin N., Andreas Z., Stefan T. (2004). Advanced adiabatic compressed air energy storage for the integration of wind energy. Proceedings of the European Wind Energy Conference, EWEC.

Chen, H. C., Thang N., Wei T., Chunqing L., Yongliang D., Yulong K. (2009). "Progress in electrical energy storage system: A critical review." Progress in Natural Science 19(3): 291-312.

Chen, N. (2011). Aerothermodynamics of turbomachinery: analysis and design, John Wiley & Sons.

Clemente, S. M., Diego R., Mauro T.,(2013). "Bottoming organic Rankine cycle for a small scale gas turbine: A comparison of different solutions." Applied Energy 106: 355-364.

Coello, A. C., Van D., and Lamont G. (2002). Evolutionary algorithms for solving multi-objective problems, Springer.

Cohen, H., Rogers, G. F. C., Saravanamuttoo H. I. H.and Saravanamutto H. (1987). "Gas turbine theory."

Cornell, J. A. (1990). How to apply response surface methodology, ASQC Milwaukee, WI.

Council, W. E. (2013). World Energy Perspective- Energy Efficiency Technologies.

Craig, H. and Cox H. (1970). "Performance estimation of axial flow turbines." Proceedings of the Institution of Mechanical Engineers 185(1): 407-424.

Crane, S. E., Berlin E. P., Abkenar, A. P., MAHALATKAR, K., Yongxi, H., Bowers T. and Stahlkopf K. E. (2012). Compressed air energy storage system utilizing two-phase flow to facilitate heat exchange, Google Patents.

Cravero, C. and Macelloni P. (2010). Design optimization of a multistage axial turbine using a response surface based strategy. 2nd International Conference on Engineering Optimization, Lisbon, Portugal.

Deb, K. (2012). Optimization for engineering design: Algorithms and examples, PHI Learning Pvt. Ltd.

Demeulenaere, A., Ligout A.and Hirsch C. (2004). Application of multipoint optimization to the design of turbomachinery blades. ASME Turbo Expo 2004: Power for Land, Sea, and Air, American Society of Mechanical Engineers.

Braembussche, R. (2008). Optimization and Computational Fluid Dynamics, Springer Berlin Heidelberg, January.

Dennis, B. H. E., Han, N., Dulikravich, Z. George S., Carlo P. (2001). "Multi-objective optimization of turbomachinery cascades for minimum loss, maximum loading, and maximum gap-to-chord ratio." International Journal of Turbo and Jet Engines 18(3): 201-210.

Denton, J. and Dawes W. (1998). "Computational fluid dynamics for turbomachinery design." Proceedings of the Institution of Mechanical Engineers, Part C: Journal of Mechanical Engineering Science 213(2): 107-124.

Denton, J. D. (1993). Loss mechanisms in turbomachines. ASME 1993 International Gas Turbine and Aeroengine Congress and Exposition, American Society of Mechanical Engineers.

Dixon, S. L. and Hall C. (2013). Fluid mechanics and thermodynamics of turbomachinery, Butterworth-Heinemann.

Dulikravich, G. S. and Dennis, B. H. (2000). Inverse design and optimization using CFD. European Congress on Computational Methods in Applied Sciences and Engineering, ECCOMAS.

Dunham, J. and Came, P. (1970). "Improvements to the Ainley-Mathieson method of turbine performance prediction." Journal of Engineering for Power 92(3): 252-256.

El-Khattam, W. and Salama M. (2004). "Distributed generation technologies, definitions and benefits." Electric power systems research 71(2): 119-128.

Elder, R., A. Tourlidakis and Yates, M. (2003). Advances of CFD in fluid machinery design, John Wiley & Sons.

Ellis, M. W., Von Spakovsky, M. R. and Nelson, D. J. (2001). "Fuel cell systems: efficient, flexible energy conversion for the 21st century." Proceedings of the IEEE 89(12): 1808-1818.

Elsayed, A. M. (2011). Heat transfer in helically coiled small diameter tubes for miniature cooling systems, University of Birmingham.

Energy, G. R. (2013). "Wind Energy Systems and Wind Farms." Retrieved 01/05, 2016.

EPA, A. (2011). Inventory of US greenhouse gas emissions and sinks: 1990-2009, EPA 430-R-11-005.

Farid, M. M., Khudhair, A. M., Razack, S. A. K. andAl-Hallaj, S. (2004). "A review on phase change energy storage: materials and applications." Energy conversion and management 45(9): 1597-1615.

Farooque, M. and Maru, H. C. (2001). "Fuel cells-the clean and efficient power generators." Proceedings of the IEEE 89(12): 1819-1829.

Fielding, L. (2000). "Turbine design: the effect on axial flow turbine performance of parameter variation."

Fonseca, C. M. and Fleming, P. J. (1993). Genetic Algorithms for Multiobjective Optimization: FormulationDiscussion and Generalization. ICGA, Citeseer.

Fort, J. (1983). "Thermodynamic analysis of five compressed-air energy-storage cycles." NASA STI/Recon Technical Report N 83: 28712.

Fraser, P. (2002). Distributed generation in liberalised electricity markets. International symposium on distributed generation: power system and market aspects.

Galanti, L. and Massardo, A. F. (2011). "Micro gas turbine thermodynamic and economic analysis up to 500kWe size." Applied Energy 88(12): 4795-4802.

Gen, M. and Cheng, R. (2000). Genetic algorithms and engineering optimization, John Wiley & Sons.

Glavatskaya, Y. P., Lemort, P., Vincent S., Osoko D. and Georges (2012). "Reciprocating expander for an exhaust heat recovery rankine cycle for a passenger car application." Energies 5(6): 1751-1765.

Goldstein, L., Hedman, B., Knowles, D., Freedman, S. I., Woods, R. and Schweizer, T. (2003). Gas-fired distributed energy resource technology characterizations, National Renewable Energy Laboratory.

Goldstein, L. H., Bruce, K., Freedman, D., Steven, I., Schweizer, R. and Tom (2003). Gas-fired distributed energy resource technology characterizations, National Renewable Energy Laboratory.

Gonzalez-Longatt, F. and Fortoul, C. (2006) "Review of the Distributed Generation Concept: Attempt of Unification."

Gorla, R. S. and Khan, A. A. (2003). Turbomachinery: design and theory, CRC Press.

Grazzini, G. and Milazzo, A. (2008). "Thermodynamic analysis of CAES/TES systems for renewable energy plants." Renewable Energy 33(9): 1998-2006.

Grazzini, G. and Milazzo, A. (2012). "A thermodynamic analysis of multistage adiabatic CAES." Proceedings of the IEEE 100(2): 461-472.

Hamzaoui, Y., Rodríguez, J., Hernández, J. and Salazar, V. (2015). "Optimization of operating conditions for steam turbine using an artificial neural network inverse." Applied Thermal Engineering 75: 648-657.

He, F., Li, Z., Liu, P., Ma, L. and Pistikopoulos, E. N. (2012). "Operation window and part-load performance study of a syngas fired gas turbine." Applied Energy 89(1): 133-141.

Hirsch, C. (2007). Numerical Computation of Internal and External Flows: The Fundamentals of Computational Fluid Dynamics: The Fundamentals of Computational Fluid Dynamics, Butterworth-Heinemann.

Holmes, A. S. H., Guodong, P., Keith, R. and Keith, R. (2004). Axial-flow microturbine with electromagnetic generator: design, CFD simulation, and prototype demonstration. Micro Electro Mechanical Systems, 2004. 17th IEEE International Conference on.(MEMS), IEEE.

Horlock, J. H. (1966). Axial flow turbines, Butterworth.

Horlock, J. H. (1973). Axial flow turbines: fluid mechanics and thermodynamics, Krieger Pub Co.

Hughes, W. L. (2001). Comments on the hydrogen fuel cell as a competitive energy source. Power Engineering Society Summer Meeting, 2001, IEEE.

Hummel, F., Lötzerich, M., Cardamone, P. and Fottner, L. (2005). "Surface roughness effects on turbine blade aerodynamics." Journal of Turbomachinery 127(3): 453-461.

Ibrahim, H., Belmokhtar, K. and Ghandour, M. (2015). "Investigation of Usage of Compressed Air Energy Storage for Power Generation System Improving-Application in a Microgrid Integrating Wind Energy." Energy Procedia 73: 305-316.

Ibrahim, H., Ilinca, A. and Perron, J. (2008). "Energy storage systems—characteristics and comparisons." Renewable and sustainable energy reviews 12(5): 1221-1250.

Ibrahim, H. Y., Ilinca, R., Dimitrova, A. and Perron, M. (2010). "Study and design of a hybrid wind–diesel-compressed air energy storage system for remote areas." Applied Energy 87(5): 1749-1762.

Ingersoll, E. D., Aborn, J. A. and Chomyszak, S. M. (2012). Compressor and/or expander device, Google Patents.

Howlett, R. L., Wang, X. Dooner, J., Clarke, M.,Krupke, J. and Christopher (2014). "6th International Conference on Sustainability in Energy and Buildings, SEB-14 Overview of Current Development in Compressed Air Energy Storage Technology." Energy Procedia 62: 603-611.

Jacobi, P., Xu, H. and David, W. (2013). VTG turbocharging-a valuable concept for traction application. CIMAC congress Shanghai.

Janiga, G. and Thévenin, D. (2008). "Optimization and computational fluid dynamics." Springer 1: 196.

Janjua, A. B., Khalil, M. S. and SAEED, M. (2013). "Blade profile optimization of kaplan turbine using cfd analysis."

Jannelli, E. M., Lavadera, M. and Falcucci, L. G. (2014). "A small-scale CAES (compressed air energy storage) system for stand-alone renewable energy power plant for a radio base station: A sizing-design methodology." Energy 78: 313-322.

Japikse, D. and Baines, N. (1994). Introduction to Turbomachinery, Concepts ETI, Inc. and Oxford University Press.

Kacker, S. and Okapuu, U. (1982). "A mean line prediction method for axial flow turbine efficiency." Journal of engineering for power 104(1): 111-119.

Kang, S. H. (2012). "Design and experimental study of ORC (organic Rankine cycle) and radial turbine using R245fa working fluid." Energy 41(1): 514-524.

Kentschke, T. (2004). Druckluftmaschinen als Generatorantrieb in Warmluftspeichersystemen, Papierflieger Verlag.

Khamis, A. B., Zulasyraf, M. A., Rahman, A., Bakar, A. Norazhar A. (2011). Development of mini scale compressed air energy storage system. Clean Energy and Technology (CET), 2011 IEEE First Conference on, IEEE.

Kim, T. S. and Ro, S. T. (1995). "Effect of control modes and turbine cooling on the part load performance in the gas turbine cogeneration system." Heat Recovery Systems and CHP 15(3): 281-291.

Kim, Y. and Favrat, D. (2010). "Energy and exergy analysis of a micro-compressed air energy storage and air cycle heating and cooling system." Energy 35(1): 213-220.

Klebanov, B. M., Barlam, D. M. and Nystrom, F. E. (2007). Machine elements: life and design, CRC Press.

Klein, A. (1966). "Investigation of the entry boundary layer on the secondary flows in the blading of axial turbines." BHRA T 1004.

Klein, A. (1966). "Untersuchungen über den Einfluß der Zuströmgrenzschicht auf die Sekundärströmungen in den Beschaufelungen von Axialturbinen." Forschung im Ingenieurwesen A 32(6): 175-188.

Klonowicz, P., Heberle, F., Preißinger, M. and Brüggemann, D. (2014). "Significance of loss correlations in performance prediction of small scale, highly loaded turbine stages working in Organic Rankine Cycles." Energy 72: 322-330.

Kokaew, V., Moshrefi, M. and Sharkh, S. M. (2013). "Maximum efficiency or power tracking of stand-alone small scale compressed air energy storage system." Energy Procedia 42: 387-396.

Korte, J., Salas, A., Dunn, H., Alexandrov, N., Follett, W., Orient, G. and Hadid, A. (2001). "Multidisciplinary approach to linear Aerospike nozzle design." Journal of Propulsion and Power 17(1): 93-98.

[99] Krahenbuhl, D., Zwyssig, C., Horler, H., and Kolar, J. (2008). Design considerations and experimental results of a 60 W compressed-air-to-electric-power system. Mechtronic and Embedded Systems and Applications, 2008. MESA 2008. IEEE/ASME International Conference on, IEEE.

L'Abbate, A., Fulli, G., Starr, F. and Peteves, S. D. (2007). "Distributed Power Generation in Europe: technical issues for further integration." Joint Research Center Institute for Energy. WWW. CARBONWARROOM. COM.

Laing, D., Lehmann, D., Bahl, C. and Züblin, A. (2008). Concrete storage for solar thermal power plants and industrial process heat. 3rd International Renewable Energy Storage Conference (IRES 2008), Berlin.

Langston, L., Nice, M. and Hooper, R. (1977). "Three-dimensional flow within a turbine cascade passage." Journal of Engineering for Power 99(1): 21-28.

Lawrence, K. L. (2012). ANSYS workbench tutorial release 14, SDC publications.

Leibowitz, H., Smith, I. and Stosic, N. (2006). Cost effective small scale ORC systems for power recovery from low grade heat sources. ASME 2006 International Mechanical Engineering Congress and Exposition, American Society of Mechanical Engineers.

Lemofouet-Gatsi, S. (2006). Investigation and optimisation of hybrid electricity storage systems based on compressed air and supercapacitors, Citeseer.

Lemofouet, S. and Rufer, A. (2005). Hybrid energy storage systems based on compressed air and supercapacitors with maximum efficiency point tracking. Power Electronics and Applications, 2005 European Conference on, IEEE.

Lemort, V., Declaye, S. and Quoilin, S. (2012). "Experimental characterization of a hermetic scroll expander for use in a micro-scale Rankine cycle." Proceedings of the Institution of Mechanical Engineers, Part A: Journal of Power and Energy 226(1): 126-136.

Lemort, V. Q., Sylvain, C., Lebrun, C. and Jean (2009). "Testing and modeling a scroll expander integrated into an Organic Rankine Cycle." Applied Thermal Engineering 29(14–15): 3094-3102.

Li, E. Y. (1994). "Artificial neural networks and their business applications." Information & Management 27(5): 303-313.

Li, S. and Dai, Y. (2014). "Design and Simulation Analysis of a Small-Scale Compressed Air Energy Storage System Directly Driven by Vertical Axis Wind Turbine for Isolated Areas." Journal of Energy Engineering: 04014032.

Li, Y., Wang, X., Li, D. and Ding, Y. (2012). "A trigeneration system based on compressed air and thermal energy storage." Applied Energy 99: 316-323.

Li, Y. W., Xiang, L., Dacheng, D. and Yulong (2012). "A trigeneration system based on compressed air and thermal energy storage." Applied Energy 99: 316-323.

Liss, W. E. (1999). "Natural gas power systems for the distributed generation market." Proc. Power-Gen Int.

Loose, V. W. (2011). "Quantifying the value of hydropower in the electric grid: Role of hydropower in existing markets." Sandia National Laboratories.

Lopes, J. P. H., Mutale, N, Djapic, J. and Jenkins, P. N. (2007). "Integrating distributed generation into electric power systems: A review of drivers, challenges and opportunities." Electric power systems research 77(9): 1189-1203.

Lundstedt, T., Seifert, E., Abramo, L., Thelin, B., Nyström, Å., Pettersen, J. and Bergman, R. (1998). "Experimental design and optimization." Chemometrics and intelligent laboratory systems 42(1): 3-40.

Luo, X. and Wang, J. (2013). "Overview of current development on compressed air energy storage." School of Engineering, University of Warwick,, Coventry, UK.

Luo, X. W., JIHONG (2013). "Overview of current development on compressed air energy storage." School of Engineering, University of Warwick,, Coventry, UK.

Luo, X. W., Jihong, D., Clarke, M., Jonathan K. and Christopher (2014). "Overview of current development in compressed air energy storage technology." Energy Procedia 62: 603-611.

Macchi, E. and Lozza, G. (1985). Comparison of Partial vs Full Admission for Small Turbines at Low Specific Speeds. ASME 1985 International Gas Turbine Conference and Exhibit, American Society of Mechanical Engineers.

Macchi, E. and Perdichizzi, A. (1981). "Efficiency prediction for axial-flow turbines operating with nonconventional fluids." Journal of Engineering for Gas Turbines and Power 103(4): 718-724.

Manual, A. U. S. (2000). "Ansys." Inc. Modeling, CFX 11.

Map watt. (2015). "PV panel works." Retrieved 22/06/2016, 2016.

Martin, J. (2009). "Distributed vs. centralized electricity generation: are we witnessing a change of paradigm." An introduction to distributed generation. Paris: HEC:< www. vernimmen. net/ftp/An_introduction_to_distributed_generation. pdf.

Massardo, A. and Satta, A. (1990). "Axial flow compressor design optimization: Part I—Pitchline analysis and multivariable objective function influence." Journal of Turbomachinery 112(3): 399-404.

Mengistu, T. T. (2005). Aerodynamic design and optimization of turbomachinery blading, Concordia University.

Micro, C. (2010). "Empowering people today for a smarter future tomorrow." COGEN EUROPE),(17.12. 2010).

Minutillo, M., Lavadera, A. L. and Jannelli, E. (2015). "Assessment of design and operating parameters for a small compressed air energy storage system integrated with a stand-alone renewable power plant." Journal of Energy Storage 4: 135-144.

Moffat, R. (1982). "Contributions to the theory of single-sample uncertainty analysis." ASME, Transactions, Journal of Fluids Engineering 104(2): 250-258.

Moroz, L., Govoruschenko, Y. and Pagur, P. (2005). Axial Turbine Stage Design: 1D/2D/3D Simulation, Experiment, Optimization—Design of Single Stage Test Air Turbine Models and Validation of 1D/2D/3D Aerodynamic Computation Results Against Test Data. ASME Turbo Expo 2005: Power for Land, Sea, and Air, American Society of Mechanical Engineers.

Moustapha, H. Z., Baines, F., Nicholas, C. and David, J. (2003). Axial and radial turbines, Concepts NREC Wilder, VT.

Moustapha, S., Kacker, S. and Tremblay, B. (1990). "An improved incidence losses prediction method for turbine airfoils." Journal of Turbomachinery 112(2): 267-276.

Murata, T. and Ishibuchi, H. (1995). MOGA: multi-objective genetic algorithms. Evolutionary Computation, 1995., IEEE International Conference on, IEEE.

Myers, R. H., Khuri, A. I. and Carter, W. H. (1989). "Response surface methodology: 1966–l988." Technometrics 31(2): 137-157.

Obayashi, S., Tsukahara, T. and Nakamura, T. (2000). "Multiobjective genetic algorithm applied to aerodynamic design of cascade airfoils." Industrial Electronics, IEEE Transactions on 47(1): 211-216.

Paloheimo, H. and Omidiora, M. (2009). A feasibility study on Compressed Air Energy Storage system for portable electrical and electronic devices. Clean Electrical Power, 2009 International Conference on, IEEE.

Peirs, J., Reynaerts, D. and Verplaetsen, F. (2004). "A microturbine for electric power generation." Sensors and Actuators A: Physical 113(1): 86-93.

Peng, W. W. (2008). Fundamentals of turbomachinery, John Wiley & Sons.

Pepermans, G. D., Haeseldonckx, J., Dries B., Ronnie, D. and William (2005). "Distributed generation: definition, benefits and issues." Energy policy 33(6): 787-798.

Perdichizzi, A. (1981). "Efficiency Prediction for Axial-Flow Turbines Operating with Nonconventional Fluids." Journal of Engineering for Power OCTOBER 103: 719.

Petrov, M. P., Arghandeh, R. and Broadwater, R. (2013). Concept and application of distributed compressed air energy storage systems integrated in utility networks. ASME 2013 Power Conference, American Society of Mechanical Engineers.

Piegl, L. and Tiller, W. (2012). The NURBS book, Springer Science & Business Media.

Pierret, S. and Braembussche, R. (1998). Turbomachinery blade design using a Navier-Stokes solver and artificial neural network. ASME 1998 International Gas Turbine and Aeroengine Congress and Exhibition, American Society of Mechanical Engineers.

Pilavachi, P. (2002). "Mini-and micro-gas turbines for combined heat and power." Applied Thermal Engineering 22(18): 2003-2014.

Pritchard, L. (1985). An eleven parameter axial turbine airfoil geometry model. ASME 1985 International Gas Turbine Conference and Exhibit, American Society of Mechanical Engineers.

Proczka, J., Muralidharan, K., Simmons, J. and Frantziskonis, G. (2013). "Guidelines for the pressure and efficient sizing of pressure vessels for compressed air energy storage." Energy Conversion and Management 65: 597-605.

Qiu, G., Liu, H. and Riffat, S. (2011). "Expanders for micro-CHP systems with organic Rankine cycle." Applied Thermal Engineering 31(16): 3301-3307.

Qiu, G. S., Li, Y., Jinxing L., Riffat, H. and Saffa, B. (2012). "Experimental investigation of a biomass-fired ORC-based micro-CHP for domestic applications." Fuel 96: 374-382.

Rahbar, K. (2016). Development and Optimization of Small Scale Radial Turbine for Waste Heat Recovery with Organic Rankine Cycle. PhD, University of Birmingham.

Rahbar, K., Mahmoud, S. and Al-Dadah, R. K. (2014). "Mean-line modeling and CFD analysis of a miniature radial turbine for distributed power generation systems." International Journal of Low-Carbon Technologies: ctu028.

Rahman, S. (2001). Fuel cell as a distributed generation technology. Power Engineering Society Summer Meeting, 2001, IEEE.

Rao, S. and Gupta, R. (1980). "Optimum Design of Axial Flow Gas Turbine Stage—Part I: Formulation and Analysis of Optimization Problem." Journal of Engineering for Gas Turbines and Power 102(4): 782-789.

Rhie, C. and Chow, W. (1983). "Numerical study of the turbulent flow past an airfoil with trailing edge separation." AIAA journal 21(11): 1525-1532.

Rogers, A. H., Wang, A., Xiongfei N. and Michael (2014). Compressed air energy storage: Thermodynamic and economic review. PES General Meeting| Conference & Exposition, 2014 IEEE, IEEE.

Ruiz-Romero, S. C., Antonio G., Rosario, M. and Antonio (2013). "Distributed generation: the definitive boost for renewable energy in Spain." Renewable energy 53: 354-364.

Saadatfar, B., Fakhrai, R. and Fransson, T. (2013). "Waste heat recovery Organic Rankine cycles in sustainable energy conversion: A state-of-the-art review." The Journal of Micro Trends in Energy and Sustainability 1(1): 161-188.

Safaei, H. and Aziz, M. J. (2014). Thermodynamic Analysis of a Compressed Air Energy Storage Facility Exporting Compression Heat to an External Heat Load. ASME 2014 12th Biennial Conference on Engineering Systems Design and Analysis, American Society of Mechanical Engineers.

Safaei, H. and Keith, D. W. (2014). "Compressed air energy storage with waste heat export: An Alberta case study." Energy Conversion and Management 78: 114-124.

Sasaki, D., Obayashi, S. and Kim, H.J. (2001). Evolutionary algorithm vs. adjoint method applied to sst shape optimization. The Annual Conference of CFD Society of Canada, Waterloo.

Schoenung, S. M. (2001). "Characteristics and technologies for long-vs. short-term energy storage." United States Department of Energy.

Sharma, A., Tyagi, V., Chen, C. and Buddhi, D. (2009). "Review on thermal energy storage with phase change materials and applications." Renewable and Sustainable energy reviews 13(2): 318-345.

Sharma, A., Tyagi, V. V., Chen, C. R. and Buddhi, D. (2009). "Review on thermal energy storage with phase change materials and applications." Renewable and Sustainable Energy Reviews 13(2): 318-345.

Shaw, D., Cai, J.Y. and Liu, C.T. (2012). "Efficiency analysis and controller design of a continuous variable planetary transmission for a CAES wind energy system." Applied Energy 100: 118-126.

Sieverding, C. (1985). "Recent progress in the understanding of basic aspects of secondary flows in turbine blade passages." Journal of Engineering for Gas Turbines and Power 107(2): 248-257.

Smith, S. (1965). A simple correlation of turbine efficiency. Von Karman Inst. for Fluid Dyn. Proc. of the Seminar on Adv. Probl. in Turbomachinery, Pt. 1 24 p(SEE N 79-21053 12-07).

SOCACIU, L. G. (2011). "Seasonal sensible thermal energy storage solutions." Leonardo Electronic Journal of Practices and Technologies(19): 49-68.

Stern, F., Muste, M., Beninati, M.L. and Eichinger, W. E. (1999). Summary of experimental uncertainty assessment methodology with example, IIHR Report.

Succar, S. and Williams, R. H. (2008). "Compressed air energy storage: theory, resources, and applications for wind power." Princeton environmental institute report 8.

Sukhatme, K. and Sukhatme, S. P. (1996). Solar energy: principles of thermal collection and storage, Tata McGraw-Hill Education.

Sun, H. L., Wang, X. and Jihong (2011). Management and control strategy study for a new hybrid wind turbine system. Decision and Control and European Control Conference (CDC-ECC), 2011 50th IEEE Conference on, IEEE.

Sun, H. W., Jihong, G., Shen, L. and Xing (2011). Study on a wind turbine in hybrid connection with a energy storage system. Electrical Engineering and Applied Computing, Springer: 39-52.

Tan, H. Z. C. (2013). Compressed Air Energy Storage.

Tempesti, D., Manfrida, G. and Fiaschi, D. (2012). "Thermodynamic analysis of two micro CHP systems operating with geothermal and solar energy." Applied Energy 97: 609-617.

Thevenin, D. and Janiga, G. (2008). " Computational Fluid Dynamics."

Tveit, T.M. and Fogelholm, C.J. (2006). "Multi-period steam turbine network optimisation. Part I: Simulation based regression models and an evolutionary algorithm for finding D-optimal designs." Applied Thermal Engineering 26(10): 993-1000.

Van den Braembussche, R. A. (2008). Numerical optimization for advanced turbomachinery design. Optimization and Computational Fluid Dynamics, Springer: 147-189.

Venkataramani, G. P., Prasanna, R., Wang,V. and Jihong (2016). "A review on compressed air energy storage–A pathway for smart grid and polygeneration." Renewable and Sustainable Energy Reviews 62: 895-907.

Villela, D. K., Vijayanathan, V., Scott, A., Frantziskonis, M., Deymier, G. and Muralidharan K. (2010). Compressed-air energy storage systems for stand-alone off-grid photovoltaic modules. Photovoltaic Specialists Conference (PVSC), 2010 35th IEEE, IEEE.

Wakeley, G. R. (1997). The Optimsation of Steam Turbine Design. PhD, University of Newcastle upon Tyne.

Wang, J. L., Yang, X., Li S., Leonid, M., Nan M., Derby, S. and James, W. (2011). "Mathematical modeling study of scroll air motors and energy efficiency analysis—part II." Mechatronics, IEEE/ASME Transactions on 16(1): 122-132.

Wei, N. (2000). "Significane of loss models in aerothermodynamic simulation for axial turbines."

Whitfield, A. and Baines, N. C. (1990). "Design of radial turbomachines."

Wilcox, D. C. (1998). Turbulence modeling for CFD, DCW industries La Canada, CA.

Wilson, D. G. and Korakianitis, T. (2014). The design of high-efficiency turbomachinery and gas turbines, MIT press.

Wolf, D. (2011). Methods for Design and Application of Adiabatic Compressed Air Energy: Storage Based on Dynamic Modeling, Laufen.

Wood, H. J. (1963). "Current Technology of Radial-Inflow Turbines for Compressible Fluids." Journal of Engineering for Gas Turbines and Power 85(1): 72-83.

Xiao, X., McCarter, A. A. and Lakshminarayana, B. (2001). "Tip clearance effects in a turbine rotor: part I—pressure field and loss." Journal of turbomachinery 123(2): 296-304.

Yahya, S. (2010). Turbines Compressors and Fans, Tata McGraw-Hill Education.

Yang, W. and Xiao, R. (2014). "Multiobjective optimization design of a pump–turbine impeller based on an inverse design using a combination optimization strategy." Journal of Fluids Engineering 136(1): 014501.

Zhai, H., Dai, Y., Wu, J. and Wang, R. (2009). "Energy and exergy analyses on a novel hybrid solar heating, cooling and power generation system for remote areas." Applied Energy 86(9): 1395-1404.

Zhang, Y.W., Yu-Ting, X., Guo-Dong, M., Chong-Fang J., Wei-Ning, L., Shan-Wei Y., Kai Y., and Fu-Bin (2014). "Development and experimental study on organic Rankine cycle system with single-screw expander for waste heat recovery from exhaust of diesel engine." Energy 77: 499-508.

Zhu, Z. and Chan, Y. (1998). An engineering study of genetic algorithms oriented to geometric design applications. Proceedings of the 7th AIAA/USAF/NASA/ISSMO Symposium on Multidisciplinary Analysis and Optimization.

Zobaa, A. and Cecati, C. (2006). A comprehensive review on distributed power generation. Power Electronics, Electrical Drives, Automation and Motion, 2006. SPEEDAM 2006. International Symposium on, IEEE.

Appendix A

Inlet Cone Modelling

The inlet cone was simulated to select the optimum cone design that can achieve good flow guidance with minimum pressure and shock losses. The steady state simulation of the inlet cone was conducted using ANSYS CFX 16.2 with unstructured mesh and SST turbulence model.

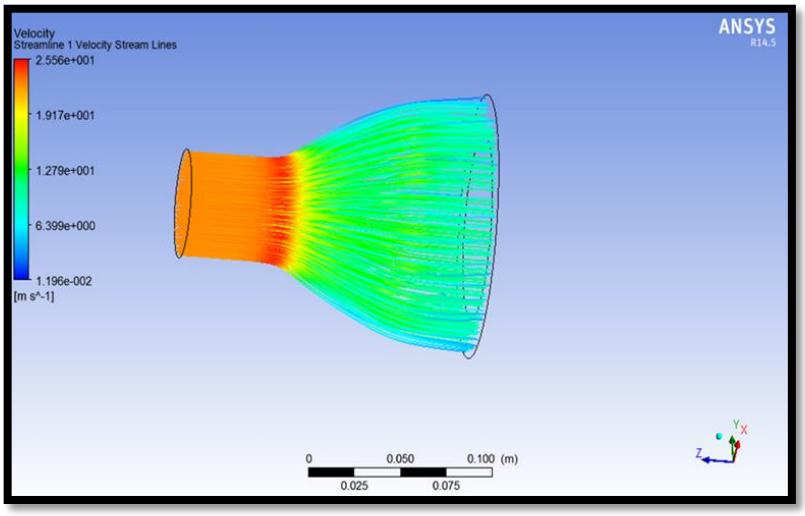

Inlet Cone with Nozzle Modelling

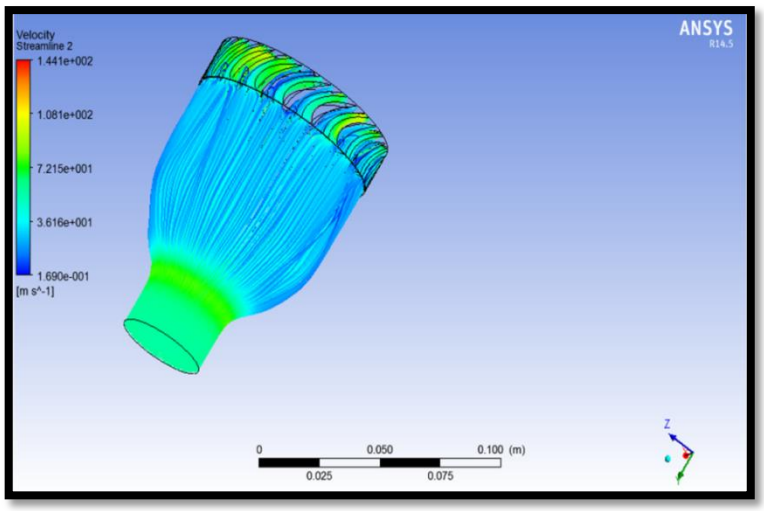

Appendix B

Uncertainty in Temperature Calculations

Mean (T_{avg})	The average of all temperature values	$T_{avg} = \frac{\sum_{i=1}^{N} T_i}{N}$
Uncertainty in measurments (ΔT)	Uncertainty in a single temperature measurments	$\Delta T = \sigma = \sqrt{\frac{\sum_{i=1}^{N}(T_i - T_{avg})^2}{N}}$
Uncertainty in Mean (ΔT_{avg})	Uncertanity in the mean (T)	$\Delta T_{avg} = \frac{\sigma}{\sqrt{N}}$
Measured value (T_m)	The final temperature value as a function of the average temperature and mean uncertanity	$T_m = T_{avg} \pm \Delta T_{avg}$

Temperature repeated measurments:

Power (W)	T_1(^{o}C)	T_2(^{o}C)	T_3(^{o}C)
397	33.61	34.22	33.84

Uncertainty Calculations:

Power	ΔT_{avg}	$(T_1 - T_{avg})^2$	$(T_1 - T_{avg})^2$	$(T_1 - T_{avg})^2$	Sum/3	Root	Uncertainty
397	33.84	0.0016	0.0324	0.0196	0.017866	0.1336	0.077172246

Appendix C

Inlet Turbine Duct

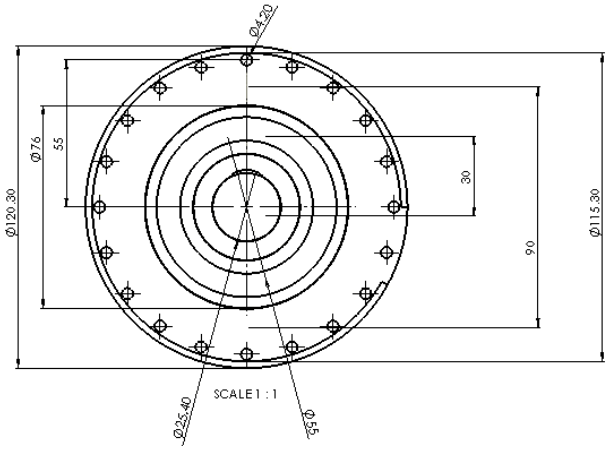

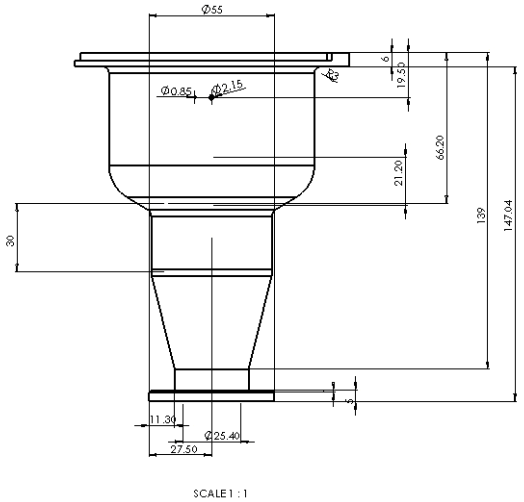

Appendix B: Inlet cone with stator

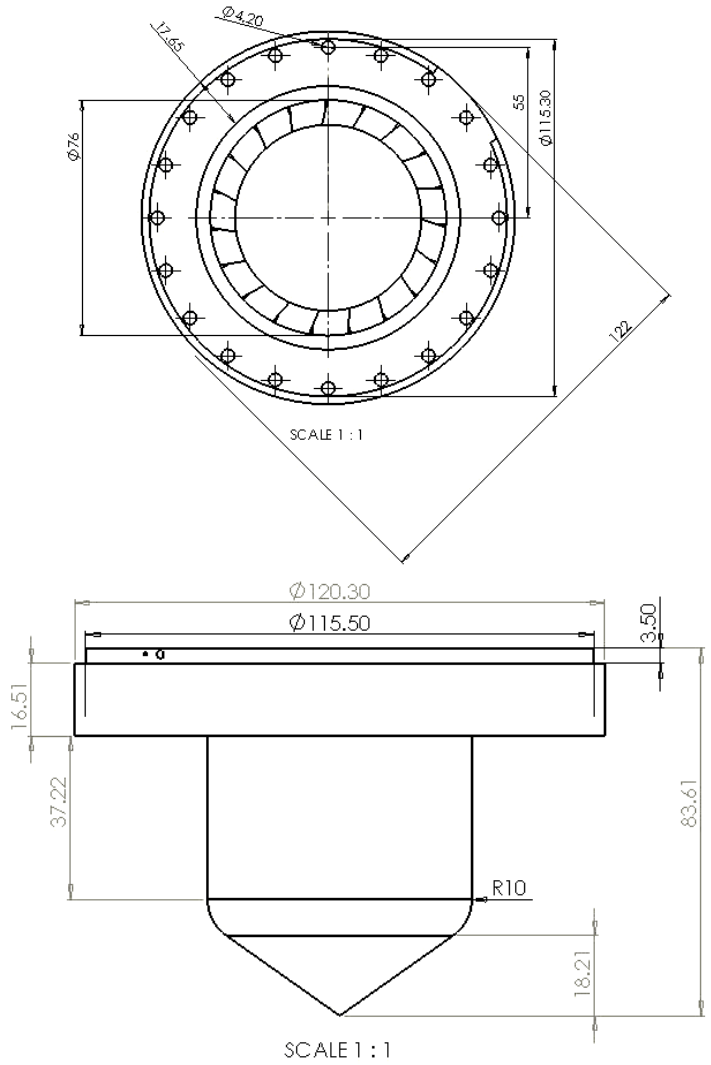

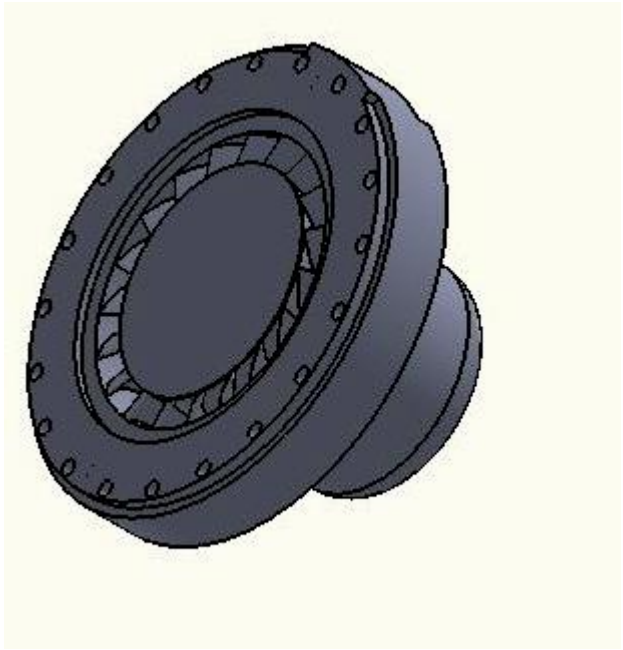

Appendix B: Rotor with shaft

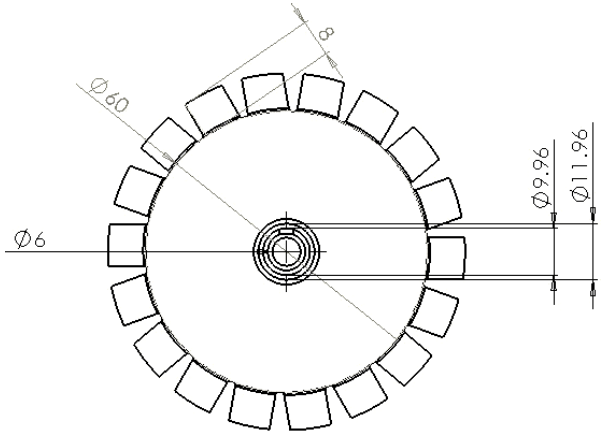

SCALE 1 : 1

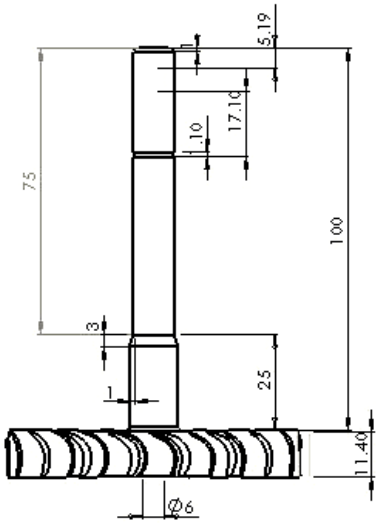

SCALE 1 : 1

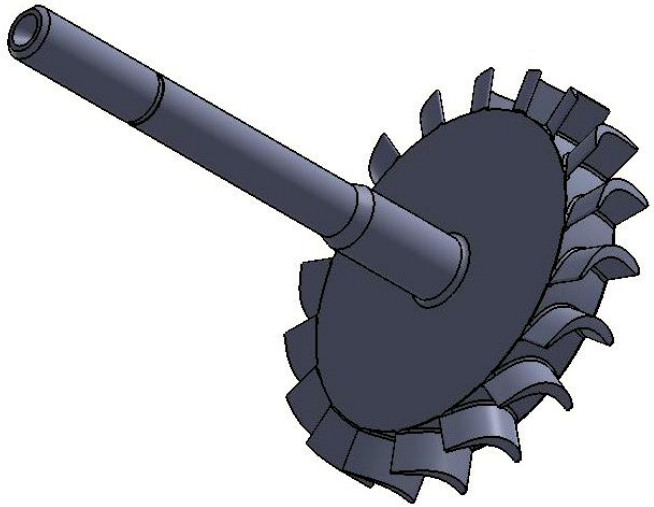

Appendix B: Rotor casing